THE ACOUSTICALLY-DRIVEN MICROFLUIDIC EXTENSIONAL RHEOMETER: DEVELOPMENT, VALIDATION, AND APPLICATION TO COMPLEX LOW-VISCOSITY FLUIDS

Amarin George M^{c}Donnell

Department of Mechanical and Aerospace Engineering

Monash University

This dissertation is submitted for the degree of

Doctor of Philosophy

Supervisor:
Dr Prabhakar Ranganathan

Associate supervisors:
Prof. James Friend
Prof. Leslie Yeo

Monash University 2016

To keep the balance is to stay happy

I would like to dedicate this thesis to my loving parents. To mum, for always believing I would finish as a matter of fact, supporting me from day-to-day, and keeping me relaxed and positive. To dad, for always making me think to aim higher, and for always being certain that I can achieve excellence in whatever I choose to pursue.
I love you both very much.

Acknowlegements

I would like to acknowledge and thank James Friend for giving me my start in research and his continued guidance, and to Prabhakar Ranganathan for helping me to get "my license to do research" and teaching me the importance of thorough analysis and explanation to move forward. I would also like to thank Leslie Yeo for his continued assistance and support through these years. I must also thank Pradipto Bhattacharjee and Duc At Nguyen, who both mentored me and were always ready to share their knowledge.

I would also like to acknowledge the fun I have had amongst my fellow PhD candidates. My fellow group members Amgad, Sarah, Sid, Chandi, and Emma were there to share the fun and the pain. I also enjoyed my collaborative work with Sharad, Jen, and Naveen very much. I fondly recall the early soccer days with Mr Collins, Sean, Nick, and Dave, and the triumphant soccer days with Ian, Rob, Nick, Andrew, Vedran and Brandon. I also enjoyed the jibes and banter with Mike, and the boys at the MCN: Sean, Ricky, and Zoran. I have also loved screaming through the hills with my motorbike boys, Mathew and Gopesh.

There are also those who mixed up my experiences on campus, Steve and Jando early on, Wenger at New Horizons later on, and my stalwart partner in crime, Russo. Off campus, I was always able to let off some steam with my teamsters in the Redwings FC: Mish, Xiao, Tze, Benny, Basim, Vic, Thanh, and Jez; The Fellas and our man seshs with Ev, Baig, Mel, and Pas; and my gamers and danger men: Ed, Gobbo, Peter, Fish, and Koenen. Of course, I have to also acknowledge my bro and sis, Conrad and Sunsanee, for keeping me routinely entertained at home and abroad. I couldn't have done any of this without the love and support of mum and dad, thank you. All these people have helped me maintain perspective and kept me loving life on the outside so that I could do what I needed to do without losing my mind.

Amarin George M^{c}Donnell

Ringwood North, March 2016

Abstract

The emergence of rheometric techniques for extensional flows is relatively recent [1, 2] when compared to methods for shear flows [3]. Two prominent extensional rheometry techniques involve creating liquid filaments that thin under the action of surface tension. Stress balances [2, 4–6] are used to determine the extensional viscosity from measurements made on such filaments. In the filament stretching extensional rheometer (FiSER) [4] a fluid sample is placed between two end-plates that are mechanically drawn apart at a controlled exponential rate. Another prominent technique, capillary break-up extensional rheometry (CaBER) [6, 7], also employs mechanical end-plates which are rapidly moved to a fixed separation to study the dynamics of liquid bridges. These two techniques have been successful in assessing the extensional properties of a wide variety of complex fluids from polymer solutions to suspensions [2, 4, 8]

Although these two uni-axial extensional flow techniques have gained acceptance they are limited in their utility when analysing low-viscosity fluids. The stresses that occur in these flows can be non-dimensionalised so that the importance of different effects can be established [7]. These experiments tend to use larger sample sizes, which can lead to an adverse asymmetry in the filament in which gravity causes the filament to sag. The mechanical operation of these devices can induce vibrations that propagate throughout the filament, which are not accounted for by stress balance analysis, and are not damped sufficiently in low-viscosity fluids. Such inertial effects are exacerbated by the large samples sizes. These issues make repeatable readings impractical in low-viscosity fluids [7]. Recent modifications of the CaBER concept permit improved access to low-viscosity fluids [9–14]. Nevertheless, it is still a challenge to obtain viscosities of complex aqueous fluids of viscosities of the order of 1 mPa·s.

This thesis proposes and demonstrates a new microfluidic technique for extensional rheometry that harnesses the unique capabilities afforded by surface acoustic waves (SAW) to generate liquid filaments that thin under surface tension effects. This approach has three key attributes that are advantageous for the analysis of thin and complex fluids in extensional flow:

- SAWs are able to generate stable fluid filaments from low-viscosity fluids.
- Small sample volume sizes mean that effects due to gravity and inertia scale down favourably. Critically, this also permits the analysis of materials that are difficult to obtain in large volumes.
- SAWs have the ability to manipulate fluids whilst not damaging delicate fluid constituents.

This technique is used to analyse many novel fluids for a variety of purposes: validating theoretical predictions, optimising promising industrial fluids, and providing insights into unusual phenomena. These studies serve to validate the acoustically-driven capillary break-up approach as a valuable rheometric technique. The thesis is presented in the "thesis including published works" format wherein publications are combined with explanatory notes and additional unpublished material[1].

The dissertation begins by providing a background on rheology, and explains the need for extensional experiments to extract the extensional properties of fluids. It also reviews the limitations of the aforementioned conventional extensional techniques, specifically the problems they encounter when analysing low-viscosity fluids. Additionally, it defines the two fundamental challenges to be overcome in a filament-based extensional rheometer: the creation of a filament to reliably measure the neck radius as a function of time, and converting this data into a measurement of rheological properties. The novel ways in which SAWs manipulate fluids is then discussed, and their ability to generate fluid filaments is proposed as a means for extensional rheometry of low-viscosity fluids.

The next chapter discusses the experimental approach that addresses the first of the fundamental challenges mentioned in the chapter above. It examines the obstacles and solutions involved with the development of the acoustically-driven capillary break-up device and those pertaining to the analysis of the low-viscosity fluid filament break-up data that it produces. Experimental challenges include the fabrication, operation, and testing of both the SAW device and the experimental rig which harnesses the device. Other challenges are the high spatial and temporal data resolution needed to distinguish differences between microfluidic break-up events of different but similar thin fluids. Despite these difficulties in development, the experimental system is shown to be suitable for rheological analysis and possesses considerable advantages, including the use of small test volumes, the stabilisation of thin filaments by SAWs, and the ability to harmlessly manipulate delicate particle suspensions and macromolecular solutions.

---

[1] Monash University allows theses that include publications, please see the link below
http://www.monash.edu/graduate-research/supervisors-and-examiners/examiners/publication

The following chapter is in the form of a publication [15] that demonstrates the validity of the acoustically-driven capillary break-up technique for rheological measurement. It also defines the conditions under which SAWs can be used to create liquid filaments, complementing the previous chapter. However, the main focus is the comparison of our experimental results with data from accepted rheological experiments, and the quantification of our data using standard rheological analysis. Good agreement is found from necking data of low-viscosity Newtonian and non-Newtonian fluids. Moreover, it is demonstrated that stress-balance analysis can be used here to convert the filament decay data from a viscoelastic strain-hardening fluid directly to stress and viscosity measurements. Finally, the technique is utilised in observing the effects of extensional flow on a small volume of low-viscosity solution containing a dissolved protein, for which measurements showed an interesting multi-stage filament break-up process.

The subsequent chapter discusses the generic difficulties of extracting extensional viscosity using stress-balance analysis from the capillary break-up of low-viscosity fluids that do not exhibit strain-hardening; it then develops a new approach for such fluids. Analysis using a simple mid-filament stress balance, as seen in the previous chapter, is appropriate when thread-like filaments are formed; this occurs in the break-up of viscoelastic solutions, where long-lived filaments develop towards final break-up. However, many other fluids, particularly low-viscosity solutions, do not form near-cylindrical filaments. This leads to stress-balance analysis being complicated by the dynamic contributions of axial filament curvature, the difficulties of which are investigated here. Thus, extensive non-dimensionalised break-up data of Newtonian fluids is used to develop a calibration method that allows the extraction of extensional viscosity for unknown fluids without resorting to the prohibitively complicated approach of using full filament analysis to determine extensional viscosity.

The next chapter is a publication [16] where the calibration method of extracting extensional viscosities is used with data from the acoustically-driven capillary break-up technique to pursue the validation of previously untested theoretical predictions of "active matter" bulk properties in extensional flow. Active matter theory [17–19] describes suspensions composed of individual particles that are self-propelled, where their net average alignment contributes to the overall stresses and viscosity of the suspension. This theory represents active bodies as axisymmetric particles that exert a net thrust along their primary axis, producing hydrodynamic dipoles that drive the surrounding fluid along their lengths. Active particles can be placed into two groups: "pushers" drive a tensile flow along their principal axis [20], while conversely "pullers" generate a contractile flow [17]; the positive hydrodynamic dipoles created by pusher particles are predicted to lower suspension viscosity below that of an equivalent passive particles suspension, while the negative hydrodynamic dipoles of pullers will increase viscosity. Predictions have been validated by experimental findings for pushers [21–23] and pullers [24] in shear flow, but not in extensional flow. Such systems are exemplified by living materials, like suspensions of motile microbes or the cytoskeletal polymers in ATP-powered white blood cells. However, such delicate biological suspensions are difficult to prepare in high volumes, and typically require aqueous media to suspend them and enable their motility, aspects that pose problems for alternative extensional techniques but are accommodated by the acoustically-driven capillary break-up technique. We measure the extensional viscosities of pushers using bacterial and mouse sperm suspensions, and pullers using algal suspensions. We extend a model previously proposed for dilute suspensions of active particles to obtain predictions at moderate and high concentrations. The experimental data is shown to be in good agreement with these predictions. The comparison identifies some key parameters that are geometry dependent that can strongly influence the extensional viscosity of these materials. The agreement between results and theoretical predictions demonstrates that the acoustically-driven capillary break-up technique is useful in testing low-viscosity suspensions that contain delicate particles whose integrity must be preserved.

The technique and approach for non-strain-hardening fluids is used in the next chapter to analyse the properties of particle suspensions with different morphologies that, unlike the swimming particles discussed above, are "passive". Particle suspensions are being used in wide-ranging applications [25], and their utility in the development of innovative electronic technologies is the focus of recent research [26–32]. The industrial scale implementation these particles is likely to occur *via* some form of spraying or jetting as low-viscosity suspensions, which will require an understanding of their extensional properties. The acoustically-driven capillary break-up technique overcomes the technical challenges posed by low viscosities and suspended particles, the latter of which can cause problems in extensional rheometers that require nozzles. We perform the rheological characterisation of these suspensions in Newtonian solutions and detail the changes in extensional viscosity with regards to particle volume fraction. We witness strong particle size and shape related behaviour and suggest an empirical relationship between relative viscosity and particle size for spherical particles. We study the potential role that particle clustering may play on suspension viscosity *via* model predictions and fractal analysis. These observations support what little experimental extensional data there is for like suspensions and reinforces the suggestion that hydrodynamic effects alone cannot explain the effects on bulk fluid properties in full. Furthermore, shear testing shows that changes in shear viscosity with volume fraction generally correlate with changes seen in extensional viscosity — although there is no universal relationship between extensional and shear viscosity for non-Newtonian fluids the general trends seen here as these suspensions approach their maximum particle packing fractions are in-line with expectations, suggesting further validation of the technique. Thus, we extract extensional viscosity data for these complex fluids and demonstrate that this experimental technique may be applied to the tailoring of other particle suspensions to facilitate the development of nano/micro particle inks and coatings.

The following chapter is a publication [33] in which we utilise the advantages of the technique to study copper nanowire suspensions, where a polymer additive is required to prevent particle aggregation. Depositions of these suspensions show favourable electrical and physical properties [29, 34] that has led to the development of novel electronics [34–39]. As discussed in the previous chapter, the routine harnessing of these suspensions will probably require them to be applied as low-viscosity fluids *via* extensional flows. These low-viscosity fluids pose difficulties for alternative extensional techniques due to the high-aspect ratio of the particles, the polymer additive, and the fact that it is currently difficult to synthesise large quantities of these particles; these challenges are surmounted by the acoustically-driven capillary break-up technique. The elastic behaviour, quantified by the relaxation time, of these suspensions is found to depend on the ratio between polymer and nanowire content. Subsequently, we optimise our suspensions to minimise the polymeric contribution to largely isolate the particle contributions to viscosity. Like the previous chapter, we find correspondence between shear and extensional viscosity measurements.

The investigation in the final chapter does not involve any particles, but studies a viscoelastic polymer-surfactant mixture using extensional rheology to reveal the interactions between the polymer and surfactant. Combining polymers and surfactants in solutions can result in interactions that have significant and counter-intuitive effects on bulk fluid properties [40, 41]. Despite the extensive study of molecular interactions between polymers and surfactants by others, and their importance to many industrial processes and applications, there are few studies pertaining to their bulk properties under extensional flow. A specific case is that of hydroxypropylmethyl cellulose (HPMC) and sodium dodecylsulfate (SDS) in an aqueous solution, which is studied in this chapter. Using our acoustically-driven capillary break-up device we demonstrate that the properties of these polymer solutions are sensitive to surfactant concentrations, particularly in extensional flows. Capillary break-up experiments also show that material properties are dependent on the evolution of filament decay.

This study once again exhibits the general correspondence between extensional and shear viscosity results, and the technique's ability to qualitatively match theoretical predictions that are based on molecular interactions.

The concluding discussion summarises the contributions this thesis has made to rheology and the understanding of novel complex fluids. It also serves to highlight the questions raised by this thesis and provides recommendations on possible future work.

General Declaration

In accordance with Monash University Doctorate Regulation 17.2 Doctor of Philosophy and Research Master's regulations the following declarations are made:

I hereby declare that this thesis contains no material which has been accepted for the award of any other degree or diploma at any university or equivalent institution and that, to the best of my knowledge and belief, this thesis contains no material previously published or written by another person, except where due reference is made in the text of the thesis.

This thesis includes 3 original papers published in peer reviewed journals. The core theme of the thesis is the development, validation, and application of a new rheometer that analyses the extensional rheological properties of complex low-viscosity fluids. The ideas, development and writing up of all the papers in the thesis were the principal responsibility of myself, the candidate, working within the Department of Aerospace and Mechanical Engineering under the supervision of Dr Prabhakar Ranganathan, and the associate supervision of Prof. James Friend and Prof. Leslie Yeo.

The inclusion of co-authors reflects the fact that the work came from active collaboration between researchers and acknowledges input into team-based research.

In the case of 3, 5, and 7 my contribution to the work involved the following:

Thesis chapter	Publication title	Publication status	Nature and extent of candidate's contribution
3	Extensional flow of low-viscosity fluids in capillary bridges formed by pulsed surface acoustic wave jetting	published	Dr Pradipto K. Bhattacharjee and Amarin G. McDonnell jointly conceived and invented the experimental technique used in this paper. Dr Bhattacharjee guided investigation and led analysis efforts; Amarin G. M^{c}Donnell performed preparation and experimentation, and data processing. The publication was written jointly by all authors.
5	Motility induced changes in viscosity of suspensions of swimming microbes in extensional flows	published	Amarin G. McDonnell performed preparation and performed and defined experimentation, data processing, and analysis. The manuscript was drafted primarily by Amarin G. M^{c}Donnell who also responded to reviewers' comments.
7	Extensional viscosity of copper nanowire suspensions in an aqueous polymer solution	published	Amarin G. M^{c}Donnell performed preparation and performed and defined experimentation, data processing, and analysis. The manuscript was drafted primarily by Amarin G. McDonnell who also responded to reviewers' comments.

I **have not** renumbered sections of submitted or published papers in order to generate a consistent presentation within the thesis.

Signed: [redacted]
Date: **23/2/2016**

Under the Copyright Act 1968, this thesis must be used only under the normal conditions of scholarly fair dealing. In particular no results or conclusions should be extracted from it, nor should it be copied or closely paraphrased in whole or in part without the written consent of the author. Proper written acknowledgement should be made for any assistance obtained from this thesis.

I certify that I have made all reasonable efforts to secure copyright permissions for third party content included in this thesis and have not knowingly added copyright content to my work without the owner's permission.

Signed: [redacted]
Date: **23/2/2016**

Contents

Contents **xv**

List of Figures **xix**

List of Tables **xxix**

1 Introduction **1**

1.1 Rheology and low-viscosity fluids 1

1.2 Manipulating fluids using surface acoustic waves 10

1.3 Thesis outline 12

1.3.1 Chapter 2 12

1.3.2 Chapter 3 13

1.3.3 Chapter 4 13

1.3.4 Chapter 5 13

1.3.5 Chapter 6 14

1.3.6 Chapter 7 14

1.3.7 Chapter 8 14

1.3.8 Chapter 9 15

2 Development of the Acoustically Driven Microfluidic Rheometer (ADMiER) **17**

2.1 Introduction 17

2.2 Principles of Surface Acoustic Waves (SAWs) 18

2.3 SAW device design and fabrication 19

2.4 SAW device operation and testing 20

2.5 Experimental concept and design 25

2.5.1 Experimental rig design 26

2.6 Videography and lighting 30

2.7 System testing and advantages 31

2.7.1 Small sample volumes 31
2.7.2 SAW induced suppression and stabilisation 32
2.7.3 Freedom from nozzle related problems 35
2.8 Data extraction 35

3 Publication: Extensional flow of low-viscosity fluids in capillary bridges formed by pulsed surface acoustic wave jetting 39
3.1 Introduction 39
3.2 Publication 40

4 Extraction of extensional viscosities for low-viscosity fluids 55
4.1 Introduction 55
4.2 Extraction of extensional rheological properties from filament break-up data 56
4.3 Mid-filament data analysis 57
4.3.1 Extensional viscosity extraction for near-cylindrical filaments close to break-up 57
4.3.2 Mid-filament stress balance for low-viscosity Newtonian fluids . . . 58
4.3.3 Tensile factor fitting 64
4.4 Calibration chart and extensional viscosity extraction 66
4.4.1 Effective tensile factor *via* analytical predictions and experimental regression curve 73

5 Publication: Motility induced changes in viscosity of suspensions of swimming microbes in extensional flows 75
5.1 Introduction 75
5.2 Publication 77

6 Extensional properties of low-viscosity particle suspensions 97
6.1 Introduction 98
6.2 Methods 100
6.2.1 Particle selection and preparation 100
6.2.1.1 Glass micro beads 100
6.2.1.2 Silver nano particles 101
6.2.1.3 Glass micro fibres 102
6.2.1.4 Silver micro nuggets 102
6.2.2 Extensional and shear rheometry 102

6.2.3 Particle imaging 102
6.3 Results and discussion 103
6.3.1 Krieger-Dougherty expression for extensional viscosity 103
6.3.2 Cuboid particles 104
6.3.2.1 Comparison of shear and extensional viscosities 104
6.3.2.2 Concentration and size dependence of extensional viscosity 105
6.3.3 Micro-nuggets and glass rods 111
6.3.3.1 Comparison of shear and extensional viscosities 111
6.3.3.2 Concentration dependence of extensional viscosity 112
6.4 Conclusion 113

7 Publication: Extensional viscosity of copper nanowire suspensions in an aqueous polymer solution 115
7.1 Introduction 115
7.2 Publication 116

8 Extensional viscosity of amphiphilic polymer and surfactant mixtures 125
8.1 Introduction 125
8.2 Experimental 128
8.2.1 Materials and preparation 128
8.2.2 Solution properties 128
8.2.3 Extensional viscosity extraction from filament break-up data 130
8.3 Results and discussion 131
8.3.1 Properties at early strains 131
8.3.2 Properties at late strains 135
8.4 Conclusion 138

9 Conclusions 141
9.1 Contributions 141
9.2 Continuing and future work 143

References 147

List of Figures

1.1 Blue arrows and their magnitude represent velocity. The velocity differences, or velocity gradient, result in stresses between regions of different velocity. 2

1.2 The stretching of a finite volume at t_0 in the z-axis (red arrows) to an elongated form at t_1 represents the deformation that occurs under uni-axial extensional flow. It can be seen that through the conservation of volume that the dimensions in the xy-plane must contract (green arrows). 4

1.3 This diagram describes the basics that lead to capillary break-up, where R_1 and P_1 are the mid-filament radius and radial pressure, respectively; R_2 and P_2 are the axial radius and pressure, respectively; and H and R_0 are the height and distal radius of the filament, respectively. P_1 exerts a contractile stress on a fluid filament, which is resisted by P_2. A certain aspect ratio H/R_0 will lead to $R_1 < R_2$ and thus $P_1 > P_2$, causing instability and resulting in filament collapse about the mid-filament. 5

1.4 An image sequence of viscoelastic fluid filament of 0.31 wt% polyisobutylene in polybutene being stretched in a FiSER. Source: [2]. 6

1.5 An image sequence of 0.1 wt% PEO in glycerol being stretched in a CaBER device. The light band denotes the point at which filament radius decay measurements are taken. Source: [42]. 7

1.6 Operability plot of the CaBER showing that cases below Oh ≈ 0.14 are difficult to assess. In the filament break-up case, the Deborah number De is the ratio of the time λ (discussed in Chapters 7 and 8) required for a material to adjust to the imposed stresses and flow of the break-up and the characteristic time of break-up. Source: [42]. 8

1.7 This schematic shows how the combination of transverse and longitudinal components result in the retrograde fashion with which a fixed particle at the surface moves when subjected to Rayleigh waves. It should be noted that the waves are largely confined to the surface, and that their amplitude diminishes exponentially with depth into the substrate [43]. Copyright 2009, AIP Publishing LLC. 11

2.1 As SAWs encounters a sessile droplet, SAW energy enters the droplet *via* the θ_R due to the difference between the speed of sound of the substrate c_s and that of the fluid c_l. The amplitude of the surface SAWs attenuates exponentially as wave energy is transferred to the droplet [43]. Copyright 2009, AIP Publishing LLC. 18

2.2 10 × 20 mm LN SAW device with a quiescent droplet resting on a hydrophobic spin-coated Teflon® strip. Note the curved chromium-aluminium IDTs focus to the point at which the droplets rests. 19

2.3 The first signal generator (SG1) sends a 1.5 ms long burst signal to the second signal generator (SG2). SG2 then produces a sinusoidal signal to the amplifier (Amp), which boosts the signal's power, where the output is then delivered to the SAW device. This results in the sessile droplet, which is resting on the SAW device, to extend into an elongated filament that then contacts with an opposing plate just as the 1.5 ms burst ends, allowing the newly formed liquid bridge to decay. 21

2.4 Plotting input power against LDV measured surface velocity on a log-log plot shows the expected slope of 1/2 relationship anticipated by Eqn. 2.5. . 24

2.5 Increasing the power injected into a sessile droplet effects large behavioural changes. As discussed in Chapter 3, the dimensionless power associated with the actuation of fluid using this technique can be defined as $\Pi = Pc_s/\sigma R_d$, where P is the SAW forcing power, c_s is the speed of sound in LN, σ is the subject fluid surface tension, and R_d is the initial droplet radius. In the case of a 1.2 mm diameter water droplet, (a) low power ($\Pi \lesssim 3$) induces slight deformation of the droplet, (b) intermediate power ($3 \lesssim \Pi \lesssim 50$) causes the droplet to turn into a high-aspect ratio filament, and (c) high powers ($\Pi \gtrsim 50$) result in the atomisation of the droplet. 25

2.6 CAD images of the 162 mm wide and 92 mm tall PVC rig with fittings designed to house and operate a SAW device to generate and view filament break-up. The image on the left shows the device turned upwards, allowing for the application of the sample droplet. The right image shows the device turned downwards so that it faces the opposing surface of the z-axis receiver plate. Also shown is the positioning of the camera and light source, with the red line denoting the line of sight that views the break-up event. Note that the z-axis tower slides out to allow the device holder to rotate, after which the z-axis tower slides back into position. 27

2.7 A montage of device operation showing a water droplet subjected to a 1.5 ms SAW burst. After the cessation of the SAW burst and the formation of a liquid bridge, surface tension driven thinning contracts the filament, driving uni-axial extensional flow. 27

2.8 (a) The sample micro-droplet is loaded onto the SAW device. (b) The device holder is then flipped so that the droplet is facing the opposing surface, where small adjustsments can be made to align the droplet with the target surface using the x-y-axis lateral screws. (c) The z-axis screw is turned to finalise the opposing target elevation, defining the resulting filament aspect ratio. The red line denotes the line of sight that the camera and light source are aligned with, which permits the viewing of the event; the event can also be viewed perpendicular to this line. The SAW device in this rig is 20 mm long and 10 mm wide. 28

2.9 A photo of the 73 mm tall and 46.5 mm deep Mark 2 rig with fittings. The SAW device can be seen secured in the device holder by conductive brass retainers, which depress their associated gold pogos upon lowering of the device holder. The holder is held in place by the two brass clips at the front of the rig 29

2.10 Input power against time taken to create a liquid bridge of dioctyl phthalate ($\eta = 63$ mPa·s, $\rho = 985$ kg/m^3 @ 20°C, $R_0 = 0.5$ mm) from a 1 μL droplet. Plate separation is held constant at 10 mm. Note how the time taken to form a fluid bridge dramatically decreases once the output power goes beyond about 5 W. 32

2.11 A montage demonstrating that a sustained 15 s SAW burst is able to maintain a filament of water beyond the critical aspect ratio. We can see that as the SAW burst ends at 15 s, the fluid filament collapses. It is believed that SAW energy is able to prevent liquid bridge decay indefinitely. The bridge is created within 1.5 ms. 33

2.12 These sequenced images show how SAW energy entering a droplet at the Rayleigh angle θ_R is believed to reflect within and propagate a fluid filament. Source: [44]. 34

2.13 The top row montage shows raw images of a typical SAW burst filament break-up experiment. The bottom row shows the binary silhouette interpretation of the above images, achieved with the custom MATLAB® image analysis script. 36

2.14 Break-up data of water showing initial transients. The red line demarcates the 50 pixel point at which transients reliably settle and that data processing begins. 36

2.15 Typical truncated and averaged dimensional diameter *versus* time filament break-up data (large red diamonds) of the experimental water results seen in Fig. 2.14. Smaller symbols represent the original data from Fig. 2.14. . . . 37

4.1 Averaged dimensional experimental diameter *versus* time break-up data for various Newtonian fluids. Note that break-up time increases with increasing viscosity (assuming negligible change across samples in surface tension and density). Thus, it can be seen how break-up data allows the identification of fluids with different viscosities. 56

4.2 The R-*vs*-t evolution as predicted by the analysis seen in Sec. 4.3.2 using $X = 1$ is plotted (solid grey line) against the linear viscous solution (dotted black line) when $X = 1$ for Oh values of 0.001, 0.01, 0.1, and 1 in Figs. a, b, c, and d, respectively. 62

4.3 Analytically predicted dimensionless mid-filament decay (black) as predicted by the analysis seen in Sec. 4.3.2 using $X = 1$. It fails to quantitatively predict or represent the behaviour of experimental results (red). . . 63

4.4 Sample filament break-up data (black) and fitted data at the final stages of break-up (red) for (a) 80% glycerol/water solution (Oh $= 0.389$), (b) 40% glycerol/water solution (Oh $= 0.0241$), (c) 10% glycerol/water solution (Oh $= 0.0121$), and (d) water (Oh $= 0.0113$). Radius is re-scaled with the original radius, and time is re-scaled as $t_s = (t_f - t)/\tau_{\mathrm{R}}$, where t_f is the final break-up time. 65

4.5 Re-scaled sample filament break-up data (black) and fitted data (red solid) with error (red dotted) at the final stages of break-up for (a) 80% glycerol/water solution, (b) 40% glycerol/water solution, (c) 10% glycerol/water solution, and (d) water. 66

4.6 A graphical representation of the data seen in Table 4.2 that shows the required X factor to fit experimental Oh, from which corresponding $\bar{\eta}$ values can be extracted. One can see the transition of X from a value of 0.5197 to the viscous solution value of 0.7127 with an increase in viscosity. 67

4.7 Open circles represent typical normalised break-up data. The point at which R^* reaches half its initial value determines the t^* value that defines $t^*_{1/2}$ for that break-up event, the process of which is graphically represented by the orange line. 69

4.8 Dimensionless half-time $t^*_{1/2}$ for a filament to reach half its diameter as a function of its Oh for Newtonian standard solutions: The continuous curve has been obtained by regression of Eqn. 4.30 through experimental data using asymptotic values for K_0 and K_2, while the dashed curve has been obtained by also freeing K_2 as a regression parameter. 70

4.9 Changes in X_{eff} with Oh to satisfy Eqn. 4.46 (red diamonds). The open circle data points represent the X_{eff} values that arise from solving Eqn. 4.32 using the experimental values of $t^*_{1/2}$ for the individual experiments used in Fig. 4.8. 73

4.10 Experimental break-up data (black) and predictions by Eqn. 4.31 (red) using X_{eff} values based on Eqn. 4.46 (Fig. 4.9 - red diamonds) for Oh = (a) 278.997, (b) 12.19, (c) 4.62, (d) 0.124, (e) 0.061, and (f) 0.00606. 74

6.1 (a) Hollow glass microspheres with diameters of 9-13 µm. (b) Silver nano particles of diameter 11.2 nm. (c) Glass micro fibres of diameter 13 µm and length of 155 µm. (d) Silver micro nuggets of 1.55 µm and 3.82 µm. 100

6.2 (a) Ag MNs $\phi = 0.01$. (b) Ag MNs $\phi = 0.1$. (c) Ag MNs $\phi = 0.13$. (d) Glass beads $\phi = 0.01$. (e) Glass fibres $\phi = 0.01$. 101

6.3 (a) Ag NP suspension relative extensional and shear viscosity as a function of volume fraction. (b) Ag NP suspension relative shear viscosity against volume fraction for shear rates $\dot{\gamma}$ of 30, 60, 90, 120, 180, and 300 s^{-1}. (c) Glass bead suspension relative extensional and shear viscosity as a function of volume fraction. (d) Glass bead suspension relative shear viscosity against volume fraction for shear rates $\dot{\gamma}$ of 100, 200, and 300 s^{-1}. Note: Shear viscosity values in (a) and (c) correspond to comparable extensional and shear rates. 104

6.4 Shear viscosity *versus* shear rate for different volume fractions for (a) Ag NP and (b) glass bead suspensions, with clear shear thinning exhibited in both cases. 105

6.5 (a) Relative extensional viscosity *versus* volume fraction accompanied by fits of the KDE for 0.01 µm silver particles ($[\eta] = 9.5$, $\phi_m = 0.63$), sand grain data from Alexandrou *et al.* [45] of both 3 µm ($[\eta] = 3.77$, $\phi_m = 0.53$) and 30 µm ($[\eta] = 2.6$, $\phi_m = 0.56$), 11 µm glass beads ($[\eta] = 3$, $\phi_m = 0.63$), and KD data for Einstein's pure hydrodynamic interaction case ($[\eta] = 2.5$, $\phi_m = 0.63$). Apart from data from [45], all fits were assigned visually. Inset: $\phi = 0.35$ Ag NP suspension break-up showing distinct non-uniformity at the mid-filament due to particle jamming. 106

6.6 Required $[\eta]$ to fit experimental data versus particles size D_p. Extensional kaolin data was taken from O'Brien (2002) [46] — where $\phi = 0.49$ for all samples — at strain rates that correspond to the rates seen in our experiments. Assuming $\phi_m = 0.55$, the necessary $[\eta]$ values for kaolin fine, feed, and coarse samples, were 7.3, 6.6, and 6, respectively. Apart from the Alexandrou (2009) sand data, all fits were assigned visually. 107

6.7 FESEM image of the fractal pattern formed by dried Ag NP suspension. These patterns possess a fractal dimension of approximately 1.85, as determined by the box-counting method [47, 48]. 108

6.8 Experimental data is shown along with data produced by the KDE by maintaining $[\eta] = 2.5$ and varying ϕ_m (grey dotted lines), with the grey numerical annotations denoting the value of ϕ_m. 109

6.9 Experimental data is shown along with data produced by the KDE by maintaining $\phi_m = 0.63$ and varying $[\eta]$ (grey dotted lines), with the grey numerical annotations denoting the value of $[\eta]$. 110

6.10 (a) Ag MN suspension relative extensional and shear viscosity as a function of volume fraction. (b) Ag MN suspension relative shear viscosity against volume fraction for shear rates $\dot{\gamma}$ of 20, 60, 120, 160, 200, and 300 s^{-1}. (c) Glass fibre suspension relative extensional and shear viscosity as a function of volume fraction. (d) Glass fibre suspension relative shear viscosity against volume fraction for shear rates $\dot{\gamma}$ of 50, 80, 100, 200, and 300 s^{-1}. Note: Shear viscosity values in (a) and (c) correspond to comparable extensional and shear rates. 111

6.11 Shear viscosity *versus* shear rate for different volume fractions for (a) Ag MN and (b) glass fibre suspensions, with clear shear thinning exhibited in both cases. 111

6.12 Relative extensional viscosity *versus* volume fraction of glass fibre ($\phi_m = 0.24$) and Ag MN ($\phi_m = 0.3$) suspensions where the KDE is fitted using using $[\eta]_{\text{rod}}$. 112

8.1 The change in *cac* due to changes in HPMC concentration at 25 ^{o}C. This data was taken from Silva *et al.* [41], where electrical conductivity tests were used to determine values. This HPMC variant (trade name Methocel K15M, methoxyl content 19–24 %, hydroxypropyl content 7–12 %) has the properties of $M_w = 430,000$ Da, $[\eta] = 8.35$ dL/g, and $c^* = 0.09$ [49], which is comparable to the one used in the study presented here and serves as an indicator. Note: the critical micelle concentration for SDS in pure water is at $cac = 8.34$ mM [41], which is the concentration at which these surfactant particles will begin to group and form micelles. 128

8.2 The dynamic surface tension changes of SDS in water over time, sourced from [50]. The data curves show dynamic surface tension for (1) 2 (2) 3 (3) 4 (4) 6 (5) 8 (6) 12 (7) 16 (8) 24 (9) 32 mM. 129

8.3 Non-dimensionalised radius as a function of time data for a polymeric HPMC solution. Break-up begins with linear Newtonian-like decay past $R = 1/2$, allowing the initial viscosity to be extracted using the approach described in Sec. 4.4, before strain-hardening effects occur. Decay then becomes exponential towards final break-up as polymeric stresses retard filament thinning; the filament at this point is long and near-cylindrical, meaning that the mid-filament stress balance discussed in Sec. 4.3.1 can be used to extract extensional viscosity during the strain-hardening phase. 130

8.4 (Left panel) Extensional viscosity as a function of SDS concentration for HPMC solutions using the first extensional viscosity extraction approach described in Sec. 8.2.3, where measurements are taken during Newtonian-like decay at $R = 1/2$ — Hencky strain of ≈ 1.4. (Right panel) Shear viscosity as a function of SDS concentration for HPMC solutions, measured at a constant shear rate $\dot{\gamma} \approx 15$ s^{-1}; the shear measuring techniques available to us were unable to resolve changes in the storage modulus G' and loss modulus G" for most of these low viscosity samples, and thus their analysis was not pursued in this study which nevertheless primarily focuses on extensional measurements. Note: these viscosities effectively assess total viscosity, including both polymeric and solvent contributions, *i.e.* $\bar{\eta} = \bar{\eta}_p + \bar{\eta}_s$ and $\eta = \eta_p + \eta_s$ for extensional and shear viscosities, respectively. Also, extensional viscosity extracted before strain-hardening sets in is at a Weissenberg number Wi$\lesssim$1 (the Wi describes the balance of elastic *versus* viscous effects and is discussed later in this chapter), and so we expect $\bar{\eta} \approx \bar{\eta}_0$ in Fig. 8.4. Similarly, $\dot{\gamma} \approx 15$ s^{-1} corresponds to a shear Wi much smaller than 1. Therefore, the shear viscositeis are likely to be close to the zero-shear-rate values. This is why we denote them as η_0. 132

8.5 Graphical depictions of polymer behaviour: in the case of increasing polymer concentration (from left to right panels) and increasing surfactant concentration (from top to bottom panels). (Top left) A polymer chain (blue) and its hydrophobes (orange) with no SDS added and below c*. (Top middle) Polymer chains expand slightly as hydrophobes between chains interact at mild polymer concentrations. (Top right) Chains overlap at high concentrations. At approximately the *cac*, coil-to-globule conformation results from the repulsion of polymer chain hydrophobes from the anionic surfactant molecules (green) in low (middle left) and high polymer concentrations (middle right); this is believed to be responsible for the reduction in viscosity measurements around the *cac*, as seen in Fig. 8.4. At high surfactant concentrations, mixed micelles create polymer-surfactant complexes, which are like-charged and cause the polymer chains to not only swell in the dilute polymer case (bottom left), but to swell and network *via* shared mixed micelles at higher polymer concentrations (bottom right). It should be noted that intramolecular interactions caused by mixed micelles are also depicted in the bottom two images. The expansion of polymer chains at high surfactant concentrations and the transient mixed micelle bonds that form are believed to reduce strain-hardening effects. 134

8.6 Relaxation time as a function of SDS concentration for HPMC solutions. Note: these results were taken towards the end of break-up when filaments were near-cylindrical. 135

8.7 The effect of SDS concentration on extensional viscosity $\bar{\eta}_p^*$ due to polymeric contribution as a function of strain: (a) 0.065 % (w/v) HPMC; (b) 0.26 % (w/v) HPMC; (c) 0.52 % (w/v) HPMC; and (d) 1 % (w/v) HPMC. Note: extensional viscosity is scaled as $\bar{\eta}_p^* = \bar{\eta}_p/\mathrm{c}_p\eta_s$, where c$_p$ is the percentage concentration of HPMC and η_s is the shear viscosity in the absence of HPMC. Note: these results were taken towards the end of break-up when filaments were near-cylindrical. It should, however, be stated that the 0.065 % (w/v) HPMC solutions with 1.11 mM of SDS and above exhibited end-pinching behaviour (as seen in Fig. 8.8), meaning that they cannot reliably be used to make extensional viscosity measurements since the filaments are not completely uniform and do not self-affinely neck. 136

8.8 (a and b) The thinning sequence of 0.065 % (w/v) HPMC with 8.8 mM of SDS near final break-up. (c) The uniform filament formed by 0.52 % (w/v) HPMC with 8.8 mM. 137
8.9 Weissenberg number against strain for: (a) 0.065 % (w/v) HPMC; (b) 0.26 % (w/v) HPMC; (c) 0.52 % (w/v) HPMC; and (d) 1 % (w/v) HPMC. Note: these results were taken towards the end of break-up when filaments were near-cylindrical. 139

9.1 Particle trajectories in cross-slot extensional flow of passive algal particles (left) and active algal swimmers (right). Both images are taken at a strain rate of 1 s^{-1} for *Dunaliella tertiolecta*. 144
9.2 Mean square displacement against time for the experiments seen in Fig. 9.1 145

List of Tables

4.1 Self-similarity solutions as adapted from the compilation reported by McKinley and Tripathi [6] 59

4.2 Water/glycerol solutions with increasing glycerol content were tested and analysed *via* a parametric study to see which X factor led to the best fit of experimental data. The Oh value is the fitted value, with the error based on the difference between experimentally calculated Oh. Here, one can see the change in appropriate X required to accommodate solutions which primarily differ in viscosities. 67

Chapter 1

Introduction

1.1 Rheology and low-viscosity fluids

The properties of fluid flow have played a determining role in our course through history. Not only have they facilitated or hindered progress but we have sought to find ways to exploit them. As the most dominant liquid in our lives, the properties of water have been inextricably linked with our development; its ability to flow freely has allowed the use of ancient innovations like Archimedes' screw and aqueducts to aid the widespread utilisation of water, and has allowed vessels both small and large to slip through rivers and seas. However, there are fluids other than water that have shaped human history. Mud's inability to support high local stresses has disrupted goods trains and armies by sucking down boots and bogging wheels alike, and its capacity to slide or be slid upon has been responsible for burying settlements, for example, which is a persisting problem today. However, our purposes have also been served by the direct manipulation of fluid properties; the thinning of tar under heat from a thick sludge to a pourable fluid has been exploited for the practical purpose of waterproofing ships, yet also for the wretched intention of scalding enemies below ramparts. Therefore, it stands to reason that as the world has become more industrialised and we explore our capacity to manipulate, exploit, and create fluids that intimately understanding their properties has become integral to our progress.

Rheology is the study of material flow properties, with the word owing its origins to the ancient Greek aphorism *panta rhei*, "everything flows". The propensity for a thin fluid to flow freely or a thick fluid to flow slowly is defined in engineering as its viscosity, where a higher viscosity represents a thicker fluid. It is technically defined as the ratio of stress and imposed strain rate. In Newtonian fluids this ratio remains constant, but in non-Newtonian fluids it varies across strain rates. In fluid mechanics, where one looks at flow across hydrofoils or within pumps, knowing a fluid's rheological response is critical in allowing the use of the conservation equations to predict flows. Conversely, in rheology one employs idealised flows in order to extract rheological properties such as viscosity; here non-Newtonian fluids are of particular focus.

Rheology describes the deformation of materials as either being shear or extensional flow (also defined as a shear-free flow) or a combination thereof. These two types of flow exhibit different kinematics, producing different stresses, necessitating separate shear and extensional experiments for complex fluids.

The earliest successful experimental designs to quantify the viscosity of a fluid were conducted independently by Mallock and Couette in 1888 and 1890, respectively, but both employed the same basic principle [3]. Using two concentric cylinders, a smaller cylinder inside a larger one, they filled the gap between the outside surface of the inner and the inside surface of the outer with a subject fluid and turned them relative to one another. By knowing the magnitude of the gap, measuring the relative speed between the cylinders, and the torque required to make the rotations they were able to extract a fluid's viscosity. This particular type of experiment would later be categorised as a shear flow experiment, which is used to extract a fluid's shear viscosity. This type of flow is seen in systems like extrusion, injection moulding, and fluid bearings, for example.

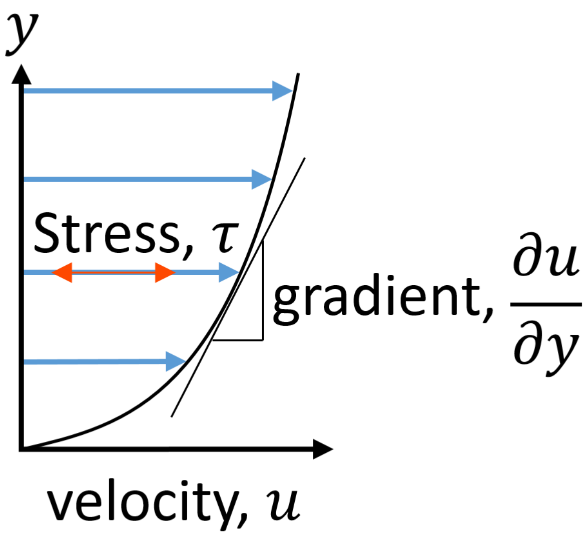

Fig. 1.1 Blue arrows and their magnitude represent velocity. The velocity differences, or velocity gradient, result in stresses between regions of different velocity. The red arrow denotes the stress that occurs along a particular slice through a region where a velocity gradient is present.

The simplest form of a shear experiment is generated by the movement of two parallel plates relative to one another with the subject fluid between them. The stress and shear strain rate are extracted and associated by Newton's law of viscosity:

$$\tau = \eta \frac{\partial u}{\partial y}, \tag{1.1}$$

where τ is the stress, the proportional term η is the viscosity, and $\frac{\partial u}{\partial y}$ is the rate of deformation or strain rate (Fig. 1.1). As mentioned earlier, in a Newtonian fluid this proportionality between the stress and the deformation rate, the viscosity, remains constant across deformation rates. For most practical purposes, substances of low molecular weight like water and oils can be considered Newtonian.

The generic form of Newton's law of viscosity is:

$$\boldsymbol{\tau} = \eta \dot{\boldsymbol{\gamma}}, \tag{1.2}$$

where $\dot{\boldsymbol{\gamma}}$ is the rate of strain tensor. This directly corresponds to the rate of strain component seen in Eqn. 1.1 and is defined as:

$$\dot{\boldsymbol{\gamma}} = \left[\nabla \boldsymbol{v} + \nabla \boldsymbol{v}^T\right], \tag{1.3}$$

where $\nabla \boldsymbol{v}$ is the gradient of the velocity vector field. In a simple shear flow this is:

$$\nabla \boldsymbol{v} = \begin{pmatrix} 0 & \dot{\gamma} & 0 \\ 0 & 0 & 0 \\ 0 & 0 & 0 \end{pmatrix}, \tag{1.4}$$

where $\dot{\gamma}$ is the strain rate. Thus shear viscosity can be defined as:

$$\eta = \frac{\tau_{xy}}{\dot{\gamma}}. \tag{1.5}$$

On the other hand there is extensional flow, which can take several forms. Planar extensional flow is described as a volume that is stretching in one dimension, contracted in the second, and maintained in the third. In biaxial extensional flow, one dimension is compressed while the other two are stretched. The counterpart to this, uni-axial extensional flow, is naturally defined as a volume that is stretched in one axis and contracted in the other two (Fig. 1.2). Such shear-free flows are seen in fluid jets, blow moulding, and flow around bubbles, for instance.

We can relate a Newtonian fluid's shear viscosity to its extensional viscosity by focusing

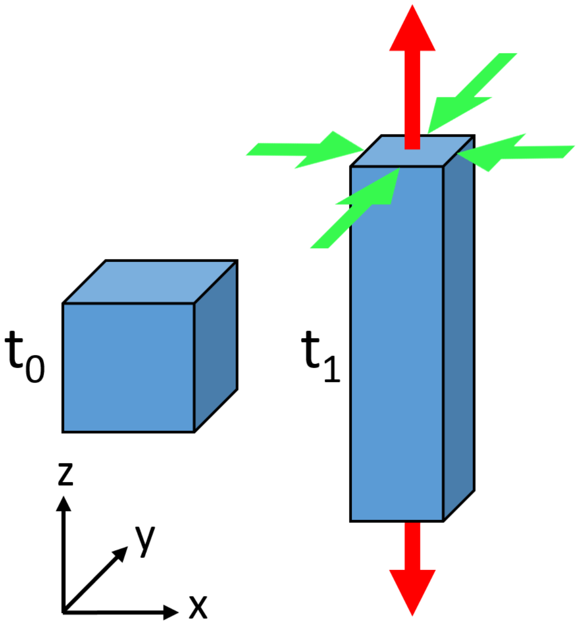

Fig. 1.2 The stretching of a finite volume at t_0 in the z-axis (red arrows) to an elongated form at t_1 represents the deformation that occurs under uni-axial extensional flow. It can be seen that through the conservation of volume that the dimensions in the xy-plane must contract (green arrows).

on the velocity fields generated by extensional flow. In contrast to Eqn. 1.4, the gradient of the velocity vector field of a uni-axial extensional flow is represented as:

$$\nabla \boldsymbol{v} = \nabla \boldsymbol{v}^T = \begin{pmatrix} -\frac{1}{2}\dot{\varepsilon} & 0 & 0 \\ 0 & -\frac{1}{2}\dot{\varepsilon} & 0 \\ 0 & 0 & \dot{\varepsilon} \end{pmatrix}, \tag{1.6}$$

where $\dot{\varepsilon}$ is the extensional strain rate. The extensional viscosity $\bar{\eta}$ is defined such that:

$$\tau_{zz} - \tau_{xx} = \tau_{zz} - \tau_{yy} = \bar{\eta}\dot{\varepsilon}. \tag{1.7}$$

In the Newtonian case:

$$\tau_{zz} - \tau_{xx} = \tau_{zz} - \tau_{yy} = 3\eta\dot{\varepsilon} = \bar{\eta}\dot{\varepsilon}. \tag{1.8}$$

Given this, a Newtonian fluid's shear viscosity can theoretically allow the prediction of its extensional viscosity too. This allows the use of the many readily available shear techniques to determine if a fluid is Newtonian and in turn predict its extensional viscosity. However, if a fluid is non-Newtonian this universal relationship between shear and extensional viscosity is no longer applicable, and it is not possible to predict a fluid's extensional properties based on shear experiments [51]— there are many fluids that are non-Newtonian. The famously novel material properties of a cornstarch and water mixture, where the material will behave like a near solid when one punches its surface but seem like honey when one presses slowly through it, clearly represent a fluid whose viscosity changes with different deformation rates. Furthermore, the shear thickening or thinning phenomena exhibited by polymer solutions and particle suspensions [51] also demonstrate fluids that do not behave in a Newtonian fashion. Thus, when dealing with non-Newtonian fluids, separate extensional flow techniques are required.

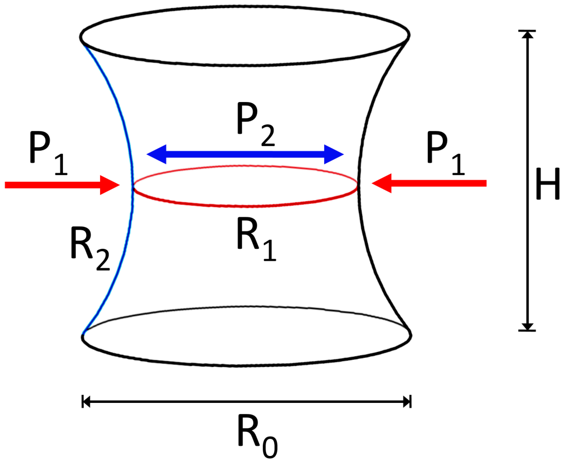

Fig. 1.3 This diagram describes the basics that lead to capillary break-up, where R_1 and P_1 are the mid-filament radius and radial pressure, respectively; R_2 and P_2 are the axial radius and pressure, respectively; and H and R_0 are the height and distal radius of the filament, respectively. P_1 exerts a contractile stress on a fluid filament, which is resisted by P_2. A certain aspect ratio H/R_0 will lead to $R_1 < R_2$ and thus $P_1 > P_2$, causing instability and resulting in filament collapse about the mid-filament.

In a shear experiment, it is reasonably simple to explore changes in a non-Newtonian fluid's shear viscosity η by changing the deformation rate; various shear flow experiments exist that routinely perform this [51] and have been available for over 100 years. However, extensional experiments have historically been more challenging to develop than their shear counterparts; this is reflected by the fact that the advent of established extensional methods is relatively recent, around 10 to 20 years ago or so [1, 2]. The operation of two established extensional techniques (discussed further in the next paragraph) centres on the concept of stretching a fluid filament. These techniques involve stretching initially stable filaments beyond a critical aspect ratio, defined by H/R_0 (see Fig. 1.3), so that static Rayleigh-Plateau stability is overcome; at this point, the magnitude of the filament's radial curvature will exceed that of its axial curvature ($R_1 < R_2$, see Fig. 1.3), which in turn will mean that radial pressure $P_1 = \frac{\gamma}{R_1}$ will exceed that of the restoring axial pressure $P_2 = \frac{\gamma}{R_2}$, as per the Young-Laplace equation. Thus, as R_1 diminishes, capillary stress will increasingly dominate and thin the filament, driving uni-axial extensional flow.

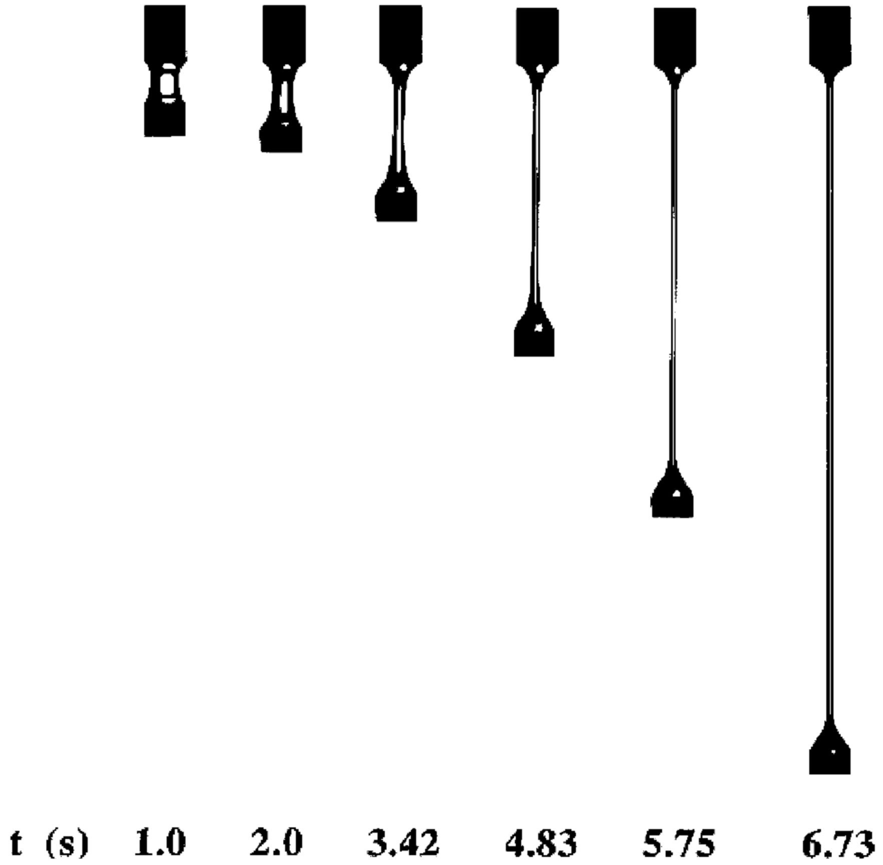

Fig. 1.4 An image sequence of viscoelastic fluid filament of 0.31 wt% polyisobutylene in polybutene being stretched in a FiSER. Source: [2].

In the filament stretching extensional rheometer (FiSER) [4] a fluid sample is placed between two end-plates, which are mechanically drawn apart at a controlled exponential rate (Fig. 1.4). During this process the mid-filament radius decay is observed whilst the filament's tensile force on the end-plates is measured using a force transducer. With this information, in addition to knowing the extension rate and independently obtained surface tension and density values, a mid-filament stress balance expression is used to extract the sample's extensional viscosity [2, 4], which balances contributions from tensile, surface tension, gravitational, inertial, and viscous stresses. This technique has found success and wide application with different types of complex fluids from polymer mixtures to fibre suspensions [2, 4, 8] .

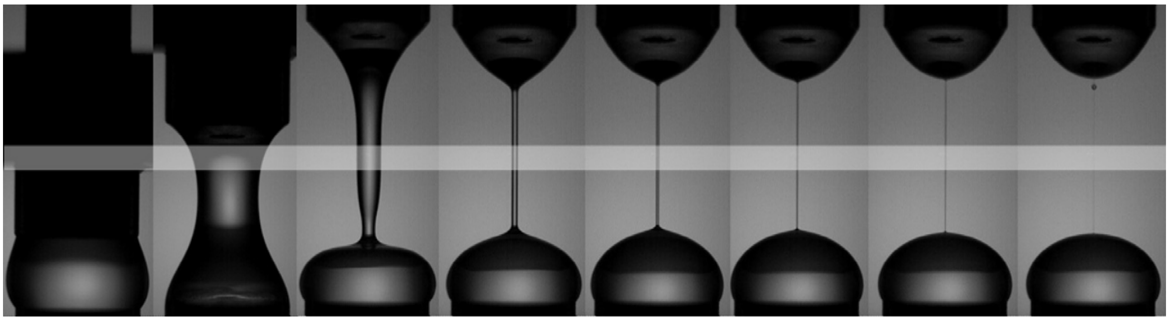

Fig. 1.5 An image sequence of 0.1 wt% PEO in glycerol being stretched in a CaBER device. The light band denotes the point at which filament radius decay measurements are taken. Source: [42].

Another prominent filament thinning technique, capillary break-up extensional rheometry (CaBER) [6, 42] differs from FiSER in operation and analysis. Although it still employs two mechanical end-plates to extend a fluid sample into a filament, the rate at which the end-plates open is not sustained or controlled (Fig. 1.5). Instead the end-plates are rapidly moved apart to a fixed distance where the critical aspect ratio is exceeded. The filament subsequently thins due to the contractile forces of surface tension about the mid-filament. Like FiSER, the decay of the mid-filament radius is measured, but the tensile force on the end-plates is not. Instead it is assumed that the tensile force plateaus and can be approximated by a self similarity solution [6]. By knowing this information, along with independently measured surface tension and density values, a filament stress balance that features tensile, surface tension, and viscous stresses can be used to extract the fluid's extensional viscosity [6].

Although these two uni-axial extensional flow techniques have gained acceptance they are limited in their utility when analysing low-viscosity fluids. These limitations can be analysed *via* a characteristic time and a set of dimensionless numbers [42], which are discussed at length in Chapters 2 and 3 but discussed here briefly. The Rayleigh time, $\tau_{\mathrm{R}} = \sqrt{\rho R^3/\sigma}$, predicts the time taken for a filament of a given radius to collapse in the absence of viscosity, where ρ is the fluid density, R is the characteristic length, and σ the surface tension. The Bond number, $\mathrm{Bo} = \rho g R^2/\sigma$, is the ratio between the effects of surface tension and gravity g. Finally, the effects of viscosity against inertia and surface tension are assessed *via* the Ohnesorge number $\mathrm{Oh} = \eta_s/\sqrt{\rho R \sigma}$.

In the context of traditional CaBER, end-plate separation times of the order of 50 ms are achievable, where the filament must not break during this time [42]. However, according to the τ_{R} expression, the break-up time of a filament of water with a radius of

3 mm (typical end-plate radii are around 3 mm) is 20 ms. This means that the filament will have already broken up before the plates have stopped moving, illustrating a problem when testing low-viscosity fluids. Additionally, these experiments use sample drop sizes with diameters of around 6 mm, which are large when compared to the scales seen in microfluidic devices. These large sample sizes can lead to an adverse asymmetry effect in the filament in which gravity causes the filament to sag, resulting in gravitational drainage affecting filament break-up [42]. This is evaluated for water by a non-trivial but typical value of B$o \approx 1.2$. Furthermore, the mechanical operation of these devices can induce vibrations that propagate throughout the filament, unaccounted for by stress balance analysis, and unable to be sufficiently damped in low-viscosity fluids [42]. These inertial effects are exacerbated by the large samples sizes, as assessed by the Oh. These issues make repeatable readings impractical. Thus it has been determined that low-viscosity fluids, fluids of around 70 mPa.s or less or systems of Oh $\lesssim 0.14$ or less (Fig. 1.6), are not well suited to analysis by traditional CaBER [42]. These limitations are discussed further in Chapter 3.

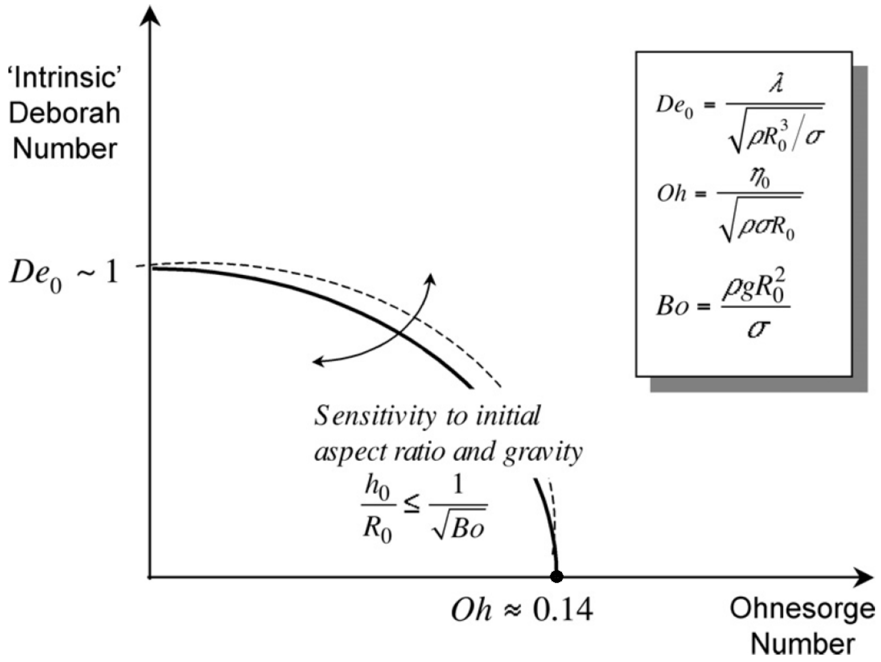
'Intrinsic' Deborah Number
$De_0 \sim 1$
$De_0 = \frac{\lambda}{\sqrt{\rho R_0^3/\sigma}}$
$Oh = \frac{\eta_0}{\sqrt{\rho\sigma R_0}}$
$Bo = \frac{\rho g R_0^2}{\sigma}$
Sensitivity to initial aspect ratio and gravity
$\frac{h_0}{R_0} \le \frac{1}{\sqrt{Bo}}$
$Oh \approx 0.14$
Ohnesorge Number

Fig. 1.6 Operability plot of the CaBER showing that cases below Oh ≈ 0.14 are difficult to assess. In the filament break-up case, the Deborah number De is the ratio of the time λ (discussed in Chapters 7 and 8) required for a material to adjust to the imposed stresses and flow of the break-up and the characteristic time of break-up. Source: [42].

Though these extensional techniques have found success in analysing highly and moderately viscous samples, they are unable to measure thin water-like fluids. Elevating viscosities to make experiments repeatable can mask subtle but critical property expressions and negate the utility of diagnostic experiments, which would preclude the comprehensive analysis of a great number of important non-Newtonian fluids such as aqueous particle suspensions, blood, and other biological fluids, for example. Many important modern-day fluids have low viscosities that exhibit complex non-Newtonian behaviour and are applied *via* many different processes, such as spraying or inkjetting, which are dominated by extensional flow [52–54]. Fluids such as the myriad of spray coatings and industrial paints require the efficient use of materials and optimised surface deposition [52–54]. Inkjet inks utilise slight polymer additives to mitigate the formation of unwanted droplets to enhance image resolution [10, 52]. Finally, aerially delivered pesticides require polymer additives to ensure that droplets dissipate their kinetic energy upon impact so that they do not bounce off their targets [55]; leaving polymers out entirely leads to the vast majority of material falling into the soil, whereas too much polymer will cause long filaments to form and make the toxins airborne. Both these extremes can lead to severe and costly environmental impacts. Thus, the absence of comprehensive analysis leaves the formulation of complex low-viscosity material as a dark art of trial and error that can expose these systems and others to undesired results.

However, recent modifications of the CaBER approach have increased the viscosity range of this system to lower viscosity fluids. The Cambridge Trimaster employs increased extension speed by mounting the end-plates to sliders that are attached to a belt that is spun by a stepper motor, driving the end-plates apart. This actuation, as well as reduced sample size by using smaller end-plate diameters (≈ 1.2 mm), surmounts premature break-up and inertial instabilities, and allows Newtonian and weakly elastic fluids of 10 mPa·s to be analysed [9, 10]. The Slow-Retraction-Method [11] is another alternative that extends a liquid filament between two end-plates to achieve a stable aspect ratio, which is then followed by a slow retraction that extends the filament beyond the critical aspect ratio to induce break-up. Electrowetting forces have also be utilised to stretch a fluid filament to trigger capillary driven break-up [12]; a fluid sample is placed between two dielectric plates, forming a stable liquid bridge. A DC voltage is then applied that charges the liquid meniscus and pulls the sample across the plates to initiate thinning in the liquid bridge. It should be noted that this approach requires aqueous or slightly charged samples, and that the forced wetting dynamics are not well characterised. A microfluidic cross-slot device that produces an annular liquid-to-liquid flow has also been developed that centres on the same principle [14], where the sample is pumped into a channel with an immiscible fluid surrounding it that is pumped at a higher rate, stretching the sample fluid. However, the flow in this device is not truly shear-free, and it requires enough sample material to be pumped *via* syringes. The new Rayleigh Ohnesorge Jetting Extensional Rheometry [13] technique involves continuously flowing a jet of sample fluid *via* a nozzle whilst periodically perturbing its surface and using stroboscopic imaging to obtain readings; it can analyse very thin weakly viscoelastic fluids, though it requires high sample volumes and its nozzle-based function would probably make it unsuitable in testing much of the large variety of particle suspensions. Nevertheless, amongst these techniques 5 mPa·s [12] and 3.21 mPa·s [13] are the lowest viscosities communicated, for Newtonian and viscoelastic fluids, respectively. However, it is not clear if this is due to fundamental limitations in the approaches themselves.

It should also be noted that opposing two fluid jets *via* nozzles [56] is a useful method for creating both uni-axial compressive and extensional flows to explore the rheology of low-viscosity fluids, though large sample volumes and nozzles pose potential difficulties for many of the fluids seen in this body of work. Also noteworthy are techniques based on planar extensional flow, such as the Optimized Shape Cross-slot Extensional Rheometer [57]; although not absolutely shear-free, the technique has been successful in exploring the extensional properties of complex low-viscosity fluids.

1.2 Manipulating fluids using surface acoustic waves

This thesis investigates the use of surface acoustic waves (SAWs) as a means of developing a new filament break-up technique that can analyse the rheological properties of low-viscosity fluids. Unlike bulk vibrations that propagate through condensed material, surface acoustic waves are restricted to travelling at the surface. Such waves are seen radiating across surfaces away from impact points and also as the rolling waves that are observed during earthquakes. More specifically, the SAWs of interest are Rayleigh waves, which are composed of transverse and longitudinal components whose amplitude diminishes exponentially with depth into the substrate [43] (Fig. 1.7). One method for producing controlled SAWs is to affix micro-scale metal interdigitated transducers (IDTs) upon a piezoelectric material. Piezoelectric crystals are composed of macroscopic structures that contain large numbers of aligned molecules, which gives them the capacity to hold high levels of charge. Thus, when a high-frequency alternating current is applied to bonded IDT fingers upon a piezoelectric crystal surface, which effectively act as capacitors, a high-frequency electric field is generated and causes a mechanical response in the piezoelectric substrate — material compression and tension between the IDTs propagate as Rayleigh waves.

The unique characteristics of SAW devices were first exploited in radar systems as fil-

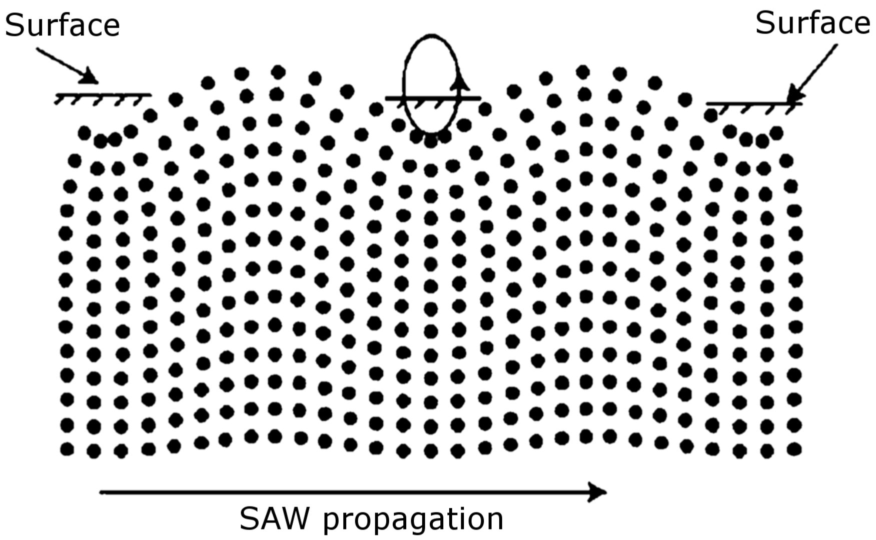

Fig. 1.7 This schematic shows how the combination of transverse and longitudinal components result in the retrograde fashion with which a fixed particle at the surface moves when subjected to Rayleigh waves. It should be noted that the waves are largely confined to the surface, and that their amplitude diminishes exponentially with depth into the substrate. Source: [43].

ters [58] and have since been industrially employed in other wireless systems for bandpass filtering and signal processing [59, 60], whilst also finding wide ranging applications from touch sensitive screens to chemical and biological sensors [61].

A notable beneficiary of the abilities of SAW devices is the burgeoning field of microfluidics. Although the amplitudes of the Rayleigh waves produced with piezoelectric SAW devices are only in the order of several nanometres, the MHz–GHz frequencies mean that accelerations as large as 10^8 m/s^2 able are routinely achievable [62] and fluids that come into contact with such waves can be manipulated in various and dramatic ways, as will be discussed in Chapter 3, and which can be exploited in a range of microfluidic devices [62]. This is particularly relevant to fluid manipulation at smaller scales since inertial forces become less prominent and the effects due to aspects such as viscosity, surface tension, and interfacial conditions become dominant. These conditions mean that traditional inertia-dominated techniques like centrifugal pumps and mechanical mixing become less effective at small scales, as well as becoming difficult to implement. On the other hand, SAW devices offer the capacity to effectively influence fluid flow at the micro-scale, and their planar micro features suit mircofluidic systems well.

Although the approach developed in this thesis was not designed to overcome the difficulties seen in other extensional flow methods, it possesses attributes that allow it to measure challenging low-viscosity fluids that were previously untested and are of academic and industrial interest. SAW technology and its distinct abilities in manipulating micro-droplets, offer a non-mechanical solution that has key advantages: it is able to generate stable fluid filaments from low-viscosity fluids; it uses very small sample sizes, mitigating adverse inertial and gravitational effects, and permitting the analysis of tiny sample volumes; and it is able to manipulate fluids whilst not damaging delicate fluid constituents. However, there are generic problems in extracting the rheological properties of low-viscosity fluids *via* filament break-up data using an analytical approach, which are addressed here by developing a calibration method that associates the break-up of unknown fluids to that of Newtonian fluids through re-scaled time and dimensionless radius data.

Thus, in developing this approach this thesis seeks to address the two fundamental challenges that must be overcome in a filament-based extensional rheometer: the creation of a filament to reliably measure the neck radius as a function of time, and converting this data into a measurement of rheological properties.

1.3 Thesis outline

This thesis details the development of a new rheometric technique that can analyse low-viscosity fluids that are problematic using alternative methods by employing the unique capabilities of SAWs in a microfluidic device. Also documented is the analysis *via* this technology of a variety of challenging fluids that have academic and industrial value that were previously untested. This thesis is presented in the following order:

Chapter 2 discusses the history of SAWs and their abilities in manipulating fluids, and the development of the experimental technique. Chapter 3 is a publication that assesses the new technique. Chapter 4 details the development of a new approach to quantify data from filament thinning techniques. Chapters 5–8, which include two publications, describe the rheological research conducted with this technique on challenging low-viscosity fluids. Finally, summarising discussion is provided in Chapter 9. The subsequent sub-sections in the current chapter elaborate on the contents of the aforementioned chapters.

1.3.1 Chapter 2

This chapter provides a background on SAWs. It also discusses the novel ways in which they manipulate fluids, and their ability to generate fluid filaments is proposed as a means of advancing the filament break-up concept to enable the analysis of the extensional properties of difficult low-viscosity fluids. The development of the SAW-based experimental device, the significant advantages it has that enable it to access challenging low-viscosity fluids, and the data it produces are then presented.

1.3.2 Chapter 3

This chapter, which is a publication, explores the conditions required to produce fluid filaments using SAWs for the purposes of extensional rheology. It compares several results from acoustically-driven microfluidic extensional rheometry against data from an established technique using conventional analysis methods, and demonstrates the potential of the technique to assess the extensional properties of non-Newtonian fluids. Also, it explores the advantages of the technique over conventional experiments and exploits them to conduct the filament break-up analysis of a solution containing a complicated blood protein for the first time, revealing a multi-stage break-up process.

1.3.3 Chapter 4

The significant difficulties in extracting extensional viscosity from the filament break-up data of low-viscosity fluids using an analytical approach are detailed in this chapter. Thus, the development of an alternative approach is described here; it is a calibration method that effectively associates the re-scaled and non-dimensionalised break-up of unknown fluids to that of known Newtonian fluids and their extensional viscosities.

1.3.4 Chapter 5

The extensional properties of delicate swimming motile microbe suspensions, quantified by the microfluidic SAW-based rheometer, are reported in this chapter. These low-viscosity microbe suspensions represent model systems of motile particles; theoretical modelling for dilute suspensions predicts that the motility of these microbes will affect bulk properties under extensional flow, which is validated for the first time by our experimental observations *via* the rheometer. Furthermore, a model, which extends the dilute model to apply to concentrated suspensions, provides further insights into the key parameters that need to be studied in order to better predict the effects of motile particles on bulk suspension viscosity in extensional flow.

1.3.5 Chapter 6

The newly developed technique and extensional viscosity extraction approach, complemented by standard shear analysis, is used in this chapter to analyse the properties of particle suspensions with different morphologies that, unlike the swimming particles discussed above, are “passive”. We witness strong particle size and shape related behaviour and perform a cursory study on the potential role that particle clustering may play on suspension viscosity. These observations support what little experimental extensional data there is for like suspensions and reinforces the suggestion that hydrodynamic effects alone cannot explain the observed effects on bulk fluid properties in full. Thus, we extract extensional viscosity data for these complex fluids, finding correlations with shear viscosities, and demonstrate that this experimental technique may be applied to the tailoring of particle suspensions to facilitate the development of suspensions of nano/micro particles as inks and coatings.

1.3.6 Chapter 7

The following chapter is a publication in which we utilise the advantages of the technique to study copper nanowire suspensions, where a polymer additive is required to prevent particle aggregation. Depositions of these suspensions show favourable electrical and physical properties, which has led to the development of novel electronics. These low-viscosity fluids pose difficulties for alternative extensional rheometry techniques due to the high-aspect ratio of the particles, the polymer additive, and the fact that it is currently difficult to synthesise large quantities of these particles, challenges that are overcome using the SAW-based technique. The elastic behaviour of these suspensions is found to depend on the ratio between polymer and nanowire content. Subsequently, we optimise our suspensions to minimise the polymeric contribution to largely isolate the particle contributions to viscosity. Like the previous chapter, we find correspondence between shear and extensional viscosity measurements.

1.3.7 Chapter 8

Chapter 8 explores the bulk effects caused by interactions between polymer and surfactant molecules in liquid, which are counter-intuitive, *via* capillary break-up experiments of low-viscosity dilute polymer-surfactant mixtures and more viscous concentrated formulas. Such solutions have long-running and extensive uses in industrial products and processes, but limited study has been conducted on their extensional properties. We demonstrate the high sensitivity of these polymer solutions to surfactant concentration, particularly in extensional flow. Additionally, it is shown that material properties change as filament evolution progresses. This study once again exhibits the general correspondence between extensional and shear viscosity results. It also demonstrates that results from this technique can qualitatively support theoretical predictions that are based on molecular interactions.

1.3.8 Chapter 9

This final chapter summarises the contributions this thesis has made to rheology and the understanding of novel complex fluids. Finally, it concludes with the questions raised by this thesis and provides recommendations on possible future work.

Chapter 2

Development of the Acoustically Driven Microfluidic Rheometer (ADMiER)

This chapter provides a background on SAWs. It also discusses the novel ways in which they manipulate fluids, and their ability to generate fluid filaments is proposed as a means of advancing the filament break-up concept to enable the analysis of the extensional properties of difficult low-viscosity fluids. The development of the SAW-based experimental device, the significant advantages it has that enable it to access challenging low-viscosity fluids, and the data it produces are then presented.

2.1 Introduction

The ability of SAW devices to produce fluid filaments make them an appealing means to advance the filament break-up concept. This chapter examines the obstacles and solutions involved with the development of the acoustically-driven capillary break-up device. The experimental challenges overcome include the fabrication, operation, and testing of both the SAW device and the experimental rig which contained the device. Further challenges were posed by the high spatial and temporal data resolution needed to distinguish the differences between microfluidic break-up events of different but similar thin fluids, as well as the challenges of data collection and processing; despite the difficulties in development, the experimental system possesses considerable advantages, including the use of small test volumes, the stabilisation of thin filaments by SAWs, and the ability to harmlessly manipulate delicate particle suspensions and complex molecule solutions.

2.2 Principles of Surface Acoustic Waves (SAWs)

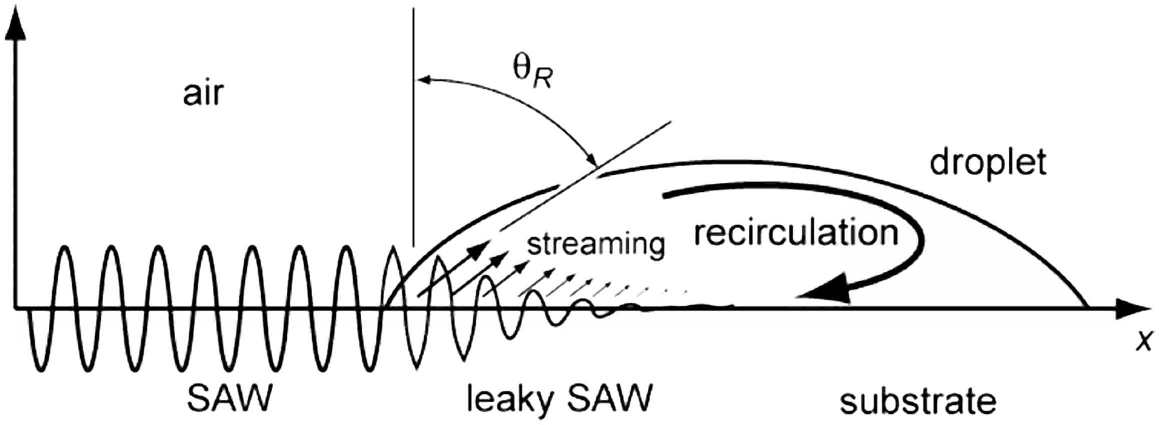

Fig. 2.1 As SAWs encounters a sessile droplet, SAW energy enters the droplet *via* the θ_R due to the difference between the speed of sound of the substrate c_s and that of the fluid c_l. The amplitude of the surface SAWs attenuates exponentially as wave energy is transferred to the droplet. Source: [43].

Waves produced by IDTs move across a substrate surface and several wavelengths deep into a substrate at the Rayleigh wave velocity, c_s; this is dependent on the material density, elastic modulus [63], and the effects of both the metal IDTs and potential fluid loading. The resonant frequency of such a device is defined by $f = c_s/\lambda_{SAW}$, where λ_{SAW} is the SAW wavelength. This is determined by the width and spacing of the IDTs, which are both $\lambda_{SAW}/4$ in the simplest versions of the IDT. Placing all IDT pairs at spacings of λ_{SAW} puts them in phase with the produced SAWs, thus every finger set constructively builds upon the wave displacement induced by the set preceding it, enhancing the wave amplitude.

Under the influence of Rayleigh waves, a particle fixed on a surface will move in a retrograde elliptical fashion [43] (Fig. 1.7). In the case of fluid loading, a sessile droplet resting on a substrate in the path of SAW energy allows the injection of the vertical and horizontal wave components into the droplet. Diffraction occurs as SAW radiation encounters the edge of the droplet due to the difference between the speed of sound of the substrate c_s and that of the fluid c_l. This causes a beam of acoustic energy to enter the droplet at an angle defined by the ratio of the two sound speeds called the Rayleigh angle, $\theta_R = \sin^{-1}(c_l/c_s)$; this phenomenon is known as leaky SAW [43] (Fig. 2.1).

Depending on a SAW device's power, frequency, and geometry a variety of behaviours can be evinced. The presence of standing waves within suspensions enables the collection of particles along nodal lines [64]. Asymmetric SAW application is able to spin sessile droplets, facilitating the centrifugation of suspended particles *via* shear induced migration

[65–67]. At high powers the projection of acoustic jets into a bulk fluid can produce radiation pressure *via* turbulent jets that have been shown to produce pressure gradients large enough to produce pumping [68]. Radiation pressure at interfaces can result in the translation of drops across a surface [62, 69–71], and result in atomization at high powers that can be used to aid pulmonary drug delivery [72–74]. At intermediate powers focused SAWs can actuate droplets into high-aspect ratio filaments [44] — an ability that is the particular focus in this body of work.

Aside from the assorted performances of SAWs in manipulating fluids and its small planar packaging characteristics, its value to microfluidics is further enhanced since it can be executed without damaging fragile suspended particles. This is owed to the small timescales at which these high-frequency SAW devices deliver energy since the resulting shear amplitudes are typically too small to cause structural damage to particles such as the lysis of cell membranes [43], for example. Hence, the utilization of SAW techniques is attractive with regards to the ever growing range of biological fluids that are the focus of many microfluidic investigations.

2.3 SAW device design and fabrication

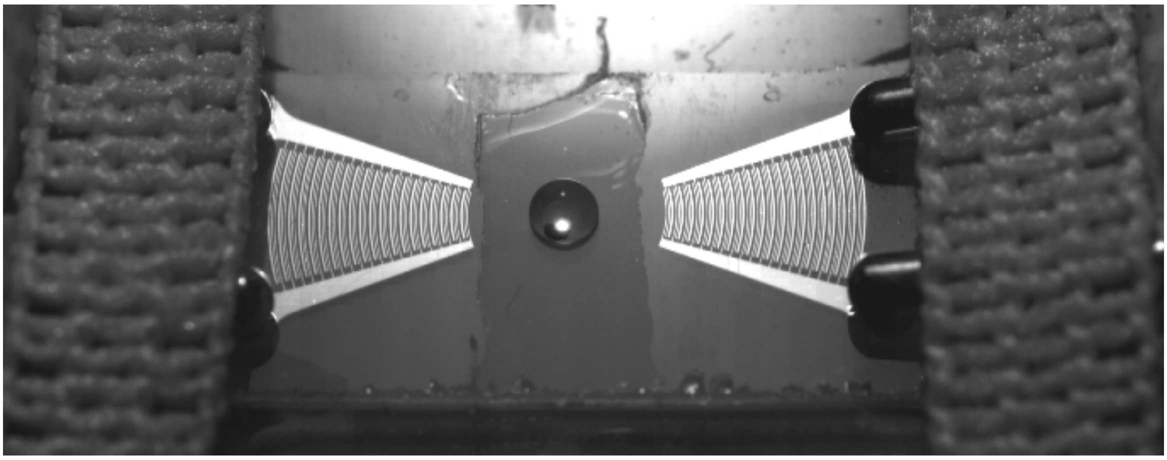

Fig. 2.2 10 × 20 mm LN SAW device with a quiescent droplet resting on a hydrophobic spin-coated Teflon® strip. Note the curved chromium-aluminium IDTs focus to the point at which the droplets rests. The droplet volume here is ≈ 3.6 μL, representing the typical sample volume used in experiments throughout this thesis.

Amongst the various combinations of IDT configuration, frequency, and power there exists a number of possible SAW devices which can produce a wide range of behaviours of a sessile fluid body on the piezoelectric substrate. The aims of this work required a device that could focus significant energy into a sessile droplet to produce a liquid filament whilst minimising heating effects and asymmetric behaviour. The device type used throughout this work featured two powerful high frequency 30 MHz single phase unidirectional transducers (SPUDT) that focus SAW energy to a point, facilitated by its curved IDTs as seen in Fig. 2.2. Excitation of a single IDT would see a droplet pushed in the direction of the SAW propagation and/or ejected at an angle of θ_R to the device surface, but the symmetry of the twin IDT feature ensures that the net motion is perpendicular to the substrate surface. This design was inspired by the jetting study of Tan *et al.* [44]; in this study, high-aspect ratio jets were created using different low-viscosity Newtonian fluids, and jets of different lengths were produced by changing the magnitude of SAW forcing. SAW forcing was treated as a body force and used in a momentum balance to relate jet length to jet velocity.

The piezoelectric substrate used in this thesis was a 0.5 mm thick 128° y-x lithium niobate (LN) single crystal wafer. The devices were created using standard techniques for UV photolithography; the wafer is spin-coated by AZ1512 positive photoresist (AZ Electronic Materials, Luxembourg) and then exposed to UV light through the device mask, which is then developed using 2:3 water/AZ 726 MIF developer. Chromium followed by aluminium is then sputtered onto the device. Finally, a sonic bath in acetone dissolves the photoresist and undercuts the excess sputtered metal, revealing the final devices, which can then be separated using diamond cutting techniques.

However, LN is hydrophilic and will cause droplet spreading that will result in a low contact angle. With the speed of sound in LN being ≈ 3990 m/s and 1495 m/s for water the necessary Rayleigh angle $\theta_R = \sin^{-1}(c_l/c_s) \approx 23°$ would not be accommodated, resulting in severely hampered injection of SAW energy into the droplet, particularly the critical longitudinal wave component (Fig. 2.1). This was overcome by creating a hydrophobic layer across the device's focal point on top of which the droplet would rest. This is achieved by temporarily shielding the IDTs using removable tape, then applying a Teflon® (Teflon AF, DuPont, Wilmington, Delaware, USA) drop between the IDTs, and then spinning the device at 3500 RPM for 3 minutes. This is followed by 2 hours of curing at 75°C, which leaves a hydrophobic strip between the IDTs, as is observable in Fig. 2.2.

2.4 SAW device operation and testing

SAW devices can readily generate enough heat or produce large enough wave amplitudes to cause their brittle structures to fail. Therefore, effective management of their frequency,

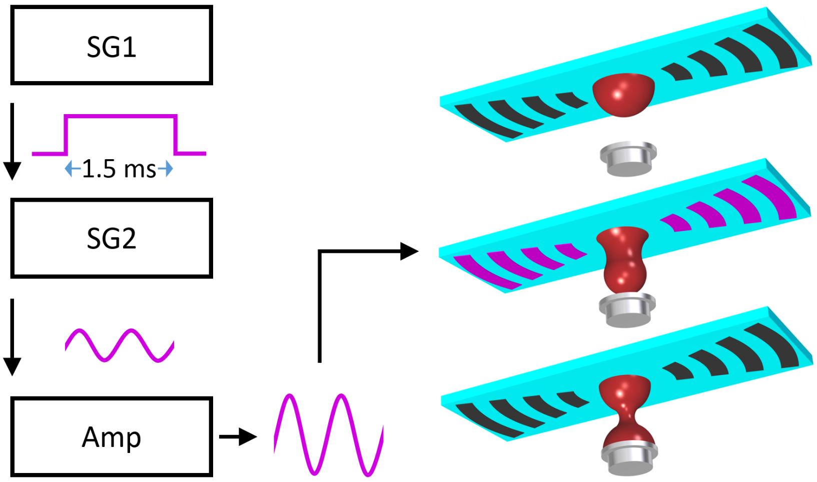

Fig. 2.3 The first signal generator (SG1) sends a 1.5 ms long burst signal to the second signal generator (SG2). SG2 then produces a sinusoidal signal to the amplifier (Amp), which boosts the signal's power, where the output is then delivered to the SAW device. This results in the sessile droplet, which is resting on the SAW device, to extend into an elongated filament that then contacts with an opposing plate just as the 1.5 ms burst ends, allowing the newly formed liquid bridge to decay.

power, and the duration of their operation is needed to ensure their practical utilisation. The operation of the device (discussed in Sec. 2.3) used in this work is depicted in Fig. 2.3; firstly, a signal burst was defined by a 20 MHz waveform generator (33220A, Agilent, Santa Clara, CA USA), the length of which could be easily adjusted — this determined the length of SAW burst produced by the device, otherwise called the burst time. This signal triggered a second signal generator (WF1966, NF Corporation, Yokohama Japan) that, for the duration of the burst time, would deliver a sinusoidal signal to an RF power amplifier (411LA, ENI, West Henrietta, NY USA), providing a fixed frequency and amplitude signal at the resonant frequency of the SAW device, 30.67 MHz. This frequency was determined by measuring the device's impedance across a frequency range using a network analyser, where the point of lowest electrical impedance corresponds to the device's resonant frequency. The amplitude of the wave was controlled by setting the voltage of the second signal generator, thus adjusting the power delivered to the SAW device. In this fashion a SAW energy burst of chosen duration and power could be determined. Single sample droplets were administered to the device focal point using a pipette (Eppendorf PhysioCare Concept $0.1 - 2.5\ \mu\ell$, Hamburg, Germany) and were typically $\approx$1.5 mm in diameter (Fig. 2.2).

Driven at ultrasonic frequencies, the longitudinal pressure waves of SAWs enter a droplet that is resting on the surface of a SAW device in the path of the radiation, causing bulk motion in the droplet (Fig. 2.1). Attenuation occurs as the momentum of the longitudinal waves, which propagate through the fluid as sound, is dissipated as heat due to the fluid's dilational viscosity [68, 75]. The horizontal component of the waves enter the droplet as transverse waves that produce velocity gradients, resulting in viscous dissipation [62]; although attenuation through this mechanism is generally 100 times smaller than that of longitudinal attenuation and is often neglected [76]. Attenuation caused by fluid loading causes SAW amplitude ξ to decay exponentially along the axis of propagation, x, which is described below [77]:

$$\xi = \xi_0 e^{j(\omega t - kx)} e^{-\alpha x}, \tag{2.1}$$

where the component normal to x is responsible for the longitudinal waves that project into the fluid resting on the surface; here ξ_0 is the original amplitude, $\omega = 2\pi f$ is the angular velocity of the SAW, k is the wavenumber, and the compressional attenuation coefficient α for the case of a liquid on a SAW device is [76, 77]:

$$\alpha = \frac{\rho_l c_l}{\rho_s c_s \lambda_{SAW}}, \tag{2.2}$$

where ρ_l and ρ_s represent the liquid and substrate densities, respectively. Incidentally, it can be seen that replacing c_l and ρ_l with the smaller corresponding values of a gas will result in much smaller attenuation than seen in a liquid case. Taking the derivative of Eqn. 2.1 gives the surface speed:

$$v = \left| \frac{\partial \xi}{\partial t} \right| = \xi_0 \omega e^{j(\omega t - kx)} e^{-\alpha x}. \tag{2.3}$$

Using the above equations it is possible to predict the total SAW power emitted by an IDT with a width of w by ignoring the imaginary components and averaging over a sufficient number of cycles [68, 76, 78]:

$$\langle P \rangle = \int_0^\infty w \rho_l c_l \omega^2 \langle \xi^2 \rangle \mathrm{d}x, \tag{2.4}$$

which gives,

$$\langle P \rangle = \frac{1}{2} \pi w \rho_s c_l^2 \xi_0^2 \omega. \tag{2.5}$$

Thus, a SAW device's power delivers kinetic energy to a fluid *via* the attenuation of SAWs. This kinetic energy, which initially just generates a loud sound that propagates into the fluid at the Rayleigh angle θ_R eventually takes the form of an acoustic jet of net bulk motion, a phenomenon that is termed acoustic streaming [79]. Simultaneously, the coupling between the substrate and fluid at the surface allows for the horizontal component of the SAWs to inject further power *via* the creation of shear gradients and viscous dissipation as mentioned earlier. The ability of SAWs to generate bulk fluid motion is discussed in further detail in the context of manipulating a sessile droplet in Sec. 2.7.2.

The complexities associated with SAW devices interacting with fluids mean that it is practically impossible to fully predict all real-world behaviour theoretically, and the simplification of the problem through significant assumptions is common practice [79–81]. Hence, in order to utilise the device effectively, understanding its characteristics and operating limits through testing was required.

The first basic test explored the range of powers within which the device could operate. Consistent measurements were obtained *via* voltage and current sensors on the device input wires. These measurements indicated that operating the device for 5 ms bursts beyond 15 W led to damage of the Teflon® coating, and that powers beyond 60 W began to fatigue and crack the device, rendering it unusable. The device was able to jet water at 0.4 W and glycerol at 15 W, which corresponds to 0.225 and 1.2 $V_{\text{p-p}}$ as read by the driving signal generator, respectively. This allowed the device to jet fluids between viscosities of 1 and 1500 mPa·s repeatedly without any degradation of the device or its Teflon® coating. However, reducing the burst time to between 1.5 and 4 ms showed that higher powers could be used while minimising damage to the Teflon® strip. This enabled the device to sustain powers of 28 W (1.9 $V_{\text{p-p}}$) and generate filaments using fluids as viscous as 27 Pa·s (silicone oil), though this would require the Teflon® coating to be replaced after several hundred bursts to ensure an effective droplet contact angle was maintained. The ability to jet viscous material not only meant that the system could accommodate a wide range of fluids, but that it also has a significant crossover into the operating regimes of FiSER and CaBER techniques (with a 70mPa·s lower limit for traditional CaBER, as discussed in Sec. 1.1) — critical for system comparison and validation.

For analysis purposes, it was necessary to quantify the conversion of electrical energy into mechanical energy, which is discussed further in Chapter 3. Moreover, understanding this relationship would allow the operator to anticipate the device's mechanical response to power input, aiding in the system's operation. To assess this a laser Doppler vibrometer (LDV - Polytec MSA-400, Polytec GmbH, Waldbronn, Germany) was used. An LDV aims a laser at the surface of a device and measures the Doppler shift of the reflected light to obtain the surface vibration amplitude and velocity. The relationship between the power and the surface velocity of SAWs is predicted by Eqn. 2.5, which is in agreement with the LDV results seen in the Fig. 2.4 where the input power consistently relates to the surface velocity squared. This indicated that predictable conversion of electrical energy to mechanical energy could be expected.

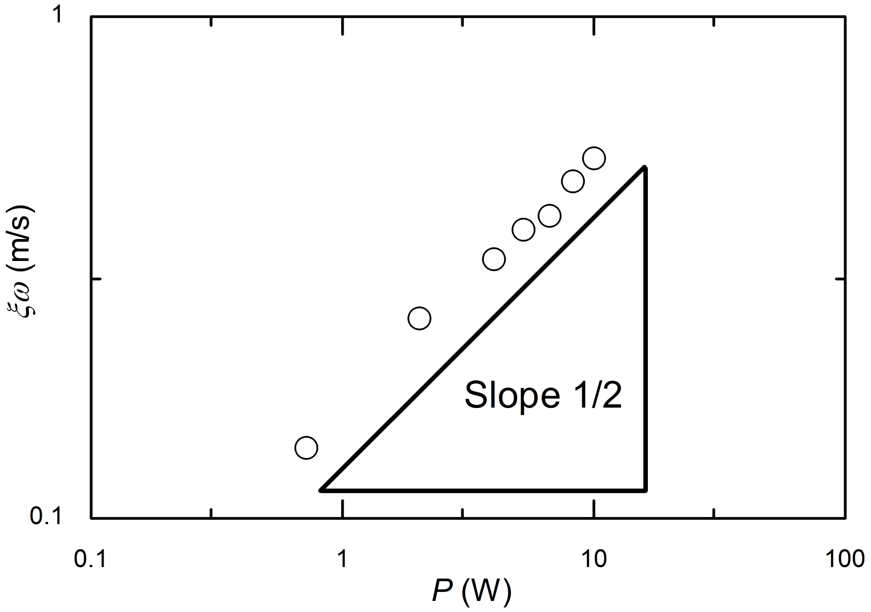

Fig. 2.4 Plotting input power against LDV measured surface velocity on a log-log plot shows the expected slope of 1/2 relationship anticipated by Eqn. 2.5.

Droplets can exhibit several different behaviours when subjected to SAW energy from this type of focused IDT device, and it was important to determine the conditions that achieve the desired high-aspect ratio filaments for our experimental system. Behaviour was found to be primarily dependent on the input power and the viscosity of the fluids; this is discussed in detail in Chapter 3. In brief, at low powers only a slight deformation of the droplet occurs, creating a 'stub' (Fig. 2.5a). At mid-range powers, high-aspect ratio filaments are produced (Fig. 2.5b). At higher powers, the samples are atomised (Fig. 2.5c). The parameters that create high-aspect ratio filaments are tested and analysed in Chapter 3.

A final assessment was required to test if the SAW device was acceptable for rheological use, and that was to explore the heating effects. As an example, glycerol's shear viscosity can change by more than 50% over 10°C, hence the concern is not trivial. Using conservative estimates (assuming that all input energy is converted into heat), the change in sample temperature due to a SAW burst can be predicted. Assuming a droplet can be treated as a hemisphere, a 1.5 mm diameter sample droplet gives a volume of 7 μL. For water at room temperature, with a $\rho = 998.3$ kg/m^3 and a specific heat $C_p = 4.183$ kJ/kgK, a SAW burst of 1.5 ms at 0.382 W is required to generate a high-aspect ratio filament; this would result in an increase of 0.019°C. For a drop of glycerol of the same volume, where $\rho = 1261$ kg/m^3 and a specific heat $C_p = 2.430$ kJ/kgK, a SAW burst of 1.5 ms at 16 W is needed to generate a high-aspect ratio filament, resulting in a change of 1.108°C. These estimates were

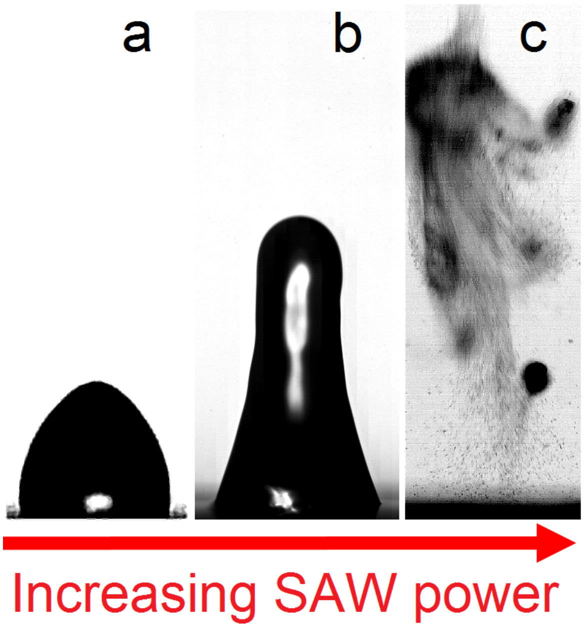

Fig. 2.5 Increasing the power injected into a sessile droplet effects large behavioural changes. As discussed in Chapter 3, the dimensionless power associated with the actuation of fluid using this technique can be defined as $\Pi = Pc_s/\sigma R_d$, where P is the SAW forcing power, c_s is the speed of sound in LN, σ is the subject fluid surface tension, and R_d is the initial droplet radius. In the case of a 1.2 mm diameter water droplet, (a) low power ($\Pi \lesssim 3$) induces slight deformation of the droplet, (b) intermediate power ($3 \lesssim \Pi \lesssim 50$) causes the droplet to turn into a high-aspect ratio filament, and (c) high powers ($\Pi \gtrsim 50$) result in the atomisation of the droplet.

supported by preliminary thermal imaging measurements. Hence, these findings of small temperature changes mean that using SAW is viable in the creation of fluid filaments for the purposes of rheology.

2.5 Experimental concept and design

The ability of the SAW device to rapidly form jets of low-viscosity fluid with minimal heating gave it the potential to be the key component of a new filament-based extensional rheometry technique. The initial approach was to jet the filament in the direction of gravity with a short SAW burst, aiming to have the effects of gravity and inertia balanced against surface tension. This would cause the filament to arrest in space, and for surface tension driven thinning to occur midway down the filament. Filament thinning solely under the influence of surface tension would then allow for the analysis of the filament neck diameter evolution to be conducted as is seen in conventional CaBER rheometry. However, it quickly became apparent that trying to repeatedly realise this behaviour was impractical. Either side of the perfect balance and the result was unusable; too little power and surface tension would retract the filament back into the original droplet, whereas too much power and the head of the filament would continue without arresting and drag the filament apart. In this form the experiment was not repeatable, especially when considering the conditions to strike the balance would dramatically change with changing fluid properties.

A conceptual improvement involved placing an opposing surface (parallel to the SAW device surface) in the path of the extending filament, which would contact with the opposing surface and arrest the filament's extension. Once in contact with the plate (given the right surface conditions) the filament would adhere and its retraction would be prevented. This approach negated the difficulties associated with trying to attain a force equilibrium.

However, several other key aspects needed to be addressed in order to create a functional and usable system that could create measurable and repeatable results. Considering the discussion in Sec. 1.1, it was clear that the aspect ratio must be controlled. Controlling this can be achieved by either changing the size of the initial droplet or the distance between the two surfaces. Seeing as exact control over the droplet size using hand-held pipette delivery could be problematic, controlling the distance between the surfaces was deemed to be the more viable approach. Another consideration was that the application of the droplet must be conducted with efficiency and precision despite the close proximity of the two surfaces. Finally, the system needed to accommodate viewing so that measurements could be taken.

2.5.1 Experimental rig design

An experimental rig was designed and fabricated to satisfy the need for a usable apparatus that could harness the SAW device and produce quick and repeatable experiments. The rig was designed using a CAD program (Solid Edge, Siemens PLM Software). It was constructed using standard engineering workshop techniques using PVC due to its chemical stability against a range of polymer solvents, which were anticipated to be the most reactive fluids envisaged for experimentation.

The basic design comprised a rotating device holder upon which a glass-slide mounted SAW device was secured by stiff brass retention paddles, and a screw-driven z-axis platform upon a sliding tower (Fig. 2.6). To operate the rig one would apply a sample droplet at the focal point of the SAW IDTs from above and then flip the platform, leaving the droplet facing down with gravity (brass retention clips would secure the SAW device upon rotation). Simultaneously, copper contacts (connected to the IDTs) would depress gold-plated pogos

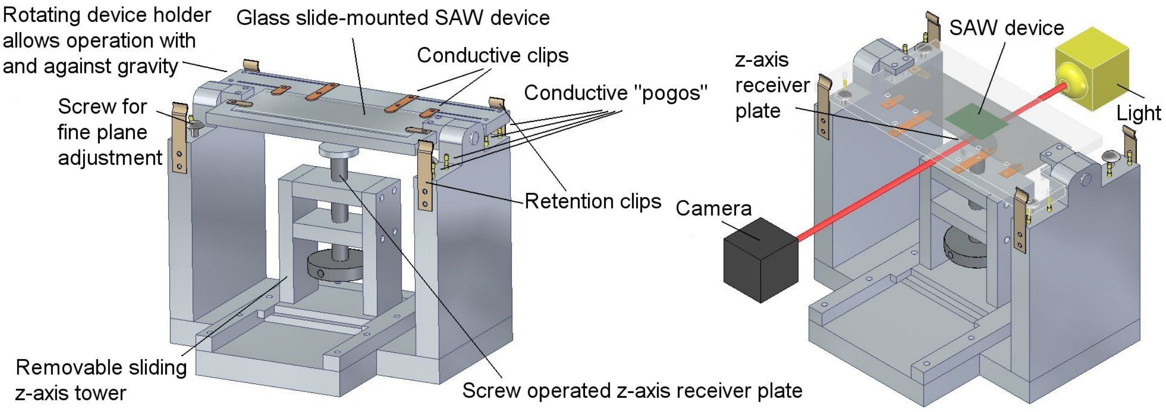
Rotating device holder allows operation with and against gravity
Glass slide-mounted SAW device
Conductive clips
Conductive "pogos"
Screw for fine plane adjustment
Retention clips
Removable sliding z-axis tower
Screw operated z-axis receiver plate
z-axis receiver plate
SAW device
Light
Camera

Fig. 2.6 CAD images of the 162 mm wide and 92 mm tall PVC rig with fittings designed to house and operate a SAW device to generate and view filament break-up. The image on the left shows the device turned upwards, allowing for the application of the sample droplet. The right image shows the device turned downwards so that it faces the opposing surface of the z-axis receiver plate. Also shown is the positioning of the camera and light source, with the red line denoting the line of sight that views the break-up event. Note that the z-axis tower slides out to allow the device holder to rotate, after which the z-axis tower slides back into position.

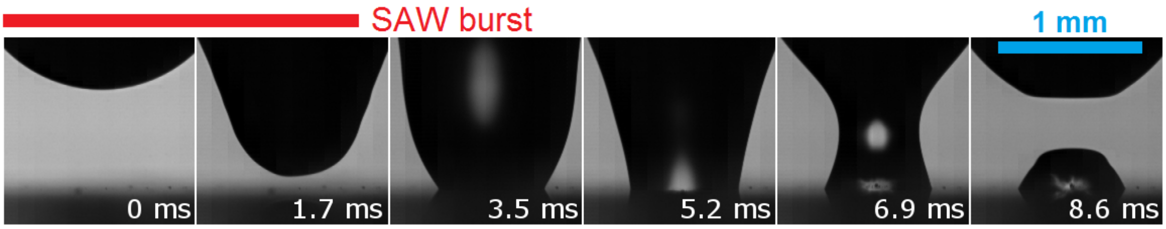
SAW burst
1 mm
0 ms
1.7 ms
3.5 ms
5.2 ms
6.9 ms
8.6 ms

Fig. 2.7 A montage of device operation showing a water droplet subjected to a 1.5 ms SAW burst. After the cessation of the SAW burst and the formation of a liquid bridge, surface tension driven thinning contracts the filament, driving uni-axial extensional flow.

that were fixed within the main vertical structure of the rig, completing the electrical circuit to operate the device. The sliding z-axis platform (with a glass plate mounted on its surface) would then be moved into place to provide an opposing surface under the droplet, upon which the extending SAW-driven filament would impinge. A low pitch screw with a large diameter dial raised and lowered the opposing surface, which allowed for fine control over the gap distance, and thus control over the filament aspect ratio. With the aspect ratio defined, SAW excitation was supplied to the droplet, resulting in a liquid bridge forming between the SAW device surface and the opposing surface — after this was achieved the SAW burst was ended, as is demonstrated in Fig. 2.7.

It was necessary to ensure that the contact area of both ends of the filament remained unchanged during filament decay, this would prevent the occurrence of irregular secondary flows due to fluid spreading or drainage and simplify analysis. However, water based low-viscosity fluids spread rapidly on hydrophilic surfaces so it was necessary to spin coat a hydrophobic Teflon® layer upon the opposing glass surface. Although, the presence of the hydrophobic surface meant that the filament contact area on the opposing surface was prone to contracting, even to the point that it would contract entirely and allow the retentive forces of surface tension to retract the filament back into the parent drop. To address this the hydrophobic surface of the opposing plate was fouled with a dabbing of a micro particle suspension. This allowed good adhesion of the filament upon initial contact and prevented the contraction of the contact patch while also preventing the spreading of the contact patch. Thus, this fixed the ends of the filament and prevented any secondary flow occurring.

The design of the rig permitted clear viewing between the two surfaces, allowing for the observation of the liquid bridge break-up event, the details of which are discussed in Sec. 2.6. This system proved sufficient in fulfilling the requirements of a usable apparatus that could produce repeatable experiments.

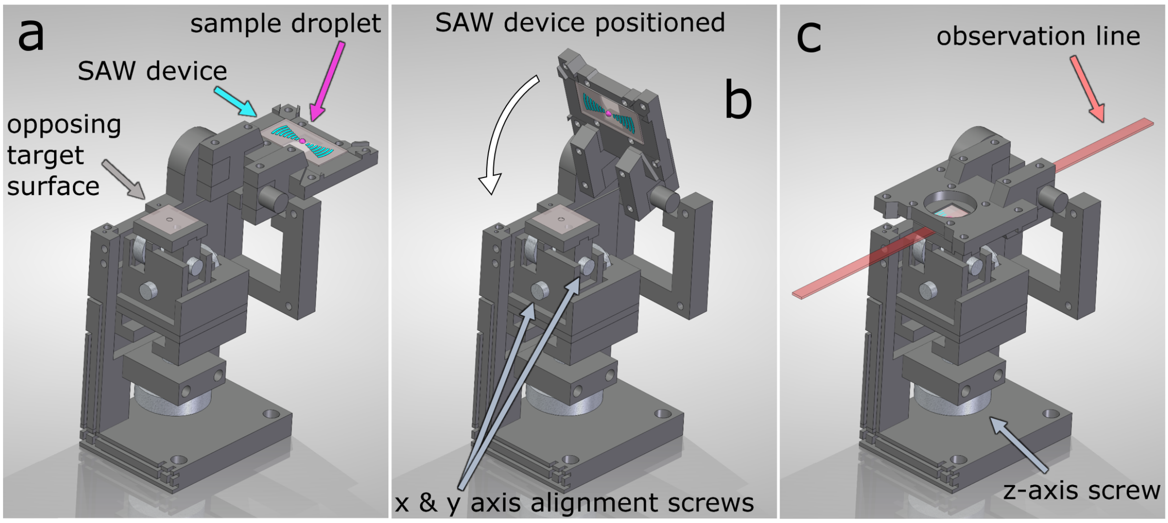

Fig. 2.8 (a) The sample micro-droplet is loaded onto the SAW device. (b) The device holder is then flipped so that the droplet is facing the opposing surface, where small adjustsments can be made to align the droplet with the target surface using the x-y-axis lateral screws. (c) The z-axis screw is turned to finalise the opposing target elevation, defining the resulting filament aspect ratio. The red line denotes the line of sight that the camera and light source are aligned with, which permits the viewing of the event; the event can also be viewed perpendicular to this line. The SAW device in this rig is 20 mm long and 10 mm wide.

As system development matured, however, the testing of a growing number of different fluids (many possessing time-dependent properties) was pursued; this, coupled with the higher experimental repetitions needed to satisfy the requirements of comprehensive error analysis, considerably increased the rate at which experiments needed to be conducted.

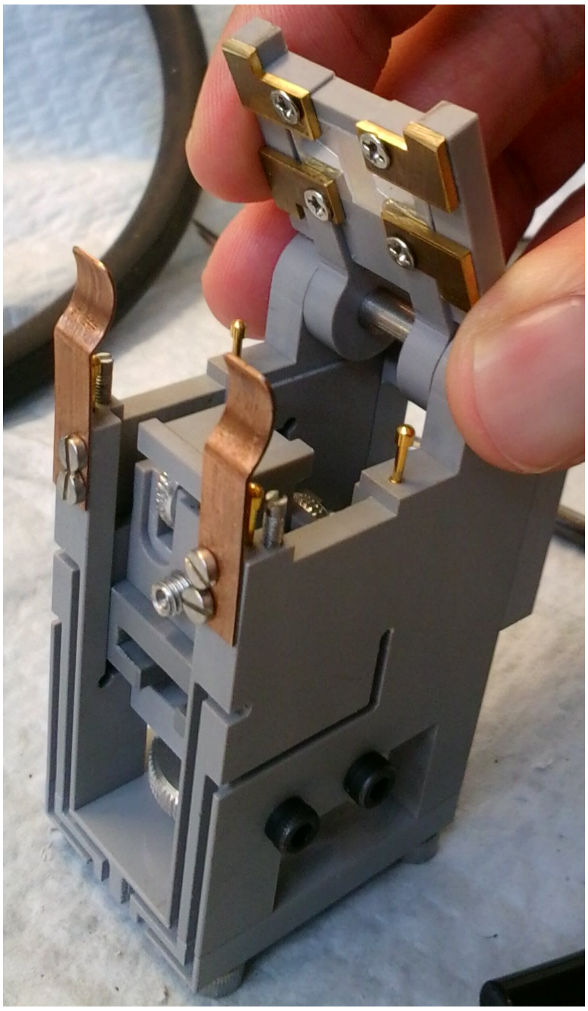

Fig. 2.9 A photo of the 73 mm tall and 46.5 mm deep Mark 2 rig with fittings. The SAW device can be seen secured in the device holder by conductive brass retainers, which depress their associated gold pogos upon lowering of the device holder. The holder is held in place by the two brass clips at the front of the rig.

Hence a quicker system was designed to meet these demands by modifying aspects of the original system (see Fig. 2.8), which was also constructed using PVC. Firstly, the SAW device holder's axis of rotation was moved away from the target surface, allowing for the removal of the sliding z-axis tower and thus removing a step in operation. Also, a hydrophilic circular plate of a similar diameter to the droplet and with squared-off edges was made the target surface instead of the broad particle-fouled surface seen in the original concept; fluid would spread to the edges of the plate but be halted at the squared-off edges by surface tension effects. This ensured that the filament contact patch on the opposing surface was consistent and negated the need to foul the opposing surface. The target plate required precise lateral positioning relative to the sample droplet in order to guarantee an axis-symmetric filament; however, slight variations in the positioning of the SAW device in the holder and the position of the droplet meant that misalignment between the droplet the target was possible. This would be further complicated by the rotation of a fixed target upon the z-axis screw if there was any misalignment. Hence, the capability for the fine lateral adjustment of the target plate was given *via* a platform that possessed both x and y axis screws, which rested atop the vertical z-axis screw (guided by grooves in the rig housing) so that it was independent of any misalignment due to rotation. Finally, the device was mounted without a glass-slide base. This not only removed a step in device preparation, but also meant that the rig's dimension were smaller than that of the original; this allowed the use of high-powered microscope lens attachments that typically have short range focal planes, and thus must be positioned closer to the target.

Therefore, the final rig, seen in Fig. 2.9, expedited experimentation by removing both preparation and operational steps and allowed for the rate of output necessary to accommodate the analysis of fluids with time-dependent properties, and handle the higher load that the increased number of samples and error analysis demanded of the system.

2.6 Videography and lighting

Filament break-up was observed and recorded *via* a camera that viewed the event through the gap between the parallel surfaces of the SAW device and the opposing surface, with a light source beyond the filament, as indicated in Fig. 2.6 and Fig. 2.8c. The break-up of these sub-millimetre liquid bridges typically occurs in a matter of milliseconds, see Fig. 2.7. Thus, a high zoom lens and high speed camera, and a powerful steady light source were required to obtain elevated spatial and temporal resolution data. Initially, images were captured using a Mikrotron high-speed camera (Mikrotron MC1310, Germany) with an Infinivar lens (InfiniVar CFM–2/S, Infinity Photo-Optical Company, Boulder, CO USA) attachment, and a mercury lamp (Fiber-Lite MH-100, Dolan Jenner, Boxborough, MA) to provide a strong light source. Usable images were taken but the lamp created glare, which was a problem towards the final thinning stages of the filament. A translucent paper was placed in front of the light source which lowered the glare and improved the definition of the images. This arrangement comfortably provided usable images up to around 5000 fps.

However, as development progressed and efforts focused on differentiating between very thin fluids necessary changes became apparent. Initial drop sizes less than 1.5 mm across were used to try to reduce inertia and the effects of gravity (characterised by the Oh and Bo number, respectively, discussed in Sec. 1.1 and Chapter 4). Moreover, thin fluids exhibit faster break-up times (characterised by τ_R, discussed in Sec. 1.1, and Chapters 3 and 4), making the task of discriminating between them more difficult. Further, it was later deemed that analysis should be targeted at the final stages of the break-up of the filaments in order to minimise the effects of initial transients and axial curvature, which is discussed later in Sec. 4.3.2 and Chapter 5; at these later stages break-up is both faster and the filament dimensions smaller. This led to the need for a more powerful system. Using a single LED lamp, long-range microscope attachment (Infinivar K2-SC), and a powerful high speed camera (Photron SA5, Japan) high clarity and high-zoom images were captured at speeds of up 62000 fps. This gave the increased resolution needed to distinguish between thin fluids using standard error analysis. During measurements a 1.25 mm diameter wire was used as a visual reference to enable dimensional scaling of images.

2.7 System testing and advantages

2.7.1 Small sample volumes

The ability to test small samples renders several advantageous attributes to this system that favour rheological analysis, where volumes are typically around 1 – 5 µl (three orders of magnitude lower than conventional techniques). Small samples mitigate the asymmetric flow and filament shape effects that are caused by gravity [7]. This is quantified by the Bo (discussed earlier in Sec. 1.1), which is below unity at ≈ 0.3 in the case of a 1.5 mm water droplet, for example. Also, smaller sample sizes reduce inertial effects that might disrupt filament formation and decay, as characterised by the Oh (discussed in Sec. 1.1 and Chapter 3). These effects can hinder systems like CaBER and FiSER where the mechanical vibrations of the end-plates can cause disruptive vibrations that are not damped out in low-viscosity fluids. Another novel advantage this system has over alternative techniques is its ability to perform analysis with micro-droplets of samples; this has enabled the testing of materials that possess a range of rheological behaviours, which are prohibitively difficult to produce in large volumes. These analyses are discussed in Chapters 3 – 7.

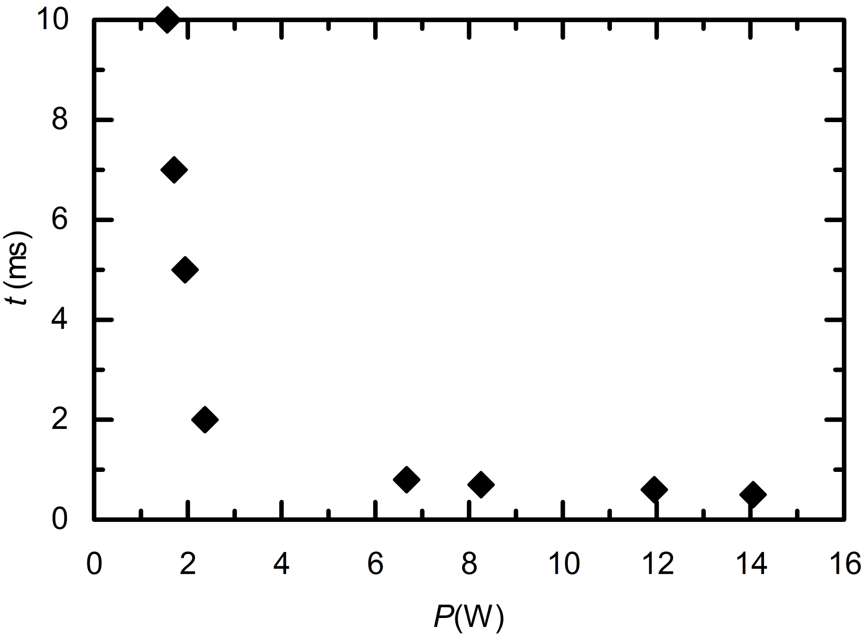

Fig. 2.10 Input power against time taken to create a liquid bridge of dioctyl phthalate (η = 63 mPa·s, ρ = 985 kg/m^3 @ 20°C, R_0 = 0.5 mm) from a 1 μL droplet. Plate separation is held constant at 10 mm. Note how the time taken to form a fluid bridge dramatically decreases once the output power goes beyond about 5 W.

2.7.2 SAW induced suppression and stabilisation

However, this system also overcomes the challenge presented by the fast break-up times of low-viscosity fluids. Recalling the time it takes for an inviscid filament to break-up, τ_R (discussed in Sec. 1.1 and Chapter 3), we can see that at scales of around 1.5 mm an anticipated break-up time of $\approx$ 7 ms is expected, which generally agrees with experimental observations for water (see Fig. 2.7). Such rapid break-up times limit traditional CaBER's access to low-viscosity fluids since it takes $\approx$ 50 ms for its extending plates to create a filament, otherwise known as the opening time [7], though this has been reduced to around 5.3 ms in recent advancements [9]. In the case of the SAW technique, testing revealed that it is possible to adjust the rapidity of a liquid bridge's creation by simply adjusting the power delivered to the SAW device (Fig. 2.10). This allows filament creation times of $\approx$ 0.5 ms, well below the thinning time predicted by τ_R — this is readily achieved by within the system's power limits, discussed in Sec. 2.4.

Yet this does not tell the whole story; observing Fig. 2.10 it can be seen that a liquid bridge can be formed in as long as 10 ms, of the order of the 7 ms break-up time predicted by τ_R. Fig. 2.11 demonstrates that a liquid bridge can be sustained indefinitely as long as SAW

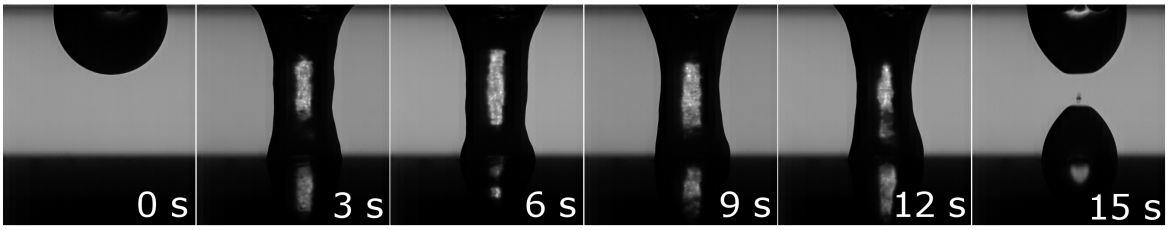

Fig. 2.11 A montage demonstrating that a sustained 15 s SAW burst is able to maintain a filament of water beyond the critical aspect ratio. We can see that as the SAW burst ends at 15 s, the fluid filament collapses. It is believed that SAW energy is able to prevent liquid bridge decay indefinitely. The bridge is created within 1.5 ms.

energy is injected. The SAW irradiation can also consistently produce a stable filament despite the potential for disruptive inertial effects posed by the high impact velocities seen when an extending filament impacts upon the opposing surface, ≈ 10 m/s. This suggests that SAW energy is able to both counter the contractile effects of surface tension and prevent the filament breaking up, whilst also countering the disruptive effects of inertia. To the author's knowledge, the only other case in which a stationary liquid filament is able to be stabilised against capillary forces is in the case of an applied voltage across dielectric liquids [82].

The capacity of acoustic energy to suppress surface tension and inertial effects is owed to its ability to generate momentum flux. An acoustic beam attenuates as its momentum is diffused, resulting in the formation of a steady jet of bulk fluid motion along its propagation length, a process that is dependent on both fluid and wave properties. Acoustic wave amplitude decays in the direction of its propagation x as $e^{-\beta_u x}$; in the MHz frequency range the acoustic wave amplitude attenuation coefficient β_u can be simplified to [63, 75]:

$$\beta_u = b\omega^2/2\rho c^3, \tag{2.6}$$

where $b = (4\eta/3 + \eta')$, with η' being the bulk viscosity, which is $\approx 2.4 \times 10^{-3}$ Pa·s in the case of water [75]. The inverse of the amplitude attenuation coefficient β_u^{-1} is the decay length of a sound beam's velocity, and in the case of a 30 MHz wave in water $\beta_u^{-1} \approx 51$ mm. This acoustic beam length is far in excess of the typical initial 1.5 mm droplet diameter used in our set-up, thus we would expect the presence of significant air-liquid interface disruptions in our observations. There is a large difference between the acoustic impedance of water Z_w and air Z_a, such that $Z_w/Z_a \approx 3.59 \times 10^3$, for example. This means that most of the acoustic energy is reflected at the air-liquid interface, as described by the power reflection coefficient, $P_{ref} = \left(\frac{Z_w - Z_a}{Z_w + Z_a}\right)^2$ [63]; meaning that $\approx 99.98\%$ of the acoustic energy is reflected back into the liquid to further dissipate its energy to bulk flow *via* momentum flux $\rho f(x)$, where $f(x)$ represents a function that determines the jet's momentum flux [68]. This can be related back to the acoustic power, defined in Eqn. 2.5, by [68]:

$$f(x) = \frac{1}{\rho c}P[1 - e^{\beta x}], \tag{2.7}$$

where $\beta = 2\beta_u$ is the attenuation coefficient for beam power, which is twice that of β_u since wave power is proportional to the square of particle displacement and velocity (see Eqn. 2.5). An additional contribution to momentum flux from travelling sound waves reflecting off the air-liquid interface, otherwise known as radiation pressure, is also likely to contribute to the deformation of the droplet [81].

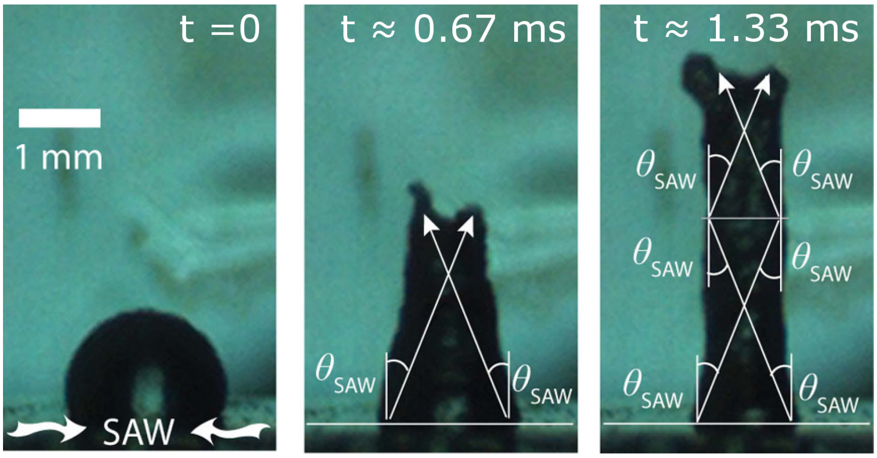

Fig. 2.12 These sequenced images show how SAW energy entering a droplet at the Rayleigh angle θ_R is believed to reflect within and propagate a fluid filament. Source: [44].

The full prediction of acoustic energy's conversion into bulk fluid motion is challenging, especially in this case as both an acoustic beam and jet reflect within a liquid body *via* a dynamic interface; however, comprehensive prediction of this is not the focus of this study. Nonetheless, SAW energy is believed to be responsible for significant interactions at the air-liquid interface, and provide a sufficient degree of momentum flux to counter the effects of surface tension. Thus, it is believed that reflection at the air-liquid interface allows SAW radiation to destabilise the interface and generate elongated filaments from sessile droplets [44], see Fig. 2.12. Therefore, SAW energy is able to sustain a filament against surface tension indefinitely, and stabilise against potential inertial induced instabilities by maintaining the filament until such effects dissipate, which are further mitigated by the small sample sizes used in this system.

2.7.3 Freedom from nozzle related problems

This technique functions without the need of a nozzle, unlike other low-viscosity extensional flow systems such as the Rayleigh Ohnesorge Jetting Extensional Rheometer (discussed in Sec. 1.1) or inkjet technology, the latter of which has be proposed as a rheometer for low-viscosity fluids, but is limited in its utility (discussed at length in Chapter 7). The limitations in testing particle suspensions posed by nozzles are also discussed further in Chapter 7, but are discussed briefly here specifically in relation to inkjets, for which there is ample literature.

It is advised that the diameter of a nozzle is at least 100 times greater than that of any suspended particles [52]; this limits the range of sizes that can be accommodated by a single system. Furthermore, nozzle clogging can result from operation using particle suspensions, which can change system characteristics and disable function altogether. Finally, the flow-rates seen in inkjets produce complex flows and large shear rates within the nozzle itself that can be as high as 2×10^4 to 2×10^6 s^{-1} [83], which can damage delicate suspended particles as they do to delicate proteins [84, 85].

The fact that the acoustically-driven microfluidic extensional device does not use nozzles frees it from the nozzle associated problems of particle size and clogging, and the risk of particle damage since SAWs can safely manipulate suspensions without causing damage to delicate particles, as discussed in Sec. 2.2.

2.8 Data extraction

High-speed imagery of a single filament break-up event requires a video that could be of the order of thousands of frames long, depending on the sample break-up time and the frame rate used. These high frame volumes demanded machine processing for speed, precision, consistency, and practicality, especially considering the high number of videos being obtained (Sec. 2.5.1).

After raw 24 bit high-contrast images were recorded (Fig. 2.13, the details of which are discussed in Sec. 2.6) and stored they were prepared using image analysis software (ImageJ) and processed *via* a custom MATLAB® (Mathworks, Natick, MA) script. Here image threshholding was employed to then convert each frame to binary, black and white, images and also identify regions of isolation (like light spots) and fill them, creating a solid silhouette of the filament, as is demonstrated in Fig. 2.13; each image of black and white pixels could be interpreted as an array of 0's and 1's, respectively. For each frame, the

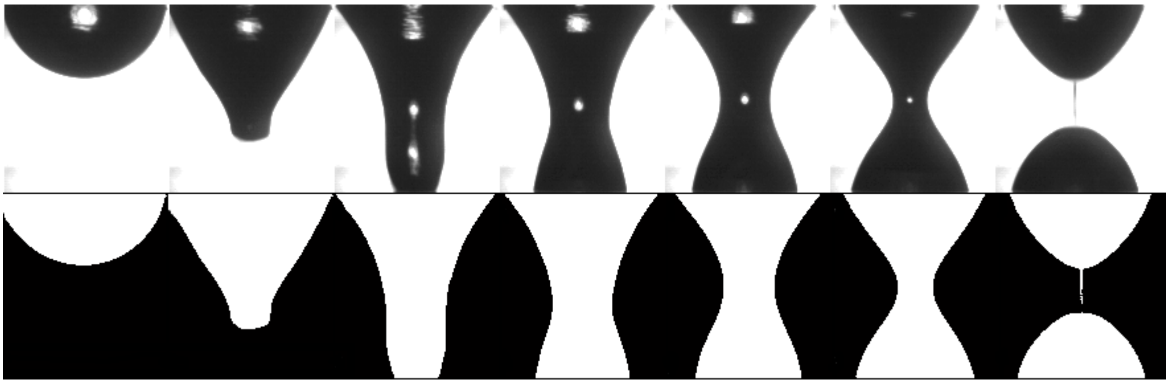

Fig. 2.13 The top row montage shows raw images of a typical SAW burst filament break-up experiment. The bottom row shows the binary silhouette interpretation of the above images, achieved with the custom MATLAB® image analysis script.

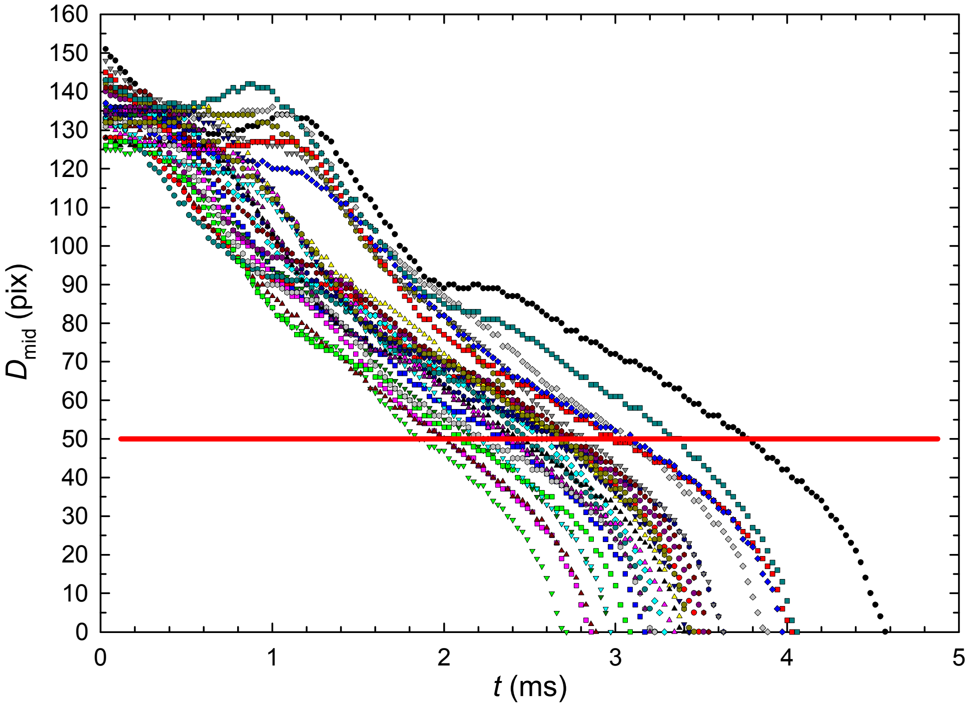

Fig. 2.14 Break-up data of water showing initial transients. The red line demarcates the 50 pixel point at which transients reliably settle and that data processing begins.

script identified the row with the minimum number of 1's within the array and recorded its magnitude, this minimum would represent the minimum filament diameter — the key variable of interest. Using the aforementioned reference wire (Sec. 2.6) this magnitude was converted from pixels to meters. The recorded minimum filament diameter and the video frame rate detailed the contracting filament's evolution over time. Processing of data begun after initial transients reliably settled, which are caused by adjustments in the filament as

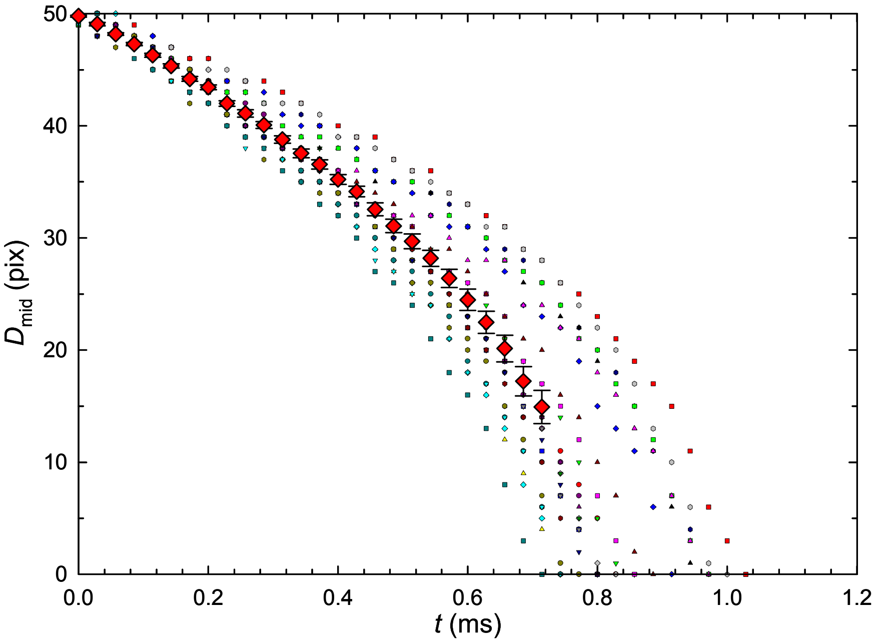

Fig. 2.15 Typical truncated and averaged dimensional diameter *versus* time filament break-up data (large red diamonds) of the experimental water results seen in Fig. 2.14. Smaller symbols represent the original data from Fig. 2.14.

the SAW is turned off; this occurs reliably after the filament diameter reduces to 50 pixels (0.352 ± 0.007 mm), as depicted in Fig 2.14. The MATLAB® script could process batches of experimental videos and return averaged data with standard error analysis, where typical data was expressed as is shown in Fig. 2.15. The extraction of rheological properties from data in this form is explained in Chapter 4.

Chapter 3

Publication: Extensional flow of low-viscosity fluids in capillary bridges formed by pulsed surface acoustic wave jetting

This chapter, which is a publication, explores the conditions required to produce fluid filaments using SAWs for the purposes of extensional rheology. It compares several results from acoustically-driven microfluidic extensional rheometry against data from an established technique using conventional analysis methods, and demonstrates the potential of the technique to assess the extensional properties of non-Newtonian fluids. Also, it explores the advantages of the technique over conventional experiments and exploits them to conduct the filament break-up analysis of a solution containing a complicated blood protein for the first time, revealing a multi-stage break-up process.

3.1 Introduction

Chapter 2 documented the development of the acoustically-driven capillary break-up device and its generation of break-up data. Chapter 3 provides complementary information which defines the conditions under which SAWs can be used to create liquid filaments, and further analyses the limitations of traditional filament break-up experiments. However, the main focus is the comparison of its experimental results with data from accepted rheological experiments, and the quantification of its data using standard rheological analysis. The technique's potential for polymer characterisation is demonstrated by quantifying the elastic properties of a low-viscosity dilute polymer solution, and also showing that it may be possible to extract $\bar{\eta}$ using this technique under certain circumstances. Finally, the technique is utilised in observing the effects of extensional flow on a small volume of low-viscosity solution containing a dissolved protein, fibrinogen, which is an important multimeric blood molecule that is responsible for functions like blood clotting, and is difficult to obtain in large quantities. These results showed a unique multi-stage filament break-up process, which suggests strong extensional flow may cause the denaturing of these complicated molecules.

Note: Dr Pradipto K. Bhattacharjee and Amarin G. M^{c}Donnell jointly developed the experimental technique used in this paper. Dr Bhattacharjee guided investigation and led analysis efforts; Amarin G. M^{c}Donnell performed preparation and experimentation, and data processing.

3.2 Publication

The following publication was reproduced from [15] by permission from the Institute of Physics.

Note: Following its publication, a couple of typographical errors in this article were brought to our attention by the examiners. “Tripathi” has been misspelt as “Tripathy” on one occasion. In the caption for Fig. 4 (b), the last line should read $R \sim (t_f - t)^{2/3}$. These errors are regretted.

Monash University

Declaration for Thesis Chapter 3

Declaration by candidate

In the case of Chapter 3, the nature and extent of my contribution to the work was the following:

Nature of contribution	Extent of contribution (%)
Dr Pradipto K. Bhattacharjee and Amarin G. McDonnell jointly conceived and invented experimental technique used in this paper. Amarin G. McDonnell performed preparation, experimentation, data processing, and performed the writing of the paper.	45

The following co-authors contributed to the work. If co-authors are students at Monash University, the extent of their contribution in percentage terms must be stated:

Name	Nature of contribution	Extent of contribution (%) for student co-authors only
Pradipto K. Bhattacharjee	Dr Pradipto K. Bhattacharjee and Amarin G. McDonnell jointly conceived and invented experimental technique used in this paper. Dr Bhattacharjee guided investigation, led analysis efforts, and performed the writing of the paper.	
R Prabhakar *	Contributed to interpretation, analysis, and draft review.	
L. Y. Yeo	Contributed to interpretation, analysis, and draft review.	
J Friend	Initiated study, contributed to interpretation and analysis, and draft review.	

The undersigned hereby certify that the above declaration correctly reflects the nature and extent of the candidate's and co-authors' contributions to this work*.

Candidate's Signature	[redacted]	**Date** 23/2/2016
Main Supervisor's Signature	[redacted]	**Date** 23/2/2016

New Journal of Physics
The open-access journal for physics

Extensional flow of low-viscosity fluids in capillary bridges formed by pulsed surface acoustic wave jetting

P K Bhattacharjee, A G McDonnell, R Prabhakar, L Y Yeo and J Friend[1]
MicroNanophysics Research Laboratory, Department of Mechanical and Aerospace Engineering, Monash University, Melbourne, VIC 3800, Australia
and
Melbourne Centre for Nanofabrication, Melbourne, VIC 3800, Australia
[redacted]

New Journal of Physics **13** (2011) 023005 (14pp)
Received 22 July 2010
Published 1 February 2011
Online at http://www.njp.org/
doi:10.1088/1367-2630/13/2/023005

Abstract. Forming capillary bridges of low-viscosity ($\lesssim 10\,\mathrm{mPa\,s}$) fluids is difficult, making the study of their capillary-thinning behavior and the measurement of the fluid's extensional viscosity difficult as well. Current techniques require some time to form a liquid bridge from the stretching of a droplet. Rapidly stretching a liquid bridge using these methods can cause its breakup if the viscosity is too low. Stretching more slowly allows the bridge to thin and break up before a suitable bridge geometry can be established to provide reliable and accurate rheological data. Using a pulsed surface acoustic wave to eject a jet from a sessile droplet, a capillary bridge may be formed in about 7.5 ms, about seven times quicker than current methods. With this approach, capillary bridges may be formed from Newtonian and non-Newtonian fluids having much lower viscosities—water, 0.04% by weight solution of high-molecular-weight (7 MDa) polystyrene in dioctyl phthalate and 0.25% fibrinogen solution in demineralized water, for example. Details of the relatively simple system used to achieve these results are provided, as are experimental results indicating deviations from a Newtonian response by the low-viscosity non-Newtonian fluids used in our study.

---

[1] Author to whom any correspondence should be addressed.

1367-2630/11/023005+14$33.00
© IOP Publishing Ltd and Deutsche Physikalische Gesellschaft

Contents

1. Introduction **2**
2. Experiment **4**
3. Results **8**
3.1. Benchmark solutions 8
3.2. Fibrinogen 11
4. Conclusions **13**
Acknowledgment **13**
References **13**

1. Introduction

Many branches of science and engineering rely upon accurate and complete knowledge of the behavior of fluids. For hydrodynamically simple—*Newtonian*—fluids, this knowledge is usually obtained without much difficulty: a constant viscosity to go with a density and surface tension. But for arguably a majority of fluids, neither the behavior nor the measurement is so simple. Complex fluids, common in biology and engineering and as diverse as blood to adhesives, possess deformable microstructure that gives rise to at least one non-constant and perhaps time-dependent viscosity. Fortunately, elongational flows offer a strong irrotational deformation; within such fluids these flows are capable of aligning such microstructure, whether flexible polymer molecules, red blood cells or asymmetric rigid bodies, along the direction of the flow. The flow-induced alignment of flexible polymer molecules enables the study of properties that arise from the intrinsic connectivity of the molecular backbone and from peculiarities in the architecture of the molecule [1]. One can employ elongational flows to determine the properties of fluids from simple to complex, and in recent times the application of elongational flows to the study of the dynamics of complex fluids has become an area of significant research activity.

Creating and sustaining uniaxial elongational flows in the laboratory, however, has been challenging, and reliable rheometric techniques using elongational flows have only been developed in the past two decades. One such technique that is particularly relevant to this study is capillary breakup elongational rheometry (CaBER), using surface tension-driven necking of a liquid bridge to study the evolution of fluid microstructure under elongational deformation [2]. However, the technique is currently limited to fluids possessing modest to extremely large viscosities. A remarkable variety of low-viscosity fluids, including biological fluids and nano-particle suspensions, cannot be currently studied using CaBER. In the following, we demonstrate that microjets generated using surface acoustic waves (SAWs) [3] can be used to replicate the CaBER technique at much smaller length scales using fluids of lower viscosities outside the range of CaBER. Because the new approach works at a physical scale much smaller than is typical with CaBER, quantitative measurements of non-Newtonian behavior of low-viscosity fluids undergoing extensional flow can be made using much less fluid, only a few microliters. This new technique permits an improved characterization of low-viscosity fluids having a small but finite elastic component, and may provide insight into the mechanisms that lead to the finite time singularity that occurs when a liquid column necks down and breaks under the influence of surface tension [4]–[7] in the limit of low fluid viscosity. As we aim to focus upon the concept and system rather than an in-depth study of non-Newtonian fluids whatever the viscosity, we will show the behavior of the system with Newtonian and non-Newtonian fluids, while only noting the deviation from typical Newtonian behavior in the latter case. Such deviations for very low-viscosity polymer solutions are reported here for the first time.

The CaBER technique allows the study of the dynamics of a fluid over a broad range of length scales, limited at the smaller end by the spatial resolution of the measurement instruments. With CaBER, a small volume of a fluid to be tested is placed in the gap formed between two parallel end-plates. By rapidly separating one of the two plates along a direction perpendicular to their faces, a liquid bridge is first formed. The motion of the end-plate is stopped when a predetermined separation between the plates is reached. The bridge then subsequently necks down and breaks under the influence of surface tension forces. The flow at the plane of the minimum neck radius is well approximated as a uniaxial extensional or stretching flow. Further, the time dependence of the approach to breakup of the minimum neck radius R_{neck} of the fluid strand under these conditions depends on the stress response of the fluid to an imposed extensional flow, and is well understood for Newtonian fluids, whereas in more complex non-Newtonian fluids, it is governed by the dynamics of the fluid microstructure. The central idea of the CaBER device is that the observed $R_{\text{neck}}(t)$ can be used to understand the behavior of complex fluids in extensional flows. An additional advantage of CaBER is the reliable location of the minimum (instantaneous) neck radius, $R_{\text{neck}}(t)$, at the mid-plane of the fluid column due to the confined geometry of the liquid bridge. This makes following the necking processes easier than other techniques like jet breakup [8] and drop pinchoff [9, 10] where the position of the neck varies in both time and space from one test to another.

For complex fluids, as the liquid bridge narrows and the length scale of the flow (ℓ) near the narrow neck region of the bridge decreases, non-Newtonian effects can be dramatically amplified as the Deborah number $De = \lambda V/\ell$ and the elasticity number $El = \eta_0\lambda/\rho\ell^2$ both increase to values greater than unity. Here η_0 is the zero-shear-rate viscosity of the fluid, λ is the characteristic relaxation time of the viscoelastic fluid, V is the characteristic velocity of flow and ρ is the density of the fluid. At small length scales, the influence of inertia decreases with the Reynolds number $Re = \rho V\ell/\eta_0$ and the non-Newtonian effects become more conspicuous even for small values of η_0 and V.

Extending the CaBER technique with current technology to low-viscosity non-Newtonian fluids is prevented by the difficulty in forming liquid bridges of these fluids. A bridge is created in a CaBER system from a fluid drop by separating the two end-plates holding the drop. If the duration of this ‘opening time’ δt_0 exceeds the viscous time, $\tau_{\text{v}} = 14.1\eta_0 R/\gamma$, where R is the radius of the droplet and γ is the surface tension coefficient of the fluid, the liquid thread can disintegrate even before the separation of the plates is completed. Additionally, inertio-capillary oscillations of the bridge that result from the abrupt halting of the end-plates in CaBER can disrupt the liquid bridge immediately after its formation if the viscosity is too low. The other problems associated with the use of the CaBER technique for extensional rheometric characterization of low-viscosity fluids are discussed in detail elsewhere [11].

Returning to the problem of bridge formation, we can estimate $\eta_{0,\text{min}}$, the minimum viscosity necessary for bridge formation, by equating plate separation and viscous times, i.e. $\delta t_0 = \tau_{\text{v}}$. Hence, $\eta_{0,\text{min}} \sim \delta t_0\gamma/(14.1R)$, and for a typical Newtonian fluid with $\gamma = 60 \times 10^{-3}\,\text{N m}^{-1}$, and for values of $R = 3$ mm and $\delta t_0 = 50$ ms typical of current CaBER designs, we find that $\eta_{0,\text{min}} \sim 50$ mPa s. In fact, CaBER has been used to create observable bridges for fluids with $\eta_0 \sim 11$ mPa s [12], but aqueous solutions of lower viscosities have not been studied. Thus,

$\eta_{0,\mathrm{min}} = 10\,\mathrm{mPa\,s}$ represents a conservative estimate for the lower limit of operability of current designs of CaBER.

The use of SAW-induced microjets circumvents this problem by allowing the creation of liquid bridges within much smaller intervals δt_0, while avoiding the problems induced by the mechanical separation of end-plates in conventional CaBER designs. A SAW is an electroacoustic wave that travels along the surface of a material, possessing an amplitude that decreases exponentially with depth in the medium. The use of SAWs to generate liquid jets from sessile droplets has been recently demonstrated [3] using a simple yet specific electrode configuration that acts to focus the energy of the electroelastic SAW (typically of 1–10 nm in amplitude). The SAW propagates along the substrate surface to a spot with a size equivalent to the wavelength of the acoustic radiation such that a part (determined by the relative acoustic impedance) of the concentrated energy 'leaks' into a droplet placed at the acoustic focal point. With sufficient acoustic wave intensity, acoustic streaming [13] results in the fluid, elongating the droplet perpendicular to the substrate and into a column of fluid—a jet—a few centimeters in length.

Over the following pages, the technique used to generate fluid bridges suitable for rheometry from Newtonian and non-Newtonian fluids possessing low viscosities is introduced. Results on the rheometry of water, polystyrene solutions and solvents follow, and are concluded by measurements of the rheology of dilute solutions of fibrinogen (FN) in water. We aim to show with these results that our system, described here for the first time, is capable of measuring the extensional rheology of low-viscosity fluids that are otherwise impossible to test using current technology.

2. Experiment

The SAW device used in these experiments is a variant of the device reported in [3] with a resonance frequency of 30 MHz. Details of the fabrication of the device are documented elsewhere [14, 15]. Briefly, the SAW was generated by supplying a sinusoidal voltage to an interdigital transducer (IDT) fabricated on a 0.5-mm-thick lithium niobate (LN) piezoelectric crystal. The section between the IDTs was coated with a thin layer of Teflon (Teflon AF, DuPont, Wilmington, Delaware, USA) in order to provide a hydrophobic surface. Single drops were placed with a pipette (Eppendorf PhysioCare Concept 0.1–2.5 $\mu\ell$, Hamburg, Germany) at the focal point of the IDTs before subjecting the fluid to a SAW burst, a controlled, intense exposure of the droplet to SAWs driven by a signal generator–amplifier combination. A photograph of the configuration with the quiescent droplet is shown in the left panel of figure 1(a). A 20 MHz waveform generator (33220A, Agilent, Santa Clara, CA, USA) was used to determine the burst time by triggering a second signal generator (WF1966, NF Corporation, Yokohama, Japan) over a fixed, predefined amount of time. The latter delivered a sinusoidal signal to an RF power amplifier (411LA, ENI, West Henrietta, NY, USA), providing a fixed frequency and amplitude signal near the resonance frequency of the SAW device. In order to obtain a liquid bridge, a glass plate was placed directly opposing the plate containing the SAW device as shown in the right panel of figure 1(a). Using this technique we have been able to create liquid bridges in 7.5 ms, about seven times quicker than existing technology, presenting us with the ability to observe the capillary-thinning behavior of fluids with viscosity of the order of 1 mPa s, much lower than $\eta_{0,\mathrm{min}}$.

An advantage of using SAWs for creating liquid bridges is that δt_0, the time taken to create a bridge using a given fluid, can be reduced by increasing the voltage driving the IDTs.

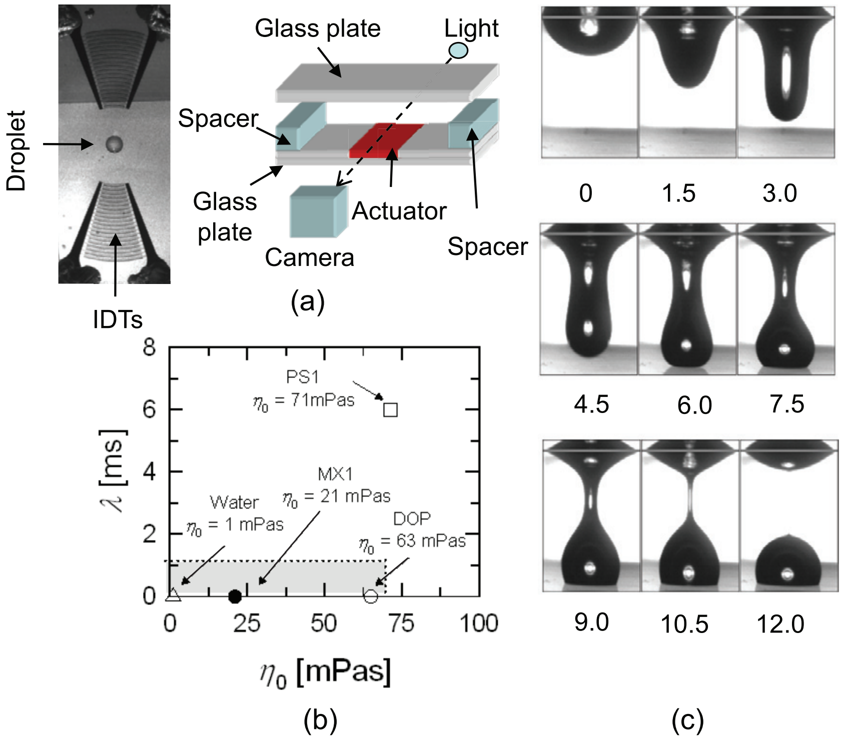

Figure 1. (a) Left panel: two focusing electrodes at the ends of an LN substrate are shown. The electrodes provide a focused SAW that progresses beneath and into the drop placed on the substrate at the focal point, causing it to deform into a coherent elongated jet. Right panel: schematic of the experimental setup for creating the liquid bridge. During experiments the setup is inverted so that the droplet jets downward and along the direction of gravity. (b) Solutions used in the study are indicated with respect to their viscosity and relaxation time in a manner similar to previous work [11]. The shaded region is difficult to access in conventional CaBER experiments due to limitations of current technology. (c) Using this system, a coherent jet forms from the droplet and subsequently becomes a liquid bridge as it reaches the opposite surface. The bridge necks down under the influence of capillary forces acting at the interface. The numbers correspond to the time in milliseconds. The gray line on the top refers to the surface of the plate containing the SAW actuator. For rheometric measurements the start time is $t_0 = 7.5$ ms, the time at which the SAW actuation is terminated for the shown experiment.

In figure 2, the decrease in time required to make a liquid bridge of DOP across two glass plates separated by 10 mm with increasing voltage is shown. The volume of test fluid required for use in the system is only about 1–5 μl, three orders of magnitude smaller than the volume required in current techniques.

The energy that leaks into the droplet is dependent on the size of the droplet relative to the aperture of the SAW IDT, the contact angle of the fluid, and the amplitude of the induced SAW in a complex, most nonlinear manner [16]. Further, as the viscosity is reduced, more accurate control of the separation distance and the alignment of the end-plates were found to be

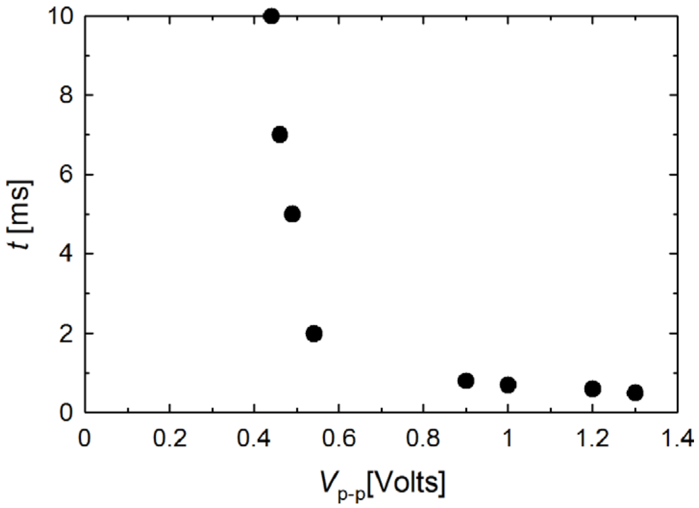

Figure 2. Voltage against time taken to create a liquid bridge of DOP from a 1 μl droplet. Plate separation is held constant at 10 mm. Note how the time taken to form a fluid bridge dramatically increases once the voltage falls below about 0.7 V.

necessary. The design described here allows only limited control of these variables. However, it was observed that careful control of the excitation voltage was sufficient to significantly enhance the reproducibility of the breakup time of liquid bridges (especially for water). Without due care in ejecting the droplet, the droplet either failed to jet or atomized—simply burst into droplets, which is indeed useful for other applications [14], [17]–[19]—in a complex manner illustrated by the non-dimensional relationship plotted as a map in figure 3.

The map was generated using several glycerol–water solutions of different viscosities. The basis for constructing the phase map is the idea that jetting occurs in sessile drops when they acquire sufficient momentum due to acoustic streaming driven by SAW irradiation. We define here a non-dimensional number that represents the ratio of SAW forcing imposed on the droplet to the resistance offered by surface tension to change in surface area,

$$\Pi = \frac{P/c_{\mathrm{s}}}{\gamma R_{\mathrm{d}}}, \tag{1}$$

where P is the power of SAW forcing, c_{s} is the speed of sound in the fluid and R_{d} is the original droplet radius. Lighthill's [20] analysis suggests that acoustic streaming can be expected when the ratio $\rho P/(c_{\mathrm{s}}\,\eta_0^2) = \Pi/Oh^2$ exceeds a value of around 10, where

$$Oh = \frac{\tau_{\mathrm{v}}}{\tau_{\mathrm{R}}} = 14.1\,\frac{\eta_0}{\sqrt{\rho\gamma R_{\mathrm{d}}}} \tag{2}$$

measures the relative importance of viscous over inertial effects, the time-scale of the latter being quantified by the Rayleigh time, $\tau_{\mathrm{R}} = \sqrt{\rho R_{\mathrm{d}}^3/\gamma}$. Thus, on a plot of Π against Oh, we expect jetting in the region above the line $\Pi \approx 10\,Oh^2$.

For any given Oh, we find that at relatively low non-dimensional values of the power, the droplet only slightly deforms from the surface as a 'stub'. As power input is increased, however, there is a transition to jetting (demarcated by + symbols). Although the expectation is that the transition from stubs to jetting should occur across a straight line of slope 2 on a log–log plot, the

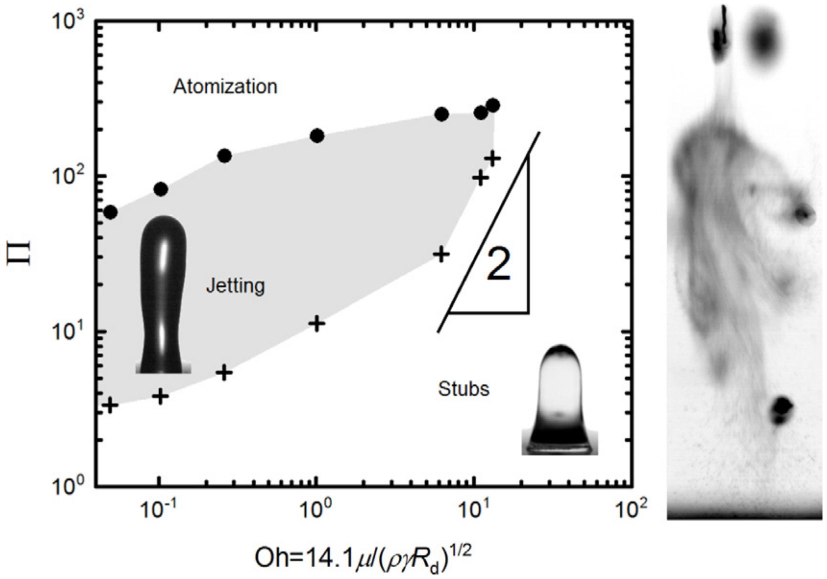

Figure 3. A map of the phenomena that can be generated by passing a SAW into a droplet sitting at the focal point atop the device shown in figure 1. Equations (1) and (2) in the text define the dimensionless numbers Π and the Ohnesorge number *Oh*. The photograph on the right shows typical behavior in the atomization regime at large values of Π.

transition line is actually slightly curved upwards in figure 3. We believe this is due to the effects of compressibility. Under most conditions in microfluidics, compressibility is negligible, but high-frequency acoustic waves induce significant density gradients, an important mechanism for acoustic streaming. The Ohnesorge number contains the density ρ in the denominator, and as the power is increased, the value of this density is left constant for the purposes of the plot, whereas in reality the actual density becomes larger as a consequence of the compression during exposure to the SAW [21]. The plotted Ohnesorge number is thus actually lower than it actually is in the experiment if we were to use the true value for the density. The problem is that the determination of the *correct* density value is very difficult.

At very high powers, we observe that jets atomize (demarcated by ● symbols and illustrated with the image to the right of the graph). Further, at large values of *Oh* we find that drops tend to atomize directly as power is increased without first forming jets. The phenomena that lead to atomization are currently not well understood. Nonetheless, the gray region represents the parameter space where SAWs can be used to create liquid bridges, and is thus useful for rheometry and rheology.

Following excitation of the droplet by SAWs and formation of the liquid bridge between the two plates, SAW excitation was turned off when a near-equal distribution of the material between the plates was obtained. As discussed above, SAW-induced jetting is the result of acoustic streaming. Therefore, once the liquid bridge is formed, we shut off SAW forcing to avoid any complications that may arise from a coupling between acoustic streaming and fluid rheology. The bridge then thins solely under the influence of surface tension, and we analyze the subsequent time evolution of R_{neck} as in the conventional CaBER device.

Images of the necking process were captured using a high-speed camera (Mikrotron MC1310, Germany) with a lens (InfiniVar CFM–2/S, Infinity Photo-Optical Company, Boulder,

Table 1. Physical properties of the fluids used in this study, organized by decreasing viscosity η_0. PS1 is a 0.04% by weight solution of high-molecular-weight polystyrene ($M_w = 7.0$ MDa) in dioctyl phthalate (DOP) (Hopkin and Williams Ltd). MX1 is a 1 : 3 solution of DOP (Hopkin and Williams Ltd) and diethyl phthalate (DEP) (Aldrich Chemical Company, Inc.). The c/c^* ratio for the polystyrene solution is 0.887 and its Deborah number $De = \lambda/\tau_v$ is 0.198[2].

Fluid	γ (N m^{-1})	η_0 (Pa s)	τ_v (s)	τ_R (s)	Oh
PS1	3.0×10^{-2}	7.1×10^{-2}	1.0×10^{-1}	2.9×10^{-2}	3.4
DOP	3.0×10^{-2}	6.3×10^{-2}	8.9×10^{-2}	2.9×10^{-2}	3.0
MX1	3.2×10^{-2}	2.1×10^{-2}	2.8×10^{-2}	2.9×10^{-2}	0.92
Water	7.2×10^{-2}	1.0×10^{-3}	5.9×10^{-4}	1.9×10^{-2}	3.6×10^{-2}

CO, USA) attachment. A single LED lamp was used to illuminate the liquid bridge in bright-field view (the bridge was placed between the lamp and the camera) and a 1.25 mm diameter wire was used as a visual reference during recording. Images were collected at 5000 frames per second and were analyzed using ImageJ (National Institutes of Health, Bethesda, MD, USA). The breakup event could be ascertained within ±0.5 ms using this approach. An example of bridge formation and necking behavior is demonstrated in figure 1(c). It can be observed from figure 1(c) that the liquid bridge is formed at around 7.5 ms and breaks up at around 12 ms.

3. Results

3.1. Benchmark solutions

Details of the fluids studied with the technique discussed above are provided in table 1, where the viscous time, $\tau_v = 14.1\eta_0 R/\gamma$, and the Rayleigh time, $\tau_R = \sqrt{\rho R^3/\gamma}$, presume a length scale of $R = 3$ mm, a typical radius used in a CaBER experiment, and is used to facilitate comparison. Also listed in the table are the values of $Oh = \tau_v/\tau_R$. Strictly speaking, only fluids having $\tau_v \ll \tau_R$ can be considered to be low-viscosity fluids [11]. However, due to the restrictions imposed by the opening time (δt_0) this limit is seldom accessible in CaBER experiments. The present experiments are, thus, significant in this context. The range of CaBER is shown in figure 1(b), where the shaded region denotes the area where CaBER experiments are impractical due to the limitations of current technology. The diagram follows the one shown by Rodd *et al* [11], although in the present case the boundaries are marked by straight lines, instead of a curve, for simplicity. These limits can be marginally altered by a judicious choice of the geometry and operating conditions, but the differences are not remarkable. The points on the diagram in figure 1(b) identify the fluids used in this work.

In figure 4 the capillary-thinning behavior of Newtonian liquids used in this work is shown. The ratio of the minimum (instantaneous) radius ($R_{\text{neck}}(t)$) normalized by the initial radius of the liquid bridge (R_0) is plotted against time (t). On all occasions the minimum in the radius was observed to occur near the mid-point of the liquid bridge. Figure 4(a) presents our measurements for viscous samples for which $Oh \gtrsim 1$. We have also included data on glycerol from McKinley

[2] The diluteness of a polymer solution is characterized in terms of the ratio of the polymer concentration c over its critical value c^* at which polymeric coils begin to interpenetrate in solution. Both c^* and the time constant λ for the polymer solution, have been calculated using standard methods [38].

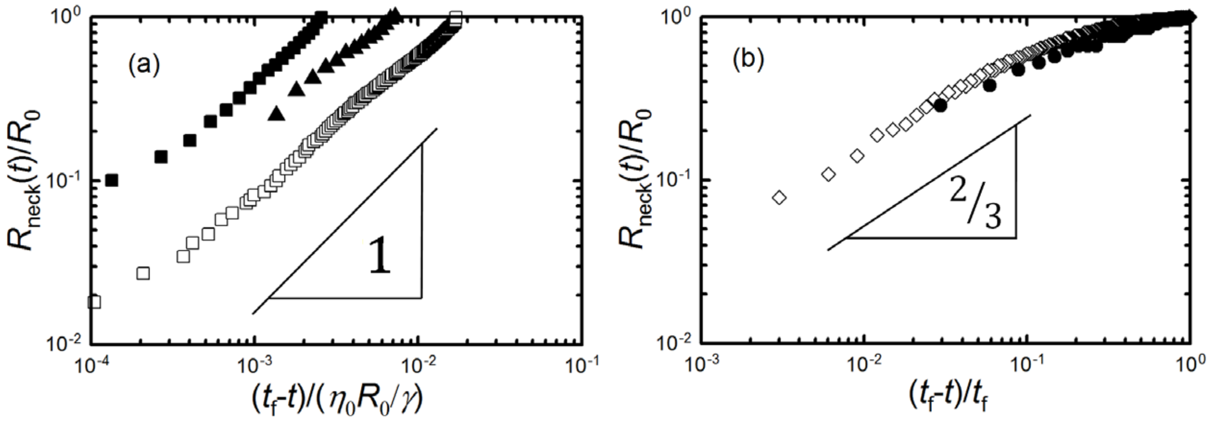

Figure 4. (a) Normalized minimum filament radii of bridges of viscous ($Oh \gtrsim 1$) fluid samples, namely, DOP (■) and MX1 (▲), plotted against time t expressed in terms of the normalized time to breakup, $(t_f - t)/t_f$, t_f being the breakup time observed in the experiments. Previous data using glycerol (□) by McKinley and Tripathi [22] are also included for comparison. Viscous Newtonian liquid bridges are expected to thin linearly with time close to breakup. (b) Data for inertia-dominated ($Oh \lesssim 1$) water liquid bridges using falling-drop (◇) and SAW (●) experiments, which are expected to thin such that $R(t_f - t)^{2/3}$ near breakup.

and Tripathi's work [22] for comparison. For viscous fluid threads undergoing surface tension-driven necking, it is expected that $R_{neck}(t) \sim (t_f - t)(\gamma/\eta_0)$, where t_f is the time at which the breakup event occurs, γ is the surface tension coefficient and η_0 is the zero-shear rate viscosity of the fluid [23]. The predicted linear trend is observed in the data in figure 4(a). It can also be seen that as the viscosity of a fluid decreases, breakup occurs earlier. For water, however, $Oh < 1$, and inertial effects become significant. In figure 4(b), we compare the data obtained on liquid bridges with the data obtained in falling-drop experiments by Amarouchene *et al* [9]. In this case, the observed decay approaches the asymptotic behavior $R_{neck} \sim (t_f - t)^{2/3}$ expected for thin filaments in the limit of vanishing viscosity [24].

The change in the capillary-thinning behavior due to the addition of a small quantity of long-chain polymer molecules is shown in figure 5(a). Here the response of the polystyrene solution PS1 is compared with that of the solvent, DOP. The neck radius for both viscous solutions initially decreases in a linear fashion with respect to time, although the rate of decrease for PS1 is slower due to its slightly higher viscosity from the dissolution of the polymer. Unlike DOP, which quickly undergoes breakup, PS1 abruptly transitions to a regime where $R_{neck}(t)$ decreases exponentially with time; the bridge narrows to a slightly smaller diameter but survives for approximately six times as long. In a capillary-thinning experiment involving a polymer solution, the elastic stresses can grow large enough to overwhelm the viscous stresses in the neck [2, 25, 26]. In fact, when the elasto-capillary stress balance dominates, the filament radius decays as $R_{neck}(t) \sim e^{-t/(3\lambda)}$, where λ is a characteristic relaxation time of the viscoelastic fluid [2, 11]. For polymer solutions, there is currently some debate concerning the interpretation of this relaxation time extracted from CaBER experiments and its relationship to the intrinsic relaxation time of polymer molecules [12, 27]. Nevertheless, this measured λ is a clear signature of polymer-induced elasticity.

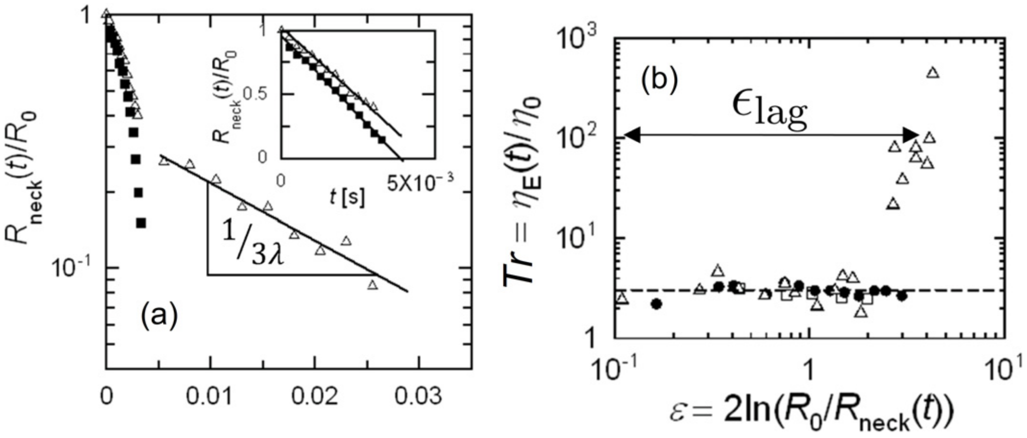

Figure 5. (a) Capillary-thinning behavior of a polymer solution PS1 (△) shows distinctly different behavior when compared to that of the solvent DOP (■). While the radius of the DOP filament decreases linearly with time, the breakup process in PS1 is arrested, and a pronounced exponential-decay regime is observed, as indicated by the solid line corresponding to an exponential fit, producing a slope of $1/(3\lambda)$. Data corresponding to the first 5 ms are shown in the inset. It can be observed that the initial necking process progresses linearly with respect to time in both cases. (b) Transient Trouton ratio evaluated using equation (3) for the solutions PS1 (△), DOP (●) and MX1 (□) plotted against Hencky strain ε. Note that PS1, DOP, MX1 and water are in order of decreasing viscosity.

Based on an analysis by McKinley and Tripathy [22], the following semi-empirical relation was suggested by Tuladhar and Mackley [28] to fit filament-thinning data and extract the transient Trouton ratio Tr, which is defined as the ratio of the transient extensional viscosity to the zero-shear rate viscosity of the fluid:

$$Tr = \frac{\eta_E(t)}{\eta_0} = (2X - 1)\left[\frac{\gamma/\eta_0}{-2\,\mathrm{d}R_{neck}/\mathrm{d}t}\right]. \tag{3}$$

For a Newtonian fluid, the extensional viscosity $\eta_E = 3\eta_0$, and hence $Tr = 3$, whereas for viscoelastic fluids such as polymer solutions, Tr is in general time dependent. The constant X is a lumped parameter that accounts for the combined effects of inertia, gravity and deviation of filament shape from a perfect cylinder. Theoretical analyses have shown that X ranges from 0.53 to 0.71 for Newtonian fluids, depending on whether inertial or viscous effects dominate. For polymer solutions, Tuladhar and Mackley used the equation to empirically fit X to ensure that $Tr = 3$ in the initial stages of filament thinning, when the contribution of the polymer to fluid stresses is negligible, and the fluid behaves as a viscous Newtonian fluid. Once the elastic stress induced by stretching polymer molecules becomes significant, Tr begins to increase above the initial Newtonian plateau. We use the same procedure to estimate the transient extensional viscosity from the data in figures 4(a) and 5(a), numerically calculating $\mathrm{d}R_{neck}/\mathrm{d}t$ from the data with a three-point central-difference formula. The values of X for PS1, MX1 and DOP are between 0.53 and 0.71. In figure 5(b), we plot the transient Trouton ratio against the Hencky strain at the necking plane, $\varepsilon = -2\ln(R_{neck}/R_0)$, for the fluids listed in table 1. The dotted line in figure 5(b) corresponds to the constant value of $Tr = 3$ for any Newtonian fluid. It can be observed from figure 5(b) that the Newtonian fluids DEP and MX1 show a constant value of $Tr = 3$ up until the resolution limit of our optical system was reached. For the polymer solution PS1, on the other hand, the value of Tr rapidly increases from a value of 3 to around 100 after a lag. It has been shown [29, 30] that polymer stresses in a dilute solution undergoing an extensional flow become significant after a Hencky strain of $\epsilon_{\text{lag}} = 0.5\ln(N_{\text{K}})$, where N_{K} is the number of Kuhn segments in the polymer. For the polymer in PS1, $N_{\text{K}} \sim 10^4$ and $\epsilon_{\text{lag}} \sim 4.5$. The data in figure 5(b) therefore indicate that typical benchmark behavior of viscoelastic fluids can be reproduced in these systems in a manner consistent with the literature, particularly with dilute polymer solutions in low-viscosity solvents, which are routinely used for polymer characterization. Although a detailed analysis is beyond the scope of this study, it is possible for instance to use ϵ_{lag} as a simple relative test of molecular weight across several samples.

It must be mentioned here that in both conventional CaBER and our experiments the exact deformation history during the creation of the liquid bridge is difficult to ascertain. The initial flow of the fluid in this ‘pre-strain’ time interval δt_0 is quite complex: the fluid jet is formed and then ejected to make contact with the top end-plate. In our experiments, drop volumes are typically 5 μl, with initial diameters of 1.5–2 mm. The time interval $\delta t_{\text{ps}} < \delta t_0$ for the ejected jet to bridge the 3 mm gap between the fixed end-plates is $O(1)$ ms for all the fluids we have tested. An upper bound on the extensional strain may hence be estimated by assuming ideal extensional flow during this entire process, and a cylindrical drop shape that gives a pre-strain $\epsilon_{\text{ps}} = \ln(\ell_{\text{final}}/\ell_{\text{initial}}) \approx \ln(3/2) \lesssim 1$. The strain rate $\dot{\epsilon}_{\text{ps}} = \epsilon_{\text{ps}}/\delta t_{\text{ps}} \sim O(10^2)\ \text{s}^{-1}$, which seems high. However, for the polymer solution (PS1) we have studied, the measured viscoelastic relaxation time $\lambda \sim O(10^{-2})$, which gives a Weissenberg number estimate $Wi_{\text{ps}} = \lambda\dot{\epsilon}_{\text{ps}} \sim O(1)$ for the pre-strain phase. For these typical values of Wi_{ps} and ϵ_{ps}, we do not expect any significant elastic stresses during bridge formation. Figure 5 further provides evidence for this: the initial necking of the PS1 liquid bridge is quite similar to that of the solvent DOP, showing that the initial deformation during liquid bridge formation does not cause polymers to stretch.

3.2. Fibrinogen

We now apply the SAW-induced microjets to observe the behavior of a multimeric blood protein, FN, in elongational flow. FN is a soluble plasma glycoprotein that plays an important role in hemostasis and cell adhesion [31]. Within the vasculature, vascular proteins such as FN encounter hydrodynamic deformation rates that can be of the order of $1000\,\text{s}^{-1}$ or more [32]. These deformation rates are capable of bringing about large changes in conformation that become important in a number of mechano-chemical responses like clotting via platelet aggregation [33, 34].

In figure 6(a), the thinning behavior of a 0.25% solution of FN (F2629, Sigma, USA) in demineralized water is shown. The zero-shear rate viscosity of the solution is close to that of water and therefore extensional rheological studies of such solutions have not been possible in the past. It can be observed from figure 6(a) that the initial profile of the thinning jet is identical to that of water (control) and deviates from it at a later time. The surface tension coefficient of FN solutions has been measured to lie between 0.04 and $0.05\,\text{N}\,\text{m}^{-1}$ [35, 36]. We thus estimate Oh for these solutions to be around 5×10^{-2}, whereas for water $Oh = 3.6 \times 10^{-2}$ (table 1). Therefore, despite changes in surface tension, the value of Oh for FN solutions is still much smaller than 1, and one would expect inertia-dominated thinning as observed for water. However, figure 6(a) shows that the thinning of the FN solution is substantially different from

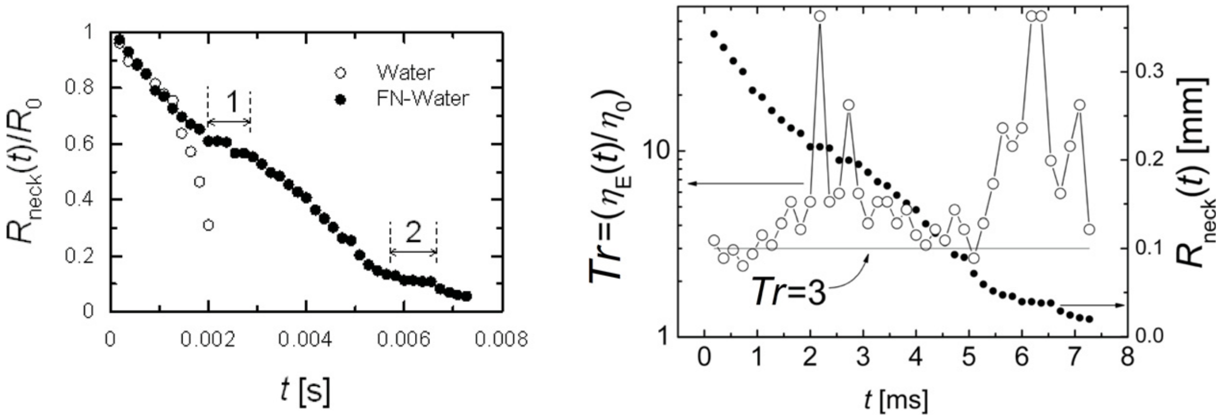

Figure 6. (a) Evolution of the normalized instantaneous diameter of 0.25% FN solution in demineralized water (○) compared with that of demineralized water alone (●). (b) Temporal evolution of the radius superposed on the calculated instantaneous Trouton ratio demonstrating the correspondence with each other. The horizontal line $Tr = 3$ is the value for a Newtonian fluid.

that of water. Further, the thinning rate for the FN solution substantially decreases (marked in figure 6(a) to facilitate identification) in between regions where the diameter shrinks steadily in time. At least two such regions can be identified in the present data.

As observed in figure 5(a) earlier, polymer-induced elastic stresses can resist the thinning of the filament, and it is possible that the two slowdowns in events in figure 6(a) are due to elastic stresses caused by the dissolved FN molecules. This is further highlighted in figure 6(b), where we plot the transient Trouton ratio calculated using equation (3) and the procedure described earlier (for the data in figure 6(b): $\gamma = 0.4\,\mathrm{mN\,m^{-1}}$, $\eta_0 = 1\,\mathrm{mPa\,s}$, $X = 0.51$). Although equation (3) is only strictly valid for viscous fluids when $Oh \gtrsim 1$, we use it as a qualitative tool to facilitate the discussion below. We have also retained the information on $R_{\mathrm{neck}}(t)$ in figure 6(b) to emphasize that the maxima in the transient Trouton ratio correspond to regions where the rate of capillary thinning is dramatically reduced.

The complexity in the response in the FN solution probably arises from the multimeric structure of the molecule, in contrast to the simple backbone architecture of a homopolymer like polystyrene. It can be observed from figure 6(b) that as time (and the strain) increases, the transient Trouton ratio ascends above the Newtonian level of 3, and is over an order of magnitude above this value when the maxima are reached. At intermediate values of strain, however, the apparent Trouton ratio rapidly decreases, almost to the Newtonian level, and suggests that the stress accrued within the filament somehow relaxes. This is particularly interesting because the strain continues to increase during this time. With a further increase in strain, the transient Trouton ratio rises again and reaches approximately the same maximum level as previously corresponding to the second region of relatively slow reduction in $R_{\mathrm{neck}}(t)$.

Single-molecule measurements using atomic-force microscopy have shown that compact domains in the secondary structure of proteins unfold under axial tension, and the force–displacement curves that result assume a sawtooth-like form that is characteristic of the protein studied [37]. The unfolding of protein domains typically manifests as sudden reductions among regular increases in the measured force with increasing elongation. It is tempting to speculate that the peaks in Tr in figure 6(b) are due to such stretch-and-yield events caused by the rearrangements brought about by strong elongational flow. What is however demonstrably clear is that the behavior of low-viscosity biological fluids in extensional flows can now be studied using the apparatus described in this study. These types of fluids have been difficult to characterize due to their low viscosity (which impedes filament formation) and relatively restricted availability in large quantities (which prevents studies using large volumes of highly concentrated fluids). Both these impediments have been overcome by the application of SAWs in forming the fluid bridge.

4. Conclusions

In summary, we have demonstrated a method of using SAW-induced fluid jetting phenomena for extensional rheometry of low-viscosity Newtonian and non-Newtonian fluids. The technique thus opens up the possibility of measuring the elastic properties of low-viscosity fluids such as biological fluids and protein solutions. Understanding their viscoelasticity could complement other methods such as single-molecule force spectroscopy in the study of the molecular structure of complex macromolecules such as FN. Another application could be the development of an inexpensive portable microfluidic analytical kit to characterize viscoelastic samples, by combining the technique presented here with electrical resistivity or capacitance measurements to measure the neck radius.

Acknowledgment

We thank Dr D A Nguyen for his help with preparing and characterizing the fluids used in this study.

References

[1] Keller A and Odell J A 1985 The extensibility of macromolecules in solution; a new focus for macromolecular science *Colloid Polym. Sci.* **263** 181–201

[2] Anna S L and McKinley G H 2001 Elasto-capillary thinning and breakup of model elastic liquids *J. Rheol.* **45** 115

[3] Tan M K, Friend J R and Yeo L Y 2009 Interfacial jetting phenomena induced by focused surface vibrations *Phys. Rev. Lett.* **103** 24501

[4] Pumir A and Siggia E D 1992 Finite-time singularities in the axisymmetric three-dimension Euler equations *Phys. Rev. Lett.* **68** 1511–4

[5] Grauer R, Marliani C and Germaschewski K 1998 Adaptive mesh refinement for singular solutions of the incompressible Euler equations *Phys. Rev. Lett.* **80** 4177–80

[6] Eggers J 1993 Universal pinching of 3D axisymmetric free-surface flow *Phys. Rev. Lett.* **71** 3458–60

[7] Eggers J 1997 Nonlinear dynamics and breakup of free-surface flows *Rev. Mod. Phys.* **69** 865–930

[8] Christanti Y and Walker L M 2002 Effect of fluid relaxation time of dilute polymer solutions on jet breakup due to a forced disturbance *J. Rheol.* **46** 733

[9] Amarouchene Y, Bonn D, Meunier J and Kellay H 2001 Inhibition of the finite-time singularity during droplet fission of a polymeric fluid *Phys. Rev. Lett.* **86** 3558–61

[10] Cooper-White J J, Fagan J E, Tirtaatmadja V, Lester D R and Boger D V 2002 Drop formation dynamics of constant low-viscosity, elastic fluids *J. Non-Newton. Fluid Mech.* **106** 29–59

[11] Rodd L E, Scott T P, Cooper-White J J and McKinley G H 2005 Capillary break-up rheometry of low-viscosity elastic fluids *Appl. Rheol.* **15** 12–27

[12] Clasen C, Plog J P, Kulicke W M, Owens M, Macosko C, Scriven L E, Verani M and McKinley G H 2006 How dilute are dilute solutions in extensional flows? *J. Rheol.* **50** 849–81

[13] Riley N 1998 Acoustic streaming *Theor. Comput. Fluid Dyn.* **10** 349–56

[14] Qi A, Yeo L Y and Friend J R 2008 Interfacial destabilization and atomization driven by surface acoustic waves *Phys. Fluids* **20** 074103

[15] Tan M K, Friend J R and Yeo L Y 2007 Microparticle collection and concentration via a miniature surface acoustic wave device *Lab Chip* **7** 618–25

[16] McHale G, Banerjee M K, Newton M I and Krylov V V 1999 Surface acoustic wave resonances in the spreading of viscous fluids *Phys. Rev.* B **59** 8262–70

[17] Qi A, Yeo L, Friend J and Ho J 2010 The extraction of liquid, protein molecules and yeast cells from paper through surface acoustic wave atomization *Lab Chip* **10** 470–6

[18] Friend J, Yeo L, Arifin D and Mechler A 2008 Evaporative self-assembly assisted synthesis of polymeric nanoparticles by surface acoustic wave atomization *Nanotechnology* **19** 145301

[19] Forde G, Friend J and Williamson T 2006 Straightforward biodegradable nanoparticle generation through MHz-order ultrasonic atomization *Appl. Phys. Lett.* **89** 064105

[20] Lighthill J 1978 Acoustic streaming *J. Sound Vib.* **61** 391

[21] Shutilov V A 1988 *Fundamental Physics of Ultrasound* (New York: Gordon and Breach)

[22] McKinley G H and Tripathi A 2000 How to extract the Newtonian viscosity from capillary breakup measurements in a filament rheometer *J. Rheol.* **44** 653

[23] Papageorgiou D T 1995 On the breakup of viscous liquid threads *Phys. Fluids* **7** 1529

[24] Eggers J and Villermaux E 2008 Physics of liquid jets *Rep. Prog. Phys.* **71** 036601

[25] Bazilevskii A V, Entov V M, Lerner M M and Rozhkov A N 1997 Failure of polymer solution filaments *Polym. Sci.* A **39** 316–24

[26] Bazilevskii A V, Entov V M and Rozhkov A N 2001 Breakup of an Oldroyd liquid bridge as a method for testing the rheological properties of polymer solutions *Polym. Sci.* A **43** 716–26

[27] Prabhakar R, Prakash J R and Sridhar T 2006 Effect of configuration-dependent intramolecular hydrodynamic interaction on elastocapillary thinning and breakup of filaments of dilute polymer solutions *J. Rheol.* **50** 925–47

[28] Tuladhar T R and Mackley M R 2008 Filament stretching rheometry and break-up behaviour of low viscosity polymer solutions and inkjet fluids *J. Non-Newton. Fluid Mech.* **148** 97–108

[29] Hinch E J 1994 Uncoiling a polymer molecule in a strong extensional flow *J. Non-Newton. Fluid Mech.* **54** 209–30

[30] Prabhakar R, Prakash J R and Sridhar T 2004 A successive fine-graining scheme for predicting the rheological properties of dilute polymer solutions *J. Rheol.* **48** 1251–78

[31] Doolittle R F 1984 Fibrinogen and fibrin *Annu. Rev. Biochem.* **53** 195–229

[32] Kroll M H, Hellums J D, McIntire L V, Schafer A I and Moake J L 1996 Platelets and shear stress *Blood* **88** 1525

[33] Schneider S W, Nuschele S, Wixforth A, Gorzelanny C, Alexander-Katz A, Netz R R and Schneider M F 2007 Shear-induced unfolding triggers adhesion of von Willebrand factor fibers *Proc. Natl Acad. Sci. USA* **104** 7899

[34] Zhang X, Halvorsen K, Zhang C Z, Wong W P and Springer T A 2009 Mechanoenzymatic cleavage of the ultralarge vascular protein von Willebrand factor *Science* **324** 1330

[35] Katona E, Neumann A W and Moscarello M A 1978 Forced unfolding of coiled-coils in fibrinogen by single-molecule AFM *Biochim. Biophys. Acta* **534** 275

[36] Hernández E M and Franses E I 2003 Adsorption and surface tension of fibrinogen at the air/water interface *Colloids Surf.* A **214** 249

[37] Brown A E X, Litvinov R I, Discher D E and Weisel J W 2007 Forced unfolding of coiled-coils in fibrinogen by single-molecule AFM *Biophys. J.* **92** L39–41

[38] Gupta R K, Nguyen D A and Sridhar T 2000 Extensional viscosity of dilute polystyrene solutions: effect of concentration and molecular weight *Phys. Fluids* **12** 1296

Chapter 4

Extraction of extensional viscosities for low-viscosity fluids

The significant difficulties in extracting extensional viscosity from the filament break-up data of low-viscosity fluids using an analytical approach are detailed in this chapter. Thus, the development of an alternative approach is described here; it is a calibration method that effectively associates the re-scaled and non-dimensionalised break-up of unknown fluids to that of known Newtonian fluids and their extensional viscosities.

4.1 Introduction

This chapter investigates the analysis of the filament break-up data that is produced in ADMiER experiments. As demonstrated in the previous chapter, if a filament is nearly cylindrical towards the final stages of filament break-up, standard rheological analysis can be applied which uses the mid-filament stresses and strain rate to extract the extensional viscosity; this occurs in samples that have high viscosity or that contain polymers, for example. However, filaments of fluids with little or no strain-hardening do not form approximately cylindrical filaments; meaning dynamic axial curvature is still present. This undermines the validity of mid-filament analysis, which is practical to use when possible since it allows the relatively quick and practical extraction of rheological properties from break-up data when compared to full filament stress balance analysis. Here we explore the challenges of an analytical approach to extracting the rheological properties of low-viscosity fluids using mid-filament stress balance analysis and find that it is not well suited to describing experimental results for low-viscosity fluids. Therefore, we develop a calibration-based approach that compares the re-scaled break-up data of unknown fluids to that of Newtonian fluids, allowing equivalent extensional viscosities to be attributed to unknown fluids.

This chapter begins by looking at the extraction of strain rate from break-up data. It then discusses the standard approach to extracting data in the case of an approximately cylindrical filament, and then the challenging case of a filament in which axial curvature is significant. Then it discusses the development and use of the calibration method that is used to extract viscosity throughout this body of work. It is concluded with a cursory investigation into the potential extraction of extensional viscosity using analytical predictions that employ a critical experimentally supported variable.

4.2 Extraction of extensional rheological properties from filament break-up data

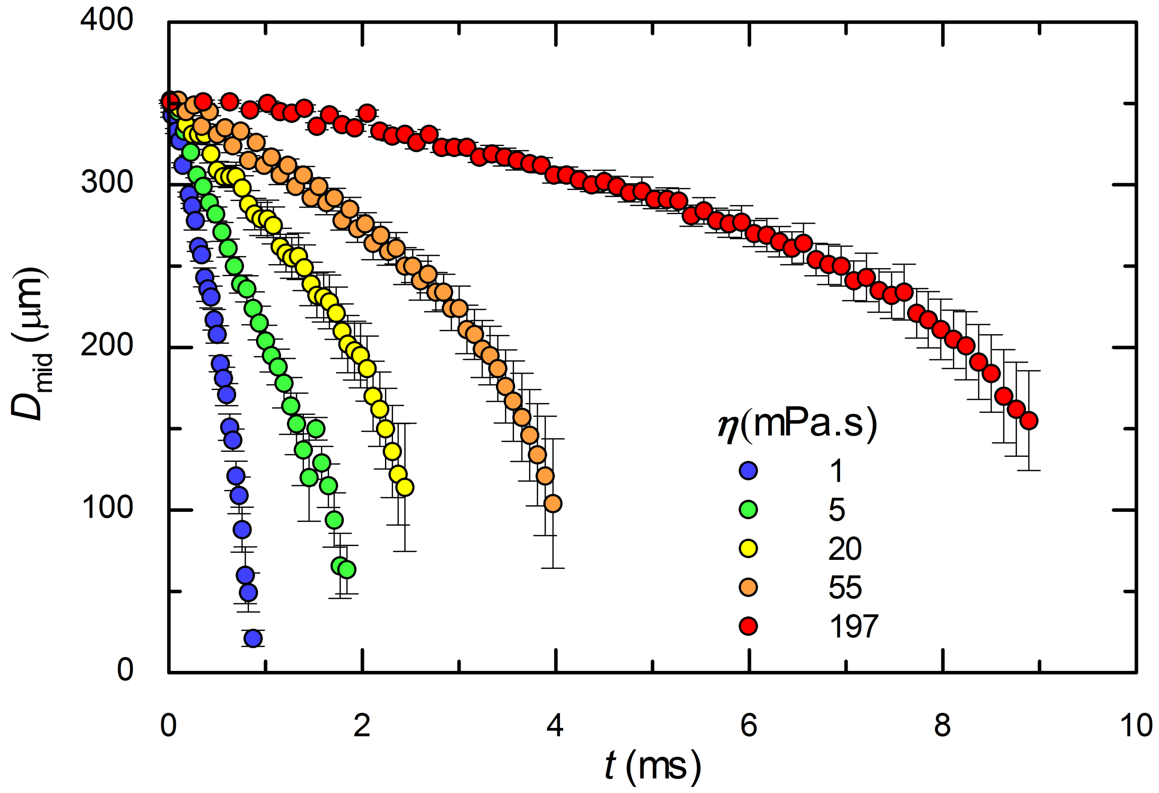

Fig. 4.1 Averaged dimensional experimental diameter versus time break-up data for various Newtonian fluids. Note that break-up time increases with increasing viscosity (assuming negligible change across samples in surface tension and density). Thus, it can be seen how break-up data allows the identification of fluids with different viscosities.

Given constant surface tension and density, increased sample viscosity is expressed *via* longer filament break-up times. Thus, it is possible to discern between fluids of different viscosities *via* their mid-filament data, as can be seen for a range of Newtonian fluids of different viscosities (Fig. 4.1). Filament break-up radius *versus* time data enables the calculation of strain rate for these extensional flows, which is needed to extract extensional properties (seen later in Sec. 4.3.2 and Sec. 4.4), as can be demonstrated by applying a conservation of volume analysis to a cylinder of changing dimensions (representing a stretching filament) as follows:

$$\pi L R^2 = \pi L_0 R_0^2, \tag{4.1}$$

where L is the cylinder's length, R its radius, and V its volume — L_0 and R_0 are the initial length and radius, respectively. One can then differentiate by time to acquire an expression for the strain rate, $\dot{\varepsilon}$, as follows:

$$\frac{dV}{dt} = 0 = 2LR\frac{dR}{dt} + R^2\frac{dL}{dt}, \tag{4.2}$$

Hence,

$$-2\frac{d\ln R}{dt} = \frac{d\ln L}{dt} = \dot{\varepsilon}. \tag{4.3}$$

Knowing the strain rate of a filament break-up event enables the calculation of stresses due to bulk viscosities, and those arising from complex additive and particle effects, as is performed in Chapters 3 – 8.

4.3 Mid-filament data analysis

Raw data such as that in Fig. 4.1 provides valuable insight into the holistic qualitative differences between fluids. On the other hand, it does not quantify the differences between viscosities nor does it account for the influences on filament break-up that effects like surface tension and density render. This was approached by using mid-filament stress balance analysis.

4.3.1 Extensional viscosity extraction for near-cylindrical filaments close to break-up

There are cases when a fluid filament can be assumed to have negligible axial curvature; for instance, in the final stages of break-up in Fig. 1.3, strain hardening due to polymeric stresses resists Rayleigh-Plateau instabilities, allowing long-lived near cylindrical filaments to form [86]. In such a case, the relative stress contributions of inertia, surface tension, solvent viscosity, and non-Newtonian stresses can be described by a simplified governing stress-balance that looks purely at the thinning region of a filament (as seen in the approach of Entov and Hinch [87] and Tirtaatmadja *et al.* [88]):

$$\frac{1}{2}\rho\dot{R}^2 = \frac{\sigma}{R} - 3\eta_s\dot{\varepsilon} + N_{1,p}, \tag{4.4}$$

where η_s is the solvent shear viscosity, $\dot{\varepsilon}$ is the strain rate (as obtain in Sec. 4.2), and $N_{1,p}$ is the time dependent normal stress difference that represents the non-Newtonian stress contribution. Through break-up data and externally measurable properties (σ, ρ and η_s) it is possible to determine $N_{1,p}$ and in turn the extensional viscosity, and investigate possible strain-hardening effects at the final stages of filament break-up. It should noted that this procedure for extracting extensional viscosity is different to that explained later in Sec.4.4.

4.3.2 Mid-filament stress balance for low-viscosity Newtonian fluids

Comparison of mid-filament predictions with experiments has been used with success with viscous fluids, where it is assumed viscosity dominates and inertia can be neglected [6]. Mid-filament analysis has also featured in the investigation of very low viscosity fluids where it is assumed that viscosity can be neglected and inertia dominates [88]. The range of the ADMiER experimental system crosses both inertia and viscous driven regimes, and to our knowledge there exists no basic mid-filament analysis that accommodates such a scenario. Thus a hybrid mid-filament stress balance (an approximate version of the detailed derivation of Szabo [5] that includes dynamic axial curvature) that incorporated both inertia and viscous contributions was formulated for a Newtonian fluid [89]:

$$\frac{1}{2}\rho\dot{R}(t)^2 = \frac{F(t)}{\pi R(t)^2} - \frac{\sigma}{R(t)} - 3\eta\left(\frac{-2\dot{R}(t)}{R(t)}\right), \tag{4.5}$$

where ρ is the density of the fluid, and $R(t)$ is the time-evolving mid-filament radius. It should also be noted that $-2\dot{R}/R = -2d\ln R/dt = \dot{\varepsilon}$, as is seen in Eqn. 4.3. The term on the left-hand side of Eqn. 4.5 represents fluid inertia; on the right-hand side $F(t)$ represents the tensile force in the filament column, σ is the surface tension, and η is the viscosity of the fluid.

Analytically predicting the behaviour of fluid filament break-up in CaBER experiments has been challenging [6]. Basic mid-filament stress balance analysis assumes a filament

Table 4.1 Self-similarity solutions as adapted from the compilation reported by McKinley and Tripathi [6]

	X	Notes
Local force balance	1	Axially uniform filament
Rennardy [92]	–	Three different similairty regimes
Papageorgiou [93]	0.7127	Valid for viscous filaments
Eggers [94, 95]	0.5912	Universal similarity solution
Brenner *et al.* [96]	0.5912	Countably infinite similarity solutions
	0.5324	
	0.5197	
	⋮	

achieves a true cylindrical form, meaning axial curvature is zero. Yet, it has been found that using a simple two-dimensional mid-filament stress balance analysis in this way provides poor agreement with experimental results [90]. In general a filament's axial curvature must be accounted for in analysis. Although, there are special experimental cases where this is not necessary. Such cases are seen in some non-Newtonian fluids, as discussed in Sec. 4.3.1, but Newtonian fluids can also exhibit approximate axial uniformity experimentally in a filament when the filament becomes a micro-thread, just before break-up, and the fluid is viscous [91]. However, apart from these limited special cases it has been found that axial cannot be ignored [6].

As a consequence, self-similarity solutions have been used to determine how the filament tensile force $F(t)$, which also accounts for non-local axial shape variations, is related to the change in the decaying mid-filament radius $R(t)$ by a coefficient of proportionality X [6] (briefly discussed in Chapter 3):

$$X \equiv \frac{F(t)}{2\pi\gamma R(t)}. \tag{4.6}$$

However, multiple solutions for X exist, as shown in Table 4.1. This term and its complexities are discussed at length in Sec. 4.3.3.

By incorporating X, then non-dimensionalising the radius with the initial filament radius R_0, and the time using the Rayleigh time scale τ_R, Eqn. 4.5 reduces to a quadratic equation in dR^*/dt^*, given any instantaneous value of R^*, and the parameter Oh:

$$\left(\frac{dR^*}{dt^*}\right)^2 - \frac{12\mathrm{Oh}}{R^*}\left(\frac{dR^*}{dt^*}\right) - \frac{2}{R^*}(2X-1) = 0, \tag{4.7}$$

where superscript * denotes dimensionless mid-filament radius and time — we shall drop the superscript * from here on. Solving Eqn. 4.7 and taking the negative root only (since the rate of change in R must be negative as the filament neck decreases) gives:

$$\frac{dR}{dt} = \frac{-6\mathrm{Oh}}{R}\left(\left(1+\frac{CR}{\mathrm{Oh}^2}\right)^{\frac{1}{2}}-1\right), \tag{4.8}$$

where

$$C = \frac{8}{144}(2X-1). \tag{4.9}$$

Making a change of variable from R to:

$$U = \left(1+\tfrac{CR}{\mathrm{Oh}^2}\right)^{\frac{1}{2}}-1,$$

observing the terminal conditions where $U(R=0)=0$ when $t=t_b$ (the time at which the filament breaks up), and that initially $t=0$ at $R=1$ such that $U(R=1)=(1+C/\mathrm{Oh}^2)^{\frac{1}{2}}-1$, the integral of Eqn. 4.8 can be expressed as:

$$\int_0^{t_b} -6\mathrm{Oh}\,\mathrm{d}t = \int_{(1+C/\mathrm{Oh}^2)^{\frac{1}{2}}-1}^{0} \frac{2\mathrm{Oh}^4}{C^2}(U^2+3U+2)\mathrm{d}U. \tag{4.10}$$

This enables the break-up time t_b to be expressed as:

$$t_b = \frac{\mathrm{Oh}^3}{3C^2}\left[\frac{(1+C/\mathrm{Oh}^2)^{\frac{3}{2}}}{3}+\frac{1+C/\mathrm{Oh}^2}{2}-\frac{5}{6}\right]. \tag{4.11}$$

In the general case, the time taken for the filament radius to reach R have the following boundary conditions:

$U(R=R)=(1+CR/\mathrm{Oh}^2)^{\frac{1}{2}}-1$, and $U(R=1)=(1+C/\mathrm{Oh}^2)^{\frac{1}{2}}-1$,

such that

$$\int_0^{t} -6\mathrm{Oh}\,\mathrm{d}t = \int_{(1+C/\mathrm{Oh}^2)^{\frac{1}{2}}-1}^{(1+CR/\mathrm{Oh}^2)^{\frac{1}{2}}-1} \frac{2\mathrm{Oh}^4}{C^2}(U^2+3U+2)\mathrm{d}U, \tag{4.12}$$

which after integration and substitution of the result seen in Eqn. 4.11 gives:

$$t = t_b - \frac{\mathrm{Oh}^3}{3C^2}\left[\frac{(1+CR/\mathrm{Oh}^2)^{\frac{3}{2}}}{3}+\frac{1+CR/\mathrm{Oh}^2}{2}-\frac{5}{6}\right]. \tag{4.13}$$

Observing that Eqn. 4.13 is a cubic in:

$$Z = (1 + CR/\mathrm{Oh}^2)^{\frac{1}{2}}; \tag{4.14}$$

results in Eqn. 4.13 being rewritten as:

$$2Z^3 + 3Z^2 - (5 + L) = 0, \tag{4.15}$$

where

$$L = \frac{18C^2(t_b - t)}{\mathrm{Oh}^3}. \tag{4.16}$$

Then substituting C (Eqn. 4.9) into L (Eqn. 4.16) gives:

$$L = \frac{1}{18Oh^3}(2X - 1)^2(t_b - t). \tag{4.17}$$

Thus, Eqn. 4.15 is a cubic in Z. This must be solved to obtain a real root for Z such that $0 < R < 1$. We now summarise the standard method [97] for obtaining roots of any cubic equation of the form:

$$aZ^3 + bZ^2 + cZ + d = 0. \tag{4.18}$$

The discriminant for such an equation is:

$$\Delta = 18abcd - 4b^3d + b^2c^2 - 4ac^3 - 27a^2d^2. \tag{4.19}$$

In Eqn. 4.15, $a = 2$, $b = 3$, $c = 0$, and $d = -(5 + L)$. The discriminant is thus:

$$\Delta = -108(5 + L)(4 + L). \tag{4.20}$$

Since $t_b > t$, $X \leq 1$, $Oh > 0$, and $L > 0$, therefore $\Delta < 0$. In this case, the cubic equation has one real root and two complex conjugate roots. The real root in this case is in general:

$$z_1 = -\frac{1}{3a}\left(b + \gamma + \frac{\Delta_0}{\gamma}\right), \tag{4.21}$$

where

$$\gamma = \left(\frac{\Delta_1 + (\Delta_1^2 - 4\Delta_0^3)^{\frac{1}{2}}}{2}\right)^{\frac{1}{3}}, \tag{4.22}$$

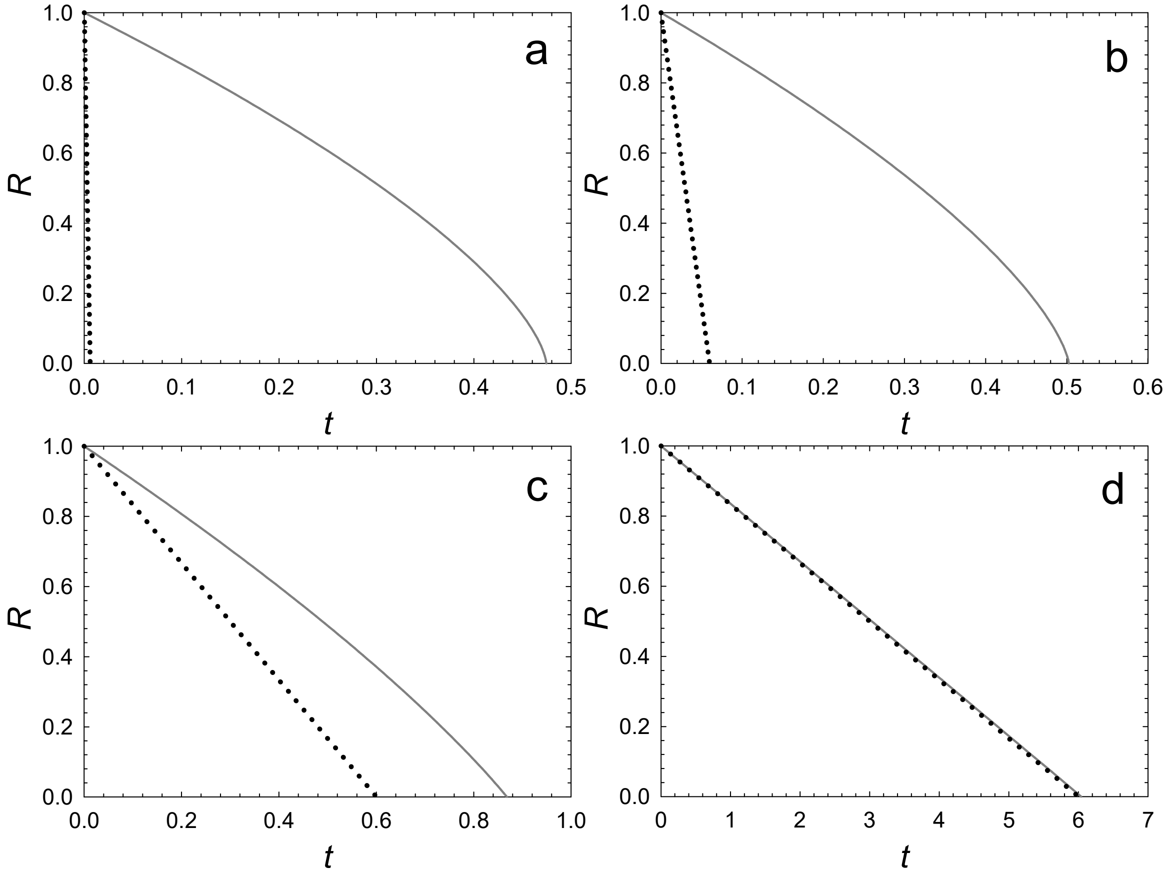

Fig. 4.2 The R-*vs*-t evolution as predicted by the analysis seen in Sec. 4.3.2 using $X = 1$ is plotted (solid grey line) against the linear viscous solution (dotted black line) when $X = 1$ for Oh values of 0.001, 0.01, 0.1, and 1 in Figs. a, b, c, and d, respectively.

$$\Delta_0 = b^2 - 3ac, \tag{4.23}$$

$$\Delta_1 = 2b^3 - 9abc + 27a^2d, \tag{4.24}$$

such that in Eqn. 4.22:

$$\Delta_1^2 - 4\Delta_0^3 = -27a^2\Delta. \tag{4.25}$$

Applying this to the cubic equation under consideration:

$$\gamma = 3\left(2((5+L)(4+L))^{\frac{1}{2}} - (9+2L)\right)^{\frac{1}{3}}, \tag{4.26}$$

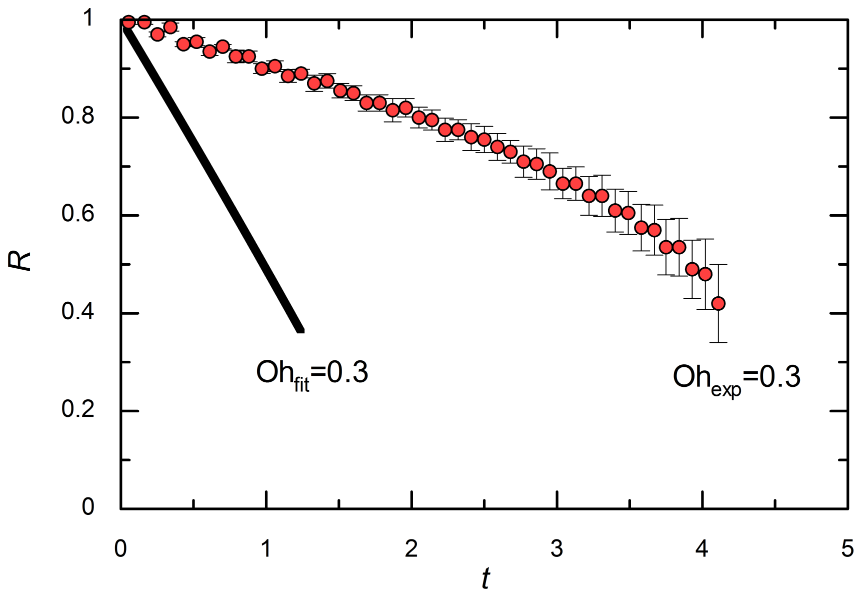

Fig. 4.3 Analytically predicted dimensionless mid-filament decay (black) as predicted by the analysis seen in Sec. 4.3.2 using $X = 1$. It fails to quantitatively predict or represent the behaviour of experimental results (red).

and the desired root is:

$$z_1 = -\frac{1}{6}\left[3+\gamma+\frac{9}{\gamma}\right], \tag{4.27}$$

from which the radius R can be obtained at every instant of t:

$$R = \frac{\mathrm{Oh}^2}{C}(z_1^2-1). \tag{4.28}$$

Observing Fig. 4.2, the nonlinearity in the R-*vs*-t curve resulting from the above analysis when Oh $\ll$ becomes apparent only when R is small. Until half-time, the curve looks linear. However, when Oh $\ll 1$, this linear part of the curve is very different from the linear viscous solution $R = (1-t/t_{vb})$, where $t_{vb} = 6\mathrm{Oh}/(2X-1)$. The curves become nearly identical when Oh $\gtrsim 1$.

Extensional break-up data of Newtonian fluids was obtained from our system, where a liquid sample is extended into a liquid bridge by a burst of SAW forcing and then collapses under surface tension. The above expression was compared with this experimental data and gave qualitative representation of filament break-up with regards to changes in viscosity, but it was unable to provide the quantitative agreement necessary to enable the extraction of extensional viscosity *via* experimental observations. The reasons for this are discussed in detail in the next section, Sec. 4.3.3.

4.3.3 Tensile factor fitting

A truly axially uniform filament would be associated to an X value of 1 [6]. This value was used in conjunction with the analytical solution discussed in Sec. 4.3.2 but was not found to be representative of our experimental data, quantitatively or in qualitative behaviour (see Fig. 4.3) as has been observed in other studies [6]. It is known that axial uniformity never occurs, rather it is approached asymptotically [93]. Through similarity analysis Papageorgiou [93] found that $X = 0.7127$ for an inertialess viscous filament; this was supported experimentally in the thinning of highly viscous Newtonian fluid filaments near the final stages of break-up, when the region about the mid-filament is slender and near-cylindrical [6]. Eggers [94, 95] determined that at the final stages of break-up a filament would transition into a profile where inertia, capillary, and viscous effects were significant, giving $X = 0.5912$. However, Brenner (1994) [98] demonstrated that infinite similarity solutions exist and that a filament will in fact transition into different self-similar profiles during a single break-up event.

Problems in analysis are believed to be further compounded by the fact that qualitative behaviour is also not captured by mid-filament stress balance predictions, as seen in Fig. 4.3; the rapidly increasing gradient seen in experimental filament decay is believed to be caused in part by a reduction in the retarding axial Laplace pressure as axial curvature decreases and the filament approaches a cylindrical form, which is not described by the two-dimensional mid-filament stress balance.

Knowing these difficulties, an investigation was carried out with the aim of obtaining an appropriate X value to use in conjunction with the hybrid stress balance analytical solution (discussed in Sec. 4.3.2) that would allow the quantitative representation of any results obtained using the SAW based experiments; the hope was that extensional viscosity could be extracted for unknown fluids from experimental data *via* the fitting of analytical predictions. This was facilitated by the high speed and high resolution data that was available near filament break-up (see Sec. 2.6), which allowed the measurement of fluid filament decay close to final break-up and thus in a near-cylindrical regime.

Experimental data from standard Newtonian samples, ranging across thick to aqueous fluids (representing a span from viscous to inertio/viscous regimes, respectively), and the predictions of the dimensionless stress balance formed the basis of a two parameter fit study (manually using least squares error fitting) that followed the progression of the best fitting X values for experimental data representing different Oh values — potential X values were sourced from the discrete values reported in [6], seen in Table 4.1. Data was taken at the final stages of filament break-up, when the filaments are as cylindrical as possible. Data

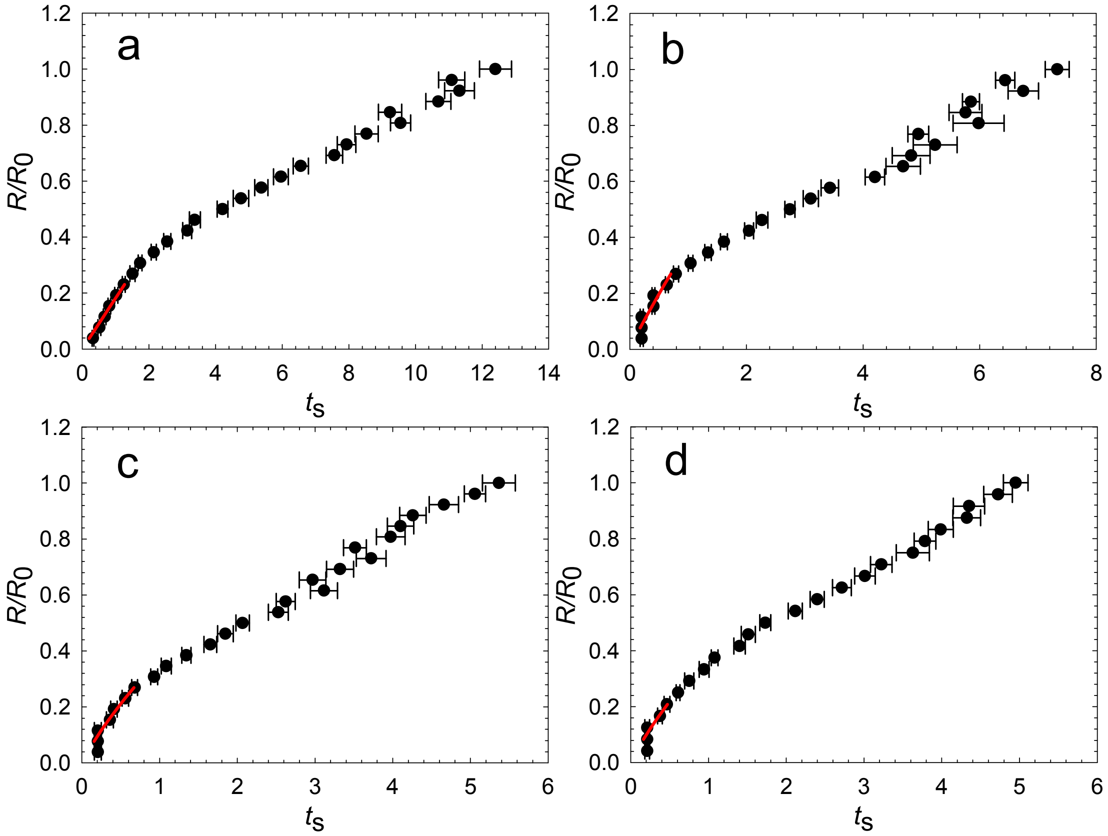

Fig. 4.4 Sample filament break-up data (black) and fitted data at the final stages of break-up (red) for (a) 80% glycerol/water solution (Oh = 0.389), (b) 40% glycerol/water solution (Oh = 0.0241), (c) 10% glycerol/water solution (Oh = 0.0121), and (d) water (Oh = 0.0113). Radius is re-scaled with the original radius, and time is re-scaled as $t_s = (t_f - t)/\tau_{\mathrm{R}}$, where t_f is the final break-up time.

showing the region of the break-up used is shown in Fig. 4.4; this region is enlarged in Fig. 4.5 to show the fitting results.

As shown by Table 4.2, we can see the best-fitting viscous and inertio/viscous X values change significantly across viscosities. This progression is also represented graphically in Fig. 4.6, where experimentally calculated and fitted Oh values (Oh is mainly a function of viscosity in our experiments) are plotted against shear viscosity data; it is worth noting that agreement was seen using $X = 0.7127$ for the viscous dominated case, as was seen by others [6]. Despite this study demonstrating that X values transition intuitively across viscous to inertio/viscous fluids, there is currently no theoretical method for predicting exactly which X is appropriate to employ when analysing experimental results; thus, it would not be possible to extract the extensional viscosity of an unknown fluid *via* the fitting of an analytical solution based on mid-filament analysis.

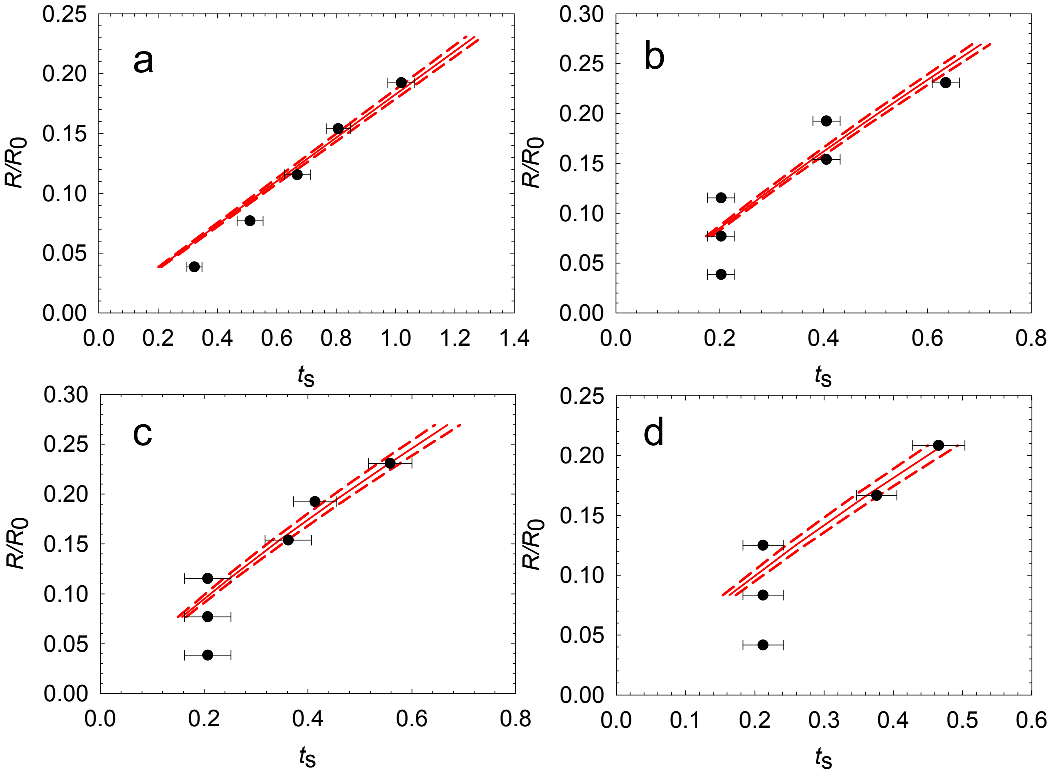

Fig. 4.5 Re-scaled sample filament break-up data (black) and fitted data (red solid) with error (red dotted) at the final stages of break-up for (a) 80% glycerol/water solution, (b) 40% glycerol/water solution, (c) 10% glycerol/water solution, and (d) water.

Hence, this study revealed that using analytical mid-filament model predictions to extract extensional fluid properties for inertio/viscous fluids was not viable. This problem is not with the measurement or device. This problem would remain even with the conventional CaBER or ROJER methods or any other instrument that does not explicitly measure stresses, but uses some kind of a stress balance to extract out the total viscous stress for a non-Newtonian fluid. Thus, an alternative method of extracting the extensional properties of unknown low-viscosity fluids from our experiments was needed, which is discussed in the next section.

4.4 Calibration chart and extensional viscosity extraction

Due to the significant unresolved issues associated with an analytical approach towards extracting extensional viscosity from the experimental capillary break-up data of low-viscosity fluids another method was required — a calibration system was developed. Essentially the concept involved comparing the break-up behaviours of unknown fluids to that of Newto-

Table 4.2 Water/glycerol solutions with increasing glycerol content were tested and analysed *via* a parametric study to see which X factor led to the best fit of experimental data. The Oh value is the fitted value, with the error based on the difference between experimentally calculated Oh. Here, one can see the change in appropriate X required to accommodate solutions which primarily differ in viscosities.

%Glyc	X	Oh	%Error
0	0.5197	0.0113	47.79
2	0.5197	0.0123	55.41
10	0.5197	0.0121	31.00
40	0.5324	0.0241	7.15
60	0.5912	0.0967	43.60
80	0.7127	0.389	10.80

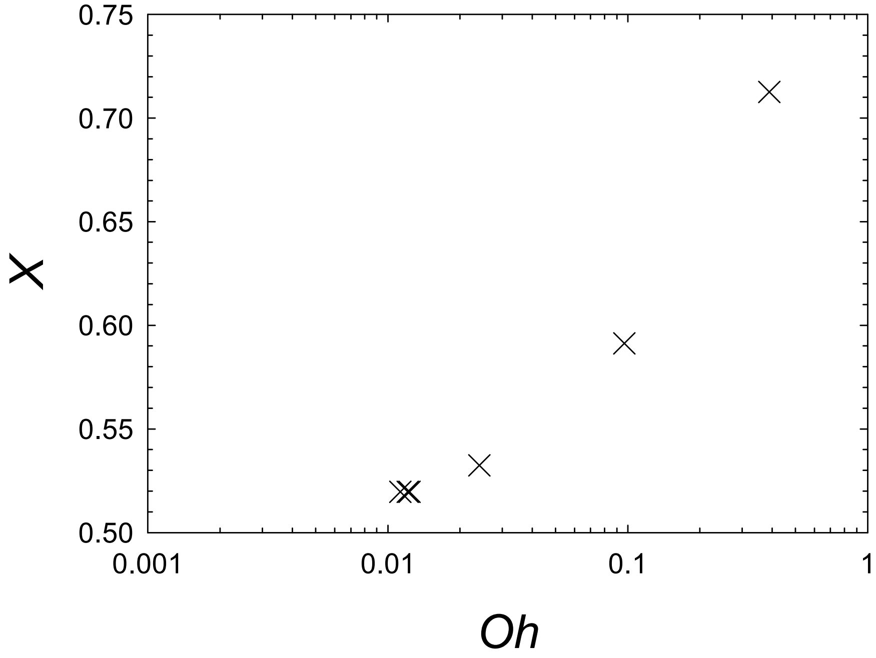

Fig. 4.6 A graphical representation of the data seen in Table 4.2 that shows the required X factor to fit experimental Oh, from which corresponding $\bar{\eta}$ values can be extracted. One can see the transition of X from a value of 0.5197 to the viscous solution value of 0.7127 with an increase in viscosity.

nian fluids, provided subject fluids exhibited approximately Newtonian-like break-up trends. By relating an unknown fluid's break-up to an equivalent Newtonian reference an effective viscosity could be provided. Filament break-up data was obtained for a range of Newtonian fluids that served as viscosity standards, with samples as viscous as 27 Pa·s to as thin as 0.96 mPa·s bounding the range. These fluids comprised sucrose/water and glycerol/water solutions, and silicone oils. In the analysis process, data extraction from a filament's decay begins before a near-cylindrical thread forms, when the filament still has strong axial curvature. This avoids the problems of high-speed imaging thin cylindrical filaments close to break-up. It also means that more data is available per break-up event, as opposed to only viewing the final moments of break-up; this aids in distinguishing between samples with subtly different properties, as does the increased spatial and temporal resolution afforded be the set-up as discussed in Sec. 2.6. This approach is also advantageous when handling particle suspensions since the effect of particle interactions with the air–liquid interface on the overall dynamics at the neck is weaker when the neck radius is large compared to particle dimensions. The development of the calibration chart is discussed here at length.

Break-up time and radius measurements of raw data, like that seen in Fig. 2.15 and Fig. 4.1, were re-scaled by the Rayleigh time-scale $t^* = t/\tau_\mathrm{R}$ and the initial radius $R^* = R/R_0$, respectively, where $\tau_\mathrm{R} \equiv \sqrt{\rho R_0^3/\sigma}$, and R_0 is the initial radius. In our experiments, droplet volumes ($R_0 \approx 1.5$ mm diameter) and the separation between bridge surfaces (≈ 1.8 mm) were kept constant— thus maintaining the liquid bridge aspect ratio 1.2. Observing the Ohnesorge and Bond numbers, as defined conventionally:

$$\mathrm{Oh} \equiv \frac{\eta}{\sqrt{\rho\sigma R_0}}; \quad Bo \equiv \frac{g\rho {R_0}^2}{\sigma}, \tag{4.29}$$

where ρ and σ can be determined independently. It was found that while Oh values spanned more than four orders of magnitude, the change in Bo values was relatively much smaller (around 33%). Therefore, the Bond number can be assumed to be relatively constant. Under such conditions, the rescaled time t^* required for a sample of a given Oh value to decay to half its initial radius is ${t_{1/2}}^*$ (*i.e.* the time to $R^* = 1/2$), Fig. 4.7, is a process that is predominantly governed by Oh. Given this, a calibration chart relating $t^*_{1/2}$ to Oh was formed, Fig. 4.8.

From the dimensional analysis, it is expected that the normalised half-time is a function of the dimensionless ratios Oh and Bo, and the aspect ratio of the bridge. Since the latter was kept constant, and the variation in Bo is typically much smaller than the variation in Oh, we expected the dimensionless $t_{1/2}$ to be largely a function of Oh. The fact that the normalised $t_{1/2}$ *versus* Oh data obtained with three different Newtonian fluids do collapse onto a master curve (Fig. 4.8) demonstrates that this expectation is correct. This is true irrespective of the variation in surface tension values as long as the Bo variation is small. The form of the data in Fig. 4.8 is inspired by the asymptotic behaviour expected in the limits of vanishing or very large Oh. When Oh→ 0, inertia dominates and capillary thinning is insensitive to viscosity, whereas when viscous stresses dominate at high Oh, the breakup-time increases

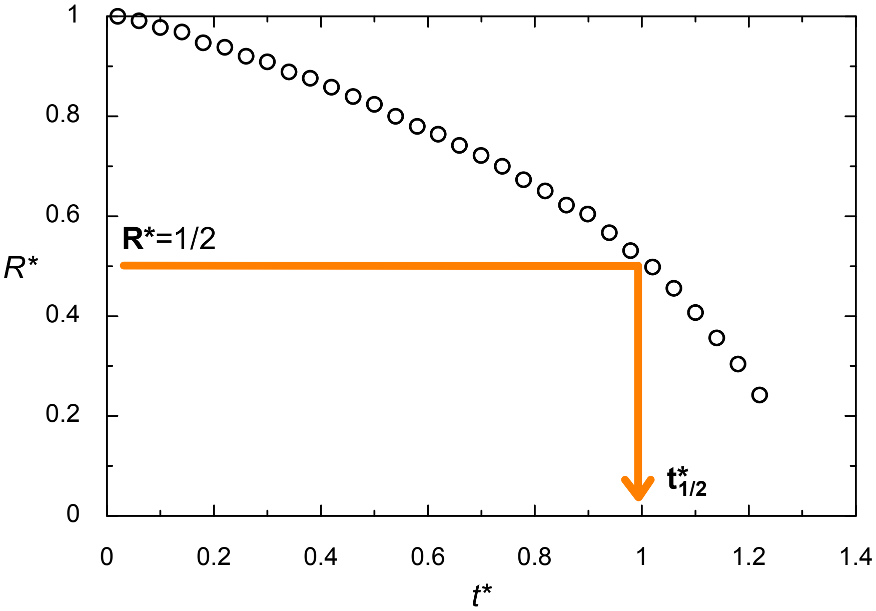

Fig. 4.7 Open circles represent typical normalised break-up data. The point at which R^* reaches half its initial value determines the t^* value that defines $t^*_{1/2}$ for that break-up event, the process of which is graphically represented by the orange line.

linearly with viscosity and Oh. We therefore fit a rational function of the following form through the experimental data:

$$t^*_{1/2} = \frac{K_0 + K_1\mathrm{Oh} + K_2\mathrm{Oh}^2}{1+\mathrm{Oh}} \tag{4.30}$$

In this expression, as Oh $\rightarrow 0$, $t^*_{1/2} \rightarrow K_0$, and as Oh $\rightarrow \infty$, $t^*_{1/2} \rightarrow K_2\mathrm{Oh}$. Recalling the description of inertio-visco fluid filaments discussed in Sec. 4.3.2, we tried to see if there is any qualitative prediction of this experimental trend from an analytical basis. Eqn. 4.13 can be rearranged to give:

$$t^* = \frac{1}{3C^2}\left[\frac{1}{3}\{(\mathrm{Oh}^2+C)^{\frac{3}{2}} - (\mathrm{Oh}^2+CR)^{\frac{3}{2}}\} + \frac{C}{2}(1-R)\mathrm{Oh}\right]. \tag{4.31}$$

Thus, when $R^* = 1/2$,

$$t^*_{1/2} = \frac{1}{9C^2}\left[\left\{(\mathrm{Oh}^2+C)^{\frac{3}{2}} - \left(\mathrm{Oh}^2+\frac{C}{2}\right)^{\frac{3}{2}}\right\} + \frac{3C}{4}\mathrm{Oh}\right]. \tag{4.32}$$

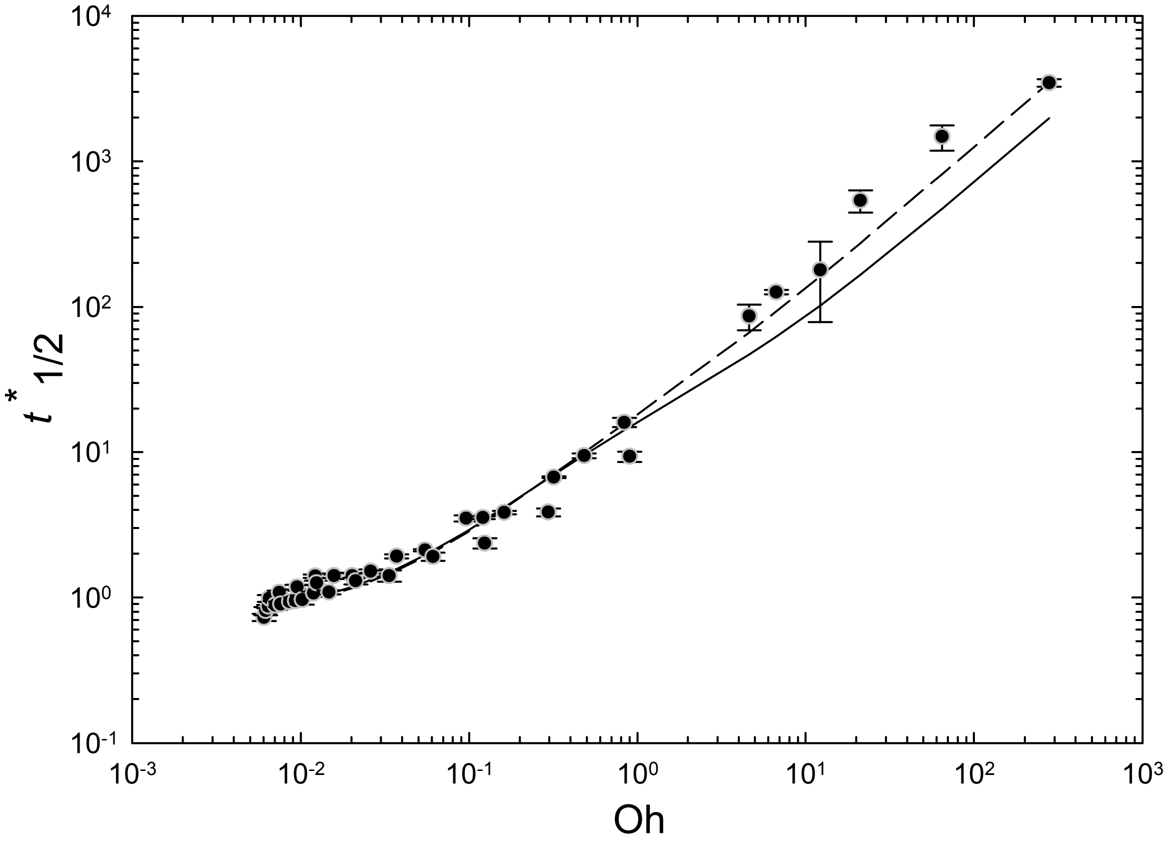

Fig. 4.8 Dimensionless half-time $t^*_{1/2}$ for a filament to reach half its diameter as a function of its Oh for Newtonian standard solutions: The continuous curve has been obtained by regression of Eqn. 4.30 through experimental data using asymptotic values for K_0 and K_2, while the dashed curve has been obtained by also freeing K_2 as a regression parameter.

When $\mathrm{Oh}^2 >> C$, then:

$$t^*_{1/2} \approx \frac{1}{9C^2}\left[\mathrm{Oh}^3\left\{\left(1+\frac{3C}{2\mathrm{Oh}^2}\right)-\left(1+\frac{3C}{4\mathrm{Oh}^2}\right)+...\right\}+\frac{3C\mathrm{Oh}}{4}\right] \approx \frac{3\mathrm{Oh}}{2X-1}. \tag{4.33}$$

Thus:

$$t^*_{1/2} \approx \frac{\mathrm{Oh}}{6C} \approx \frac{3\mathrm{Oh}}{2X-1}. \tag{4.34}$$

Therefore, $t^*_{1/2}$ increases as Oh^1 as $\mathrm{Oh} \to \infty$. On the other hand, when $\mathrm{Oh} << C/2$

$$t^*_{1/2} \approx \frac{1}{9C^2}\left[C^{\frac{3}{2}}\left(1+\frac{3\mathrm{Oh}^2}{2C}+...\right)-\left(\frac{C}{2}\right)^{\frac{3}{2}}\left(1+\frac{3\mathrm{Oh}^2}{C}+...\right)+\frac{3C\mathrm{Oh}}{2}\right]. \tag{4.35}$$

$$t^*_{1/2} \approx \frac{1}{9C^2}\left[C^{\frac{3}{2}}\left(1-\frac{1}{2^{\frac{3}{2}}}\right)+\frac{3C\mathrm{Oh}}{2}+O(\mathrm{Oh}^2)...\right]. \tag{4.36}$$

Hence, as $\mathrm{Oh} \to 0$,

$$t^*_{1/2} \to \frac{1}{9\sqrt{C}}\left(1-\frac{1}{2^{\frac{3}{2}}}\right)=\frac{2^{\frac{3}{2}}-1}{6\sqrt{2X-1}} \tag{4.37}$$

As discussed in Sec. 4.3.3, there is more than one value for X. Viscosity dominates filament break-up as $\mathrm{Oh} \to \infty$, making it suitable to use $X = 0.7127$. Observing Eqn. 4.34, this indicates that $t^*_{1/2} \to 7.0522$. Alternatively, inertial effects become important to filament thinning when $\mathrm{Oh} << 1$, where it is appropriate to use $X = 0.5912$. Observing Eqn. 4.37, this indicates that $t^*_{1/2} \to 0.7135$. According to these asymptotic predictions, values of $K_2 = 7.0522$ and $K_0 = 0.7135$ were used in Eqn. 4.30. Despite this approach only being expected to be accurate when axial curvature of the filament is negligible it was found to have surprisingly good agreement with experimental results (Fig. 4.8). Using these values we determined $K_1 = 23 \pm 0.3$ *via* linear regression through experimental data. Freeing K_2 as a regression parameter and leaving K_0 fixed, results in $K_2 = 12.51 \pm 0.5$ and $K_1 = 22.97 \pm 0.3$ (Fig. 4.8).

In calculating the error in Eqn. 4.30 we can say $\mathrm{Oh}(t^*_{1/2}, K_1, K_2)$, which must always satisfy Eqn. 4.30. Rearranging Eqn. 4.30:

$$t^*_{1/2} + \mathrm{Oh}t^*_{1/2} = K_0 + K_1\mathrm{Oh} + K_2\mathrm{Oh}^2, \tag{4.38}$$

and then differentiating Eqn. 4.38 with respect to $t^*_{1/2}$ gives:

$$1 + \mathrm{Oh} + t^*_{1/2}\frac{\partial \mathrm{Oh}}{\partial t^*_{1/2}} = K_1\frac{\partial \mathrm{Oh}}{\partial t^*_{1/2}} + 2K_2\mathrm{Oh}\frac{\partial \mathrm{Oh}}{\partial t^*_{1/2}}, \tag{4.39}$$

or

$$\frac{\partial \mathrm{Oh}}{\partial t^*_{1/2}} = \frac{1+\mathrm{Oh}}{K_1 + 2K_2\mathrm{Oh} - t^*_{1/2}}. \tag{4.40}$$

Differentiating Eqn. 4.38 with respect to K_1:

$$t^*_{1/2}\frac{\partial \mathrm{Oh}}{\partial K_1} = \mathrm{Oh} + K_1\frac{\partial \mathrm{Oh}}{\partial K_1} + 2K_2\mathrm{Oh}\frac{\partial \mathrm{Oh}}{\partial K_1}, \tag{4.41}$$

or

$$\frac{\partial \mathrm{Oh}}{\partial K_1} = \frac{\mathrm{Oh}}{-K_1 - 2K_2\mathrm{Oh} + t^*_{1/2}}. \tag{4.42}$$

Differentiating Eqn. 4.38 with respect to K_2:

$$t^*_{1/2}\frac{\partial \mathrm{Oh}}{\partial K_2} = K_1\frac{\partial \mathrm{Oh}}{\partial K_2} + \mathrm{Oh}^2 + 2K_2\mathrm{Oh}\frac{\partial \mathrm{Oh}}{\partial K_2}, \tag{4.43}$$

or

$$\frac{\partial \mathrm{Oh}}{\partial K_2} = \frac{\mathrm{Oh}^2}{-K_1 - 2K_2\mathrm{Oh} + t^*_{1/2}}. \tag{4.44}$$

Thus, we can calculate the error in using the calibration curve to generate an Oh given a $t^*_{1/2}$ according to:

$$\Delta\mathrm{Oh} = \sqrt{\left(\frac{\partial \mathrm{Oh}}{\partial t^*_{1/2}}\right)^2 \left(\Delta t^*_{1/2}\right)^2 + \left(\frac{\partial \mathrm{Oh}}{\partial K_1}\right)^2 \left(\Delta K_1\right)^2 + \left(\frac{\partial \mathrm{Oh}}{\partial K_2}\right)^2 \left(\Delta K_2\right)^2} \tag{4.45}$$

From the definition of Oh (Eqn. 4.29) the extensional viscosity can be expressed as $\bar{\eta} \equiv 3\mathrm{Oh}\sqrt{\rho\sigma R_0}$, the pre-factor of 3 is a consequence of the convention used to define Oh (relating to Eqn. 1.8); no assumption is made here about a relationship between the extensional and shear viscosities of the sample. Thus with the calibration curve, the Oh and hence an effective $\bar{\eta}$ for an unknown fluid sample can be extracted from the observed $t^*_{1/2}$ *via* the inverse of Eqn. 4.30, as long as it exhibits a Newtonian-like break-up.

We note that as Oh $\to 0$, $R - vs. - t$ data becomes insensitive to Oh. This is reflected in the levelling-off of the $t^*_{1/2}$ data in Fig. 4.8 to a constant value at small Oh. Therefore, the method presented here becomes unreliable at very low values of Oh, since small errors in $t^*_{1/2}$ imply large errors in Oh. In our experiments, the trend in $t^*_{1/2}$ when Oh $= 0.01$ is sufficient to allow us to back out Oh from measured half-times such that the error in the Oh backed out due to the noise in the calibration data in Fig. 4.8 is smaller than that due to the measurement error in $t^*_{1/2}$ of the test sample.

Nevertheless, this method for extracting extensional viscosity means that measurements are not complicated by phenomena that can arise during the final stages of filament break-up. This technique was used to extract extensional viscosities throughout this body of work, where significant differences between suspensions and suspending media were observed in break-up behaviour, and there were no difficulties extracting their viscosities. Although, in the case of long lived polymeric filaments where strain-hardening occurs towards final break-up, as seen in Chapter 8, the simple mid-filament stress balance analysis (Sec. 4.3.1) is appropriate.

4.4.1 Effective tensile factor *via* analytical predictions and experimental regression curve

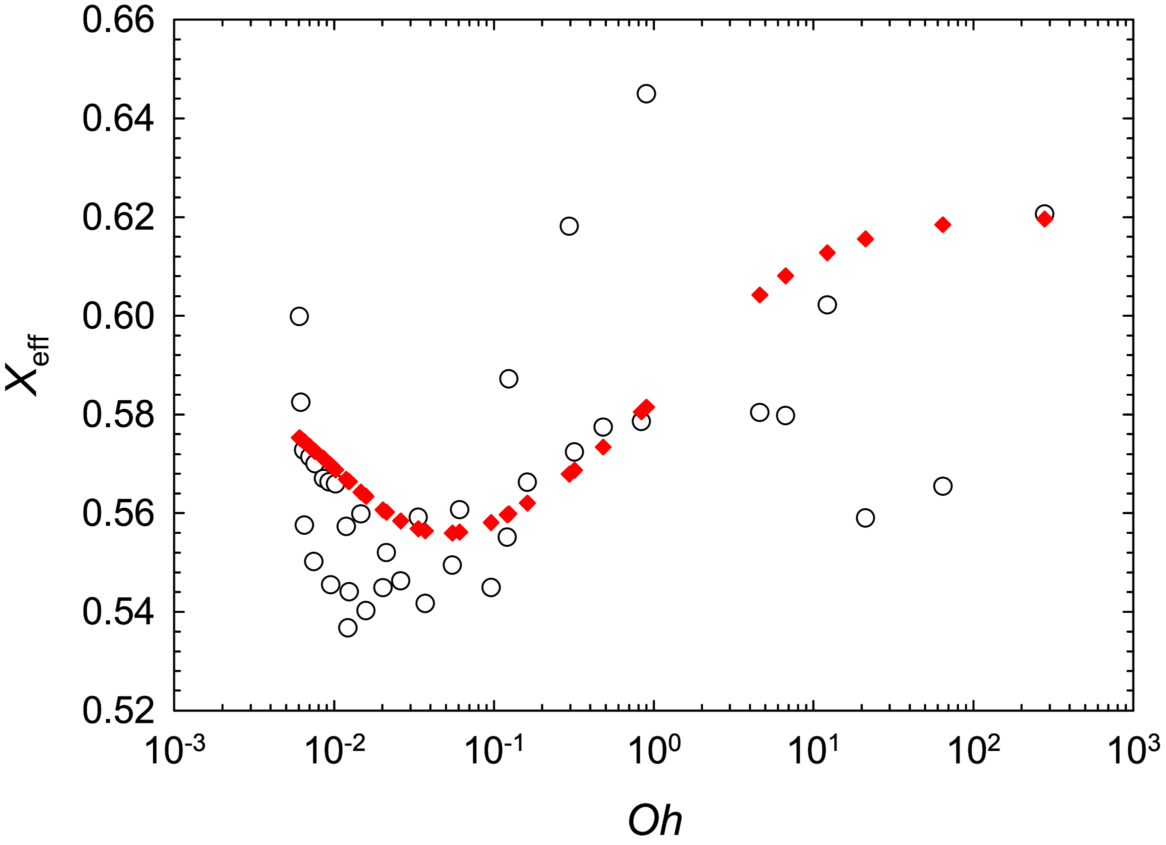

Fig. 4.9 Changes in X_{eff} with Oh to satisfy Eqn. 4.46 (red diamonds). The open circle data points represent the X_{eff} values that arise from solving Eqn. 4.32 using the experimental values of $t^*_{1/2}$ for the individual experiments used in Fig. 4.8.

The hybrid mid-filament analysis in Sec. 4.3.2 and the experimental data in Sec. 4.4 allow the definition of an effective X. Equating the empirical correlation in Eqn. 4.30 with the analytical result for t^* in Eqn. 4.31 gives:

$$\frac{K_0+K_1\mathrm{Oh}+K_2\mathrm{Oh}^2}{1+\mathrm{Oh}} = \frac{1}{3C^2}\left[\frac{1}{3}\{(\mathrm{Oh}^2+C)^{\frac{3}{2}}-(\mathrm{Oh}^2+CR)^{\frac{3}{2}}\}+\frac{C}{2}(1-R)\mathrm{Oh}\right]. \quad (4.46)$$

Since C is related to X through Eqn. 4.9, and since K_0, K_1, and K_2 are known from the curve-fit of the experimental data, we can solve the equation above for X as a function of Oh. We describe this result as X_{eff} (Fig. 4.9), which is a complicated function of Oh that we do not attempt to characterise. It should be stated that this X_{eff} is not obtained in the same way as literature values for X at all, which are obtained through self-similarity arguments. Moreover, these arguments for X are only valid in the final stages of break-up, whereas the X_{eff} we are introducing is to obtain an improved description of the initial phase of the break-up; where reliable data can be obtained easily with less sophisticated cameras and lighting, compared to what is required to image final break-up. However, we do see that X_{eff} resides between the literature values for X of 0.5197 and 0.7127 (Table 4.1).

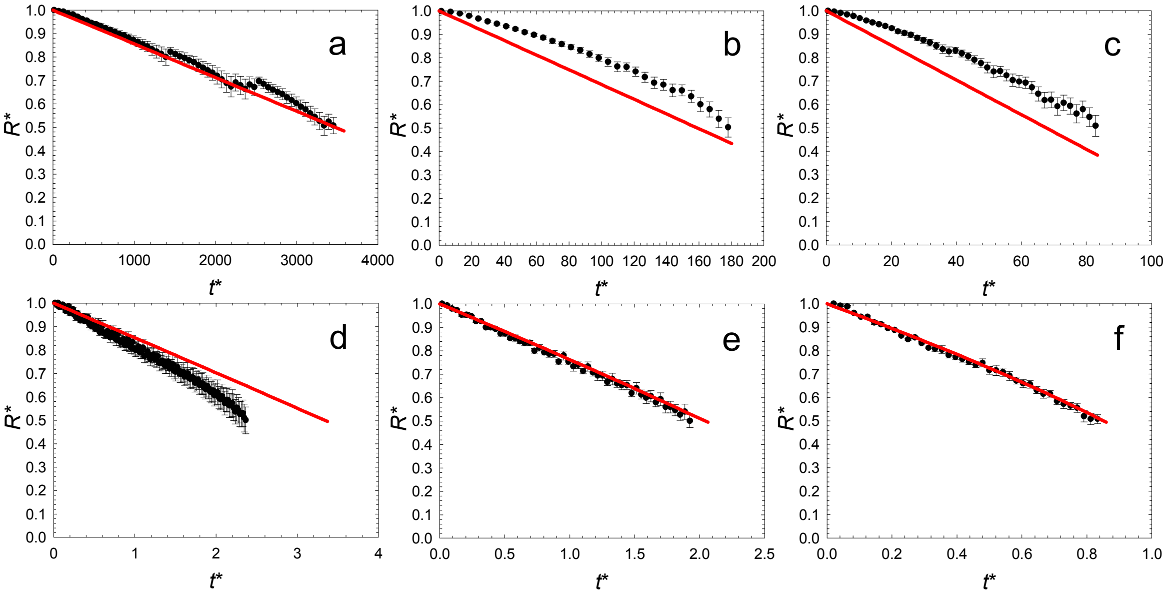

Fig. 4.10 Experimental break-up data (black) and predictions by Eqn. 4.31 (red) using X_{eff} values based on Eqn. 4.46 (Fig. 4.9 - red diamonds) for Oh = (a) 278.997, (b) 12.19, (c) 4.62, (d) 0.124, (e) 0.061, and (f) 0.00606.

As experimental data was taken at $t^* = t^*_{1/2}$, we only expected general correlation with the experimental curves up until $R^* = 1/2$. Fig. 4.10 demonstrates that approximate predictions of experimental break-up until $R^* = 1/2$ are possible for samples with various Oh values by using X_{eff} values based on Eqn. 4.46. Although, there are clear discrepancies that highlight the sensitivity of predictions to the value of X_{eff}, as well as deviations by predictions from the curvature of experimental data. Further investigation here and characterisation of the change in X_{eff} with Oh could improve the predictions. With X_{eff} as a smooth function of Oh, it would be possible to fit model predictions to break-up data (in the range of $0 < t^* < t^*_{1/2}$) for an unknown sample to extract Oh, rather than just using a single $t^*_{1/2}$ value, which would make the process a useful tool for extracting extensional viscosity. However, without understanding the changes in X_{eff} for values of Oh we persist with the calibration method in Sec. 4.4 to extract extensional viscosities throughout this body of work.

Chapter 5

Publication: Motility induced changes in viscosity of suspensions of swimming microbes in extensional flows

The extensional properties of delicate swimming motile microbe suspensions, quantified by the microfluidic SAW-based rheometer, are reported in this chapter. These low-viscosity microbe suspensions represent model systems of motile particles; theoretical modelling for dilute suspensions predicts that the motility of these microbes will affect bulk properties under extensional flow, which is validated for the first time by our experimental observations via the rheometer. Furthermore, a model, which extends the dilute model to apply to concentrated suspensions, provides further insights into the key parameters that need to be studied in order to better predict the effects of motile particles on bulk suspension viscosity in extensional flow.

5.1 Introduction

Chapters 2 and 3 discussed the advantages of ADMiER and illustrated its ability to detect subtle material property signals using small volumes of delicate low-viscosity solutions. In Chapter 5, after presenting the calibration approach to extracting effective extensional viscosities for non-Newtonian fluids, we exploit the abilities of ADMiER to pursue the validation of previously untested theoretical predictions of rheological properties of "active matter" in extensional flow. Active matter theory [17–19] describes systems composed of individual sub-units that are self-propelled, where their net average alignment contributes to the overall stresses in the system and in turn its total viscosity. Such systems are exemplified by living materials, like suspensions of motile microbes or the cytoskeletal polymers in ATP-powered white blood cells. This theory represents active bodies as axisymmetric particles that exert a net thrust along their primary axis, producing hydrodynamic dipoles that drive the surrounding fluid along their lengths. Active particles can be placed into two groups: "pushers" drive a tensile flow along their principal axis [20], while conversely "pullers" generate a contractile flow [17]. The positive hydrodynamic dipoles created by pusher particles are predicted to lower suspension viscosity below that of an equivalent passive particles suspension, and have even been seen to induce negative viscosities such that all viscous dissipative effects are neutralised, resulting in so called “superfluids” [99]. On the other hand, the negative hydrodynamic dipoles of pullers will increase viscosity. Predictions have been validated by experimental findings for pushers [21–23] and pullers [24] in shear flow, but not in extensional flow. Suspensions of swimming microbes are model active matter systems as they provide reproducible motile particles. However, they can be difficult to prepare in high volumes, and typically require aqueous media to suspend them and enable their motility. These aspects pose problems for alternative extensional techniques, which can require large volumes and have difficulties accessing low-viscosities, as discussed in Sec. 1.1 and Chapters 2 and 3. However, the ability of our technique to accommodate small volumes of low-viscosity suspension containing delicate particles surmounts these challenges. Thus, we assess the extensional viscosities of pushers using bacterial and mouse sperm suspensions, and pullers using algal suspensions.

The theory central to this study [100] focuses on the intrinsic viscosity of active particles, which includes stress contributions due to external flow over particles, Brownian torques on particles, and particle activity. This intrinsic viscosity, which was developed for dilute suspensions, is used here with the Krieger-Dougherty expression to enable the modelling of both dilute and concentrated suspensions of active particles. This modelling required auxiliary studies to obtain the appropriate values for the variables featured in the model. Among these studies was that of observing particle swimming, where particle tracking of the swimming microbes allowed mean squared displacement analysis, which provided estimations of both particle activity and diffusivity. Our results, where suspensions ranged into high volume fractions, show qualitative agreement with the theoretical predictions for dilute suspensions of active matter in extensional flow. Furthermore, our extended model, which describes extensional viscosity for dilute and concentrated suspensions, quantifies our experimental findings and determines that several key particle parameters are believed to greatly influence the extensional viscosity of these materials. Namely, these parameters are the effective length to physical length ratio, and the effective head-tail hydrodynamic interaction on the propulsive dipole. These particles are difficult to characterise, and treating the aforementioned parameters as having unity values shows significant disagreement, whereas assigning believable values provides reasonable model agreement with experimental data.

5.2 Publication

The following publication was reproduced from [16] by permission from The Royal Society of Chemistry.

Note: Following its publication, examiners brought to our attention that “Tripathi” has been misspelt as “Tripathy” on one occasion in the supplementary information section. This error is regretted.

Monash University

Declaration for Thesis Chapter 5

Declaration by candidate

In the case of Chapter 5, the nature and extent of my contribution to the work was the following:

Nature of contribution	**Extent of contribution (%)**
Amarin G. McDonnell led project, performed preparation, performed and defined experimentation, performed data processing, contributed to interpretation, performed analysis, and performed the writing of the paper.	50

The following co-authors contributed to the work. If co-authors are students at Monash University, the extent of their contribution in percentage terms must be stated:

Name	**Nature of contribution**	**Extent of contribution (%) for student co-authors only**
T. C. Gopesh	Contributed to interpretation, analysis, and modelling.	10
J. Lo	Prepared mouse sperm samples.	5
M. O'Bryan	Contributed to interpretation and review of draft.	5
L. Y. Yeo	Contributed to interpretation and review of draft.	5
J Friend	Contributed to interpretation and review of draft.	5
R Prabhakar *	Overall supervision, performed writing of the paper and review of draft, contributed to interpretation, analysis, and modelling.	20

The undersigned hereby certify that the above declaration correctly reflects the nature and extent of the candidate's and co-authors' contributions to this work*.

Candidate's Signature	[redacted]	**Date** 23/2/2016
Main Supervisor's Signature	[redacted]	**Date** 23/2/2016

Soft Matter

PAPER

View Article Online
View Journal

Cite this: DOI: 10.1039/c4sm02742f

Published on 30 April 2015. Downloaded by Monash University on 13/05/2015 22:47:32.

Motility induced changes in viscosity of suspensions of swimming microbes in extensional flows†

Amarin G. McDonnell,[a] Tilvawala C. Gopesh,[a] Jennifer Lo,[b] Moira O'Bryan,[b] Leslie Y. Yeo,[c] James R. Friend‡[c] and Ranganathan Prabhakar*[a]

Received 10th December 2014,
Accepted 29th April 2015

DOI: 10.1039/c4sm02742f

www.rsc.org/softmatter

Suspensions of motile cells are model systems for understanding the unique mechanical properties of living materials which often consist of ensembles of self-propelled particles. We present here a quantitative comparison of theory against experiment for the rheology of such suspensions in extensional flows. The influence of motility on viscosities of cell suspensions is studied using a novel acoustically-driven microfluidic capillary-breakup extensional rheometer. Motility increases the extensional viscosity of suspensions of algal pullers, but decreases it in the case of bacterial or sperm pushers. A recent model [Saintillan, *Phys. Rev. E: Stat., Nonlinear, Soft Matter Phys.*, 2010, **81**, 56307] for dilute active suspensions is extended to obtain predictions for higher concentrations, after independently obtaining parameters such as swimming speeds and diffusivities. We show that details of body and flagellar shape can significantly determine macroscale rheological behaviour.

1 Introduction

Many living materials, such as suspensions of motile microbes or of ATP-powered cytoskeletal polymers, are large ensembles of nearly identical and motile subunits that interact strongly with their neighbours. Understanding the properties of such systems presents unique conceptual challenges. Since each elemental subunit such as a motile cell is by itself a driven–dissipative system, their collectives operate well out of equilibrium even in the absence of any external forcing. Local fluctuations in motion further have a non-thermal origin, and the fluctuation–dissipation theorem has been shown to be inapplicable in these systems.[1]

The recent development of a continuum framework that shows that these intrinsically non-equilibrium systems share universal features is therefore a significant theoretical breakthrough.[2,3] This theory of "active matter" suggests that a net average local alignment of self-propelled particles must, in a continuum description, lead to a contribution to the stress tensor arising from propulsive forces or "activity" of the particles. An interesting prediction is that particle activity must change the macroscopic viscosity of the suspension. An axisymmetric self-propelled particle exerting a net propulsive thrust along its principal axis generates a hydrodynamic force dipole. The flow field around a single *E. coli* cell has been measured to be approximately that of a positive hydrodynamic dipole[4] which forces the ambient fluid around each particle axially outward towards its two ends. The suspension viscosity for such "pushers" is predicted to decrease below its value for a passive suspension of inactive particles of the same size, shape and concentration.[5] Conversely, a suspension of "pullers" with negative hydrodynamic dipoles will have a higher viscosity than a passive suspension. Quantitative microstructural models relating particle size, shape, concentration and motility to rheological properties are just beginning to emerge.[6–9]

These predictions are supported by experimental observations in shear flows with bacterial pushers[10–12] and algal pullers.[13] We present here the first measurements of *extensional* viscosities of suspensions of wild-type strains of the microalga *Dunaliella tertiolecta*, the bacterium *Escherichia coli* and mouse spermatozoa. *D. tertiolecta* uses its pair of flagella in a manner similar to the puller *Chlamydomonas reinhardtii* studied by Rafaï *et al.*,[13] whereas *E. coli* and the sperm use flagellar tails to push forward, like *B. subtilis* studied by Sokolov and Aranson.[10] *E. coli* cells have multiple flagella and use run-and-tumble swimming by bundling and unbundling their flagella. Sperm were cultured under conditions to induce capacitation and hyperactive swimming.[14] Trajectories of cells swimming were analyzed to characterize their motility under quiescent conditions. Measurements of the extensional viscosity of live and dead cell suspensions were obtained with a novel microfluidic rheometer developed by

---

[a] Department of Mechanical and Aerospace Engineering, Monash University, Clayton, Australia. [redacted]

[b] Department of Anatomy and Developmental Biology, Monash University, Clayton, Australia

[c] Micro/Nanophysics Research Laboratory, RMIT University, Melbourne, Australia

† Electronic supplementary information (ESI) available. See DOI: 10.1039/c4sm02742f

‡ Present address: Department of Mechanical Engineering, University of California-San Diego, San Diego, California, USA.

Published on 30 April 2015. Downloaded by Monash University on 13/05/2015 22:47:32.

ref. 15. A recent model for dilute suspensions of self-propelled hydrodynamic dipoles[7,8] is extended here to the non-dilute regime to relate the non-Newtonian elongational viscosity of active suspensions to particle volume fraction. We compare predictions with this model against experimental data to demonstrate that despite the wide range of particle size, shape and motility characteristics, bulk mechanical behaviour of active suspensions may be accurately characterized in terms of a small number of parameters.

2 Experiments

2.1 Cell culture and suspensions

D. tertiolecta Butcher was collected and isolated from Port Phillip Bay, Victoria, in December 2009. Cultures were maintained at 20 °C in modified F-medium (30 g L^{-1} aquarium salt, 250 mg L^{-1} $NaNO_3$, 18 mg L^{-1} KH_2PO_4, 9 mg L^{-1} iron(III) citrate ($C_6H_5O_7Fe$), 9 mg L^{-1} citric acid ($C_6H_8O_7$), 0.2 mg L^{-1} $MnCl_2 \cdot 4H_2O$, 0.023 mg L^{-1} $ZnSO_4 \cdot 7H_2O$, 0.011 mg L^{-1} $CoCl_2 \cdot 6H_2O$, 0.005 mg L^{-1} $CuSO_4 \cdot 5H_2O$, 0.008 mg L^{-1} $Na_2MoO_4 \cdot 2H_2O$, 0.65 μg L^{-1} H_2SeO_3 and traces of vitamin B12, biotin and thiamine[16]). 20 mL of inoculum were added to 400 mL of F-medium and incubated in 2 L glass bottles in a laboratory growth cabinet at 20 °C 0.1 °C with a 16 : 8 light dark cycle using white fluorescent lights with a photon flux of 60 μmol photons per m^2 per s. Cultures were bubbled with air through an aquarium air stone to provide a source of inorganic carbon (CO_2). After 5 days, F-medium was added to bring the total culture volume to 1.5 L. Samples for experimentation were harvested after a further 6 days during the log-phase of growth into 50 mL polypropylene capped-tubes and centrifuged at 3500 rpm at 20 °C for 10 minutes to collect cell pellet.[16]

Wild-type *E. coli* K 12 strain was procured from ATCC, USA (#10798). Standard media in the form of Luria Bertini (LB) broth (#L3022, Sigma Aldrich; 10 g L^{-1} tryptone, 5 g L^{-1} yeast extract, 5 g L^{-1} NaCl) and/or Luria Agar (#L2897, Sigma Aldrich) was used for bacterial culture. A UV-VIS spectrophotometer (#UV-2450, Shimadzu) was used to characterize the bacterial growth by measuring absorbance/optical density at 600 nm. About 0.5 mL of sterile LB broth was put into the sterile ATCC vial containing lyophilized culture. A small amount of the suspended culture (around 0.05 mL) was inoculated on to sterile Luria agar slants, and incubated at 37 °C for 18–20 hours. A single colony from an agar slant was transferred to 5 mL of sterile LB broth and incubated at 37 °C for 6–7 hours with vigorous shaking (at 170 rpm), till absorbance at 600 nm reached 0.4. About 0.3 mL of 50 wt% glycerol–water solution was added to 0.7 mL of this mid-log phase culture and stored at −73 °C for future use. From the glycerol-freeze stock, a tiny amount is scraped off and inoculated under aseptic conditions to 5 mL of sterile LB medium. The culture was incubated at 37 °C for 16–18 hours with vigorous shaking (at 170 rpm). A small amount (around 0.05 mL) was transferred into sterile LB media of 160 mL volume in a shake-flask. Cultures were incubated at 37 °C for 6–7 hours with vigorous shaking (at 170 rpm).

Sperm from C57BL (wild-type) mice, extracted from cauda epididymii using the back-flushing method[17] was added to 5 mL pre-warmed MT6 medium (125 mM NaCl, 2.7 mM KCl, 1 mM $MgCl_2 \cdot 6H_2O$, 0.35 mM $NaH_2PO_4 \cdot 2H_2O$, 5.5 mM glucose, 25 mM $NaHCO_3$, 1.7 mM $CaCl_2 \cdot 2H_2O$, 60 μM bovine-serum albumin) containing methylcellulose and incubated at 37 °C for 90 min.

Algal cultures were centrifuged at 3500 rpm for 8 min at 20 °C and pellets were re-suspended in growth medium at desired concentrations. Lugol's iodine (100 g L^{-1} KI, 50 g L^{-1} iodine crystals) was added to Eppendorf tubes to kill algal cells. These were centrifuged, the supernatant removed and re-suspended in growth medium again. *E. coli* cultures after log-phase growth were centrifuged at 4550 rpm for 10 min at 4 °C, and pellets were re-suspended after weighing in a (pH 8.2) buffer of 10 mM K_2HPO_4, 0.1 mM EDTA and 0.2 wt% glucose to prepare suspensions of various cell volume fractions. Suspensions were exposed to UV light for 30–60 min to kill cells without significant lysis. Fresh sperm samples prepared as above were first tested in capillary-thinning experiments. Standing sperm suspensions for 90 min inactivated motility.

2.2 Particle tracking

Image-analysis was used to determine the average fractional area covered by cells at the focal plane; this was assumed to be equal to the volume fraction. In bacteria and algae, flagellar filaments were not resolved in the image analysis, and do not contribute to the volume fraction. Sample droplets were placed on Teflon-coated glass slides, with a coverslip on top. The gap width between slide and coverslip was typically 1 mm. Microscope videos for bacteria and algae were captured with 20× and 100× (Olympus) lenses, respectively, and a high-speed camera (SA5, Photron; 50 fps; 768 × 816 pixels). Swimming speeds and diffusivities were determined by processing images (ImageJ) and cell tracking (Imaris). Sperm suspensions were loaded onto both chambers on a 2×-Cel 80 μm slides chambers covered with 2×-Cel Cover Glass (Hamilton Thorne Research). Slides were inserted into a Hamilton Throne IVOS for computer-aided semen analysis (CASA). At least 1000 sperm were counted in each chamber. Sperm motility characteristics were analyzed through image analysis as done for the algae and bacteria. Sperm flagella were much thicker and were accounted for in the volume calculation.

2.3 Acoustically-driven microfluidic extensional rheometry

Unlike shear rheometry, techniques for reliable measurement of fluid properties in extensional flows have been established only relatively recently.[18] In capillary-breakup extensional rheometry (CaBER), a liquid bridge is usually first created by rapidly moving apart end-plates between which a sample drop is sandwiched. If the end-plate separation is large enough, the bridge subsequently begins to thin due to the Rayleigh–Plateau instability. The rate at which a liquid bridge thins is governed largely by the balance of the capillary stress against the inertial and viscous stresses induced by the extensional flow about the necking plane and hence it is in principle possible to extract the viscosity by monitoring the neck radius as a function of time.[19]

This journal is © The Royal Society of Chemistry 2015

Published on 30 April 2015. Downloaded by Monash University on 13/05/2015 22:47:32.

This technique has in the past been used for highly viscous samples.[20] Obtaining reliable measurements with low-viscosity complex fluids such as aqueous cell suspensions however presents two challenges. Firstly, mechanical motion of end-plates sets off inertial instabilities that quickly break up liquid bridges.[18] The motion within the liquid bridge following the sudden stopping of the end-plates is complex and is not described by a simple stress balance. Secondly, CaBER and other techniques based on capillary thinning of filaments are well established for viscoelastic fluids such as polymer solutions where liquid bridges thin exponentially in time, creating long-lived, slender and almost cylindrical filaments.[21] This permits the use of a simple stress-balance equation to extract the viscoelastic fluid stress at the necking plane from just a measurement of the radius R as a function of time t. For fluids with little or no elasticity, directly calculating the viscosity through the stress-balance has thus far been shown to be practicable again only for very viscous fluids where a cylindrical filament can form towards the final stages of breakup.[20] Thin cylindrical filaments do form close to break-up, but imaging these require the combination of ultra-fast and very high resolution photography.[22]

Several novel modifications to the original CaBER have been proposed to address the first of these issues. End-plates are moved at sufficiently high speeds in the Cambridge Trimaster device to overcome initial inertial instabilities.[23,24] In the slow-retraction-method, a low-viscosity liquid-bridge is first stabilized at an aspect-ratio smaller than that required to initiate capillary thinning, and then the end plates are moved apart slowly to initiate thinning in a controlled manner.[25] Microfluidic devices exploiting capillary thinning and breakup of a microjet ejected into an annular flow of another outer fluid have also been proposed.[26] Other forces have also been used in microfluidic devices to trigger capillary thinning in initially stable liquid bridges.[27]

Here, we use a method developed by Bhattacharjee *et al.*,[15] wherein the liquid-bridge is created and stabilized against capillary forces initially by power input from surface acoustic radiation (Fig. 1). In our experiments, a 20 MHz waveform generator (33220A, Agilent) was used to generate a surface acoustic wave (SAW) burst triggered by a second signal generator (WF1966, NF Corporation). The latter delivered a sinusoidal signal to an RF power amplifier (411LA, ENI), providing a fixed frequency and amplitude signal near the 36.7 MHz resonance frequency of the SAW substrate. An arrangement of curved inter-digitated transducers (IDTs) bonded to a piezoelectric substrate[15] focussed Rayleigh waves towards the point where a sessile droplet (1 μl; approximately 1 mm dia.) rests (Fig. 1(b)). Energy from the SAW leaks into the droplet causing recirculation and bulk motion, leading to an elongated liquid that bridges a gap to an opposing parallel surface located 1.5 mm away from the SAW substrate. The opposing surface was coated with Teflon and was partially fouled to ensure that the jet adheres to the surface but does not spread. The SAW burst was ended after 1.5 ms which was found to be sufficient to create stable liquid bridges in all our samples. The liquid bridge then thins under the action of capillary forces, generating an extensional flow at the necking plane (Fig. 1(c)). The motion of the entire liquid bridge was captured using a high-speed camera (Photron SA5; 62 000 fps; image size: 1.35 mm × 2.14 mm (192 × 304 pixels)) with a long-distance video microscope attachment (K2/SC, Infinity). The set-up is lit by a single LED lamp placed behind the filament. The radius of the neck in each image frame was obtained using standard image-analysis techniques. Initial transients were discarded in each case until the neck attained a diameter of 50 pixels (0.352 ± 0.007 mm); this was taken as the initial time (t = 0) for all samples.

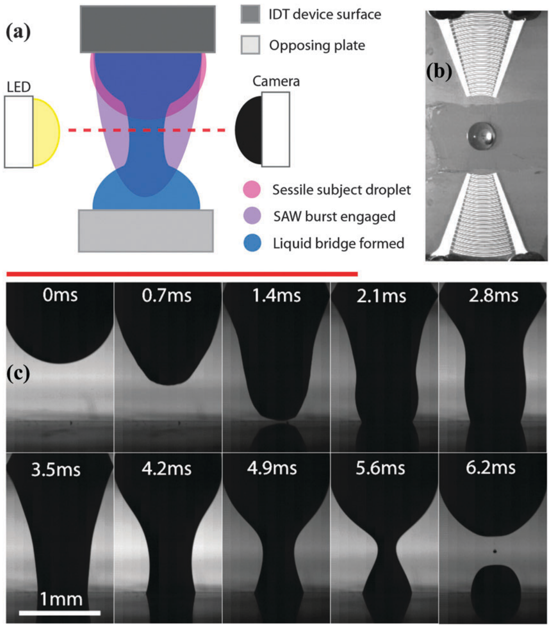

Fig. 1 (a) Schematic of experimental setup. (b) Curved inter-digitated transducers for focussing SAW into a sessile droplet. (c) Time-lapse images of the formation of a liquid bridge after ejection of a jet due to actuation of a sessile drop by SAW; the red-line indicates duration of the SAW pulse.

We avoid problems with imaging thin cylindrical filaments close to break-up altogether by using neck radius data during the early stages of the thinning while the axial curvature is still large. This is furthermore advantageous when handling particle suspensions since the effect of particle interactions with the air–liquid interface on the overall dynamics at the neck is weaker when the neck radius is large compared to particle dimensions. Rescaling the governing equations for slender but non-cylindrical Newtonian liquid-bridges[28] with the mid-filament radius R_0 at t = 0 (as defined above) and the Rayleigh time-scale,

$$\tau_{\mathrm{R}} \equiv \sqrt{\frac{\rho {R_0}^3}{\gamma}}, \tag{1}$$

the decay of the rescaled neck radius $R^* = R/R_0$ with rescaled time $t^* = t/\tau_{\mathrm{R}}$ is parametrized by the dimensionless volume and aspect ratio of the liquid bridge, and the Ohnesorge and Bond numbers, defined conventionally as

$$\mathrm{Oh} \equiv \frac{\bar{\eta}}{3\sqrt{\rho\gamma R_0}}; \quad \mathrm{Bo} \equiv \frac{g\rho {R_0}^2}{\gamma}, \tag{2}$$

Published on 30 April 2015. Downloaded by Monash University on 13/05/2015 22:47:32.

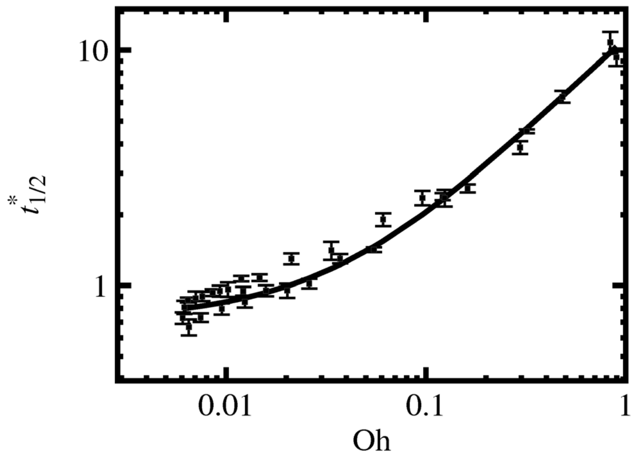

Fig. 2 Variation of liquid-bridge half-times with Oh: the curve is a linear least-squares fit of eqn (3) through the data.

where, ρ, γ and $\bar{\eta}$ are the density, surface tension coefficient and extensional viscosity respectively of a fluid sample and g is the gravitational acceleration. In our experiments, droplet volumes, R_0 and the separation between bridge surfaces were kept constant. The Ohnesorge number for our samples varied by almost three orders of magnitude, whereas the variation in Bo was relatively much smaller (around 33%). Therefore, the Bond number can be assumed to be relatively relatively constant. Under such conditions, the rescaled time $t_{1/2}$* taken for the filament to neck to half its initial radius (*i.e.* the time to $R^* = 1/2$) is predominantly governed by Oh.

Fig. 2 shows half-time data obtained for a range of Newtonian glycerol–water and sucrose–water mixtures whose properties ($\eta = 3\bar{\eta}$, γ and ρ) were independently measured. Surface tension of suspensions were measured using a tensiometer (Analite; Selby Scientific). Shear viscosities were measured with a Haake Mars (Thermo Scientific) shear rheometer. The form of the regression curve through the data in Fig. 2 is inspired by the asymptotic behaviour expected in the limits of vanishing or very large Oh. When Oh → 0, inertia dominates and capillary thinning is insensitive to viscosity, whereas when viscous stresses dominate at high Oh, the breakup-time increases linearly with viscosity and Oh. We therefore fit a rational function of the following form through the experimental data:

$$t_{1/2}{}^* = \frac{K_0 + K_1\mathrm{Oh} + K_2\mathrm{Oh}^2}{1 + \mathrm{Oh}}. \tag{3}$$

The values of the coefficients for generating the empirical fit through the data as shown in Fig. S2 are given in the ESI.†

For a given non-Newtonian test sample that does not exhibit significant strain-hardening, the capillary breakup half-time is first extracted and normalized. The inverse of the rational function above in eqn (3) is then used to back out the Oh from observed $t_{1/2}$*. From the definition of Oh in eqn (2), the extensional viscosity of the sample is obtained as $\bar{\eta} = 3\mathrm{Oh}\sqrt{\rho\gamma R_0}$. The pre-factor of 3 is a consequence of the convention used to define Oh; no assumption is made here about a relationship between the extensional and shear viscosities of the sample.

We further note that as Oh → 0, *R-vs.-t* data become insensitive to Oh. This is reflected in the levelling-off of the $t_{1/2}$* data in Fig. 2 to a constant value at small Oh. Therefore, the method presented here becomes unreliable at very low values of Oh, since small errors in $t_{1/2}$* imply large errors in Oh. In our experiments, the trend in $t_{1/2}$* when Oh 0.01 is sufficient to allow us to back out Oh from measured half-times such that the error in the Oh backed out due to the noise in the calibration data in Fig. 2 is smaller than that due to the measurement error in $t_{1/2}$ of the test sample. Significant differences between suspensions and suspending media are observed in plots of the decay of filament radius with time,† and there is no difficulty extracting their viscosities.

3 Modeling

3.1 Rheology

We are interested in quantitatively comparing theoretical predictions with experimental measurements of extensional viscosity on active suspensions with the aim of extracting the strengths of the active hydrodynamic dipoles for each of the organisms studied here. As we shall show later, a nonlinear dependence on particle volume fraction is observed which indicates that the suspensions are not dilute. We therefore need an analytical expression for the extensional viscosity of an active suspension as a function of the active dipole strength, particle concentration and other parameters such as the extensional strain-rate. Theoretical predictions are available in shear flows for non-dilute active suspensions,[8,29] but in extensional flows, only dilute suspensions have been analyzed so far.[6,7] As a first step, we use the Krieger–Dougherty equation (KDE)[30–32] to extend those results to more concentrated suspensions. The advantages and limitations of this approach will be discussed later after comparing predictions with experimental data.

The KDE was originally suggested for suspensions of (passive) spherical particles to describe the strong growth of viscosity as the particle density approaches the close-packing limit.[30] It has since then been applied for suspensions of non-spherical particles[33] as well as soft particles.[34] The KDE makes the mean-field assumption that when a new particle is added into the free-volume of a suspension, all its interactions with other particles and solvent can be modeled by treating the rest of the suspension as a homogeneous effective medium of a higher viscosity than the original suspending fluid.[31,32] The relative incremental influence of this particle on the overall viscosity is however assumed to be independent of the particle concentration itself and thus equal to its value at infinite dilution, all other parameters such as the strain-rate held constant. In dilute suspension theory, this relative influence exerted by each particle is described in terms of the intrinsic viscosity ration, which in extensional flows is defined as $[\bar{\eta}] = \lim_{\phi\to 0}(\bar{\eta} - 3\eta_s)/(3\eta_s\phi)$, where $\bar{\eta}$ is the extensional viscosity of the suspension, $3\eta_s$ is the extension viscosity of the Newtonian suspending medium of shear viscosity η_s, and $\phi = nv_p$ is the volume fraction of particles, each of volume v_p and at a number density n.

Published on 30 April 2015. Downloaded by Monash University on 13/05/2015 22:47:32.

This argument leads to the following equation for the relative extensional viscosity of a non-dilute suspension:[31]

$$\bar{\eta}_{\mathrm{rel}} = \frac{\bar{\eta}}{3\eta_{\mathrm{s}}} = \left(1 - \frac{\phi}{\phi_{\mathrm{m}}}\right)^{-[\bar{\eta}]\phi_{\mathrm{m}}}, \tag{4}$$

where ϕ_{m} is a maximum volume fraction at which the steady-state viscosity diverges.

The intrinsic viscosity $[\bar{\eta}]$ encodes for the effect of all parameters other than the concentration on suspension viscosity. Recent studies by Haines *et al.*[6] and Saintillan[7] have modeled the statistics of an axisymmetric self-propelled particle that stochastically changes its swimming direction while moving in an externally imposed homogeneous extensional flow, to obtain expressions relating $[\bar{\eta}]$ to motility characteristics and strain-rate. We use Saintillan's expression here since it is applicable across a broader range of strain-rates.

In Saintillan's model, swimming cylinders of length L_{h} and diameter d translate with a mean speed U and autonomously change direction in an apparently random manner which gives rise to a non-Brownian rotational diffusivity, D_{r}. Passive particles (*e.g.* dead cells) on the other hand only have a diffusivity $D_{\mathrm{r},0}$ that is solely due to thermal fluctuations. For a dilute suspension undergoing a homogeneous extensional flow of strain-rate $\dot{\varepsilon}$, Saintillan[7] showed that

$$[\bar{\eta}] = \tilde{\chi}\left[\frac{1}{2}\left(M + \frac{1}{3}\right) + \frac{3}{\mathrm{Pe}}\left(\tilde{\gamma} + \tilde{\sigma} - \frac{1}{\tilde{\beta}}\right)\left(M - \frac{1}{3}\right)\right], \tag{5}$$

where the Péclet number—Pe $\equiv \dot{\varepsilon}/D_{\mathrm{r}}$ (or $\dot{\varepsilon}/D_{\mathrm{r},0}$)—quantifies the ability of the extensional flow to reorient a particle against random orientational changes. The function M is a weak monotonically-increasing function of $\tilde{\beta}$Pe, where $\tilde{\beta}$ is a constant shape-factor in the coupling of particle rotation to the straining motion of the ambient flow.† [35] Besides $\tilde{\beta}$ and Pe, the equation above contains three other dimensionless parameters—$\tilde{\chi}$, $\tilde{\sigma}$ and $\tilde{\gamma}$—characterizing the dipole moments of the hydrodynamic forces exerted by the straining flow around each particle, the propulsive thrust and the torques exerted by thermal fluctuations. These dimensionless parameters need to be related to measurable particle characteristics.

Cells that swim with flagella have complex shapes that on average can be approximated as being axisymmetric. We assume that the average frictional characteristics a cell can be represented by an effective cylinder of hydrodynamic length L_{h}. This length cannot however be directly measured. Instead, we express it terms of a ratio $\lambda = L_{\mathrm{h}}/L$, where L is the measurable sum of the lengths of the head and the tail when completely stretched out. Then, the dimensionless strength of the flow-induced dipole is[7,36]

$$\tilde{\chi} = \frac{\pi\lambda^3 L^3}{12 v_{\mathrm{p}} \ln(2\lambda L/d)}. \tag{6}$$

The propulsive thrust generated by the inertialess swimmer and the corresponding frictional resistance to swimming are equal and opposite to one another, but act at different locations on the axis. A scaling argument for the strength of this propulsive dipole leads to[7]

$$\tilde{\sigma} = \pm\frac{\alpha \ln(2\lambda L/d) U}{\lambda^3 L D_{\mathrm{r}}}, \tag{7}$$

where $\alpha > 0$ is an unknown geometry-dependent pre-factor in the scaling analysis. The dipole is positive for pullers and negative for pushers, while for passive particles, $\tilde{\sigma}_0 = 0$. Torques due to thermal fluctuations tend to relax the orientational distribution of particles to its isotropic equilibrium state; their relative strength in an active suspension is represented by

$$\tilde{\gamma} = \frac{6k_{\mathrm{B}}T\ln(2\lambda L/d)}{\pi\eta_{\mathrm{s}}\lambda^3 L^3 D_{\mathrm{r}}}, \tag{8}$$

where k_{B} is the Boltzmann constant and T is the thermodynamic absolute temperature of the suspension. The fluctuation–dissipation theorem (FDT) is valid for passive particles, in which case the rotational diffusivity for slender rods is related to friction and

$$D_{\mathrm{r},0} = \frac{3k_{\mathrm{B}}T\ln(2(\lambda L)/d)}{\pi\eta_{\mathrm{s}}(\lambda L)^3}. \tag{9}$$

Substituting this in eqn (8) above leads to $\tilde{\gamma}_0 = 2$ for dead cells. No such simple relation is currently available in active systems for which D_{r} needs to be explicitly measured to obtain $\tilde{\gamma}$.

The model above for $[\bar{\eta}]$ requires, besides the solvent conditions $k_{\mathrm{B}}T$ and η_{s}, independent measurement of the following parameters: the average geometric characteristics of the swimmers, L, d, v_{p}; their motility characteristics U and D_{r} (or $D_{\mathrm{r},0}$ for dead cells); and the hydrodynamic ratios λ and α. The constant $\tilde{\beta}$ is taken to be unity, which is appropriate for slender particles of large aspect ratio.[7,35] Out of these, the solvent parameters are obtained by standard techniques and the particle size characteristics L, d and v_{p} are obtained through microscopy. As noted above, the value of $D_{\mathrm{r},0}$ is effectively set by invoking the FDT and using $\tilde{\gamma}_0 = 2$. We discuss below the estimation of the motility parameters, U and D_{r}. It is more difficult to directly determine the ratios λ and α, which are therefore treated as free parameters to be obtained by comparing model predictions to experimental data for $\bar{\eta}_{\mathrm{rel}}$. Keeping in mind their physical significance, we assess later if the values for λ and α obtained thus are plausible.

3.2 Active diffusivity

In the absence of flow, the trajectory of an active particle swimming in with a speed U along its principal axis with random reorientations of that axis can be modeled by a pair of Langevin equations for its instantaneous position $\mathbf{r}(t)$ and orientation. The rescaled mean-squared displacement for such a particle in two dimensions is[37]

$$\widetilde{\mathrm{MSD}} = \frac{\left\langle(\mathbf{r}(t) - \mathbf{r}(0))^2\right\rangle}{(U/D_{\mathrm{r}})^2} = 4\xi\tilde{t} + 2\left(\tilde{t} - 1 + \mathrm{e}^{-\tilde{t}}\right), \tag{10}$$

where $\tilde{t} = D_{\mathrm{r}}t$ and $\xi = D_t D_{\mathrm{r}}/U^2$. The rescaled translational diffusivity ξ controls the shape of the $\widetilde{\mathrm{MSD}}$-*versus*-$\tilde{t}$ curves:

$$\widetilde{\mathrm{MSD}} \approx \begin{cases} (4\xi + \tilde{t})\tilde{t}, & \text{if} \quad \tilde{t} \ll 1 \\ (4\xi + 2)\tilde{t}, & \text{if} \quad \tilde{t} \gg 1 \end{cases}. \tag{11}$$

If translational diffusion is dominant and $\xi \gg 1$, then $\widetilde{\mathrm{MSD}} \approx 4\xi\tilde{t}$ always. When $0 < \xi < 1$ on the other hand, one observes

Published on 30 April 2015. Downloaded by Monash University on 13/05/2015 22:47:32.

diffusive-ballistic-diffusive behaviour. At short times when $\tilde{t} \ll 4\xi$, $\widetilde{\mathrm{MSD}} \approx 4\xi\tilde{t}$. At long time scales too, the behaviour is diffusive and $\widetilde{\mathrm{MSD}} \approx (4\xi + 2)\tilde{t}$. Therefore, if the effective long-time translational diffusivity D_{eff} is defined such that MSD = $4D_{\mathrm{eff}}t$, then $D_{\mathrm{eff}} = D_t + (U^2/2D_{\mathrm{r}})$. When $4\xi \ll \tilde{t} \lesssim 1$, the motion is ballistic with $\widetilde{\mathrm{MSD}} \approx \tilde{t}^2$. Values of D_{r}, D_t and U can be obtained from shift-factors by shifting experimental MSD-*versus*-t data to match one of the dimensionless theoretical curves on a log–log plot.

4 Results and discussion

Experimental MSD data was obtained using suspensions of very low volume fractions with cell number densities smaller than L^{-3}. We find that this data for all the three organisms resembled the $\xi = 0$ curve, indicating that translational diffusivity during swimming has a negligible influence (Fig. 3). The values of swimming speed and diffusivity thus extracted are reported in Table 1. The value of D_{r} for algae is comparable to those observed by Rafaï *et al.*[13] in another blue-green algal species *C. reinhardtii*: they measured an average speed of U = 40 μm s^{-1}, and a long-time effective diffusivity of $D_{\mathrm{eff}} \approx$ 995 μm^2 s^{-1}, which corresponds to a rotational diffusivity of $D_{\mathrm{r}} \approx$ 0.8 s^{-1} assuming that the true translational diffusivity is negligible in that species as well. For *E. coli*, analysis of the 3D cell-tracking data suggests $D_{\mathrm{r}} \approx$ 3.5 s^{-1},[38] although a much lower value of D_{r} = 0.057 s^{-1} was reported by Drescher *et al.*[4] Some of this variability can be attributed to differences in strains and the media and protocols used for cell-tracking. In addition, there are also significant differences in the analyses of the run-and-tumble motion of *E. coli* cells to assign effective diffusivities. Although computer-aided analysis of sperm motility is well established in mammalian reproductive biology,[39] to our best knowledge, mean-square displacements have not been analyzed to determine effective diffusivities. The values of U extracted by fitting the theoretical prediction in eqn (10) through the mean-squared displacement data for the algae and bacteria are close to the values measured by direct observation (45 and 4.7 μm s^{-1}, respectively). In the case of sperm however, the extracted value is significantly different from the direct measurement of an average speed 70 μm s^{-1} for the motion of the sperm head which is comparable to average head speeds of around 100–150 μm s^{-1} in hyperactive mice sperm.[40,41] This difference could be due to the fact that the sperm head oscillates about the mean trajectory of the cell.[39]

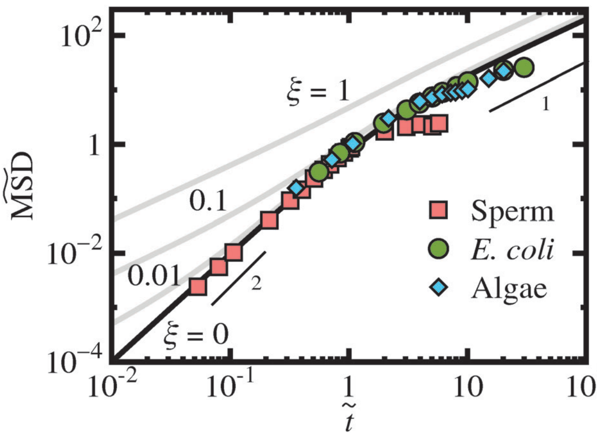

Fig. 3 Comparison of experimental data for the mean-squared displacement for algae, *E. coli* and mouse sperm with predictions for various values of the relative translational diffusivity ξ; $\widetilde{\mathrm{MSD}} = \mathrm{MSD}(D_{\mathrm{r}}/U)^2$ and $\tilde{t} = D_{\mathrm{r}}t$.

Table 1 Particle characteristics and model parameters

	Algae	Bacteria	Sperm
Geometric and motility characteristics			
L (μm)	36	13	95
d (μm)	2.8	1	3
L/d (μm)	12.9	13	32
U (μm s^{-1})	30	5.5	31
D_{r} (s^{-1})	3	10	0.8
Free parameters			
α	15	1	30
λ	0.6	0.3	0.7
ϕ_{m}	0.7	0.7	0.7
Calculated parameters			
$\tilde{\chi}$	5.2	6.7	100
$\tilde{\gamma}$	4.5×10^{-3}	1.2×10^{-2}	5.4×10^{-5}
$\tilde{\sigma}$	40	−2.7	−97
F (pN)	46	0.6	260
$D_{\mathrm{r},0}$ (s^{-1})	6.8×10^{-3}	6.1×10^{-2}	2.2×10^{-5}

Fig. 4 presents the key results in our study. The top panel in the figure shows the evolution of the neck radius during capillary thinning for the highest volume fractions studied in each species; data at lower volume fractions is presented in the ESI.† We observe that capillary thinning of samples of live algal suspensions progresses more slowly than of samples of dead cell suspensions at the same volume fraction (top-panel, Fig. 4). The opposite behaviour is observed in bacterial and sperm suspensions. This is in line with the expectation that motility of pullers like *D. tertiolecta* tends to increase the viscosity whereas in pushers such as *E. coli* and sperm, viscosity decreases. The middle and bottom panels in Fig. 4 shows that the differences between the radius-*versus*-time data, and thus between the viscosities, of live and dead cell suspensions. These differences in *E. coli* are small but significant relative to experimental uncertainty. In comparison, the differences are larger in algae over a similar range of volume fractions. Data for sperm could only be obtained at low concentrations due to the small sample volumes collected from mice and limitations in concentrating them further. However, even at these low concentrations, the effect of motility on viscosity appears clear. The difference in viscosity between live and dead cell samples appears to increase with volume fraction for all three species.

To use the model to understand these trends, we first need to determine the strain rates in the experiments. As is well known, the instantaneous strain-rate $\dot{\varepsilon} = -2d\ln R/dt$ at the necking plane in CaBER experiments cannot be directly controlled but are determined by the liquid bridge dimensions and fluid properties. The radial decay in all our samples was observed to be approximately linear when $t < t_{1/2}$. The instantaneous strain-rate in this observation period for linear radial decay

Published on 30 April 2015. Downloaded by Monash University on 13/05/2015 22:47:32.

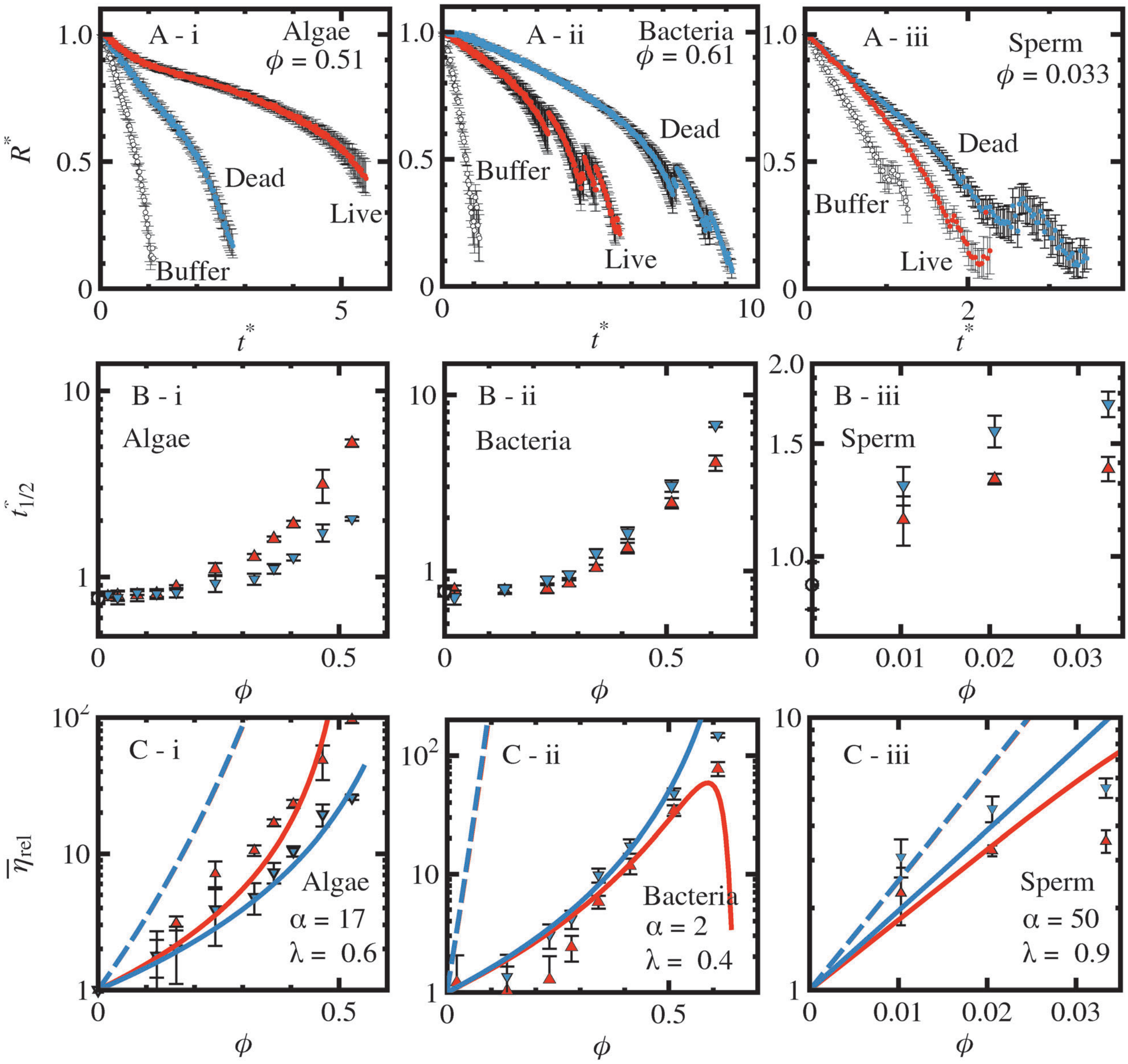

Fig. 4 Top panel (A i–iii): radial decay observed during capillary thinning for the most concentrated algal, bacterial and sperm suspensions studied; middle panel (B i–iii): variation of dimensionless capillary thinning half-times with particle volume fraction; bottom panel (C i–iii): comparison of predictions of relative extensional viscosity $\bar{\eta}_{\text{rel}} = \bar{\eta}/(3\eta_s)$ with experimental values extracted from measured $t_{1/2}^* = t_{1/2}/\tau_R$. In B and C, up- and down-triangles represent data for live and dead cell suspensions, respectively. Continuous curves in the bottom panel have been obtained with values of α and λ as shown on the plots whereas dashed curves are predictions with both these parameters set to unity.

increases from $1/t_{1/2}$ to $2/t_{1/2}$. We can thus estimate the average strain-rate from the observed $t_{1/2}$ as $\dot{\varepsilon}_{\text{avg}} \approx \varepsilon_{1/2}/t_{1/2} = 1.4/t_{1/2}$ since the Hencky strain at $t_{1/2}$ for a linear radial decay can be shown to be $\varepsilon_{1/2} = 2\ln 2$. It is therefore clear from the systematic increase in $t_{1/2}$ with concentration (Fig. 4B(i–iii)) that the average strain-rate $\dot{\varepsilon}_{\text{avg}}$ decreases with concentration as the increasing viscosity slows down capillary thinning. The strain-rate at any concentration in the range covered in the experiments was obtained using a cubic polynomial fit through the experimental $\dot{\varepsilon}_{\text{avg}}$-*vs.*-$\phi$ data.† Values of $\dot{\varepsilon}_{\text{avg}}$ in our experiments ranged from about 250 s^{-1} at higher concentrations to 2000 s^{-1} for pure buffers.

Values of model parameters and other derived quantities for the three species are listed in Table 1. The ratio λ of the hydrodynamic length to the total end-to-end length L is a parameter that is estimated by visually bringing the predictions for dead cell suspensions into agreement with the experimental data. Since we are interested in order of magnitude estimates for this and the other free parameters α and ϕ_m in the model, a more rigorous least-squares fit was not pursued. The estimation of the parameter λ is not independent of the maximum packing fraction ϕ_m. While $\phi_m \approx 0.63$ is often used for spheres, there is no consensus on its value for anisotropic rod-like particles. It has been shown that ϕ_m for such systems depends

Published on 30 April 2015. Downloaded by Monash University on 13/05/2015 22:47:32.

on particle aspect ratio for dilute systems.[32] More concentrated suspensions of rod-like particles undergo an isotropic-to-nematic transition which is expected to occur at $\phi \sim O((L/d)^{-1})$ at equilibrium.[32,42] The aspect ratios (based on the total end-to-end length; Table 1) of all three species are quite large. The concentrations of the algal and bacterial suspensions in our experiments are thus possibly well above the isotropic–nematic transitions for those systems. Although the volume fractions of the sperm suspensions are low, significant orientational effects due to interparticle interactions cannot be ruled out due to their large aspect ratios. A value of $\phi_{\text{m}} = 0.7$ gives reasonable agreement of model prediction with dead cell data for all three species. With λ and ϕ_{m} determined in this manner, α is estimated to match predictions for live cells with experimental data for $\bar{\eta}_{\text{rel}}$.

How reasonable are the values in Table 1 of the key free parameters: the prefactor α in eqn (7) for the active dipole, and the ratio λ of the hydrodynamic length to the total head–tail length of a swimmers? If both these parameters are set to unity, the values of the activity $\tilde{\sigma}$ are too low for all three species and predictions for live and dead cell suspensions are virtually indistinguishable, and these predictions are substantially different from the experimental data (dashed curves in Fig. 4C(i–iii)). The values of $\lambda \lesssim O(1)$ required to obtain agreement with experiment appear reasonable given that flagella are never fully stretched out in swimming cells. Hydrodynamic interactions between the head and tail cause the parameter α to be strongly geometry dependent. This can be seen by modeling a flagellar swimmer modeled as an asymmetric rigid dumbbell with Stokeslets of different hydrodynamic radii located at the head and tail respectively (Appendix A).[43] We obtain for such a dumbbell $\alpha = 12(L_{\text{ht}}/L)^2/[(L_{\text{ht}}/a_{\text{h}}) - 3/2]$, where L_{ht} is the distance between the head and tail centres and a_{h} is the hydrodynamic radius of the head. Although finite-size corrections can be expected to modify the singular behaviour when $L_{\text{ht}}/a_{\text{h}} = 3/2$, this result suggests that α can vary over a wide range depending on the ratio L_{ht} and a_{h}. Viewed in this light, the variation in values of α for the three very differently shaped cells appears plausible.

It if further possible to estimate propulsive forces (using the definition of $\tilde{\sigma}$ in eqn (7) and its values in Table 1) as $F = \sigma/L_{\text{h}}$. Bayly *et al.*[44] analyzed the flagellar stroke of a single *C. reinhardtii* using resistive force theory to estimate an average power dissipation of about 5 fW, which when combined with an average speed of around 40 μm s^{-1} in that species,[13] yields F = 125 pN. Drescher *et al.*[4] estimated a propulsive force of F = 0.43 pN directly in a wild-type *E. coli* cell by measuring the flow field around it during a straight run. Schmitz *et al.*[45] used a microprobe to measured the force required to stall the motion of a bull sperm flagellum to be F = 250 pN. These values from direct single cell or flagellum measurements are comparable to the values of F in Table 1.

The predictions of $\bar{\eta}_{\text{rel}}$ in the bottom panel of Fig. 4 were generated using the KDE after first calculating the intrinsic viscosities $[\bar{\eta}]$ with eqn (5) for the ranges of Péclet numbers observed for live and dead cells. The Péclet numbers calculated as $\text{Pe} = \dot{\varepsilon}_{\text{avg}}D_{\text{r}}$ with the rotational diffusivities for live cells in Table 1 are plotted in Fig. 5(a). The Péclet number governs the competition between flow and diffusion and the values of $\text{Pe} \gg 1$ in Fig. 5(a) indicate that the flow completely overcomes the tendency for diffusion to make the orientational distribution isotropic and that particles are aligned along the principal stretching axis of the uniaxial extensional flow. It is typically expected that at such high values of Pe, the flow-induced dipole will dominate to such an extent that no difference between live and dead cells suspensions should be observed. How does one then explain the clear differences observed between live and dead samples in Fig. 4?

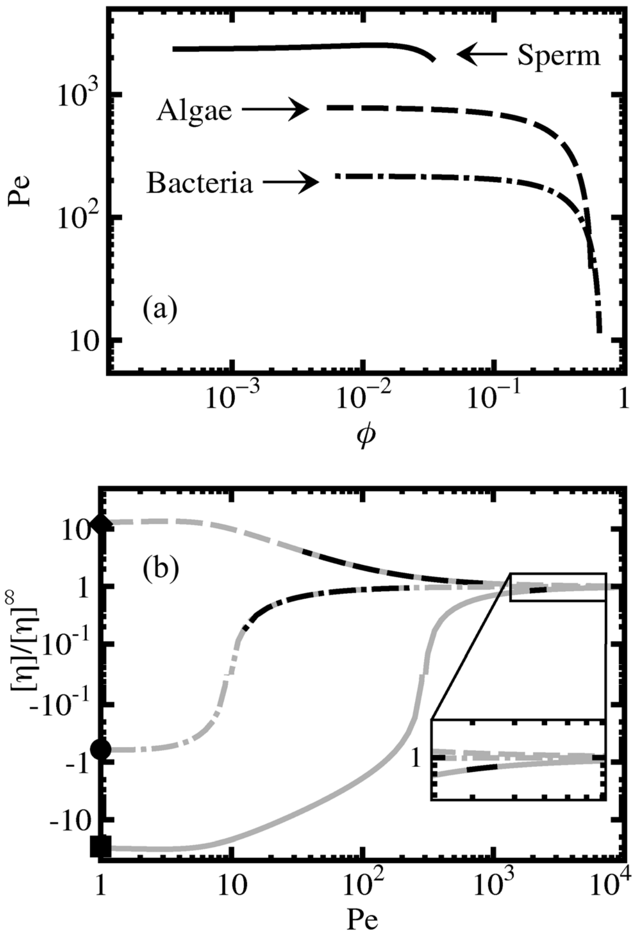

Fig. 5 (a) Experimentally observed variation of Pe with volume fraction in live samples; the curves have been obtained by polynomial regression of strain-rate data.† (b) Effect of flow strength on intrinsic viscosity of live cell suspensions of sperm (continuous), algae (dashed) and bacteria (dot-dashed curve): the black portions of the curves represent the experimentally observed Pe values in (a); the filled symbols on the co-ordinate axis represent the zero-Pe limit $[\bar{\eta}]^0/[\bar{\eta}]^\infty$ obtained with the model parameters in Table 1.

To answer this question, we firstly note that the small rotational diffusivities (Table 1) of dead cells mean that their Péclet numbers are very large for all the three species and across the entire range of volume fractions studied. In fact, the values of $[\bar{\eta}]$ for dead cells are nearly identical to the value $[\bar{\eta}]^\infty = 2\tilde{\chi}/3$ in the limit $\text{Pe} \to \infty$ purely due to the flow-induced dipole. The Péclet numbers of the live samples on the other hand, while still high, are much smaller than those of the dead samples at the same volume fraction. Fig. 5(b) plots as a function

Published on 30 April 2015. Downloaded by Monash University on 13/05/2015 22:47:32.

of Pe the ratio of $[\bar{\eta}]$ for the live samples with the value of $[\bar{\eta}]^{\infty}$ for the dead cells of that species. The curves have been generated using the parameters in Table 1; the portions of the curves in the range of live-cell Pe in the experiments in Fig. 5(a) are shown in black in Fig. 5(b). The plots show that the magnitude of the parameter $\tilde{\sigma}$ in an active suspension can be such that the contribution of propulsive dipole can still be relatively large even when Pe $\gg$ 1 and cells are highly aligned by the flow. Therefore, $[\bar{\eta}]/[\bar{\eta}]^{\infty}$ is significantly different from unity and live and dead cell samples have clearly different viscosities even over the range of experimentally observed Pe values. Moreover, with increasing cell volume fraction, not only are there more cells per unit volume contributing propulsive stresses, the strain-rate and Pe numbers decrease (Fig. 5(a)) boosting the relative contribution of active dipole.

The effect of activity on $\bar{\eta}_{\text{rel}}$ in Fig. 4 appears strongest in algae because of the combination of a large propulsive dipole and particle concentrations. The dipole is much weaker in *E. coli* pushers, leading to a smaller effect of activity, although they have the largest swimming diffusivity and lowest Pe values among the three species. In contrast, $\tilde{\sigma}$ in sperm appears to be so large that their live suspensions show a clearly measurable effect of motility even at very low cell densities and despite very large Pe values.

Interestingly, in the bottom panel of Fig. 4, a maximum is predicted by the model for live *E. coli* suspensions. This is because the projected Pe at high concentrations decreases to low enough values at which $[\bar{\eta}]$ for *E. coli* falls rapidly (Fig. 5(b)). In fact, at even lower Pe values, the negative values of $\tilde{\sigma}$ for the pushers *E. coli* and sperm are predicted to lead to negative $[\bar{\eta}]$ (Fig. 5(b)), which will result in live cell suspensions being less viscous than the suspending medium. This intriguing effect has been predicted previously in a number of theoretical studies.[6–8,29] Although such low strain-rates cannot be practically realized with extensional rheometers currently, they are accessible in shear rheometers. Gachelin *et al.*[11] recently reported this effect with *E. coli* suspensions in a microfluidic shear rheometer. Fig. 5(b) shows that the effect is likely to be much more dramatic at with sperm suspensions at low Pe: in extensional flows, the parameters we have obtained for sperm lead to a very large negative zero-Pe limit $[\bar{\eta}]^0 = \tilde{\chi}(2/9 + \tilde{\beta}/15(\tilde{\gamma} + \tilde{\sigma} - 1/\tilde{\beta})) = -1.9 \times 10^3$.

The model presented here is but a first step towards a more complete understanding of the role of concentration on the extensional rheology of active particle suspensions. The use of the KDE to model the effect of concentration has its limitations. It does not for instance directly take into account changes in particle motility in pusher suspensions brought about by the emergence of large-scale coherent structures and collective motion due to inter-particle hydrodynamic interactions.[12,46,47] However, although U and D_{r} in Saintillan's equations for $[\bar{\eta}]$ in principle describe the motility of isolated swimmers, it may be possible to use concentration-dependent average speeds and long-time diffusivities measured in non-dilute suspensions as particles execute collective motion.

Another limitation is that the KDE cannot predict non-monotonic concentration dependence when all other parameters including the strain-rate are held fixed. Ryan *et al.*[29] used simulations of swimming hydrodynamic dipoles with short-range excluded-volume repulsion to show that the shear viscosity of pusher suspensions can display a minimum with respect to concentration at a fixed shear-rate. As pointed out earlier, if the active dipole $\tilde{\sigma}$ is strongly negative, the intrinsic viscosity can be negative in pusher suspensions. In such a case, the viscosity decreases linearly with concentration in the dilute regime. The contribution to the viscosity due to pair-wise excluded-volume repulsions between particles on the other hand always increases more strongly with concentration. The initial decrease with concentration is thus followed by an increase at higher concentration with a minimum at a particular concentration. Such behaviour has been observed in experiments with *E. coli* by Gachelin *et al.*[11] Negative intrinsic viscosities nevertheless do not always occur in pushers, as shown in Fig. 5(b). In either shear or extensional flows, the intrinsic viscosity is positive above a critical strain-rate whose value depends on the effective rotational diffusivity and the magnitude of the active dipole.[6,8] For pullers, and obviously for passive suspensions or dead cells, the intrinsic viscosity is always positive. In all these cases, the KDE-based model provides a good semi-empirical description of the monotonic growth of viscosity with concentration.

5 Conclusions

Our experimental observations with a surface-acoustic-wave driven microfluidic rheometer indicate that particle motility has a clearly measurable influence on the rheology of suspensions. Capillary thinning of liquid bridges proceeded more slowly in suspensions of algal pullers than those of dead cells at the same volume fraction, whereas bacterial and sperm pushers tended to hasten thinning. The difference in the effective viscosity between suspensions of live and dead cells was found to systematically increase with concentration.

Predictions with a model that combined the Krieger–Dougherty equation for the relative viscosity of suspensions with an equation derived by Saintillan[7] for the intrinsic extensional viscosity of active suspensions were found to be in good qualitative agreement with the experimental observations. Our results show that the propulsive dipole even in weak swimmers such as *E. coli* can contribute significantly to fluid stresses even at high Péclet numbers when flow dominates over swimming noise. While parameters such as the properties of the suspending medium, the physical dimensions of the cells, and their swimming speeds and effective rotational diffusivities could be determined from independent measurements, model predictions appear to depend crucially on hydrodynamic details such as the effective hydrodynamic length of the swimmer and the contribution of hydrodynamic interactions between the head and tail to the propulsive dipole moment. Values of these parameters required to match predictions with experimental data lead to estimates for propulsive forces in the three species that are in line with data in literature on direct force measurements with single cells or flagella.

Published on 30 April 2015. Downloaded by Monash University on 13/05/2015 22:47:32.

The principal advantages of using the Krieger–Dougherty equation to model the influence of particle concentration are its simplicity, and that it enables comparison of the rheological behaviour of different active or passive suspensions in terms of a few quantitative parameters. The agreement between predictions and experiments suggests that improved models for non-dilute active suspensions may be derived by combining more accurate alternatives of the Krieger–Dougherty equation for describing concentration effects with refinements of the dilute solution theory for active suspensions that account for the hydrodynamic characteristics of swimming particles and their propulsion. Such models open up the possibility of routinely and precisely extracting propulsive forces in motile cells by rheometry of active suspensions.

A Self-propelled asymmetric dumbbells

A swimmer is modeled as a rigid asymmetric dumbbell with Stokeslets of hydrodynamic radii a_h and a_t located at the hydrodynamic centres of the head and tail respectively.[43] The rigid swimmer translates with a velocity $\mathbf{u}$ relative to the unperturbed ambient fluid as a result of the actuation of the tail (Fig. 6). The tail generates a thrust of $\mathbf{F}_p$. The total hydrodynamic force on the tail is the sum of $\mathbf{F}_p$ and its frictional resistance to the translational motion:

$$\mathbf{F}_t = -\zeta_t(\mathbf{u} + \boldsymbol{\Omega}\cdot\mathbf{F}_h) + \mathbf{F}_p, \tag{12}$$

where $\zeta_t = 6\pi a_t \eta_s$ is the drag coefficient of the tail and $\boldsymbol{\Omega}$ is the tensor describing the hydrodynamic interaction tensor between the head and tail such that the velocity perturbation at the tail due to the hydrodynamic force $\mathbf{F}_h$ on the head is $-\boldsymbol{\Omega}\cdot\mathbf{F}_h$.[48] The head only experiences frictional resistance, and

$$\mathbf{F}_h = -\zeta_h(\mathbf{u} + \boldsymbol{\Omega}\cdot\mathbf{F}_t). \tag{13}$$

The total hydrodynamic force on the inertialess swimmer must be zero in the absence of external forces:

$$\mathbf{F}_h + \mathbf{F}_t = 0. \tag{14}$$

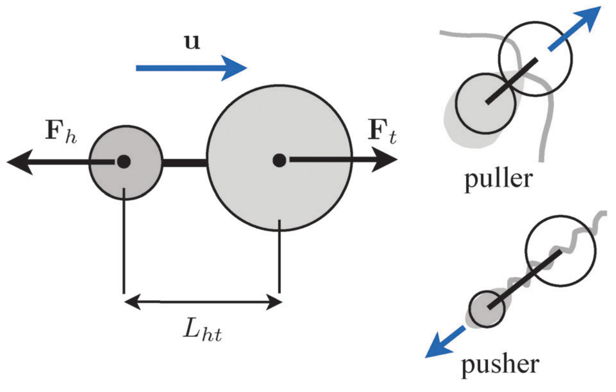

Fig. 6 Self-propelled asymmetric dumbbell model of a microswimmer with a flagellar tail.

The three equations above can be solved for $\mathbf{F}_h$, $\mathbf{F}_t$ and $\mathbf{F}_p$, given the frictional characteristics (ζ_h, ζ_t and $\boldsymbol{\Omega}$) and the velocity $\mathbf{u}$. Assuming that all forces and the velocity are directed along the axis of the dumbbell, if $\mathbf{F}_h$, $\mathbf{F}_t$ and $\mathbf{F}_p$, and $\mathbf{u}$ are the axial force and velocity components, we obtain,

$$\mathbf{F}_t = -\mathbf{F}_h = \frac{\zeta_h}{1 - \boldsymbol{\Omega}\zeta_h}\mathbf{u}, \tag{15}$$

where $\boldsymbol{\Omega} = 1/(4\pi\eta_s L_p)$ for Oseen–Burgers hydrodynamic interaction, and L_p is the distance between the head and tail centres. The magnitude of propulsive dipole is then

$$|\sigma| = |\mathbf{F}_h|L_p = \frac{12(\pi/2)\eta_s {L_p}^2|\mathbf{u}|}{(L_p/a_h) - (3/2)}. \tag{16}$$

With α defined as before *i.e.* $|\sigma| = (\pi/2)\alpha\eta_s L^2|\mathbf{u}|$ where L is the total end-to-end length of the swimmer, we obtain

$$\alpha = \frac{12(L_p/L)^2}{(L_p/a_h) - (3/2)}. \tag{17}$$

Acknowledgements

The authors thank Sharadwata Pan (IITB-Monash Research Academy, Mumbai, India), David Hill (University of Melbourne, Australia) and Michael K. Danquah (Curtin University, Sarawak, Malaysia) for training AGM in microbiological techniques for culturing and preparing live/dead-cell suspensions of *E. coli* and *D. tertiolecta*.

References

1 D. Chen, A. Lau, L. Hough, M. Islam, M. Goulian, T. Lubensky and A. Yodh, *Phys. Rev. Lett.*, 2007, **99**, 148302.
2 S. Ramaswamy, *Annu. Rev. Condens. Matter Phys.*, 2010, **1**, 323–345.
3 M. C. Marchetti, J. Joanny, S. Ramaswamy, T. B. Liverpool, J. Prost, M. Rao and R. A. Simha, *Rev. Mod. Phys.*, 2013, **85**, 1143–1189.
4 K. Drescher, J. Dunkel, L. H. Cisneros, S. Ganguly and R. E. Goldstein, *Proc. Natl. Acad. Sci. U. S. A.*, 2011, **108**, 10940–10945.
5 Y. Hatwalne, S. Ramaswamy, M. Rao and R. Simha, *Phys. Rev. Lett.*, 2004, **92**, 118101.
6 B. Haines, A. Sokolov, I. Aranson, L. Berlyand and D. Karpeev, *Phys. Rev. E: Stat., Nonlinear, Soft Matter Phys.*, 2009, **80**, 041922.
7 D. Saintillan, *Phys. Rev. E: Stat., Nonlinear, Soft Matter Phys.*, 2010, **81**, 056307.
8 D. Saintillan, *Exp. Mech.*, 2010, **50**, 1275–1281.
9 D. Saintillan and M. J. Shelley, *C. R. Phys.*, 2013, **14**, 497–517.
10 A. Sokolov and I. Aranson, *Phys. Rev. Lett.*, 2009, **103**, 148101.
11 J. Gachelin, G. Miño, H. Berthet, A. Lindner, A. Rousselet and E. Clement, *Phys. Rev. Lett.*, 2013, **110**, 268103.
12 R. Karmakar, R. Gulvady, M. S. Tirumkudulu and K. V. Venkatesh, *Phys. Fluids*, 2014, **26**, 071905.

Published on 30 April 2015. Downloaded by Monash University on 13/05/2015 22:47:32.

13 S. Rafaï, L. Jibuti and P. Peyla, *Phys. Rev. Lett.*, 2010, **104**, 098102.
14 E. A. Gaffney, H. Gadêlha, D. J. Smith, J. R. Blake and J. C. Kirkman-Brown, *Annu. Rev. Fluid Mech.*, 2011, **43**, 501–528.
15 P. K. Bhattacharjee, A. G. McDonnell, R. Prabhakar, L. Y. Yeo and J. R. Friend, *New J. Phys.*, 2011, **13**, 023005.
16 R. R. L. Guillard and J. H. Ryther, *Can. J. Microbiol.*, 1962, **8**, 229–239.
17 G. M. Gibbs, G. Orta, T. Reddy, A. J. Koppers, P. Martínez-López, J. L. de la Vega-Beltrán, J. C. Lo, N. Veldhuis, D. Jamsai, P. McIntyre, A. Darszon and M. K. O'Bryan, *Proc. Natl. Acad. Sci. U. S. A.*, 2011, **108**, 7034–7039.
18 G. McKinley and T. Sridhar, *Annu. Rev. Fluid Mech.*, 2002, **34**, 375–415.
19 P. Szabo, *Rheol. Acta*, 1997, **36**, 277–284.
20 G. McKinley and A. Tripathi, *J. Rheol.*, 2000, **44**, 653–670.
21 V. Entov and E. Hinch, *J. Non-Newtonian Fluid Mech.*, 1997, **72**, 31–53.
22 A. U. Chen, P. K. Notz and O. A. Basaran, *Phys. Rev. Lett.*, 2002, **88**, 174501.
23 D. C. Vadillo, T. R. Tuladhar, A. C. Mulji, S. Jung, S. D. Hoath and M. R. Mackley, *J. Rheol.*, 2010, **54**, 261–282.
24 D. C. Vadillo, W. Mathues and C. Clasen, *Rheol. Acta*, 2012, **51**, 755–769.
25 L. Campo-Deano and C. Clasen, *J. Non-Newtonian Fluid Mech.*, 2010, **165**, 1688–1699.
26 J. Arratia, P. E. Gollub and D. Durian, *Phys. Rev. E: Stat., Nonlinear, Soft Matter Phys.*, 2008, **77**, 36309.
27 W. C. Nelson, H. P. Kavehpour and C.-J. Kim, *Lab Chip*, 2011, **11**, 2424–2431.
28 J. Eggers and T. F. Dupont, *J. Fluid Mech.*, 1994, **262**, 205–221.
29 S. D. Ryan, B. M. Haines, L. Berlyand, F. Ziebert and I. S. Aranson, *Phys. Rev. E: Stat., Nonlinear, Soft Matter Phys.*, 2011, **83**, 050904.
30 I. M. Krieger and T. Dougherty, *J. Rheol.*, 1959, **3**, 137–152.
31 R. C. Ball and P. Richmond, *Phys. Chem. Liq.*, 1980, **9**, 99–116.
32 R. G. Larson, *The Structure and Rheology of Complex Fluids*, Oxford University Press, Oxford, 1999.
33 A. M. Wierenga and A. P. Philipse, *Colloids Surf., A*, 1998, **137**, 355–372.
34 B. H. Tan, K. C. Tam, Y. C. Lam and C. B. Tan, *J. Rheol.*, 2004, **48**, 915–926.
35 E. Hinch and L. Leal, *J. Fluid Mech.*, 1976, **76**, 187–208.
36 G. K. Batchelor, *J. Fluid Mech.*, 1970, **44**, 419–440.
37 B. ten Hagen, S. van Teeffelen and H. Löwen, *J. Phys.: Condens. Matter*, 2011, **23**, 194119.
38 J. Saragosti, P. Silberzan and A. Buguin, *PLoS One*, 2012, **7**, e35412.
39 S. T. Mortimer, *Hum. Reprod. Update*, 1997, 403–409.
40 H. Qi, M. M. Moran and B. Navarro, *Proc. Natl. Acad. Sci. U. S. A.*, 2007, **104**, 1219–1223.
41 S. D. Olson, S. S. Suarez and L. J. Fauci, *J. Theor. Biol.*, 2011, **283**, 203–216.
42 M. Doi and S. F. Edwards, *The Theory of Polymer Dynamics*, Oxford University Press, 1986.
43 J. Dunstan, G. Miño, E. Clement and R. Soto, *Phys. Fluids*, 2012, **24**, 011901.
44 P. V. Bayly, B. L. Lewis, E. C. Ranz, R. J. Okamoto, R. B. Pless and S. K. Dutcher, *Biophys. J.*, 2011, **100**, 2716–2725.
45 K. A. Schmitz, D. L. Holcomb-Wygle, D. J. Oberski and C. B. Lindemann, *Biophys. J.*, 2000, **79**, 468–478.
46 G. Subramanian and D. L. Koch, *J. Fluid Mech.*, 2009, **632**, 359–400.
47 A. A. Pahlavan and D. Saintillan, *Phys. Fluids*, 2011, **23**, 011901.
48 R. B. Bird, C. F. Curtiss, R. C. Armstrong and O. Hassager, *Dynamics of Polymeric Liquids*, Wiley-Interscience, New York, 2nd edn, 1987, vol. 2, Kinetic theory.

Electronic Supplementary Material (ESI) for Soft Matter.
This journal is © The Royal Society of Chemistry 2015

Supplementary Material for: “Motility induced changes in viscosity of suspensions of swimming microbes in extensional flows”

(Dated: April 7, 2015)

I. CALIBRATION CURVE FOR THE ACOUSTICALLY DRIVEN MICROFLUIDIC EXTENSION RHEOMETER

A rational function of the following form is chosen to fit the experimental $t^*_{1/2}$-vs-Oh data:

$$t^*_{1/2} = \frac{K_0 + K_1\,\mathrm{Oh} + K_2\,\mathrm{Oh}^2}{1 + \mathrm{Oh}}\,. \tag{1}$$

With this expression, as Oh → 0, $t^*_{1/2} \to K_0$, and when Oh → ∞, $t^*_{1/2} \to K_2\,\mathrm{Oh}$.

To fix the constants K_0 and K_2, we consider a simple toy model. The thinning of perfectly cylindrical filaments can be modeled by an inertio-viscous capillary stress balance:(Entov and Hinch, 1997; McKinley and Sridhar, 2002; Rodd et al., 2005; Tirtaatmadja et al., 2006)

$$\frac{1}{2}\,\rho\dot{R}^2 = (2X - 1)\,\frac{\gamma}{R} + \frac{6\,\eta_s\,\dot{R}}{R}\,, \tag{2}$$

where X is the ratio of the instantaneous axial tension in the liquid bridge and $2\pi\gamma R$. If X is treated as a constant, the algebro-differential equation above can be treated as a quadratic equation above for $\dot{R}$ at any R and t. The negative root of the rescaled equation,

$$\frac{dR^*}{dt^*} = -\frac{6\,\mathrm{Oh}}{R^*}\left(\sqrt{1 + C\,R^*} - 1\right), \tag{3}$$

where $C = (2X - 1)/18$ can be integrated with $R^* = 1$ as the initial condition to obtain

$$t^*_{1/2} = \frac{1}{36\,C^2}\left[4\left\{\left(\mathrm{Oh}^2 + C\right)^{3/2} - \left(\mathrm{Oh}^2 + \frac{C}{2}\right)^{3/2}\right\} + 3\,C\,\mathrm{Oh}\right]. \tag{4}$$

The equation recovers the expected results in the limits Oh → 0 where $t^*_{1/2}$ approaches a constant ($= (2^{3/2} - 1)/(6\sqrt{2X - 1})$), and when Oh → ∞ where $t^*_{1/2}$ increase linearly with Oh ($t^*_{1/2} \to 3\,\mathrm{Oh}/(2X - 1)$).

Strictly speaking, X itself depends on time; it has been shown however that, if the neck diameter is significantly smaller than the two drops at the end plates, the axial filament profile and its dynamics can be well approximated as being self-similar. As mentioned earlier, we begin taking measurements of R only after the neck is well formed with a radius about half the drop radius at the end-plate. The values of X given by similarity solutions under different conditions have been summarized by McKinley and Tripathy(McKinley and Tripathi, 2000). When inertia is important and Oh ≪ 1, $X = 0.5912$ is the value most likely to be observed in an experiment(McKinley and Tripathi, 2000; Eggers, 1997a,b) and hence $t^*_{1/2} \to 0.7135$ as

Oh → 0. When viscosity is dominant on the other hand, $X = 0.7127$(McKinley and Tripathi, 2000; Papageorgiou, 1995) and $t^*_{1/2} \to 7.0522\,\mathrm{Oh}$ as $\mathrm{Oh} \to \infty$.

These asymptotic predictions suggest therefore the values of $K_0 = 0.7135$ and $K_2 = 7.0522$ in in Eqn. (1) for the empirical calibration curve. Although the model presented above is expected to be accurate only when the axial curvature of the filament is small, we surprisingly find good agreement of the asymptotic behaviours predicted with the experimental data shown in Fig. 2 of the main text. We therefore use the values above for K_0 and K_2 in Eqn. (1) and determine $K_1 = 14.7 \pm 0.2$ by linear regression of the curve through the experimental $t^*_{1/2}$-vs-Oh data. The reasons behind this good agreement with the asymptotic trends predicted by the toy model are unknown. It is possible that this is a fortuitous result of the combination of the liquid-bridge aspect ratio, the Bond number and the range of Oh values in our experiments. A different choice of these parameters may require K_0 and K_2 also to be determined by regression.

II. CAPILLARY THINNING DATA FOR CELL SUSPENSIONS

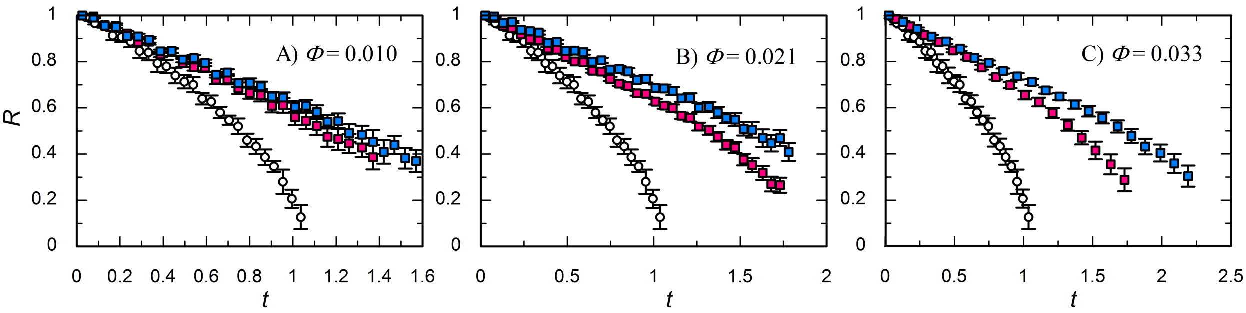

FIG. 1. Capillary thinning of liquid bridges of mouse sperm suspensions

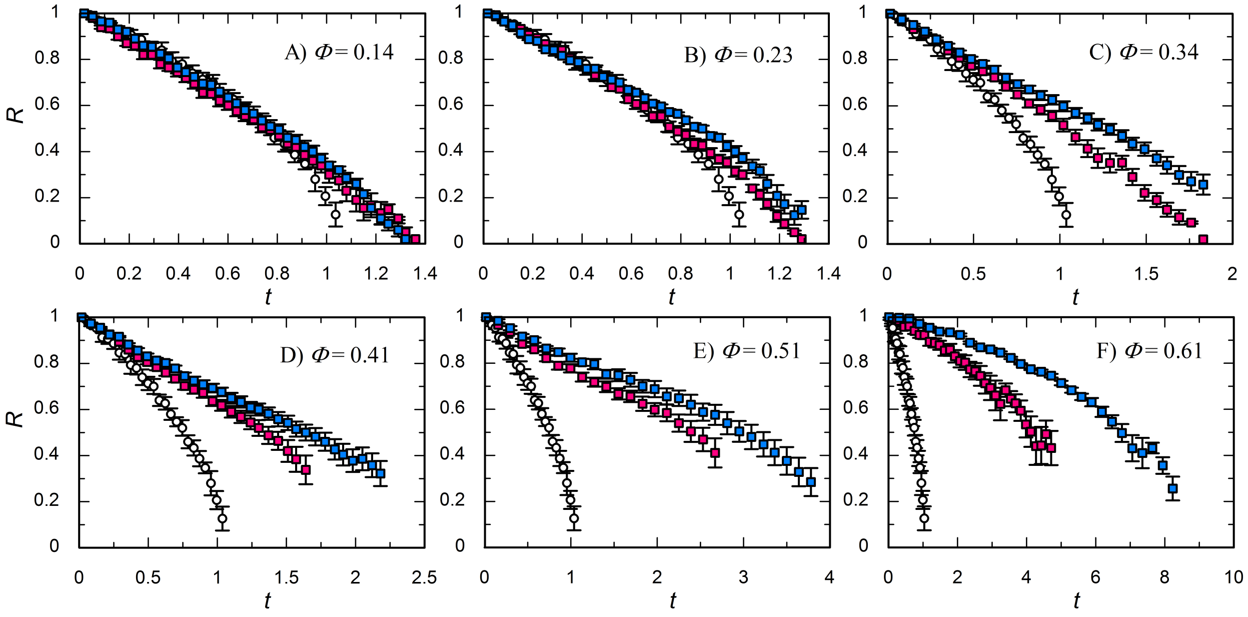

FIG. 2. Capillary thinning of liquid bridges of suspensions of *E. coli*

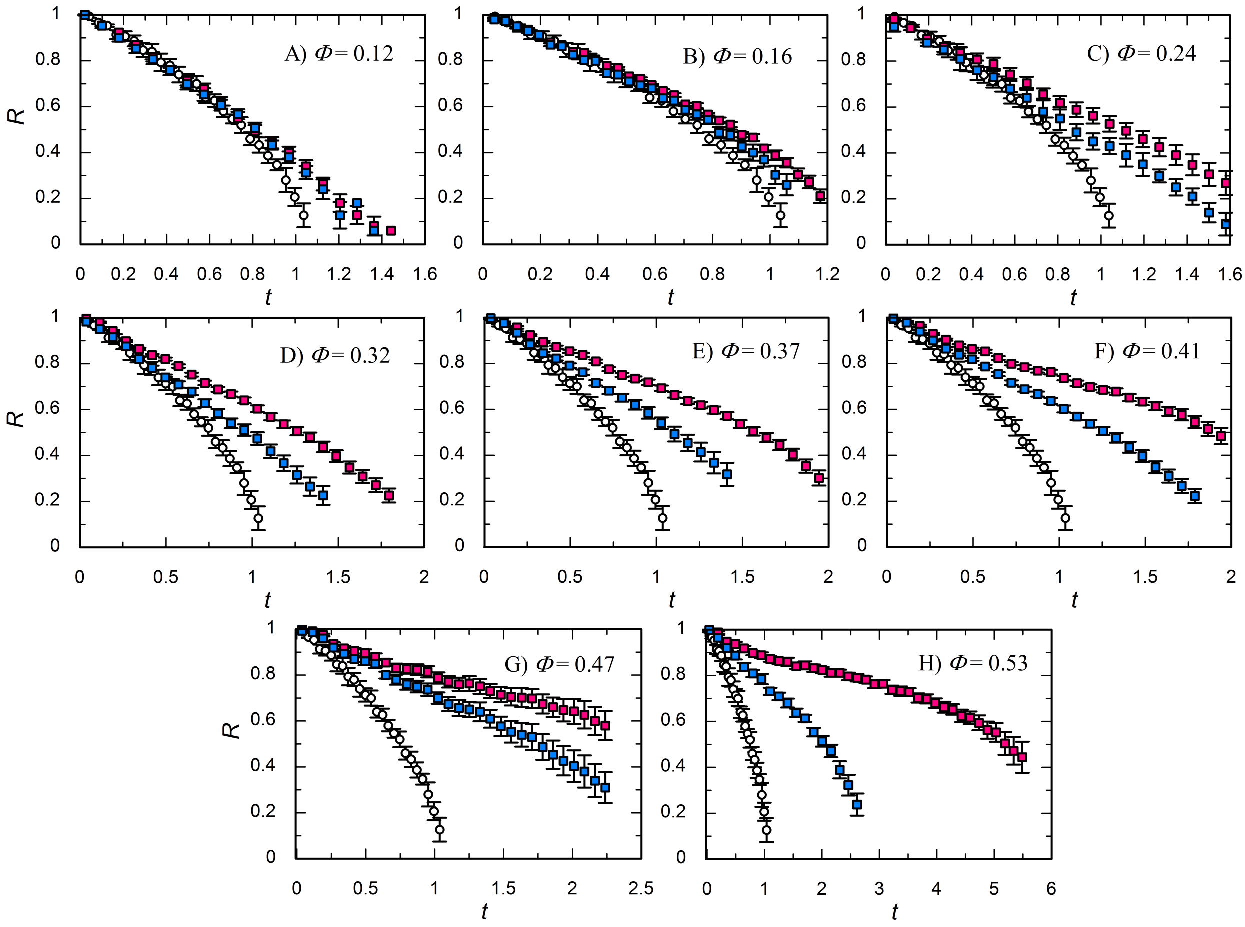

FIG. 3. Capillary thinning of liquid bridges of suspensions of *D. tertiolecta*; red, blue and white symbols correspond to live and dead cell suspensions, and pure buffer, respectively.

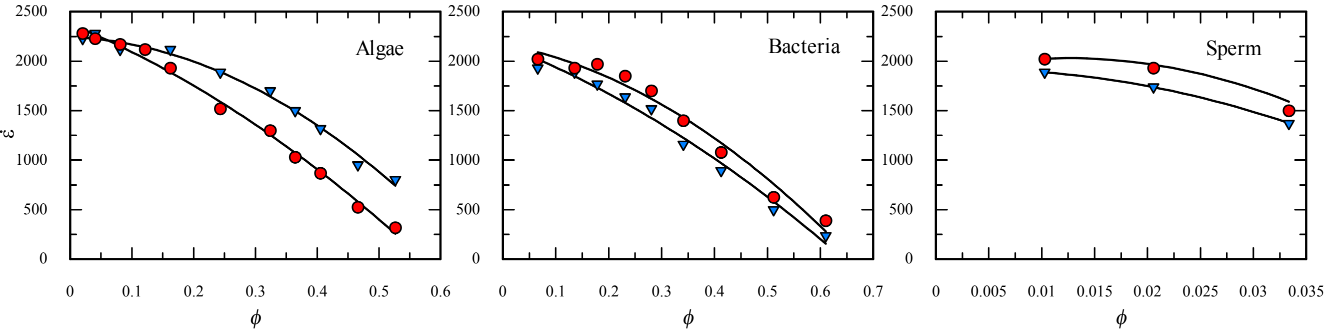

FIG. 4. Strain-rate variation with volume fraction of live (red circles) and dead (blue triangles) cell suspensions; smooth curves are cubic polynomial fits through data.

III. ADDITIONAL INFORMATION FOR THE VISCOSITY MODEL

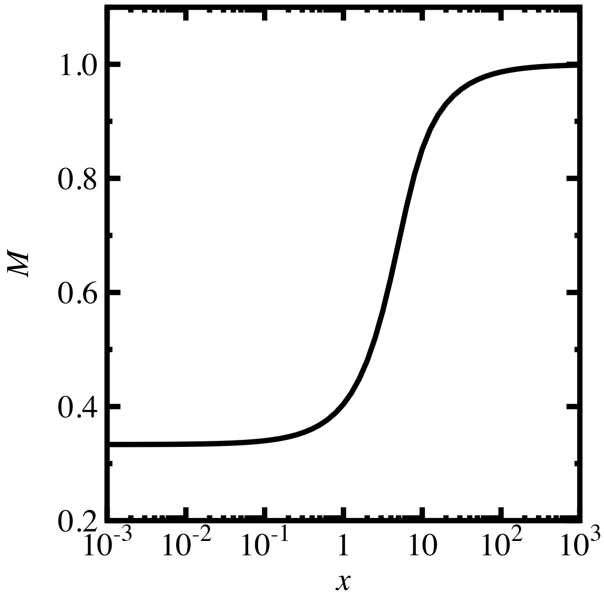

FIG. 5. The function $M(x)$

The function (Fig. 5)

$$M(x) = \frac{1}{2\,x\,D(x)} - \frac{1}{2\,x^2}\,, \tag{5}$$

where $D(x) = \exp(-x^2)\int_0^x \exp(y^2)\,dy$ is Dawson's integral. In the equation for the intrinsic extensional viscosity in the main text, $x = \sqrt{3\,\widetilde{\beta}\,\mathrm{Pe}/4}$. As $x \to 0$, $M = 1/3 + 4/45\,x^2 + O(x^4) = 1/3 + \widetilde{\beta}\mathrm{Pe}/15 + O(\mathrm{Pe}^2)$, and when $x \to \infty$, $M(x) = 1 - x^{-2} + O(x^{-4}) = 1 - 4/(3\widetilde{\beta}\mathrm{Pe}) + O(\mathrm{Pe}^{-2})$.

V.M. Entov and E.J. Hinch. Effect of a spectrum of relaxation times on the capillary thinning of a filament of elastic liquid. *J. Non-Newtonian Fluid Mech.*, 72:31–53, 1997.

G.H. McKinley and T. Sridhar. Filament-stretching rheometry of complex fluids. *Annu. Rev. Fluid Mech.*, 34:375–415, 2002.

L.E. Rodd, T. P. Scott, and G. H. Cooper-White, J. J.; McKinley. Capillary break-up rheometry of low-viscosity elastic fluids. *Appl. Rheol.*, 15:12–27, 2005.

V. Tirtaatmadja, G. H. McKinley, and J. J. Cooper-White. Drop formation and breakup of low viscosity elastic fluids: Effects of molecular weight and concentration. *Phys. Fluids*, 18:043101, 2006.

G.H. McKinley and A. Tripathi. How to extract the Newtonian viscosity from capillary breakup measurements in a filament rheometer. *J. Rheol.*, 44:653–670, 2000.

J. Eggers. Universal pinching of 3D axisymmetric free-surface flows. *Phys. Rev. Lett.*, 71:3458–3490, 1997a.

J. Eggers. Nonlinear dynamics and breakup of free-surface flows. *Rev. Mod. Phys.*, 69:865–930, 1997b.

D. T. Papageorgiou. On the breakup of viscous liquid threads. *Phys. Fluids*, 7:1529–1544, 1995.

Chapter 6

Extensional properties of low-viscosity particle suspensions

The newly developed technique and extensional viscosity extraction approach, complemented by standard shear analysis, is used in this chapter to analyse the properties of particle suspensions with different morphologies that, unlike the swimming particles discussed above, are "passive". We witness strong particle size and shape related behaviour and perform a cursory study on the potential role that particle clustering may play on suspension viscosity. These observations support what little experimental extensional data there is for like suspensions and reinforces the suggestion that hydrodynamic effects alone cannot explain the observed effects on bulk fluid properties in full. Thus, we extract extensional viscosity data for these complex fluids, finding correlations with shear viscosities, and demonstrate that this experimental technique may be applied to the tailoring of particle suspensions to facilitate the development of suspensions of nano/micro particles as inks and coatings.

Protocols to produce silver particles were developed by Prof. Wenlong Cheng's group at Monash University, and Naveen N. Jason of said group produced the silver particles and performed the particle imaging used in this study. Literature review, experimental work (including preparation of glass particle suspensions), and analysis were conducted by Amarin G. M^{c}Donnell.

6.1 Introduction

Further validation of the ADMiER was pursued by comparing the extensional viscosities it measured against the quantitative results of an established extensional technique: CaBER. Validation was also sought be comparing the extensional viscosities of the SAW technique to the viscosities measurement *via* traditional shear experiments using well characterised particles; though it is stressed that directly relating extensional and shear viscosities is problematic for non-Newtonian fluids, as discussed in Sec. 1.1, and qualitative agreement was hoped for at best. The biological particles of Chapter 5, which possess irregular shapes, deformable bodies, and long flagella, would likely complicate stresses and interpretation; this is also true for the high-aspect ratio and flexible nanowire particles seen in Chapter 7. Therefore, we perform experiments using suspensions of rigid particles that are more easily characterised. These suspensions include synthesised metal particles, which are interesting in themselves for industrial purposes, and glass particles that act as reference systems.

Nanoparticles (NPs) are being used in wide-ranging applications including sunscreens, ceramic pigments, and motor oil [25], with the variety in particles available becoming so wide that a ‘periodic table’ of NPs has also been proposed [101]. However, the majority of recent research has primarily been aimed at the electronics industry, with high-precision conductive inkjet-printable and draw-able inks the subjects of particular focus [26, 102–109]. These are anticipated to enable the development of new flexible [30–32] and transparent electronics [110–116], leading to the development of deformable and transparent electrodes for solar panels [27–29], touch-screens [38, 117], and sensors [30–32, 108], for example. These materials also have the potential to enable electronic circuits to be quickly produced on varied substrates and eliminate the need for expensive and toxic lithography and metal etching processes, as well as the complex and hazardous processes used in traditional printed circuit board manufacturing methods [118]. Metal NPs like silver [26, 102–104], core-shell NPs such as Ag-Cu NPs [105], and high-aspect ratio particles like carbon nanotubes [106, 107] have been printed as electrically conductive inks using inkjet printing, which typically requires low viscosities in the vicinity of 2-20 mPa·s. However, other techniques have also been used, such as ballpoint pens [108], Meyer-Rod coating [119–121], spin coating [122], and even brush painting [123, 124]. The challenge of developing NP inks and coatings not only lies in the formation of the particles, but also in their bulk fluid properties, end application, method of delivery, and the target substrate; these considerations are coupled, and the endeavour is a balancing act between the core aims and the system compromises necessary to realise these aims. As a number of the aforementioned processes suggest, the industrial scale implementation of thin and uniform coatings or high precision component features composed of these suspensions would most likely be achieved *via* some form of spraying or jetting. Extensional flow dominates these processes, and is also a significant component in other processes, which complicates matters for two reasons. Firstly, these suspensions are likely to be non-Newtonian [125–127]. Secondly, these processes predominantly require low-viscosity fluids to function [52–54]. Such difficulties are exacerbated by the lack of extensional-flow experimental techniques that can accommodate low-viscosity fluids and quantify their extensional properties. In the absence of comprehensive extensional analysis, the development and application system optimization for NP inks could be a wasteful and expensive process, making the swift modification of such materials impractical.

The difficulties in performing extensional flow analysis of low-viscosity fluids and the limitations of alternative techniques that can include the requirement of larger samples sizes, limited accessible viscosity ranges, or incompatibility with particle suspensions are discussed in detail in Chapters 1, 3, 5, and 7. Thus, we employ the SAW actuated capillary break-up device, which can analyse the extensional properties of small volumes of low-viscosity fluids in conjunction with the varied particle types featured in this investigation. With it we perform the rheological characterisation of suspensions of a group of metallic and glass micro/nano particles with different morphologies. We detail the changes in extensional viscosity with regards to particle volume fraction for aqueous to highly viscous samples. The use of polymer additives and other dispersants is avoided altogether, which can be used to aid the suspension of dense particles [104, 105, 107, 108, 128, 129], so that only changes arising due to particle concentration effects are observed. We also make basic model predictions of viscosity for comparison and to draw phenomenological insights. We witness strong particle size and shape related behaviour and suggest an empirical relationship between relative viscosity and particle size for cuboidal particles. Further, we study the potential role that particle clustering may play on suspension viscosity *via* model predictions. These observations support what little experimental extensional data there is for like suspensions and reinforces the suggestion that hydrodynamic effects alone cannot explain the effects on bulk fluid properties in full. Most importantly we extract extensional viscosity data for these complex fluids, many of them with low viscosities, and demonstrate that this experimental technique may be applied to the tailoring of other particle suspensions to facilitate the development of micro/nano particle inks and coatings.

6.2 Methods

6.2.1 Particle selection and preparation

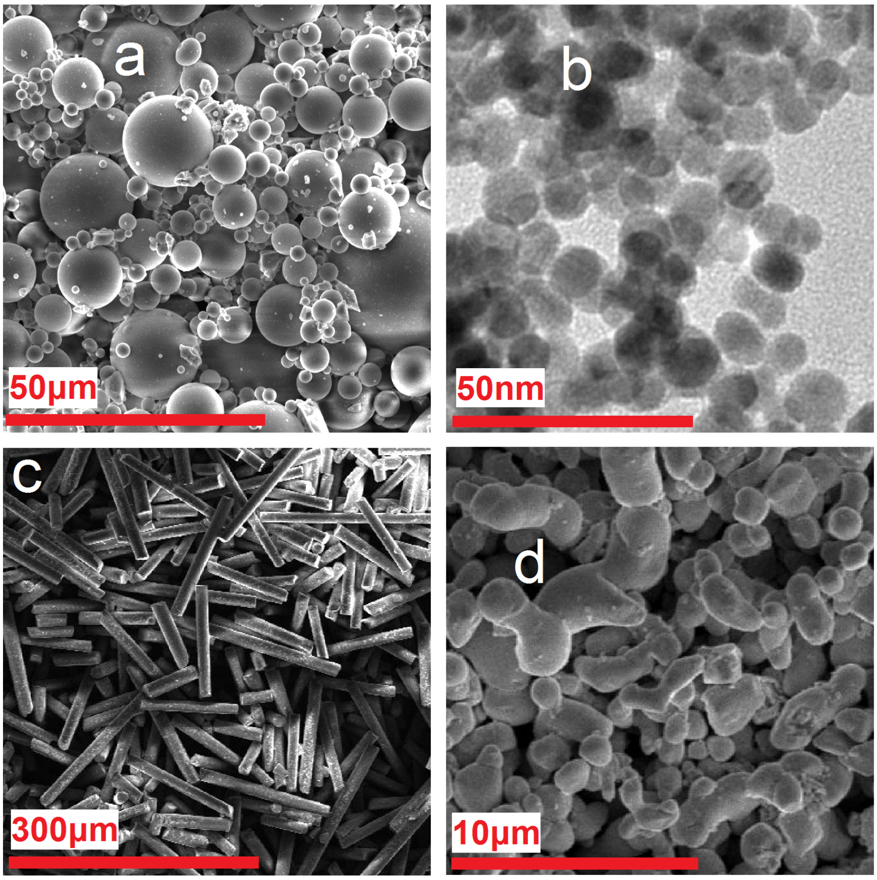

Fig. 6.1 (a) Hollow glass microspheres with diameters of 9-13 μm. (b) Silver nano particles of diameter 11.2 nm. (c) Glass micro fibres of diameter 13 μm and length of 155 μm. (d) Silver micro nuggets of 1.55 μm and 3.82 μm.

6.2.1.1 Glass micro beads

Since these larger glass particles (Fig. 6.1a) exhibit low particle aggregation (Fig. 6.2d) they were used as a reference for the modelling of purely hydrodynamic interaction predictions for spheres. They also provide validation of the extensional technique against other studies of cuboidal particles in extensional flow [45]. Here 9-13 μm hollow glass beads (Sigma, Aldrich) with a density of 1100 kg/m^3 were suspended in water (1 mPa·s).

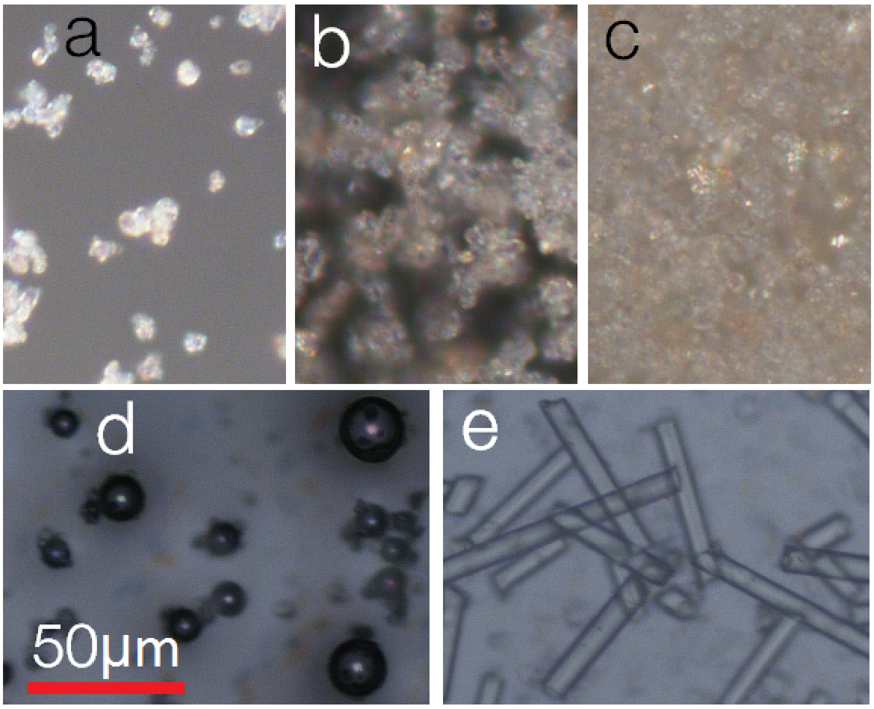

Fig. 6.2 (a) Ag MNs $\phi = 0.01$. (b) Ag MNs $\phi = 0.1$. (c) Ag MNs $\phi = 0.13$. (d) Glass beads $\phi = 0.01$. (e) Glass fibres $\phi = 0.01$.

6.2.1.2 Silver nano particles

In our experiments 50 nm silver nanoparticles (Ag NPs, Fig. 6.1b) were prepared, using the method described by Russo (2011) [108], by mixing 3.83 gm of poly(acrylic acid)(PAA - Sigma Aldrich), 80 gm of diethanolamine (DEA - Sigma Aldrich) with 100 ml of water in a 500 ml screw cap borosilicate bottle, and magnetically stirring at 1000 rpm at room temperature for 2 hours. Then 40 gm of $AgNO_3$ (Sigma Aldrich) dissolved in 30 ml of water was added drop-wise into the solution, and after 15 minutes the stirring speed was reduced to 400 rpm and stirred for 22 hours. The solution gradually turns dark black indicating formation of the 5 nm Ag NPs. The solution in the bottle was filled to 500 ml with ethanol, an anti-solvent to promote precipitation of the Ag NPs, and the bottle was put in a water bath with the cap loosely screwed on and heated at 70^{o}C for 1.5 hours. The majority of the Ag NPs can be seen to have settled to the bottom of the bottle, which are again re-dispersed by stirring for a few minutes. The solution was then centrifuged at 7500 rpm for 20 minutes. The Ag NPs neatly collected at the bottom of the tube revealing an iridescent bluish green mirror surface pellet. To wash the pellet it was again re-dispersed in ethanol, centrifuged, and the supernatant then discarded, a process that was repeated not more than 2-3 times in order to avoid the loss of particles. The pellets were then dried in an oven overnight at 60°C. The dried pellets were then crushed to a fine powder and suspended in 72.5%wt glycerine-water (38 mPa·s) solution.

6.2.1.3 Glass micro fibres

These rigid glass fibres (Fig. 6.1c) were used to validate modelling of rod-like particles since they do not exhibit the clustering seen in suspensions of smaller scale particles, see Fig. 6.2e. We used 14 by 155 µm glass fibres (Fibertec, MA, USA) that were suspended in 71%wt glycerine/water solution (24 mPa·s).

6.2.1.4 Silver micro nuggets

Silver micro-nuggets (Ag MNs, Fig. 6.1d) were prepared by heating 50 ml of Ethylene Glycol (Merck) in a 250 ml borosilicate screw-cap bottle for 1 hour at 150°C in an oil bath, with magnetic stirring at 260 rpm. The reactants were made in ethylene glycol (Sigma Aldrich) as solvent. To this 400 µL of 4 M $CuCl_22H_2O$ was added, and after 15 minutes 15 ml of 0.147 M polyvinylpyrrolidone (PVP)(Sigma Aldrich) was added. After 15 minutes 15 ml of 0.094 M $AgNO_3$ was added drop by drop and thereafter heated for 1.5 hours, and then the reaction was stopped. Ag MNs of dimensions 1.6 – 3.8 µm are formed and can be seen as a greyish white powder in the solution. The solution was cooled down to room temperature and centrifuged at 5000 rpm for 10 minutes. The supernatant was carefully decanted and the pellet was mixed again with ethanol and centrifuged. The ethanol wash was repeated 3 times and the ethanol was decanted, after which the Ag MNs were dried overnight in the oven at 60°C. The Ag MNs were then suspended in 81.5%wt glycerine-water (76mPa ·s) solution. Thicker buffer was required here since settling occurred quickly without higher viscosity, which is thought to be due to particle aggregation (Figs. 6.2a, b, and c).

6.2.2 Extensional and shear rheometry

The SAW actuated capillary break-up method for determining extensional viscosity that is used in this chapter is discussed in Chapters 2, 5, and 7. Shear viscosities were measured using the conventional system described in Chapter 7.

6.2.3 Particle imaging

High resolution images of dry particles were captured using the FEI Nova NanoSEM 450 FESEM. Optical images and videos of particles in their suspending medium were obtained using a Nikon Ni darkfield microscope. Optical imaging was not possible for the suspended Ag NPs as they are of nanometer dimensions and can only be resolved using electron microscopy, which operates under high vacuum conditions and must be liquid free.

6.3 Results and discussion

6.3.1 Krieger-Dougherty expression for extensional viscosity

In order to gain some insight into the changes in suspension extensional viscosity with particle concentration and size we use the Krieger-Dougherty expression (KDE). This expression is discssued and used in Chapter 5. In brief, the change in particle suspension viscosity as a function of concentration is commonly described by the KDE, seen in Eqn. 6.1 in its relative extensional viscosity $\bar{\eta}_{rel}$ form. It assumes a fluid is homogeneous and that it possesses a single viscosity, which increases above the solvent viscosity with the introduction of particles [130–132]. Each new particle is influenced by this single bulk viscosity and in turn incrementally contributes to it. It is widely recognised that the KDE expression is limited in its ability to provide detailed system information. Yet, it often empirically performs well, and is commonly used to describe particle suspension viscosity below the transition from fluid to solid-like slurry [45]. As a result, it sees common use due to the lack of more sophisticated expressions.

$$\bar{\eta}_{rel} = \frac{\bar{\eta}}{3\eta_s} = \left(1 - \frac{\phi}{\phi_m}\right)^{-[\bar{\eta}]\phi_m} \tag{6.1}$$

In Eqn. 6.1, η_s is the solvent shear viscosity, and ϕ is the particle volume fraction. ϕ_m represents the maximum packing fraction, which is the volume fraction at which no more particles can be suspended, at which point the material takes on semi-solid characteristics. Obtaining exact real-world values for this can be challenging and hence we use a common value for spheres of $\phi_m \approx 0.63$ when analysing our spherical particle samples. In the cases of the non-spherical particles in Sec. 6.3.3 we estimate ϕ_m from the value of ϕ at which samples take on a slurry-like consistency. The KDE exponent, $[\bar{\eta}]$, represents what is often described as the intrinsic viscosity, and was theoretically evaluated by Einstein to be 2.5 when purely accounting for hydrodynamic forces in the case of rigid spheres [130]. In Sec. 6.3.2.2, $[\bar{\eta}]$ is an adjustable parameter for fitting the KDE to experimental data in the absence of more sophisticated expressions for cuboid particles in extensional flow, as has been done by others [45]. However, in the case of particles with appreciable aspect ratio, Sec. 6.3.3.2, the $[\bar{\eta}]$ is determined by an intrinsic viscosity expression that accounts for variables such as extensional strain rate and particle dimensions [100] that has been used in the same fashion in Chapter 5. Thus, the KDE is used here to give basic quantification and insight into observed viscosity changes due to particle concentration and particle dimensions.

6.3.2 Cuboid particles

6.3.2.1 Comparison of shear and extensional viscosities

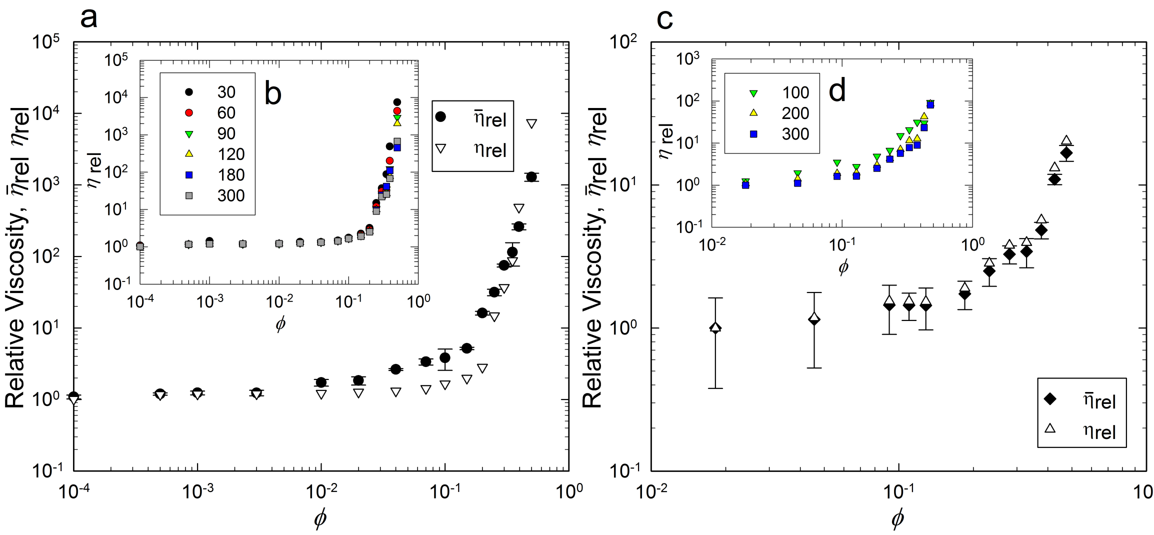

Fig. 6.3 (a) Ag NP suspension relative extensional and shear viscosity as a function of volume fraction. (b) Ag NP suspension relative shear viscosity against volume fraction for shear rates $\dot{\gamma}$ of 30, 60, 90, 120, 180, and 300 s^{-1}. (c) Glass bead suspension relative extensional and shear viscosity as a function of volume fraction. (d) Glass bead suspension relative shear viscosity against volume fraction for shear rates $\dot{\gamma}$ of 100, 200, and 300 s^{-1}. Note: Shear viscosity values in (a) and (c) correspond to comparable extensional and shear rates.

Figs. 6.3a and c show that the relative extensional and shear viscosities of these spherical particle suspensions largely increase together with increasing volume fraction, both rising sharply towards a commonly used maximum packing fraction for spheres of $\phi_m \approx 0.63$. These results show that although both types of suspensions have spherical particles, the viscosities of Ag NP particle suspensions increase much more quickly with volume fraction than they do for glass bead suspensions, showing order of magnitude differences. The possible reasons for this are explored further in Sec. 6.3.2.2. Notably, the relative extensional viscosity appears to be larger than the relative shear viscosity for Ag NPs across most of the range of volume fractions, but a crossover is observed at high strain rates. This is also

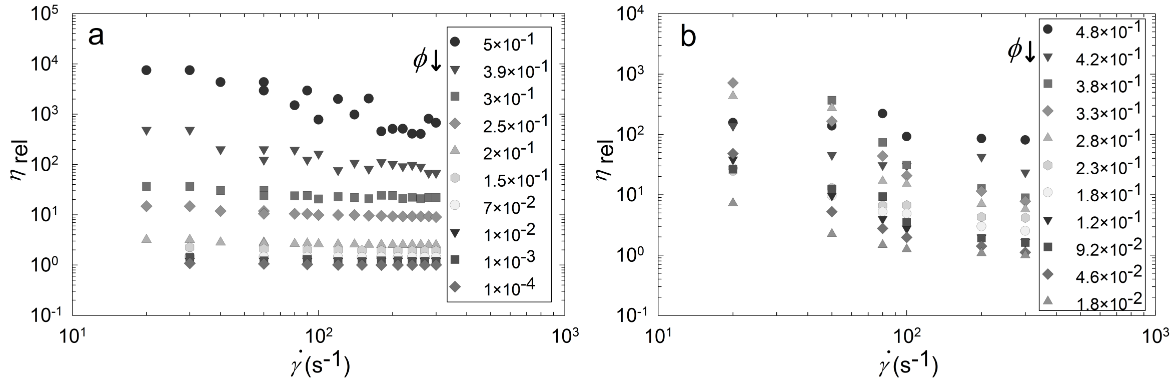

Fig. 6.4 Shear viscosity *versus* shear rate for different volume fractions for (a) Ag NP and (b) glass bead suspensions, with clear shear thinning exhibited in both cases.

observed in the nanowire particle-polymer mixtures discussed in Chapter 7. The reasons for this are not understood. Figs. 6.4a and b show clear shear thinning for both spherical particle suspensions, as is expected.

6.3.2.2 Concentration and size dependence of extensional viscosity

Fig. 6.5 shows relative extensional viscosity data for our spherical particles and those of the break-up of sand suspensions in CaBER experiments by Alexandrou (2009) [45]. Notably, these CaBER experiments on sand suspensions compare well with our glass bead suspensions, which share comparable particle dimensions. This illustrates the validity of our novel experimental technique in extracting extensional viscosities against an established method.

Fig. 6.5 also shows the relative extensional viscosity curve calculated by Einstein's prediction for rigid spheres, where $[\eta] = 2.5$ in the KDE, representing the changes in viscosity with respect to volume fraction that occur when only hydrodynamic stresses are considered. It demonstrates a base-line reference from which experimental data can be compared. Fitting the KDE to our experimental data for our spherical particle suspensions is done by using $\phi_m = 0.63$ (commonly used for spheres as mentioned earlier) and leaving $[\eta]$ as a free parameter, resulting in $[\eta] = 9.5$ and $[\eta] = 3$ for Ag NP and glass bead suspensions, respectively. The KDE fitting of experimental data done by others [45] for sand suspensions is also presented for comparison. A closer look at the Ag NP data at $\phi = 0.5$ shows that viscosity is significantly lower than that predicted by fitting the KDE, though the data indicates deviation may occur as early as $\phi = 0.35$. This is probably due to particle clustering and jamming at the distal regions of the filament, resulting in particle dilution at the filament's centre and thus reducing the apparent suspension viscosity. This is supposed in other suspension studies at elevated volume fractions using capillary break-up experiments [45], and

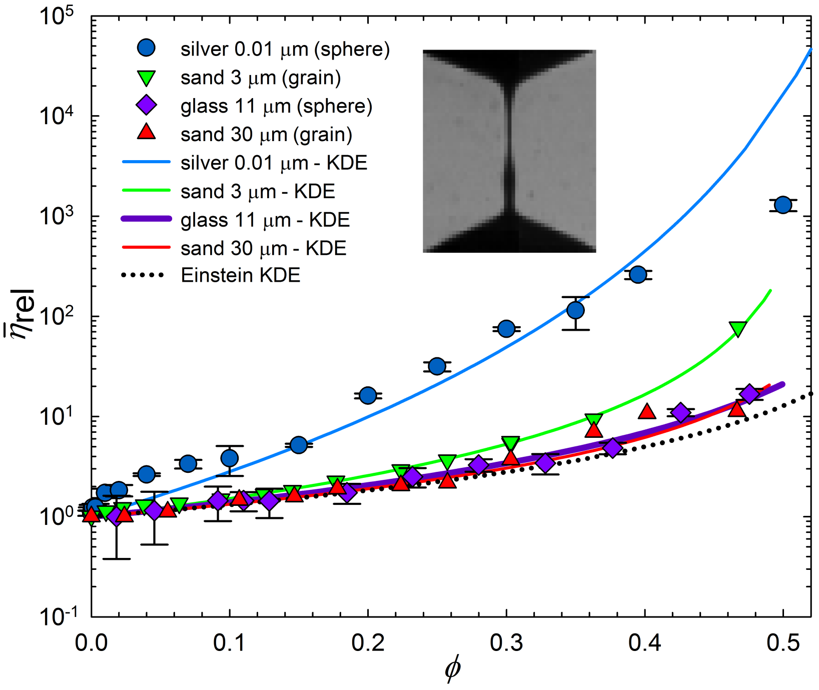

Fig. 6.5 (a) Relative extensional viscosity *versus* volume fraction accompanied by fits of the KDE for 0.01 μm silver particles ($[\eta] = 9.5$, $\phi_m = 0.63$), sand grain data from Alexandrou *et al.* [45] of both 3 μm ($[\eta] = 3.77$, $\phi_m = 0.53$) and 30 μm ($[\eta] = 2.6$, $\phi_m = 0.56$), 11 μm glass beads ($[\eta] = 3$, $\phi_m = 0.63$), and KD data for Einstein's pure hydrodynamic interaction case ($[\eta] = 2.5$, $\phi_m = 0.63$). Apart from data from [45], all fits were assigned visually. Inset: $\phi = 0.35$ Ag NP suspension break-up showing distinct non-uniformity at the mid-filament due to particle jamming.

is supported by correlating visual observations as low as $\phi = 0.35$ (Fig. 6.5 inset), where a distinct non-uniformity in radius develops at the mid-filament. Contrasting the curves that result from fitting the KDE to experimental data for the suspensions shown in Fig. 6.5, we can see that Eisntein's $[\eta] = 2.5$ is exceeded in all cases. This demonstrates that accounting for hydrodynamic interactions alone does not completely describe observed changes in extensional viscosity for particle suspensions.

The data in Fig. 6.6 shows that the $[\eta]$ necessary for fitting the KDE to experimental data (with the addition of extensional viscosity results for sub-micron short kaolin platelets from O'Brien (2002) [46]) increases with decreasing particle size D_p. Hence, extensional viscosity has a strong dependency on D_p, where it increases with decreasing particle size. The data in Fig. 6.6 reveals an empirical power law relationship between $[\eta]$ and D_p, $[\eta] = 0.442 D_\mathrm{p}^{-0.17}$. This relationship suggests that when dealing with low-aspect ratio particles one could predict extensional viscosities by fitting the KDE expression for break-up

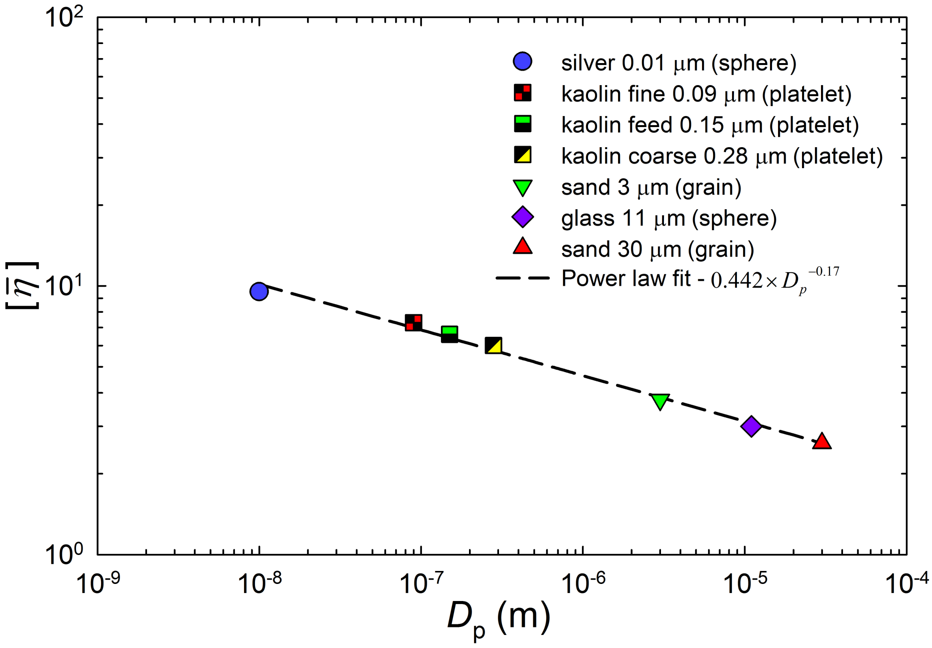

Fig. 6.6 Required $[\eta]$ to fit experimental data versus particles size D_p. Extensional kaolin data was taken from O'Brien (2002) [46] — where $\phi = 0.49$ for all samples — at strain rates that correspond to the rates seen in our experiments. Assuming $\phi_m = 0.55$, the necessary $[\eta]$ values for kaolin fine, feed, and coarse samples, were 7.3, 6.6, and 6, respectively. Apart from the Alexandrou (2009) sand data, all fits were assigned visually.

experiments, given that D_p and η_s are known. This indicates that systematic changes in viscosity due to particle size occur, but a detailing analytical foundation for this empirical relationship is nevertheless beyond the scope of this study.

The dependence of extensional viscosity on particle size is suspected to be due to the formation of low density particle clusters; fractal clusters of small spherical particles like 10 nm gold particles have been observed by others [133], for example, which are similarly sized to the 11.2 nm Ag NPs in this study. These clusters are induced by the rapid process of diffusion limited cluster aggregation (DLCA). This is reinforced by the observation of fractal clusters formed by the drying of Ag NP suspension (Fig. 6.7), which possess a fractal dimension of approximately 1.85 — typical of clusters formed by DLCA [134]. These effects have been observed and are anticipated to strengthen with decreasing particle dimensions due to the growth of the influence of van der Waals attraction as surface energies increase relative to volume [133–135]. Moreover, a viscosity dependence on particle size and aggregation has been posited by others [136, 137]. The significance of the formation of clusters is that they are believed to increase the effective volume fraction of a suspension by "capturing" suspension media within their structures [46, 138–140], thus causing very

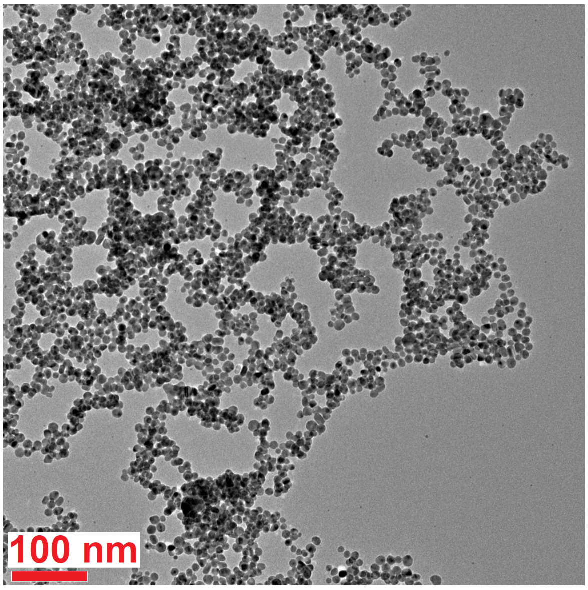

Fig. 6.7 FESEM image of the fractal pattern formed by dried Ag NP suspension. These patterns possess a fractal dimension of approximately 1.85, as determined by the box-counting method [47, 48].

strong influences on NP suspensions and increasing their viscosities. Notably, the effects of DLCA on colloid aggregation have been found to be universal and independent of chemical nature [134]; this may be relevant to the power-law trend seen in Fig. 6.6, which features particles of varied chemical composition. It is also worth noting that flow itself is also believed to be able to form clusters [141, 142], though we did not observe evidence to suggest that this occurs in our experiments.

An analytical theory that describes the role of suspended clusters on viscosity has been developed [138] and is adapted here for extensional viscosity:

$$\bar{\eta}_{rel} = \frac{\bar{\eta}_{rel}}{3\eta_s} = \left(1 - \frac{\phi}{\phi_{m,c}}\right)^{-[\eta]_c \phi_{m,c}} \tag{6.2}$$

Here $\phi_{m,c}$ is the averaged packing density of particles within clusters, thus a cluster formed by one particle would be represented by $\phi_{m,c} = 1$. The exponent $[\eta]_c \phi_{m,c}$, where $[\eta]_c$ is the intrinsic viscosity of a clustered suspension, is dependent on the averaged friction force of the clusters. Differences in friction exists not only because clusters expose less solid surface that resists flow than a solid particle of the same diameter, for example, but because they can also partially allows flow to pass through. Although it is possible to calculate these friction forces for spherical and non-spherical clusters in some cases [143, 144], clusters may take on different arrangements, sizes, network with one another, and can be broken apart or formed by flow [138, 141, 142], and determining the influence of these variables on friction forces and the average packing density of clusters is beyond the scope of this study.

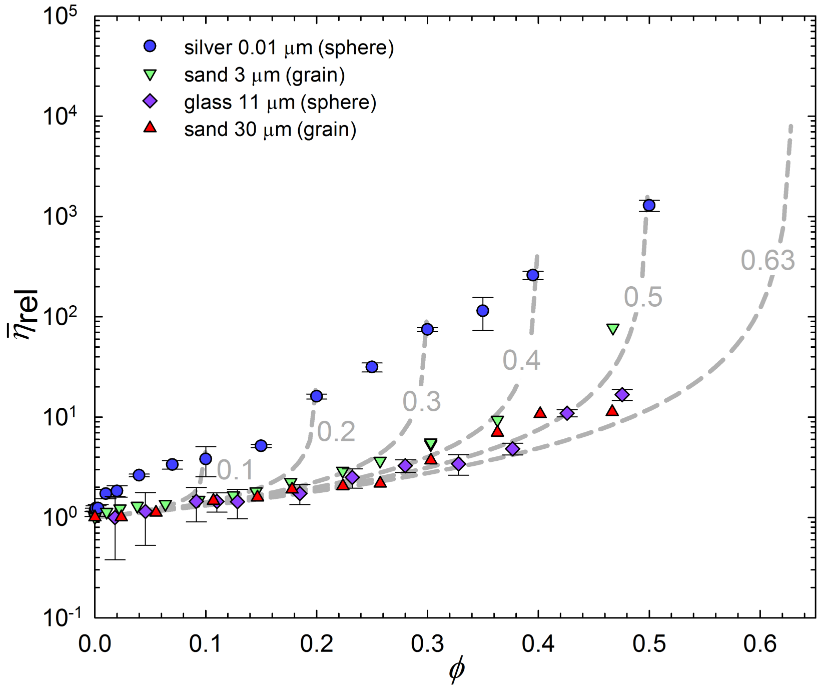

Fig. 6.8 Experimental data is shown along with data produced by the KDE by maintaining $[\eta] = 2.5$ and varying ϕ_m (grey dotted lines), with the grey numerical annotations denoting the value of ϕ_m.

It is possible to probe the effects of clustering on viscosity to some degree using the KDE. Earlier packing of suspensions due to the increased void fraction caused by clustering may effectively lead to different ϕ_m values for different volume fractions. Such a condition is represented in Fig. 6.8; here we can see that changing ϕ_m, whilst maintaining $[\eta] = 2.5$, allows the KDE to pass through experimental data, and we can see that in the case of suspended Ag MNs (Figs. 6.2a, b, and c) that cluster sizes do appear to change with volume fraction. Alternatively, maintaining $\phi_m = 0.63$ in the KDE and changing the value of $[\eta]$ provides predictions that are generally representative of experimental data, Fig. 6.9. As the effect of clustering becomes more significant one would actually expect the intrinsic viscosity $[\eta]$ to be reduced as more particles are shielded from the flow, but this does not appear to be the case, and the reasons are not understood. It is probable that clustering contributes to effects on both ϕ_m and $[\eta]$, but it is difficult to know to what extent. Conditions such as high flow rates may break up clusters [136, 145] and affect the effective ϕ, as characterised by Pe= $\dot{\gamma}/D_c$, where D_c is the cluster diffusivity. Yet, without understanding the time-scales at play, which would depend on particle size, diffusivity, and aggregation kinetics (van der

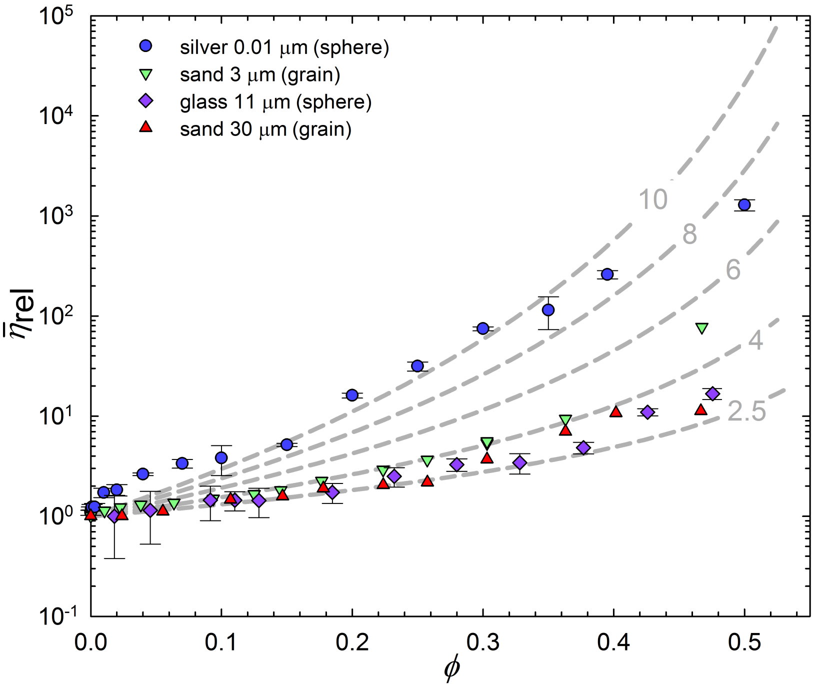

Fig. 6.9 Experimental data is shown along with data produced by the KDE by maintaining $\phi_m = 0.63$ and varying $[\eta]$ (grey dotted lines), with the grey numerical annotations denoting the value of $[\eta]$.

Waals or charge driven, for instance), we cannot determine the magnitude of their effects on cluster integrity. Furthermore, these clusters are unlikely to be rigid, and given that hydrodynamic stress is anticipated to be proportional to the cube of the primary dimension of non-spherical clusters in a shear flow plane (meaning that elongated clusters will contribute far more to viscosity than spherical ones) [146], it is reasonable to suggest that the stretching of extensional flow will stretch clusters and increase their stress contributions; this again is not well understood. Finally, there may be inter-particle friction stresses within clusters that are forced to rearrange, and between clusters that interact with each other [147], which may also affect the intrinsic viscosity. Additionally, all the data points of Fig. 6.6 reflect average strain rates, making data difficult to interpret. However, despite all these factors there is still a coherent trend in Fig. 6.6 relating particle size to extensional viscosity. It is also interesting to note that others have determined that inducing repulsive inter-particle forces has been effective at reducing cluster formation and in turn has lowered the suspension viscosities [146]. Furthermore, ultrasonication is believed to break up formations of aggregated nanoparticles, leading to a reduction in fluid viscosity [136].

6.3.3 Micro-nuggets and glass rods

6.3.3.1 Comparison of shear and extensional viscosities

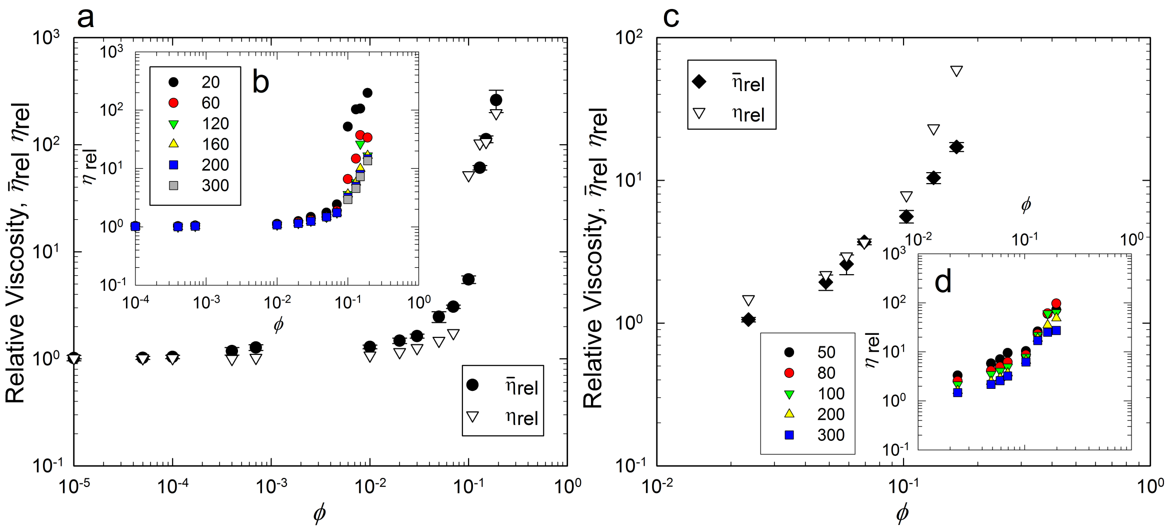

Fig. 6.10 (a) Ag MN suspension relative extensional and shear viscosity as a function of volume fraction. (b) Ag MN suspension relative shear viscosity against volume fraction for shear rates $\dot{\gamma}$ of 20, 60, 120, 160, 200, and 300 s^{-1}. (c) Glass fibre suspension relative extensional and shear viscosity as a function of volume fraction. (d) Glass fibre suspension relative shear viscosity against volume fraction for shear rates $\dot{\gamma}$ of 50, 80, 100, 200, and 300 s^{-1}. Note: Shear viscosity values in (a) and (c) correspond to comparable extensional and shear rates.

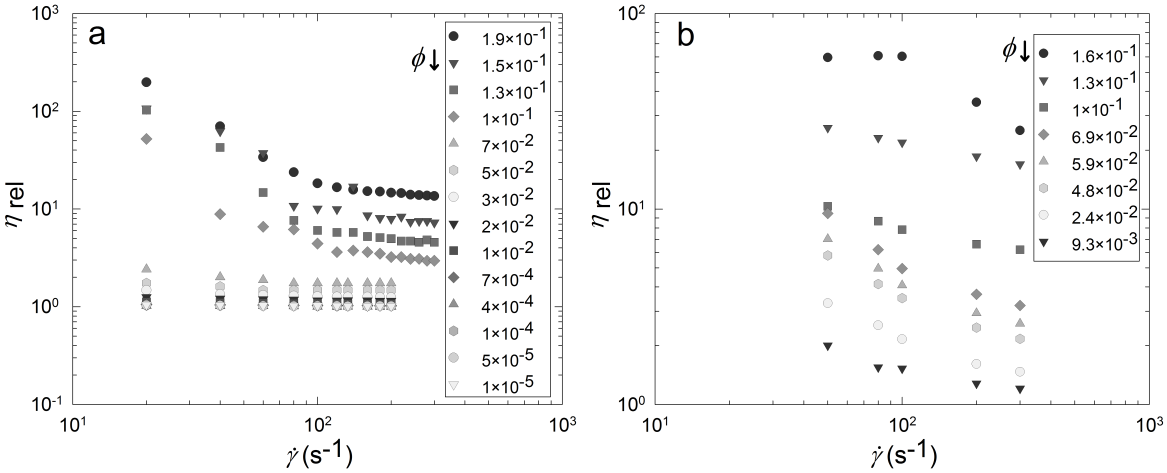

Fig. 6.11 Shear viscosity *versus* shear rate for different volume fractions for (a) Ag MN and (b) glass fibre suspensions, with clear shear thinning exhibited in both cases.

The relative extensional and shear viscosity results in Figs. 6.10a and c are not unlike those seen in Figs. 6.3a and c for Ag NP and glass bead suspensions. Figs. 6.10a and c show that the relative extensional and shear viscosities of Ag MN and glass fibre suspensions generally increase with a similar behaviour with increasing volume fraction, both rising dramatically towards their experimentally determined maximum packing values of $\phi_m = 0.3$ and $\phi_m = 0.24$ — these values are lower than spherical particles, as is expected for higher aspect ratio particles. Like the Ag NP suspensions, the relative extensional viscosity appears to generally be larger than the relative shear viscosity for Ag MNs across the volume fraction range, but the reasons for this are not understood. Figs. 6.11a and b show clear shear thinning for both Ag MN and glass rod suspensions, as is expected.

6.3.3.2 Concentration dependence of extensional viscosity

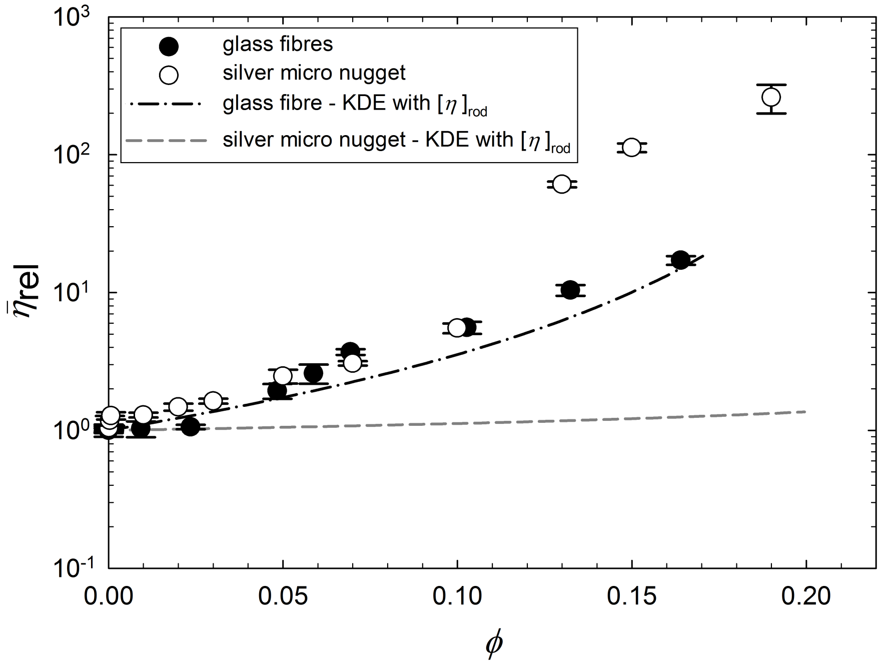

Fig. 6.12 Relative extensional viscosity *versus* volume fraction of glass fibre ($\phi_m = 0.24$) and Ag MN ($\phi_m = 0.3$) suspensions where the KDE is fitted using using $[\eta]_{\text{rod}}$.

In the case of particles with appreciable aspect ratio, the intrinsic viscosity used in the KDE is represented by $[\eta]_{\text{rod}}$, the value of which is determined by variables such as extensional strain rate and particle dimensions [100]. This approach is also used in Chapter 5.

The glass fibres are the largest of the particles in this study and appear to be free of the clustering behaviour associated with smaller particles, Fig. 6.2e. This makes them an ideal reference for the KDE relative extensional viscosity prediction of elongated particle suspensions, where clustering is not accounted for. The relative extensional viscosity prediction of the KDE, using the experimentally determined ϕ_m and the $[\eta]_{\text{rod}}$ (calculated using the experimental strain rate and particle dimensions), is validated by a reasonable agreement with experimental data, as seen in Fig. 6.12. This successful use of the KDE with $[\eta]_{\text{rod}}$, using rigid and easily characterised rod-like particles, also validates the analytical process used in Chapter 5.

However, using this same approach on the much smaller Ag MNs results in a significant underestimation of the relative extensional viscosities, exhibited by the difference between the Ag MN experimental data and the KDE prediction (Fig. 6.12). It is believed that particle clustering, as discussed in Sec. 6.3.2.2, is responsible for this discrepancy; this is reinforced by the clear clustering seen when these particles are suspended, see Fig. 6.2a, b, and c. As discussed in Sec. 6.3.2.2, clusters will likely trap suspending fluid and change the effective ϕ. Between volume fractions $\phi = 0.1$ and $\phi = 0.13$, a large increase in relative extensional and shear viscosity occurs (Fig. 6.11) — it is noteworthy that the Ag MN suspensions are visually observed to abruptly transition from a free-flowing to a paste-like consistency at $\phi = 0.1$. The reasons for this are not understood. However, as discussed in Sec. 6.3.2.2, friction effects due cluster rearrangement and interaction may also be responsible for the increased stresses seen here, which may occur as clusters become large enough to interact with one another. It is also supposed that the irregular shapes of Ag MNs may further exacerbate inter-particle stresses. Further investigation is require here, but this is beyond the scope of this study.

6.4 Conclusion

Experimental observations with our novel SAW driven microfluidic rheometer were validated here against extensional viscosity data for particle suspensions obtained by others who used an established extensional flow technique, using particles that are comparable to ones used in this study. Extensional data produced by the SAW technique also qualitatively agreed with shear data. This study demonstrated that the extensional viscosity of these dispersant-free nano/micro particles suspensions are not only sensitive to volume fraction, but also very sensitive to size. Moreover, a particle size dependent empirical power-law was revealed in this study that may serve as a tool for the prediction of extensional viscosity for cuboidal particle suspensions *via* the KDE. Detailed analytical reasoning behind this empirical relationship is beyond the scope of this study.

This size dependency was highlighted by KDE predictions of relative extensional viscosity that account purely hydrodynamic stresses, where experimental data deviated significantly. It is believed that this is due to particle clustering effects that occur at small scales due to DLCA effects (as indicated by an observed fractal dimension of 1.85 for Ag NPs); an effect that increases as particle size decreases. Deviations from hydrodynamic model predictions appear to occur with particle sizes as large as 30 µm. Furthermore, clustering of suspended Ag MN particles was observed, with cluster packing appearing to change with volume fraction. The effects of clustering are believed to contribute to changes in both the effective packing fraction of suspensions, as well as their intrinsic viscosities. The void fraction caused by clusters "trapping" fluid is believed to cause changes in effective suspension volume fraction. Increased hydrodynamic and frictional stresses induced by high flow rates and the rearrangement and increased interaction of clusters are suggested to affect the intrinsic viscosity of these suspensions.

Direct visual observation and the fitting of the KDE to Ag NPs indicated that particle jamming occurred during filament break-up at $\phi = 0.35$ and above, explaining the extensional viscosity values at higher volume fractions being lower than expected.

This study highlights the need for the further understanding of the complexities of small scale particle suspensions, and cluster formation and interaction effects under both extensional and shear flow. More theory and modelling is required to understand these effects, so that industrial processing of particle solutions can benefit from a deeper understanding of these types of suspensions. Nevertheless, it should be possible to estimate suitable extensional viscosities of these particle suspensions and those of similar morphologies for extensional techniques, such as inkjetting and spraying, *via* the appropriate selection of volume fractions using the data presented here. Additionally, utilising the presented technique's ability to analyse small amounts of low viscosity can further aid in probing the extensional properties of other micro/nano suspensions. Thus, we anticipate that this data and technique will aid in accelerating the industrial development of these complex but promising materials as inks and coatings.

Chapter 7

Publication: Extensional viscosity of copper nanowire suspensions in an aqueous polymer solution

The following chapter is a publication in which we utilise the advantages of the technique to study copper nanowire suspensions, where a polymer additive is required to prevent particle aggregation. Depositions of these suspensions show favourable electrical and physical properties, which has led to the development of novel electronics. These low-viscosity fluids pose difficulties for alternative extensional rheometry techniques due to the high-aspect ratio of the particles, the polymer additive, and the fact that it is currently difficult to synthesise large quantities of these particles, challenges that are overcome using the SAW-based technique. The elastic behaviour of these suspensions is found to depend on the ratio between polymer and nanowire content. Subsequently, we optimise our suspensions to minimise the polymeric contribution to largely isolate the particle contributions to viscosity. Like the previous chapter, we find correspondence between shear and extensional viscosity measurements.

7.1 Introduction

In Chapters 3 and 5 we saw the development and validation of acoustically-driven microfluidic extensional rheometry, and its application to challenging and novel fluids that currently have a largely academic importance. In Chapter 7, however, we utilise the unique advantages of the technology to aid in the rapidly expanding study of advanced particle suspensions as inks and coatings for new electronic devices and processes, building on the findings presented in Chapter 6. The subjects of this study are copper nanowire suspensions, which show favourable electrical properties when deposited while uniquely also demonstrating high flexibility, optical transparency, and stability [29, 34]. This has made them appealing in the development of devices like LEDs, solar cells, stretchable conductors, photodetectors, solar control windows, and touch screens, to mention some [34–39]. Like the particle suspensions of the previous Chapter, the precise harnessing these materials on an industrial scale will most probably require them to be applied as low-viscosity fluids in extensional flow techniques like inkjetting and spraying. The paucity of extensional analysis techniques that can analyse fluids in extensional flow is compounded by the need accommodate low-viscosity fluids, the problems posed by the high-aspect ratio of these particles, the polymer-doped buffer of these suspensions, and the fact that it is currently difficult to synthesise large quantities of these particles. We reveal that the elastic behaviour (quantified by the relaxation time) of these suspensions is heavily dependent on the ratio between polymer and nanowire content, falling from 819 to just 59 μs when a critical ratio is reached. Subsequently, we optimise our suspensions to minimise polymeric expression. Through changes in volume fraction we observe extensional viscosities ranging from 3 mPa·s (1 mPa·s shear viscosity) to 37.2 Pa·s and find that the maximum packing fraction of these long particles is only 0.027. The high sensitivity to volume fraction and polymer content of these suspensions illustrates the need to carefully formulate these suspensions so that they can be exploited in extensional flow application techniques, which typically have narrow operating conditions. Thus, data from this study and the technique are anticipated to be valuable in efficiently developing these materials for industrial-scale use.

7.2 Publication

The following publication was reproduced from [33] by permission from The Royal Society of Chemistry.

Monash University

Declaration for Thesis Chapter 7

Declaration by candidate

In the case of Chapter 7, the nature and extent of my contribution to the work was the following:

Nature of contribution	**Extent of contribution (%)**
Amarin G. McDonnell led project, performed preparation, performed and defined experimentation, performed data processing, contributed to interpretation, performed analysis, and performed the writing of the paper.	60

The following co-authors contributed to the work. If co-authors are students at Monash University, the extent of their contribution in percentage terms must be stated:

Name	**Nature of contribution**	**Extent of contribution (%) for student co-authors only**
N. N. Jason	Prepared samples and performed particle imaging.	10
L. Y. Yeo	Contributed to interpretation and draft review.	5
J Friend	Contributed to interpretation and draft review.	5
W. Cheng	Contributed to interpretation and draft review.	5
R Prabhakar *	Overall supervision, and contributed to interpretation, and analysis, and draft review.	15

The undersigned hereby certify that the above declaration correctly reflects the nature and extent of the candidate's and co-authors' contributions to this work*.

Candidate's Signature	[redacted]	**Date** 23/2/2016

Main Supervisor's Signature	[redacted]	**Date** 23/2/2016

Published on 27 August 2015. Downloaded by Monash University on 06/09/2015 10:42:59.

Soft Matter

PAPER

View Article Online
View Journal

Cite this: DOI: 10.1039/c5sm01940k

Extensional viscosity of copper nanowire suspensions in an aqueous polymer solution

Amarin G. McDonnell,[a] Naveen N. Jason,[b] Leslie Y. Yeo,[c] James R. Friend,[d] Wenlong Cheng[b] and Ranganathan Prabhakar*[a]

Received 4th August 2015,
Accepted 26th August 2015

DOI: 10.1039/c5sm01940k

www.rsc.org/softmatter

Suspensions of copper nanowires are emerging as new electronic inks for next-generation flexible electronics. Using a novel surface acoustic wave driven extensional flow technique we are able to perform currently lacking analysis of these suspensions and their complex buffer. We observe extensional viscosities from 3 mPa s (1 mPa s shear viscosity) to 37.2 Pa s *via* changes in the suspension concentration, thus capturing low viscosities that have been historically very challenging to measure. These changes equate to an increase in the relative extensional viscosity of nearly 12 200 times at a volume fraction of just 0.027. We also find that interactions between the wires and the necessary polymer additive affect the rheology strongly. Polymer-induced elasticity shows a reduction as the buffer relaxation time falls from 819 to 59 µs above a critical particle concentration. The results and technique presented here should aid in the future formulation of these promising nanowire suspensions and their efficient application as inks and coatings.

1 Introduction

Copper nanowires are novel building blocks in nanotechnology, exhibiting a wide range of applications in electronics, field emission transistors, heat management, and electrochemical detectors.[1] Networks of thin and long copper nanowires (CuNWs) (see Fig. 1) demonstrate very good electron transport in sparse concentrations after deposition and low temperature annealing (100 to 200 °C—permitting the use of flexible plastic substrates). This leaves large spaces between the wires for the transmittance of light, spanning UV to infra-red wavelengths. Simultaneously, they also display high flexibly and stability.[2] These attributes make them appealing in the production of fully transparent and flexible conductive electrodes. Thus, they have been exploited in the development of devices such as light-emitting diodes, photovoltaic cells, stretchable conductors, photodetectors, solar control windows, and touch screens, to name a few.[1,3–7]

The utilisation of these particles is most likely to take the form of high-precision deposition or thin uniform coatings *via* a deposited suspension. Thus, there is a need for inks and coatings that are suitable for inkjetting, spraying, and drawing (among others) to be formulated, requiring a balance between the bulk fluid properties, method of delivery, and the target substrate. These application processes are dominated by extensional flow, complicating the development of suitable fluids for three reasons. First, these extensional processes predominantly require low-viscosity fluids to function[8–10] (the buffer used in this study was only 1 mPa s). Second, suspensions of CuNWs

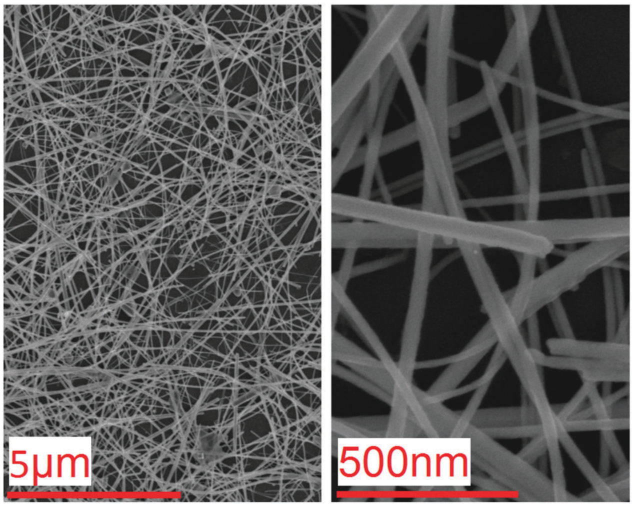

Fig. 1 Network-forming nature of long and thin CuNWs (approximately 27.6 nm in diameter, 62.36 µm long, and possessing an aspect ratio of 2200 on average). A vast number of connections that is a result of annealing can be seen while a large area for light to penetrate is maintained.

---

[a] *Department of Mechanical and Aerospace Engineering, Monash University, Clayton, Australia.* [redacted]

[b] *Department Chemical Engineering, Monash University, Clayton, Australia*

[c] *Micro/Nanophysics Research Laboratory, RMIT University, Melbourne, Australia*

[d] *Department of Mechanical and Aerospace Engineering, University of California-San Diego, San Diego, California, USA*

This journal is © The Royal Society of Chemistry 2015

Published on 27 August 2015. Downloaded by Monash University on 06/09/2015 10:42:59.

are likely to be highly non-Newtonian.[11–13] Third, these particles require polymer additives in order to stay suspended, lest they aggregate and settle. Hence, phenomena observed in polymer solutions in extensional flow such as long lived filaments and beads-on-a-string[14] must also be addressed. These challenges are compounded by the dearth of experimental extensional-flow methods that can handle low-viscosity fluids and quantify these surface-tension driven systems.

Inkjet technology generates extensional flows using low-viscosity fluids and it has been proposed that it can be used to characterise them.[15] However, inkjet systems have their limitations. Fromm (1984)[16] states that the critical properties that determine whether or not a particular fluid is suitable for inkjetting are the viscosity, density, surface tension, and the nozzle diameter. Given typical nozzle diameters of 10 and 40 μm, ink viscosities of 2–20 mPa s and 5–50 mPa s are recommended, respectively, as evidenced by recent particle suspension ink work.[17–23] These viscosity ranges are not only narrow but also range below the lower limit of technologies like CaBER, an important consideration for characterising the complex low-viscosity buffers and dilute suspensions in this study. This point is further complicated here since the viscosity of these high-aspect ratio particle suspensions is anticipated to be highly sensitive to volume fraction, a potential hurdle in ink formulation when balancing conductivity against light transmittance. Further, it is recommended that the nozzle diameter is at least 100 times greater than the suspended particles,[8] limiting the range of sizes that can be handled by any one system—an issue likely complicated by these very high-aspect ratio particles, by which logic would potentially require nozzles of 6236 μm. Further compounding the use of inkjets in the analysis of these long and thin wires are the complex flows and large shear rates generated within the nozzle itself that can be 2×10^4 to 2×10^6 s^{-1},[24] which may cause damage to NWs as they do to delicate proteins.[25,26] Moreover, if thermal inkjet technology (as opposed to piezo) were used then the raised temperatures of around 300 °C exceed the annealing temperature for these particles, probably damaging them and possibly causing nozzle clogging. Exacerbating all this is the fact that every inkjet system has its own characteristics that produce system-specific results that can vary considerably. Though inkjet technology may be useful for delivering these suspensions in certain formulations, it is unlikely to be suitable for characterising them or complex buffers. Hence, finding a workable recipe to make inks from these NWs would otherwise be trial and error.

Although accepted shear rheometry techniques have long been available,[27] established extensional measurement methods are comparatively recent.[28,29] Capillary-breakup extensional rheometry (CaBER) involves rapidly extending a drop of sample fluid between two end-plates to a finite distance, creating a liquid filament with a critical aspect ratio that then thins due to surface tension. The thinning evolution is described by the balance of surface tension against inertial and viscous stresses caused by the extensional flow. Through this balance it is possible to extract the extensional viscosity by measuring the decay of the neck radius as a function of time.[30] This technique has been used for highly viscous samples[31] but encounters problems with low-viscosity fluids. Rapid stoppage of the end plates causes vibrations to propagate through the fluid filament, leading to inertial instabilities which are not accounted for in the stress balance. These instabilities dissipate and can be ignored in higher viscosity samples or in samples with elasticity, where long-lived cylindrical polymeric filaments allow the use of a simple stress balance to extract the viscoelastic stresses.[32]

Recent advancements of the CaBER concept provide further access to low-viscosity fluids. The Cambridge Trimaster increases the end-plate retraction speed to overcome inertial instabilities and allow Newtonian and weakly elastic fluids of 10 mPa s to be tested.[33,34] Another is the Slow-Retraction-Method,[35] in which a liquid filament is extended between two end-plates to a stable aspect-ratio, followed by a slow extension that pulls the filament beyond the critical aspect-ratio to initiate break-up. Electrowetting forces can also be used to pull a fluid filament to initiate capillary thinning.[36] A liquid to liquid annular flow microfluidic device has also been developed.[37] The recently developed Rayleigh Ohnesorge Jetting Extensional Rheometry[38] technique involves stroboscopic imaging of a continuously flowing jet with controlled surface perturbations and has allowed access to very thin weakly viscoelastic fluids, though higher sample volumes would make such a device unsuitable for this study.

We use a novel variant of the CaBER technique that uses surface acoustic waves (SAW) to create and stabilise liquid bridges of very low viscosities; distinct advantages of this technique make it suitable for the development and analysis of these NW suspensions as inks and coatings. Firstly, it can process Newtonian fluids possessing shear viscosities from 27 Pa s down to 0.96 mPa s, giving it the range to encompass both viscous and characteristically difficult low-viscosity fluids.[39] Moreover, despite delivering large bulk mechanical energy the shear amplitudes created by high frequency SAW are so small that they can manipulate delicate particles, such as DNA, proteins and cells, without causing damage.[40–43] Further, SAWs have also been employed to pattern liquid crystals[44] and nanotubes[45] without damage. Additionally, heating effects for the short bursts required to jet a droplet of water or glycerol have been determined to be less than 0.02 and 1 °C, respectively—favourable for rheological analysis and well below the annealing temperatures of these metallic particles. Furthermore, there is no nozzle that can be clogged or that can restrict particle size. Finally, the fact that the technique only requires micro-droplets lends itself to the analysis of novel fluids such as biological samples that are difficult to produce in large volumes[46] (another microfluidic rheometric technique has also been recently proposed to handle small sample volumes[47]). This is an important advantage since it is currently difficult to synthesise large quantities of CuNW particles.

Hence, we report changes in the extensional viscosity as a function of the particle concentration from dilute to highly concentrated and viscous suspensions. Additionally, the extensional properties of the polymer-doped aqueous buffer were also analysed, with unexpected phenomenological changes as the CuNW : polymer ratio was changed. The availability of this

This journal is © The Royal Society of Chemistry 2015

Published on 27 August 2015. Downloaded by Monash University on 06/09/2015 10:42:59.

data and technique is anticipated to assist in the development and application of these promising particles.

2 Results and discussion

2.1 Polymeric buffer analysis

Phase separation and settling due to depletion interaction has been reported in previous experiments with suspensions of particles in polymeric buffer.[48] However, we observed no settling in our samples. This suggests that in our case polymers may absorb onto wires and serve to repel other coated wires, preventing aggregation and stabilising these suspensions.

Capillary thinning of pure polymer solutions has been widely studied.[32,49–53] It is known that when a liquid bridge starts thinning, polymeric stresses are negligible, until polymer molecules have stretched sufficiently in the extensional flow at the necking plane. Molecular stretching leads to strain-hardening of the polymeric stresses and at some point, these stresses begin to dominate over the viscous stresses from the rest of the fluid. At that point, the decrease in filament radius changes from an approximately power-law like decay in low-viscosity solvents to an exponential decay. The relaxation time of this exponential decay is used as an indicator of the elasticity induced by the polymeric component.

We are interested in extracting the viscosity of the particle suspension alone without the interference from the polymeric component. A reduction in polymeric effects, quantified by the relaxation time λ_e, is seen with an increase in the CuNW:polymer ratio (see Fig. 2). The relaxation time drops from 819 μs for pure buffer to 59 μs at a volume fraction of 4.15×10^{-3}. We reason that as polymers bond to the wires they lose their ability to stretch under flow and the addition of more wires leaves fewer polymer molecules free to influence bulk fluid behaviour.

We then use the CuNW:polymer ratio at which λ_e is the smallest, while still maintaining the suspension, to minimise interference from the polymer, in either shear or extensional viscosity measurements.

2.2 Viscosity measurements

Fig. 3a shows the progressive change in the relative extensional viscosity $\bar{\eta}_{\rm rel} = \bar{\eta}/3\eta_{\rm s}$ with nanowire volume fraction, where $\eta_{\rm s}$ = 1.01 mPa s is the shear viscosity of the buffer with the polymeric solute. A comparable growth in shear viscosities is also observed. It must be noted that each data point in Fig. 3a is at a different strain-rate. In capillary break-up experiments, the strain-rate cannot be set *a priori* but is self-determined by the fluid. In general, the average extensional strain-rate experienced by a sample prior to viscosity extraction decreases as volume fraction increases and viscosity increases. In shear rheometers on the other hand the strain rate can be pre-set. The shear data in Fig. 3a were obtained at strain-rates comparable to the corresponding extensional flow experiment at the same volume fraction. The shear viscosity data obtained at fixed strain-rates are shown in Fig. 3b and c. Since the polymeric component is expected to shear thin, and at any given volume fraction, the zero-shear-rate viscosity contribution of the polymer is small compared to the nanowire contribution (as demonstrated by the lack of significant exponential decay at small times during capillary break-up), the shear data in Fig. 3b and c can also be considered to be free of polymeric interference.

Acute viscosity sensitivity to volume fraction is expected for these CuNW suspensions since these wires have the potential to directly interact with large numbers of particles along their lengths, and thus quick growth in the effects of inter-particle interaction relative to increased volume fraction was anticipated. In fact, the extensional viscosity more than doubled the

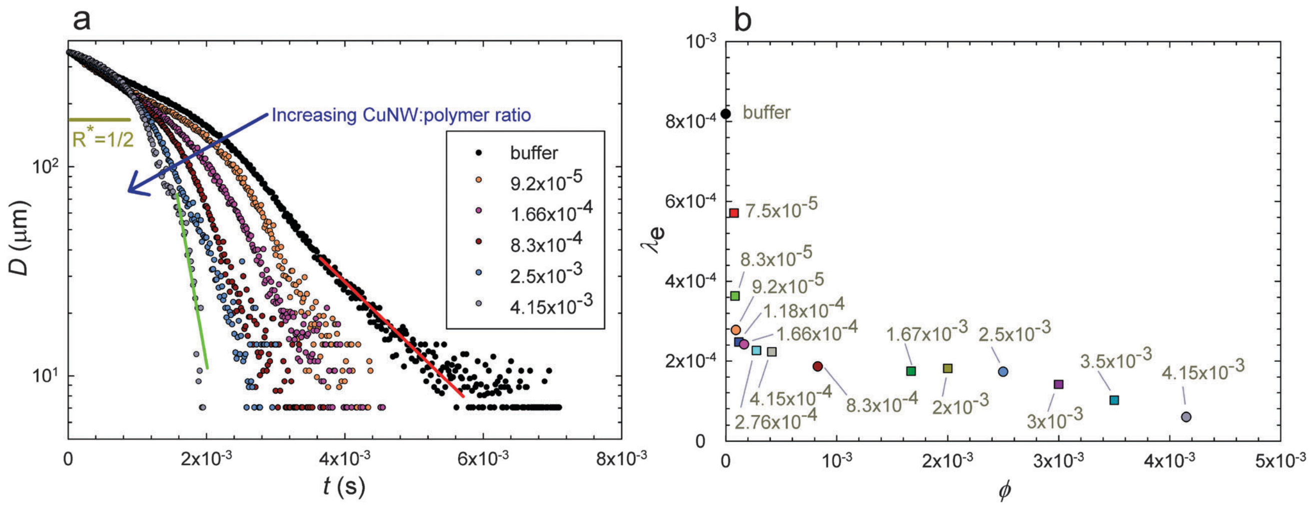

Fig. 2 (a) Filament break-up data clearly showing the reduction in polymeric effect with an increase in the CuNWs : polymer ratio. The red and green lines indicate the polymeric regions used to calculate the relaxation times λ_e for the buffer and $\phi = 4.15 \times 10^{-3}$, respectively. Break-up above $R^* = 1/2$ shows Newtonian-like behaviour, allowing extensional viscosity extraction as described in Section 3.2. The optical lower limit in these experiments occurs at 4 μm. (b) Relaxation times showing a stark drop from 819 to 248 μs at a CuNW volume fraction of $\phi = 1.18 \times 10^{-4}$, indicating a drop in the amount of free polymer in the solution. A more gently approached reduction to 59 μs occurs at 4.15×10^{-3}. Grey annotations denote volume fractions.

Published on 27 August 2015. Downloaded by Monash University on 06/09/2015 10:42:59.

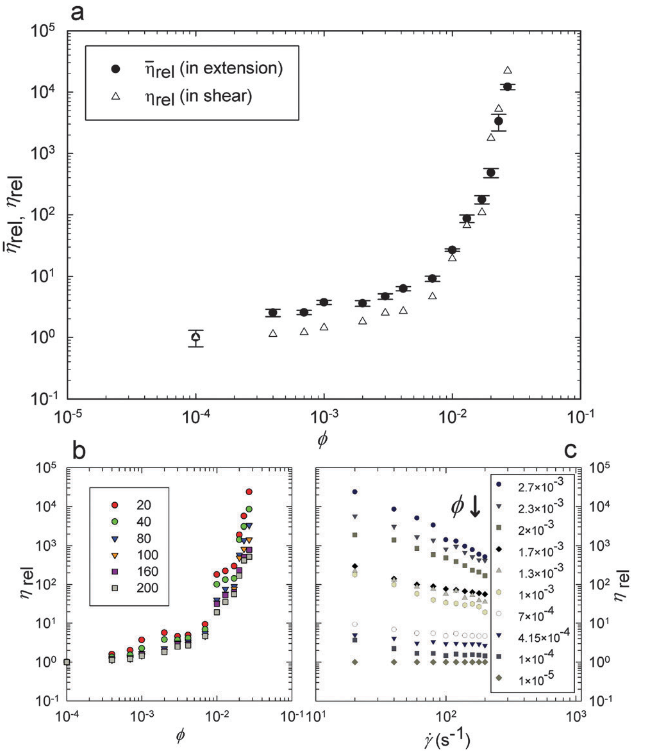

Fig. 3 (a) Relative extensional $\bar{\eta}_{rel}$ and shear viscosity η_{rel} showing similar behavioural trends as a function of the volume fraction ϕ. The shear viscosity values correspond to comparable extensional and shear strain rates. It should be noted that Section 3.2 describes how the extensional viscosities seen here were extracted. (b) Relative shear viscosity against volume fraction for shear rates $\dot{\gamma}$ of 20, 40, 80, 160, and 200 s^{-1}. (c) Relative shear viscosity against shear rate for different volume fractions, displaying pronounced shear thinning.

buffer viscosity at a volume fraction of 1×10^{-3}. At $\phi = 1.3 \times 10^{-2}$, an extensional viscosity of 265 mPa s was reached, well in excess of the typical inkjet system capability discussed in Section 1. Further, the relative extensional viscosity nearly rose to 12 200 times ($\bar{\eta}$ = 37.2 Pa s) at only $\phi = 2.7 \times 10^{-2}$. The steep gradient at this point indicates that the maximum particle packing fraction was being approached even at this low volume fraction, which may be expected for such high aspect ratio particles.[54]

It can be seen in Fig. 3a that the shear viscosity overtakes the extensional viscosity in magnitude at about $\phi = 1.7 \times 10^{-3}$. To our best knowledge, this has not been observed before. The reasons for this effect are not clear at present and may be attributed to the difference in the interplay between flow and particle orientation. The bare nanowires have an aspect-ratio of approximately $A = 2 \times 10^3$. Even after accounting for an absorbed polymer layer, the aspect-ratio $A \approx O(10^3)$. The volume fraction for the isotropic-nematic transition is expected to be around $1/A \approx 10^{-3}$. Most of the samples in Fig. 3 are well above this concentration. Extensional rheology of liquid-crystalline materials is relatively unexplored and the few studies thus far have focused on high-temperature liquid-crystalline polymer melts.[55–57] Extensional viscosities larger than shear viscosities have been observed in liquid-crystalline carbon-nanofibre suspensions, but at a single volume fraction.[58] CuNW suspensions could serve as model room-temperature liquid crystalline materials for more detailed explorations for understanding the effect of particle concentration on behaviour in extensional and shear flows. On the applied front, the data in Fig. 3a show that to a large extent, shear viscosity can provide a good estimate of extensional viscosity for use in designing inkjet applications of CuNW suspensions.

3 Experiments

3.1 Particle and buffer preparation

CuNWs 25–30 nm in diameter and 50–65 μm long were synthesised *via* a hydrothermal method.[59] 900 mg hexadecylamine (HDA) (Sigma-Aldrich) was dissolved in 50 ml water in a closed 100 ml screw cap borosilicate glass bottle, and magnetically stirred at 1000 rpm at 100 °C for 1 hour in an oil bath. To this, 100 mg $CuCl_2{\cdot}2H_2O$ was added and stirred for another 30 minutes, after which 500 mg of α or β glucose (Merck) was added and stirred at 400 rpm for 6 hours. The reaction solution takes on the appearance of a creamy white liquid with just the HDA after 1 hour. After the addition of $CuCl_2{\cdot}2H_2O$ the solution turns sky blue after 30 minutes. Finally, after addition of glucose, the solution starts turning pale brown at first, then gradually dark brown, then reddish brown. The reaction is stopped after 6 hours and removed from the oil bath allowing it to cool for 10 minutes, after which it is transferred into 50 ml vials and centrifuged at 6500 rpm for 5 minutes. The CuNWs are collected at the bottom of the centrifuge tube, which can be easily separated by carefully decanting the waste supernatant. The pellet is carefully rinsed a few times with Milli-Q water at room temperature to remove any loosely bound HDA remaining.

Hydroxypropyl cellulose (HPC) (Sigma Aldrich, 20 mesh, M_w = 1 000 000) was the polymer used as a dispersant to help suspend the CuNWs and prevent aggregation. A 2 wt% solution of HPC in ethanol was made from of which a 0.6 ml aliquot was sperated into a test tube and diluted with Milli-Q water to make a 2.2 ml solution. This aqueous solution was used as the buffer, and the same amount of HPC solution was used with increasing volume fractions of CuNWs to find the optimum CuNW : polymer ratio through extensional analysis.

3.2 Acoustically-driven microfluidic extensional rheometry

We overcame the challenges discussed in Section 1 by using an experimental technique developed by Bhattacharjee *et al.*, explained in detail elsewhere.[39,46] Briefly, we used a 20 MHz waveform generator (33220A, Agilent) to trigger a second signal generator (WF1966, NF Corporation), which produces a 1.5 ms burst. The second generator outputs a sinusoidal signal to an RF power amplifier (411LA, ENI), resulting in a fixed amplitude and frequency signal of approximately 36.7 MHz that is then supplied to a piezoelectric SAW chip. This device comprises of a pair of curved inter-digitated transducers bonded to a piezoelectric lithium niobate substrate that focus Rayleigh waves towards a central target where a sessile droplet in placed

Published on 27 August 2015. Downloaded by Monash University on 06/09/2015 10:42:59.

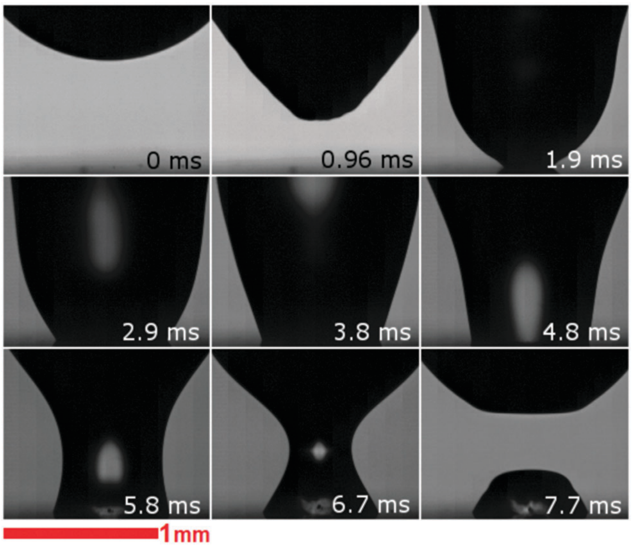

Fig. 4 A montage showing the SAW-actuated jetting, resulting from a 1.5 ms SAW burst, and subsequent surface tension-driven thinning of pure water at a temperature of 22 °C (0.96 mPa s).

(1 μl; approximately 1 mm dia—Fig. 4). The SAW burst, focused beneath the droplet, concentrates considerable inertial energy within it, thus forcing a jet to form.[40] The SAW energy then stabilises the jet as it impacts onto an opposing surface and establishes a liquid bridge of a critical aspect ratio that will result in break-up. Upon relaxation of the SAW burst, the filament is allowed to thin under surface tension, the decay of which is recorded using a high speed camera (Photron SA5; 62 000 fps; image size: 1.35 mm × 2.14 mm (192 × 304 pixels)) with a long-distance video microscope attachment (K2/SC, infinity). The event is lit by a single LED lamp placed beyond the fluid filament. The radius of the neck in each image frame is extracted using standard image-analysis techniques.

The method for extracting extensional viscosity for this technique is detailed elsewhere.[46] In short, the aforementioned difficulties of extracting data from thin cylindrical threads are addressed by beginning the measurement of filament thinning at a larger filament diameter, but not so large that initial transients affect data—50 pixels (0.352 ± 0.007 mm). A series of filament break-up data was acquired for a range of Newtonian fluids that represent viscosity standards, from low-viscosity to viscous samples. Break-up time and radius were re-scaled by the Rayleigh time-scale $t^* = t/\tau_R$ and the initial radius $R^* = R/R_0$, respectively, where $\tau_R \equiv \sqrt{\rho R_0{}^3/\sigma}$, ρ is the density, R_0 is the initial radius, and σ is the surface tension. When experimental conditions such as sample size were held constant, it was determined that the time $t_{1/2}{}^*$ for R^* to decrease to a value of half was primarily a function of the Ohnesorge number $\mathrm{Oh} \equiv \bar{\eta}/3\sqrt{\rho\sigma R_0}$, where $\bar{\eta}$ is the extensional viscosity, which is 3 times the shear viscosity η for Newtonian fluids. A calibration curve through $t_{1/2}{}^*$—*versus*—Oh data for the Newtonian viscosity standards was obtained. With this calibration curve, the Oh and hence $\bar{\eta}$ of a test fluid sample with negligible elastic effects can be extracted from the observed $t_{1/2}{}^*$ measured. This method for extracting extensional viscosity is valid as long as viscoelastic effects due to the dissolved polymer are not significant, since the original calibration of dimensionless half-time against Ohnesorge number was only performed with Newtonian viscosity standards.

3.3 Characterisation of polymeric filaments

The addition of polymer to the suspension buffer necessitates quantification of viscoelastic properties. Polymer chains stretch under extensional flow, retarding the rate at which a fluid filament breaks up. These elastic stresses can dominate towards the later stages of break-up, resulting in long-lived filaments and can be characterised by a relaxation time $\lambda_e = -t/3\ln(R(t)/R_0)$.[28,49] Although in reality there may actually be more than one relaxation mode, it has been found that the slowest mode dominates in extensional flow, thus a single relaxation time is commonly used to characterise viscoelastic stress experimentally and theoretically.[32]

3.4 Particle imaging

High resolution images of the CuNWs were captured using field-effect scanning electron microscopy (Nova NanoSEM 450, FEI, Oregon, USA).

3.5 Shear rheometry

A cone (60 mm/1°, gap distance 0.041 mm) and plate rheometer was used to perform the shear viscosity analysis (HAAKE MARS III, Thermo Fisher Scientific, Massachusetts, USA).

4 Conclusions

The capabilities of SAW-driven microfluidic extensional rheometery enabled the extensional analysis of NW suspensions, overcoming the challenges that low-viscosities, high-aspect ratio particles, and small sample volumes present.

The reduction of polymeric-induced elasticity with the addition of CuNWs, indicated by the relaxation time decreasing from 819 down to 59 μs, suggests that polymer molecules bond to the CuNWs. Beyond a certain CuNW : polymer ratio, few free polymer molecules remain to influence bulk properties. Under these conditions, filament thinning was initially not significantly affected by the dissolved polymer, and Newtonian-like behaviour was observed at small strains. Hence, utilising this optimal ratio enabled the creation of sedimentation-free suspensions that did not exhibit complicating polymeric behaviours, thus allowing the observation of changes in viscosity that arise primarily as a function of CuNW volume fraction.

It was demonstrated that the viscosity of suspensions of these long and thin wires is highly sensitive to volume fraction, with increases of 4 orders of magnitude in their relative extensional and shear viscosities, at a volume fraction of just 2.7×10^{-2}.

In summary, it is anticipated that the reported technique and viscosity data, particularly that of problematic low-viscosity fluids in extensional flow, will assist in the formulation of

Published on 27 August 2015. Downloaded by Monash University on 06/09/2015 10:42:59.

workable inks and coatings where controlling polymeric expression and extensional viscosity is key, thus expediting the application of these promising particles for the next generation of electronics.

Acknowledgements

The authors thank the Monash Center for Electron Microscopy facilities (MCEM) for the generous use of the FEI Nova Nano-SEM 450 FESEM and the Victorian International Research Scholarship (VIRS).

References

1 S. Bhanushali, P. Ghosh, A. Ganesh and W. Cheng, *Small*, 2015, **11**, 1232–1252.

2 H. Guo, N. Lin, Y. Chen, Z. Wang, Q. Xie, T. Zheng, N. Gao, S. Li, J. Kang, D. Cai and D.-L. Peng, *Sci. Rep.*, 2013, **3**, 2323.

3 J. Wu, J. Zang, A. R. Rathmell, X. Zhao and B. J. Wiley, *Nano Lett.*, 2013, **13**, 2381–2386.

4 I. E. Stewart, A. R. Rathmell, L. Yan, S. Ye, P. F. Flowers, W. You and B. J. Wiley, *Nanoscale*, 2014, **6**, 5980–5988.

5 Y. Tang, S. Gong, Y. Chen, L. W. Yap and W. Cheng, *ACS Nano*, 2014, **8**, 5707–5714.

6 S. Han, S. Hong, J. Ham, J. Yeo, J. Lee, B. Kang, P. Lee, J. Kwon, S. S. Lee and M.-Y. Yang, *et al.*, *Adv. Mater.*, 2014, **26**, 5808–5814.

7 Y. Tang, K. L. Yeo, Y. Chen, L. W. Yap, W. Xiong and W. Cheng, *J. Mater. Chem. A*, 2013, **1**, 6723–6726.

8 S. Magdassi, *The chemistry of inkjet inks*, World scientific, Singapore, 2010.

9 A. A. Tracton, *Coatings technology handbook*, CRC Press, 2005.

10 R. Fernando, L.-L. Xing and J. Glass, *Prog. Org. Coat.*, 2000, **40**, 35–38.

11 J. Mewis and A. Metzner, *J. Fluid Mech.*, 1974, **62**, 593–600.

12 G. Batchelor, *J. Fluid Mech.*, 1977, **83**, 97–117.

13 C. J. Petrie, *J. Non-Newtonian Fluid Mech.*, 1999, **87**, 369–402.

14 R. P. Mun, J. A. Byars and D. V. Boger, *J. Non-Newtonian Fluid Mech.*, 1998, **74**, 285–297.

15 O. A. Basaran, H. Gao and P. P. Bhat, *Annu. Rev. Fluid Mech.*, 2013, **45**, 85–113.

16 J. Fromm, *IBM J. Res. Dev.*, 1984, **28**, 322–333.

17 W. Shen, X. Zhang, Q. Huang, Q. Xu and W. Song, *Nanoscale*, 2014, **6**, 1622–1628.

18 B. K. Park, D. Kim, S. Jeong, J. Moon and J. S. Kim, *Thin Solid Films*, 2007, **515**, 7706–7711.

19 Y. Lee, J.-r. Choi, K. J. Lee, N. E. Stott and D. Kim, *Nanotechnology*, 2008, **19**, 415604.

20 K. Lawrie, A. Mills and D. Hazafy, *Sens. Actuators, B*, 2013, **176**, 1154–1159.

21 M. Grouchko, A. Kamyshny and S. Magdassi, *J. Mater. Chem.*, 2009, **19**, 3057–3062.

22 P. Chen, H. Chen, J. Qiu and C. Zhou, *Nano Res.*, 2010, **3**, 594–603.

23 Y. Tao, Y. Tao, L. Wang, B. Wang, Z. Yang and Y. Tai, *Nanoscale Res. Lett.*, 2013, **8**, 147.

24 B. Derby, *J. Mater. Chem.*, 2008, **18**, 5717–5721.

25 G. M. Nishioka, A. A. Markey and C. K. Holloway, *J. Am. Chem. Soc.*, 2004, **126**, 16320–16321.

26 C. C. Cook, T. Wang and B. Derby, *Chem. Commun.*, 2010, **46**, 5452–5454.

27 P. Dontula, C. W. Macosko and L. Scriven, *J. Rheol.*, 2005, **49**, 807–818.

28 A. Bazilevsky, V. Entov and A. Rozhkov, Third European Rheology Conference and Golden Jubilee Meeting of the British Society of Rheology, 1990, pp. 41–43.

29 G. H. McKinley and T. Sridhar, *Annu. Rev. Fluid Mech.*, 2002, **34**, 375–415.

30 M. I. Kolte, H. K. Rasmussen and O. Hassager, *Rheol. Acta*, 1997, **36**, 285–302.

31 G. H. McKinley and A. Tripathi, *J. Rheol.*, 2000, **44**, 653–670.

32 V. Entov and E. Hinch, *J. Non-Newtonian Fluid Mech.*, 1997, **72**, 31–53.

33 D. Vadillo, T. Tuladhar, A. Mulji, S. Jung, S. Hoath and M. Mackley, *J. Rheol.*, 2010, **54**, 261–282.

34 D. C. Vadillo, W. Mathues and C. Clasen, *Rheol. Acta*, 2012, **51**, 755–769.

35 L. Campo-Deano and C. Clasen, *J. Non-Newtonian Fluid Mech.*, 2010, **165**, 1688–1699.

36 W. C. Nelson, H. P. Kavehpour and C.-J. C. J. Kim, *Lab Chip*, 2011, **11**, 2424–2431.

37 P. E. Arratia, J. P. Gollub and D. J. Durian, *Phys. Rev. E: Stat., Nonlinear, Soft Matter Phys.*, 2008, **77**, 036309.

38 B. Keshavarz, V. Sharma, E. C. Houze, M. R. Koerner, J. R. Moore, P. M. Cotts, P. Threlfall-Holmes and G. H. McKinley, *J. Non-Newtonian Fluid Mech.*, 2015, **222**, 171–189.

39 P. Bhattacharjee, A. McDonnell, R. Prabhakar, L. Yeo and J. Friend, *New J. Phys.*, 2011, **13**, 023005.

40 L. Y. Yeo and J. R. Friend, *Biomicrofluidics*, 2009, **3**, 012002.

41 H. Li, J. Friend, L. Yeo, A. Dasvarma and K. Traianedes, *Biomicrofluidics*, 2009, **3**, 034102.

42 A. E. Rajapaksa, J. J. Ho, A. Qi, R. Bischof, T.-H. Nguyen, M. Tate, D. Piedrafita, M. P. McIntosh, L. Y. Yeo, E. Meeusen, R. L. Coppel and J. R. Friend, *Respir. Res.*, 2014, **15**, 60.

43 C. Cortez-Jugo, A. Qi, A. Rajapaksa, J. R. Friend and L. Y. Yeo, *Biomicrofluidics*, 2015, **9**, 052603.

44 Y. J. Liu, X. Ding, S.-C. S. Lin, J. Shi, I.-K. Chiang and T. J. Huang, *Adv. Mater.*, 2011, **23**, 1656–1659.

45 K. M. Seemann, J. Ebbecke and A. Wixforth, *Nanotechnology*, 2006, **17**, 4529.

46 A. G. McDonnell, T. C. Gopesh, J. Lo, M. O'Bryan, L. Y. Yeo, J. R. Friend and R. Prabhakar, *Soft Matter*, 2015, **11**, 4658–4668.

47 P. Erni, M. Varagnat, C. Clasen, J. Crest and G. H. McKinley, *Soft Matter*, 2011, **7**, 10889–10898.

48 A. Bazilevskii, D. Koroteev, A. Rozhkov and A. Skobeleva, *Fluid Dyn.*, 2010, **45**, 626–637.

49 R. Liang and M. Mackley, *J. Non-Newtonian Fluid Mech.*, 1994, **52**, 387–405.

This journal is © The Royal Society of Chemistry 2015

Published on 27 August 2015. Downloaded by Monash University on 06/09/2015 10:42:59.

50 S. L. Anna and G. H. McKinley, *J. Rheol.*, 2001, **45**, 115–138.
51 C. Clasen, J. Plog, W.-M. Kulicke, M. Owens, C. Macosko, L. Scriven, M. Verani and G. H. McKinley, *J. Rheol.*, 2006, **50**, 849–881.
52 V. Tirtaatmadja and T. Sridhar, *J. Rheol.*, 1993, **37**, 1081–1102.
53 R. Prabhakar, J. R. Prakash and T. Sridhar, *J. Rheol.*, 2006, **50**, 925–947.
54 J. Parkhouse and A. Kelly, *Proc. R. Soc. London, Ser. A*, 1995, **451**, 737–746.
55 A. Gotsis and M. Odriozola, *J. Rheol.*, 2000, **44**, 1205–1223.
56 T. S. Wilson and D. G. Baird, *J. Non-Newtonian Fluid Mech.*, 1992, **44**, 85–112.
57 Y. Lin and H. Winter, *Macromolecules*, 1988, **21**, 2439–2443.
58 J. Xu, S. Chatterjee, K. W. Koelling, Y. Wang and S. E. Bechtel, *Rheol. Acta*, 2005, **44**, 537–562.
59 M. Jin, G. He, H. Zhang, J. Zeng, Z. Xie and Y. Xia, *Angew. Chem., Int. Ed.*, 2011, **50**, 10560–10564.

Chapter 8

Extensional viscosity of amphiphilic polymer and surfactant mixtures

Chapter 8 explores the bulk effects caused by interactions between polymer and surfactant molecules in liquid, which are counter-intuitive, via capillary break-up experiments of low-viscosity dilute polymer-surfactant mixtures and more viscous concentrated formulas. Such solutions have long-running and extensive uses in industrial products and processes, but limited study has been conducted on their extensional properties. We demonstrate the high sensitivity of these polymer solutions to surfactant concentration, particularly in extensional flow. Additionally, it is shown that material properties change as filament evolution progresses. This study once again exhibits the general correspondence between extensional and shear viscosity results. It also demonstrates that results from this technique can qualitatively support theoretical predictions that are based on molecular interactions.

Our group was approached by Shakti Singh, Prof. Jim R. Jones, and Prof. Richard H. Archer from Massey University, New Zealand, to test the materials in this study, which were provided and the formulations defined by them. Literature review, experimental work, and analysis were conducted by Amarin G. M^{c}Donnell.

8.1 Introduction

Polymer-surfactant solutions can be used to great effect to enable phase separation, colloid stability, emulsification, gel formation, solubilisation, viscoelastic modification [148, 149], and even self-healing [150]. As a result, these effects have been exploited in the production of a large range of industrial goods, such as detergents, cosmetics, pharmaceutical drugs, foods, paints, and pesticides [41, 151].

Combining polymers and surfactants in solutions can result in interactions that have significant and counter-intuitive effects on chemical and rheological properties, and these systems have been studied for decades for various applications [40, 41]. The properties and molecular structures that arise from the combination of polymers and surfactants in liquid (particularly aqueous liquid) are dependent on the characteristics and concentrations of the polymer and the surfactant additives, and the properties of the solvent [40, 152–154]. Certain formulations will result in repulsive effects between ionic surfactant molecules and hydrophobic polymer segments, or cause surfactant molecules to attach to polymers as singular molecules or as mixed micelles that can potentially link with multiple surrounding polymer chains, or produce solutions of surfactant saturated polymers and free surfactant micelles [40]; these different system states produce varied bulk properties. It is worth noting that polymer-surfactant systems are not the only systems exploited to tailor favourable rheological properties. Hydrophobically modified alkali-soluble emulsion (HASE) systems comprise polymer molecules that have hydrophobic macromonomers attached along their lengths. These polymers have negative charges and are coiled in low pH solution. However, raising the pH induces electrostatic repulsion between these charges and results in the expansion of the coil, allowing the hydrophobic groups to associate; these associations can create networks between polymer molecules. This can produce large changes in viscosity, which can vary strongly with changes in the ionic strength of the fluid and the charge density along the polymer molecules [155]. Hydrophobically modified ethoxylate-urethane (HEUR) polymers are nonionic, and they can be used to greatly modify the viscosity of solutions without making pH adjustments. These polymers have hydrophobes attached at their ends that minimise their exposure to water by attaching to themselves or surround polymers, creating loops that group into micelles, or bridge between micelles to create micellar networks and form supramolecular structures. These structures, which heavily influence viscosity, depend on variables such as polymer concentration, molecular weight, hydrophobe characteristics, temperature, and deformation [156].

Polymer-surfactant systems can be placed in one of three categories [40]. First, solutions of oppositely charged polymer and ionic surfactant where the most intense interactions occur, such as phase separation. Second, a system of uncharged polymer and ionic surfactant, which demonstrate mild strength interactions. Finally, the weakest interaction is that of uncharged polymer and a nonionic surfactant.

A specific example of the second case is that of hydroxypropylmethyl cellulose (HPMC) and sodium dodecylsulfate (SDS) in an aqueous solution. Water-soluble HPMC is one of many nonionic cellulose derivative polymers that are biocompatible. It is considered to be physiologically harmless and possesses favourable mechanical properties, which lends it to extensive use in foods [157–159], drug production [159, 160] and printing technologies [161] — it can provide an efficient means for thickening, the ability to form films, and modify surface activity [162]. The presence of methyl and hydroxypropyl groups means that this form of cellulose has hydrophobic centres along it. This provides available adsorption sites for low molar mass surfactants such as anionic SDS. The strength of potential interactions is anticipated to increase with increased hydrophobicity, depending on the interaction mechanisms in question [163, 164]. Ionic surfactants such as SDS can induce significant changes in polymer solution properties, such as thickening [148, 165–171], swelling [166] compaction [172], and phase separation [148, 169], to name some. Variations across the hydrophobic substitutions used in different HPMC types can lead to variations in the strength of interactions and the conditions under which they occur. Thus, each HPMC-SDS system requires separate study, as is the case with every varied polymer-surfactant solution.

There are two important and well documented points at which polymer-surfactant interaction mechanisms change due to increases in surfactant concentration in an aqueous polymer solution, which in turn cause significant behavioural changes [40, 41]. First, there is the critical association concentration (*cac*), which is the minimum surfactant concentration at which surfactant molecules will begin to bind to the hydrophobic adsorption sites along the polymers. Second, surfactant concentration can become so high that polymer adsorption sites will no longer be able to accommodate more surfactant molecules, the so called polymer saturation point (*psp*); at this point, the further addition of surfactant will lead to free micelles forming in the solution. These effects and their influence on bulk properties have been explored in detail in other studies [40, 41, 173–175].

The industrial importance of polymer-surfactant solutions and the interesting theory behind their capabilities have made them the subject of many studies. However, there have been few studies done on the extensional properties of polymer-surfactant systems [174, 175], the understanding of which is important for extensional flows in industrial processes such as oil recovery [176] and coating flows [174], for example. Thus, we assess the extensional properties of polymer-surfactant systems *via* low-viscosity HPMC-SDS solutions, which, to our knowledge, have not benefited from study *via* capillary break-up experiments and the potential insights that they permit.

8.2 Experimental

8.2.1 Materials and preparation

HPMC (trade name Methocel F4M, methoxyl content 28 %, hydroxypropyl content 5 %) was sourced from The Dow Chemical Company. It has a reported intrinsic viscosity of $[\eta] = 6.56$ dL/g and molecular weight $M_w = 302,300$ Da [49]. SDS (99 %) was obtained from Sigma-Aldrich. SDS was added to deionised water and stirred for 15 minutes. HPMC was then added gradually, and mixed slowly for 24 h before experiments in order to preserve polymer integrity and to ensure that the solutions were bubble-free. This process was performed at room temperature.

8.2.2 Solution properties

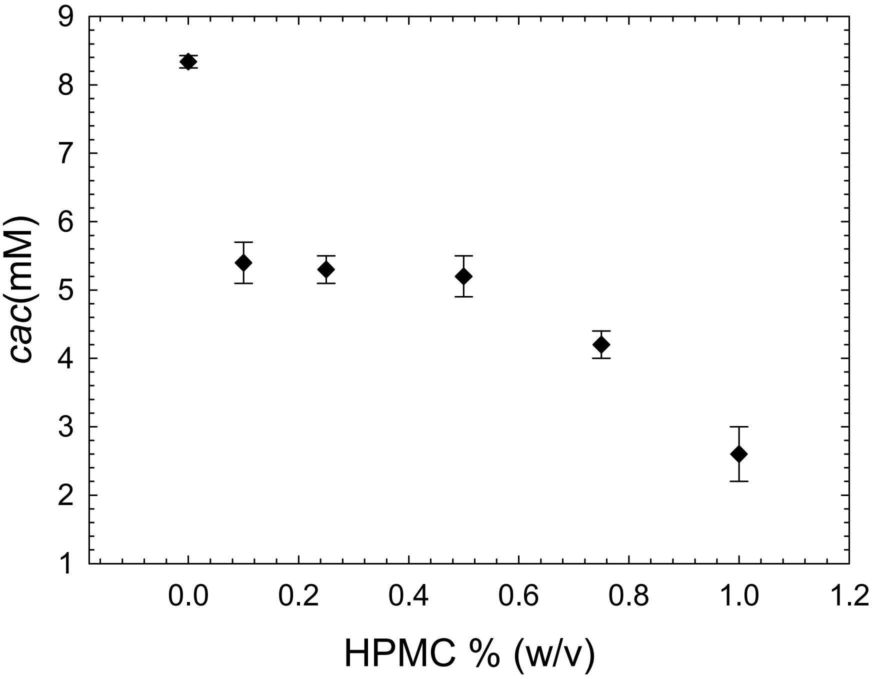

Fig. 8.1 The change in *cac* due to changes in HPMC concentration at 25 ^{o}C. This data was taken from Silva *et al.* [41], where electrical conductivity tests were used to determine values. This HPMC variant (trade name Methocel K15M, methoxyl content 19–24 %, hydroxypropyl content 7–12 %) has the properties of $M_w = 430,000$ Da, $[\eta] = 8.35$ dL/g, and $c^* = 0.09$ [49], which is comparable to the one used in the study presented here and serves as an indicator. Note: the critical micelle concentration for SDS in pure water is at $cac = 8.34$ mM [41], which is the concentration at which these surfactant particles will begin to group and form micelles.

For HPMC, it is implied that coil overlap occurs at a critical concentration of $c^* = 0.77/[\eta] = 0.117$ % (w/v) [177]. The data in Fig 8.1 indicates that the *cac* plateaus at lower HPMC concentrations, but falls significantly at higher concentrations. It has been suggested that the likely reason for this is that hydrophobic regions begin to grow as the degree of overlap between HPMC molecules increases, which increases hydrophobic site association [41]; at low HPMC concentration, hydrophobic parts within each HPMC molecule associate with each other and not many of them are available to associate with the surfactant. Hence, high surfactant concentrations are required to achieve *cac*. At high concentrations of HPMC, intermolecular associations dominate, causing open networks to form. This exposes more hydrophobic segments (per molecule) to the surfactant, thus requiring lower *cac* levels.

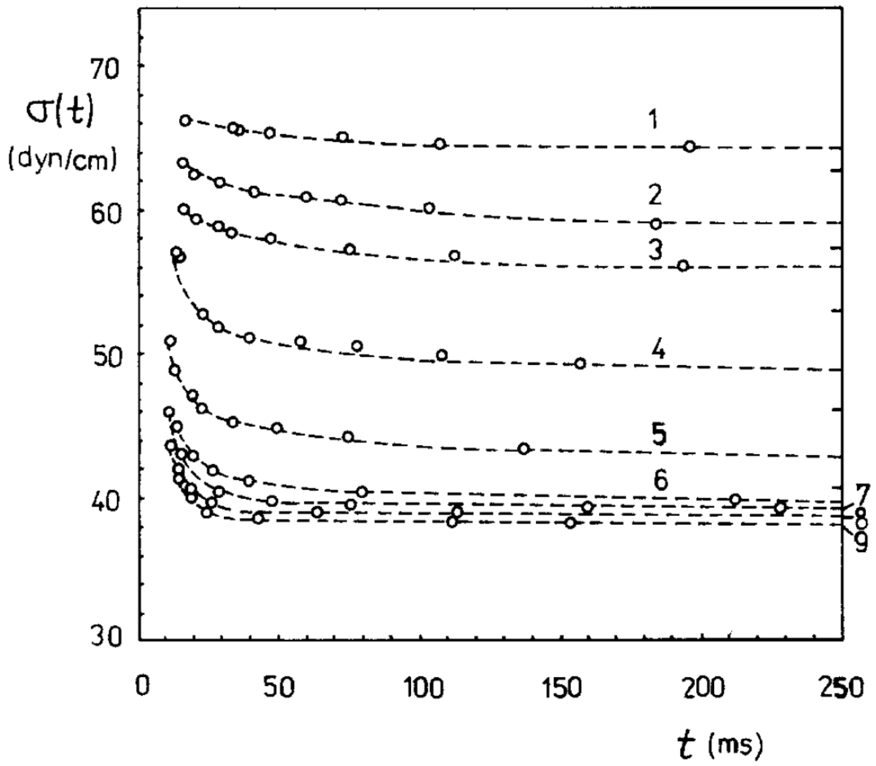

Fig. 8.2 The dynamic surface tension changes of SDS in water over time, sourced from [50]. The data curves show dynamic surface tension for (1) 2 (2) 3 (3) 4 (4) 6 (5) 8 (6) 12 (7) 16 (8) 24 (9) 32 mM.

Being a surfactant, the dynamic surface tension that arises from an additive such as SDS must be considered as the creation of a filament from a drop exposes new surface area and may affect analysis. The largest changes in surface tension for SDS in water occur in the first 10 – 20 ms or so of exposure [50]. Our experiments range from several ms to tens of ms, so surface tensions may be dynamic during our filament break-up experiments in some cases. Despite this, the changes in surface tension are quite mild, with the most severe changes spanning only 6 or so dyn/cm in 10 ms. Therefore, we use the steady state values of surface tension in our extensional viscosity extraction analyses.

8.2.3 Extensional viscosity extraction from filament break-up data

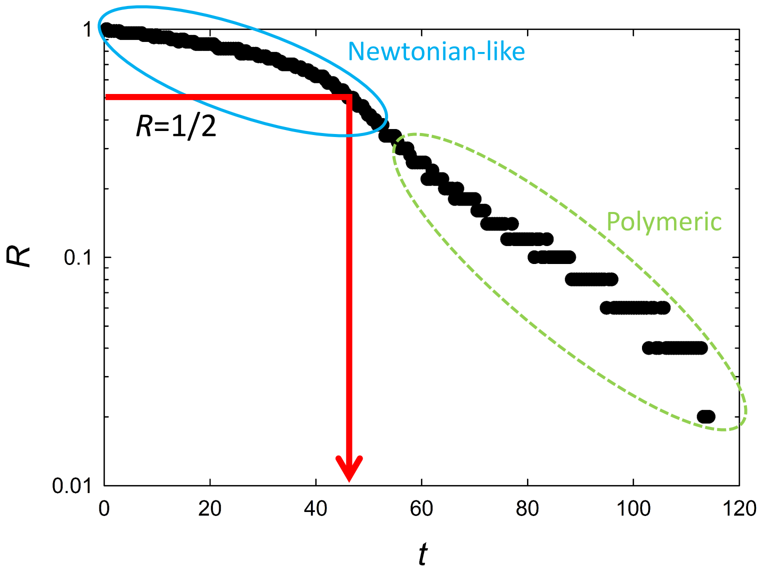

Fig. 8.3 Non-dimensionalised radius as a function of time data for a polymeric HPMC solution. Break-up begins with linear Newtonian-like decay past $R = 1/2$, allowing the initial viscosity to be extracted using the approach described in Sec. 4.4, before strain-hardening effects occur. Decay then becomes exponential towards final break-up as polymeric stresses retard filament thinning; the filament at this point is long and near-cylindrical, meaning that the mid-filament stress balance discussed in Sec. 4.3.1 can be used to extract extensional viscosity during the strain-hardening phase.

Two methods are used in this chapter to extract extensional viscosities. The first approach extracts data when the filament still has high curvature (discussed in Sec. 4.4, and Chapters 5, and 7), and is used here to quantify the break-up before stresses due to the stretching of polymer chains dominate near final break-up, like the decay seen in the initial stages of break-up in Fig. 8.3.

The second approach is discussed in Sec. 4.3.1, and is applied when long-lived near-cylindrical fluid filaments form near break-up due to dominating polymeric stresses (like the filament decay seen in the latter stages of break-up in Fig. 8.3), permitting the assumption that the fluid filament has negligible axial curvature. This allows the use of a simplified mid-filament governing stress balance; this comprises the relative stress contributions of inertia, surface tension, solvent viscosity, and non-Newtonian stresses, as is seen in the approach of Entov and Hinch [87] and Tirtaatmadja *et al.* [88];

$$\frac{1}{2}\rho\dot{R}(t)^2 = \frac{\sigma}{R(t)} - 3\eta_s\dot{\varepsilon} + N_{1,p}, \tag{8.1}$$

where η_s is the solvent shear viscosity, $\dot{\varepsilon}$ is the strain rate, and $N_{1,p}$ is the time-dependent normal stress difference that represents the stress contribution from the polymer. $\dot{R}(t)$ data was obtained by fitting a polynomial to *R versus t* break-up data, which could then be differentiated accordingly. Using break-up data and externally measurable properties (σ, ρ and η_s) it is possible to determine $N_{1,p}$ and in turn the polymer contribution to the extensional viscosity $\bar{\eta}_p = -N_{1,p}/\dot{\varepsilon}$. This procedure was employed to extract extensional viscosities at the final stages of break-up when the necking portion of the filaments could be assumed to be cylindrical, also allowing the investigation of possible strain-hardening effects near filament break-up.

8.3 Results and discussion

Preliminary testing was required to determine that SDS did not induce any unusual phenomena as a sole additive to water. Concentrations as high as 35.51 mM of SDS only had the effect of increasing shear viscosity by 0.3 mPa·s over pure water. Furthermore, Newtonian-like break-up was also observed at concentrations as high as 35.51 mM. Therefore, subsequent observed rheological changes of polymer and surfactant mixtures could be attributed to the combination of water, HPMC, and SDS. For the purposes of discussion, SDS concentrations of 0.55 mM will be termed low, 1.11 and 2.22 mM will be termed mid, and 4.44 and 8.88 mM will be termed high.

8.3.1 Properties at early strains

Fig. 8.4, left panel, shows that a steep drop in extensional viscosities occurred as SDS was added to the HPMC solutions, the data of which were obtained during linear filament decay using the first technique described in Sec. 8.2.3 (and in Sec. 4.4, and Chapters 5 and 7). The gradient of this decrease plateaued for all samples, but for 0.52 and 1 % (w/v) HPMC concentrations viscosity increased at higher SDS concentrations. Corresponding qualitative behaviour occurred in shear viscosity data obtained *via* constant shear experiments (Fig.

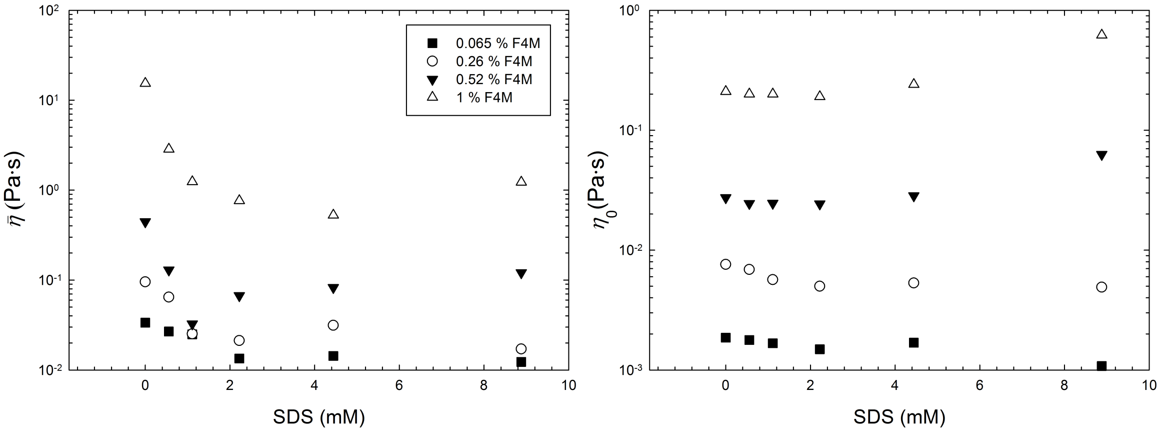

Fig. 8.4 (Left panel) Extensional viscosity as a function of SDS concentration for HPMC solutions using the first extensional viscosity extraction approach described in Sec. 8.2.3, where measurements are taken during Newtonian-like decay at $R = 1/2$ — Hencky strain of ≈ 1.4. (Right panel) Shear viscosity as a function of SDS concentration for HPMC solutions, measured at a constant shear rate $\dot{\gamma} \approx 15$ s^{-1}; the shear measuring techniques available to us were unable to resolve changes in the storage modulus G' and loss modulus G" for most of these low viscosity samples, and thus their analysis was not pursued in this study which nevertheless primarily focuses on extensional measurements. Note: these viscosities effectively assess total viscosity, including both polymeric and solvent contributions, *i.e.* $\bar{\eta} = \bar{\eta}_p + \bar{\eta}_s$ and $\eta = \eta_p + \eta_s$ for extensional and shear viscosities, respectively. Also, extensional viscosity extracted before strain-hardening sets in is at a Weissenberg number Wi$\lesssim$1 (the Wi describes the balance of elastic *versus* viscous effects and is discussed later in this chapter), and so we expect $\bar{\eta} \approx \bar{\eta}_0$ in Fig. 8.4. Similarly, $\dot{\gamma} \approx 15$ s^{-1} corresponds to a shear Wi much smaller than 1. Therefore, the shear viscositeis are likely to be close to the zero-shear-rate values. This is why we denote them as η_0.

8.4, right panel), though the order of magnitude changes in viscosity that occurred in the non-dilute solutions were not seen; it should be noted that the shear viscosities for the dilute solutions range as low as 1.1 mPa·s, which are problematic to analyse in typical FiSER or CaBER experiments. The lowest extensional and shear viscosity values of 0.52 and 1 % (w/v) HPMC solutions occurred between SDS concentrations of 2.2 and 4.4 mM, which approximately correlate with the *cac* values seen in Fig. 8.1. Moreover, the lowest extensional and shear viscosities for the lower polymer concentrations, 0.065 and 0.26 % (w/v) HPMC, were seen at 8.9 mM of SDS; this SDS concentration also roughly agrees with the corresponding *cac* values seen in Fig. 8.1.

The coincidence of reduced viscosities with the *cac* seen in our results has also been reported by others, as has the theoretical reasoning for this behaviour [40, 41, 174, 175] ; summarising the literature briefly, before the *cac* is reached the hydrophobic (charge neutral) sites on the HPMC polymer chains are repulsed by the free anionic surfactant molecules in the aqueous medium. This repulsion leads to a shrinking of the polymer molecules, progressing them towards a coil-to-globule conformation [41], see Figs. 8.5 (middle row). As the *cac* is reached the surfactant molecules begin to bind to the hydrophobic sites along the polymer. This charges the association sites along the polymer, which are then repulsed by one another, leading to the polymer-surfactant complex to swell, see Figs. 8.5 (bottom row). Furthermore, the creation of mixed micelles at the hydrophobic sites along the polymer chains above the *cac* are believed to not only result in some intramolecular bonding, but also promote cross-linking between polymer molecules to form polymer-surfactant complex networks, see Figs. 8.5 (bottom row). This expansion of the polymers — increasing intermolecular interactions — and the occurrence of intermolecular cross-linking is believed to be responsible for the increases in viscosity seen in these solutions above the *cac*. Furthermore, the data in Fig. 8.4 demonstrates that there is a clear difference in the magnitude of viscosity sensitivity to changes in SDS concentration between extensional capillary break-up experiments and constant shear flows. The initial reduction in viscosities were greater in the break-up experiments than for the shear experiments, with the magnitude of change increasing with increasing HPMC concentration. This may be attributed to the effects of extensional flow itself; it stretches polymers and effectively increases the number of intermolecular interactions that occur, which does not occur to the same degree in shear flows [174], although we would expect increased viscosity signals in oscillatory shear flow experiments. Thus, as SDS is added and polymer chains shrink (while below the *cac*) it is reasonable to suggest that the effect will be greater in extensional flow as the stretching of polymers is hindered and intermolecular interactions diminish, an effect that is more pronounced at higher polymer concentrations due to increased polymer chain overlap [174].

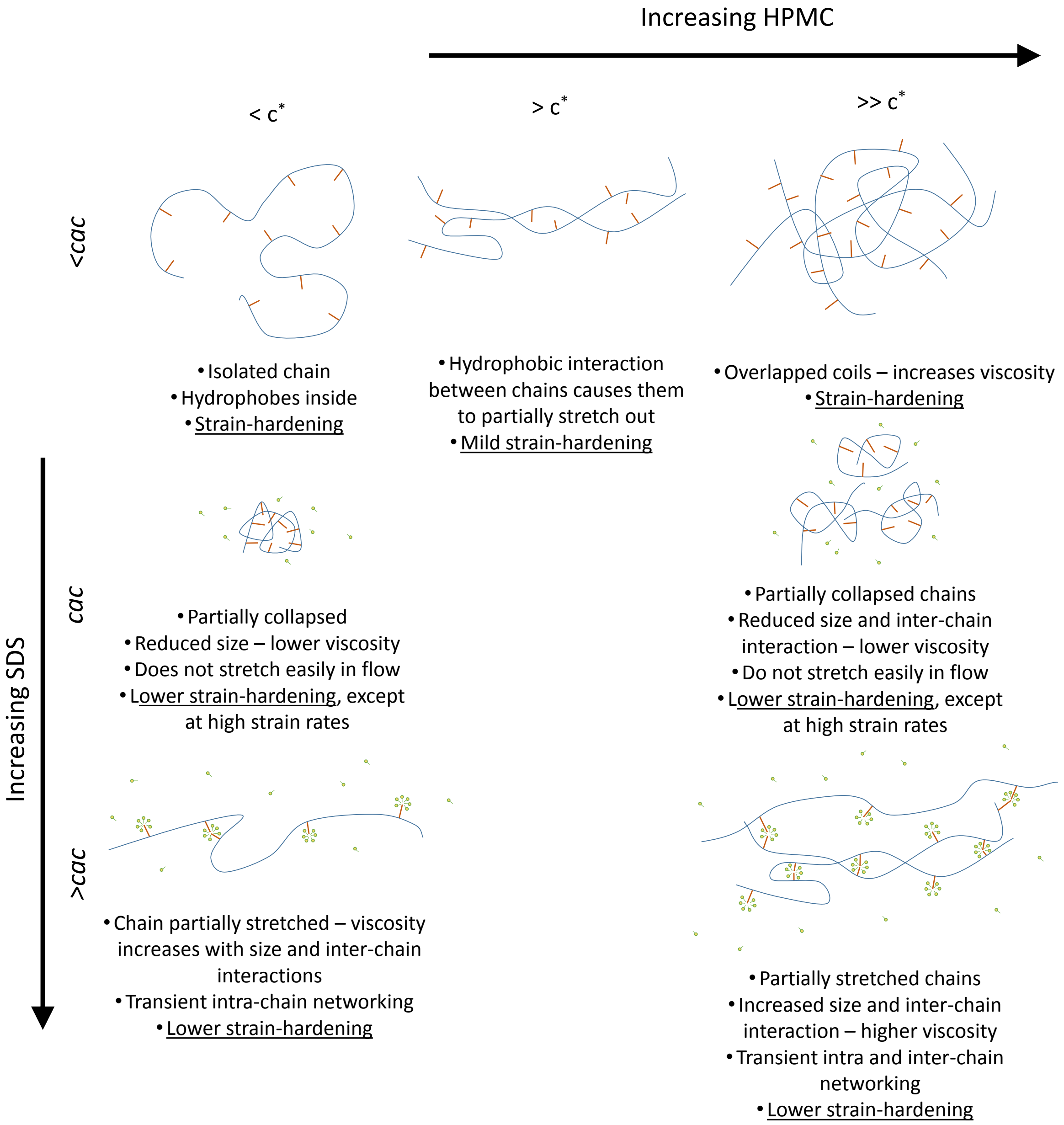
Increasing HPMC
< c*
> c*
>> c*
<cac
• Isolated chain
• Hydrophobes inside
• Strain-hardening
• Hydrophobic interaction between chains causes them to partially stretch out
• Mild strain-hardening
• Overlapped coils – increases viscosity
• Strain-hardening
Increasing SDS
cac
• Partially collapsed
• Reduced size – lower viscosity
• Does not stretch easily in flow
• Lower strain-hardening, except at high strain rates
• Partially collapsed chains
• Reduced size and inter-chain interaction – lower viscosity
• Do not stretch easily in flow
• Lower strain-hardening, except at high strain rates
>cac
• Chain partially stretched – viscosity increases with size and inter-chain interactions
• Transient intra-chain networking
• Lower strain-hardening
• Partially stretched chains
• Increased size and inter-chain interaction – higher viscosity
• Transient intra and inter-chain networking
• Lower strain-hardening

Fig. 8.5 Graphical depictions of polymer behaviour: in the case of increasing polymer concentration (from left to right panels) and increasing surfactant concentration (from top to bottom panels). (Top left) A polymer chain (blue) and its hydrophobes (orange) with no SDS added and below c*. (Top middle) Polymer chains expand slightly as hydrophobes between chains interact at mild polymer concentrations. (Top right) Chains overlap at high concentrations. At approximately the *cac*, coil-to-globule conformation results from the repulsion of polymer chain hydrophobes from the anionic surfactant molecules (green) in low (middle left) and high polymer concentrations (middle right); this is believed to be responsible for the reduction in viscosity measurements around the *cac*, as seen in Fig. 8.4. At high surfactant concentrations, mixed micelles create polymer-surfactant complexes, which are like-charged and cause the polymer chains to not only swell in the dilute polymer case (bottom left), but to swell and network *via* shared mixed micelles at higher polymer concentrations (bottom right). It should be noted that intramolecular interactions caused by mixed micelles are also depicted in the bottom two images. The expansion of polymer chains at high surfactant concentrations and the transient mixed micelle bonds that form are believed to reduce strain-hardening effects.

8.3.2 Properties at late strains

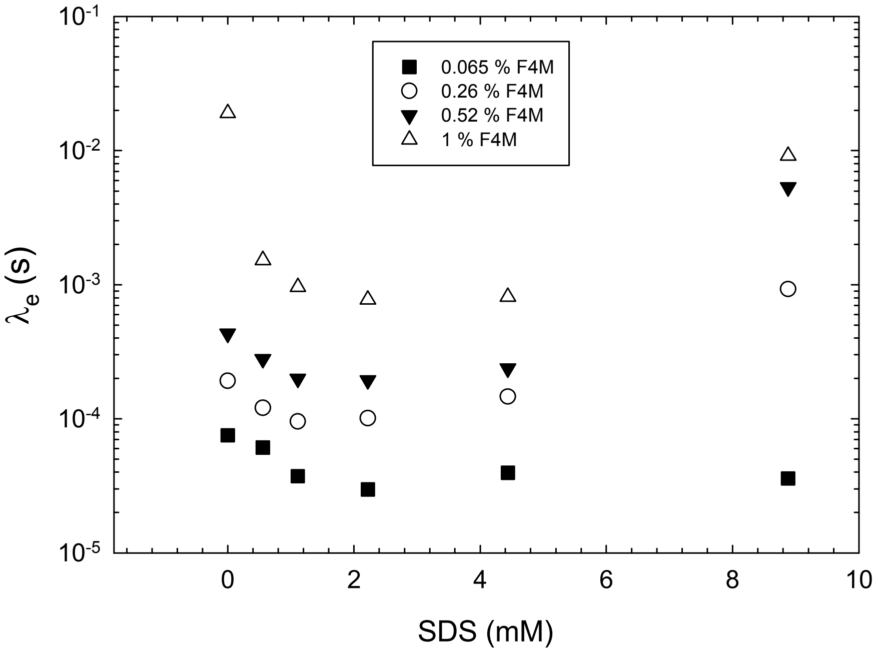

Fig. 8.6 Relaxation time as a function of SDS concentration for HPMC solutions. Note: these results were taken towards the end of break-up when filaments were near-cylindrical.

Extensional properties can also be quantified by the relaxation time λ_e (see Fig. 8.6), which acts as an indicator of the elasticity caused by the polymeric component, as described in Chapter 7. This analysis was applied at the very final moments before filament break-up when total strain is high, as opposed to the extensional viscosity measurements seen in Fig. 8.4 which begin at earlier strains. The most notable behaviour at this point was that all HPMC concentrations saw dramatic increases in elastic effects after a minimum between 1.1 and 2.2 mM SDS, which roughly coincides with the *cac* seen at the highest HPMC concentration in Fig. 8.1. The general qualitative increases seen after the minima in Fig. 8.6, as opposed to the behaviours seen in Fig. 8.4, may be due to modified intermolecular interactions induced by the stronger flows that occur as filaments decay. Others have observed extensional thickening occurring at critical strain rates, which are typically high in capillary experiments towards final break-up, in semi-dilute polymer-surfactant solutions [174]. It is supposed that elongational flow can be strong enough to break the temporary intramolecular bonds between hydrophobic sites along a polymer that can occur above the *cac* (Fig. 8.5, bottom row)) and expose polymer chain hydrophobes to more intermolecular cross-linking through shared mixed micelles, which would lead to further stress increases as filaments become thinner since intermolecular bonding is believed to be stronger than intramolecular bonding [155, 174].

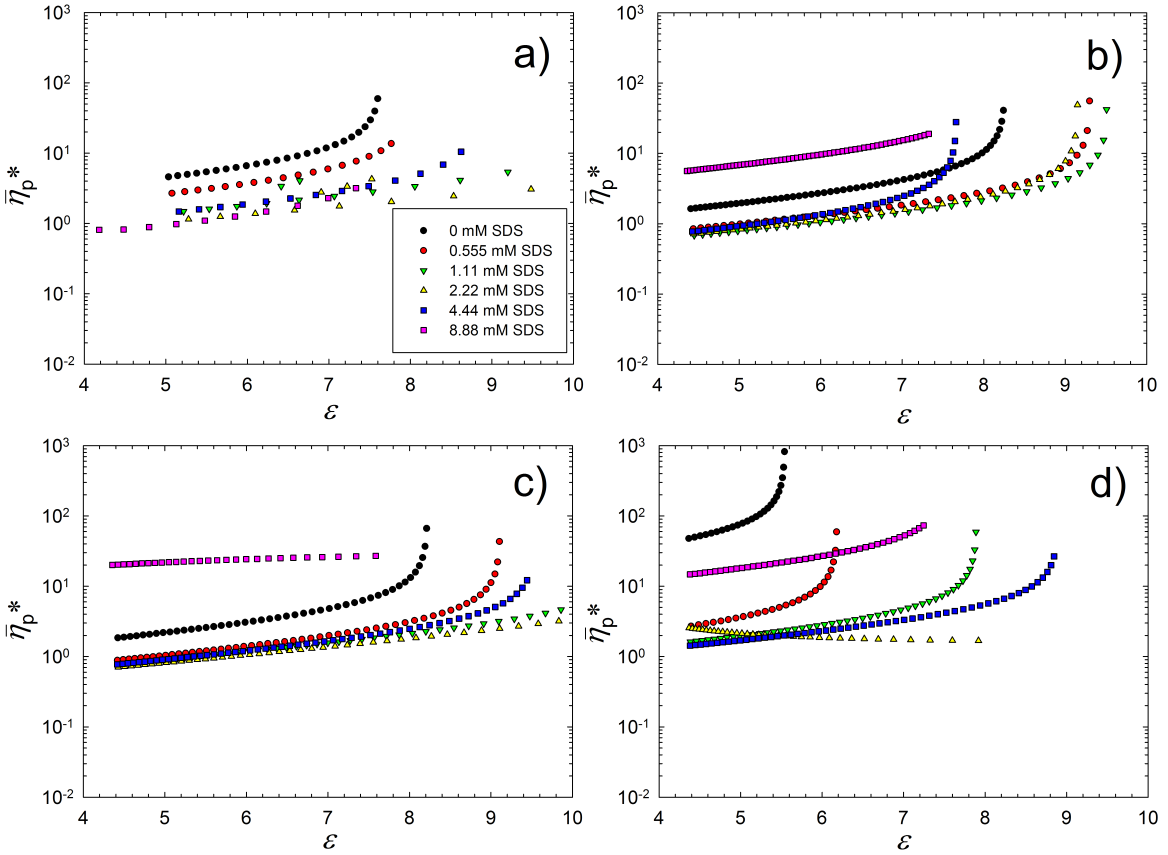

Fig. 8.7 The effect of SDS concentration on extensional viscosity $\bar{\eta}_p^*$ due to polymeric contribution as a function of strain: (a) 0.065 % (w/v) HPMC; (b) 0.26 % (w/v) HPMC; (c) 0.52 % (w/v) HPMC; and (d) 1 % (w/v) HPMC. Note: extensional viscosity is scaled as $\bar{\eta}_p^* = \bar{\eta}_p / c_p \eta_s$, where c_p is the percentage concentration of HPMC and η_s is the shear viscosity in the absence of HPMC. Note: these results were taken towards the end of break-up when filaments were near-cylindrical. It should, however, be stated that the 0.065 % (w/v) HPMC solutions with 1.11 mM of SDS and above exhibited end-pinching behaviour (as seen in Fig. 8.8), meaning that they cannot reliably be used to make extensional viscosity measurements since the filaments are not completely uniform and do not self-affinely neck.

Extensional viscosity data at the final stages of filament break-up is shown Fig. 8.7, which uses the mid-filament analysis described in Sec. 8.2.3 (also seen in Sec. 4.3.1). At dilute HPMC concentrations, overall extensional viscosities were lower after SDS was added and strain-hardening was reduced significantly, as shown in Fig. 8.7a; though, it should be noted that at mid to high SDS concentration filaments tended to pinch at their ends and form mid-filament globules, as seen in the image sequence Fig. 8.8a and 8.8b, meaning that observing the thinning of the thinnest part of the filament was not representative of the

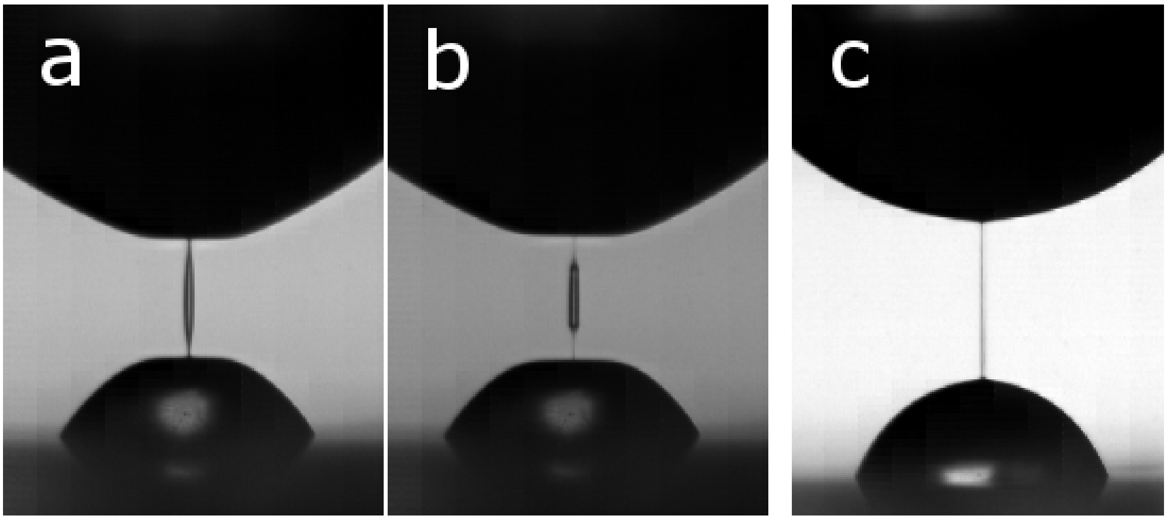

Fig. 8.8 (a and b) The thinning sequence of 0.065 % (w/v) HPMC with 8.8 mM of SDS near final break-up. (c) The uniform filament is formed by 0.52 % (w/v) HPMC with 8.8 mM of SDS.

whole filament. This phenomena was not observed for non-dilute HPMC solutions with high SDS content, see Fig. 8.8c, where filaments decayed with a uniform radius until break-up. The reason for this difference is not understood, but perhaps discrete polymer-surfactant complex networks form at dilute HPMC concentrations, resulting in inertia dominated thinning occurring around them. These types of break-up behaviours are anticipated for purely polymeric solutions [178].

In non-dilute cases, Figs. 8.7b, 8.7c, and 8.7d, all extensional viscosities initially decreased with the addition of SDS and then increased when SDS went above a concentration of 2.2 mM, which largely agrees with the point at which increases were seen in relaxation time values (Fig. 8.6), around the *cac* of 1 % (w/v) HPMC. Furthermore, at intermediate HPMC concentrations (Figs. 8.7b, and 8.7c), solutions with 8.8 mM SDS exceeded the extensional viscosities of their SDS-free counterparts, probably due to the stress contributions of polymer-surfactant complex swelling and networking. At the highest HPMC concentration (Fig. 8.7d), 8.8 mM SDS solution viscosities were exceeded by the SDS-free formula, which is believed to be due to the reduced availability of surfactant molecules to create mixed micelles relative to the elevated polymer concentrations. Interestingly in Fig. 8.7, SDS-doped solutions above the *cac* appeared to have relatively steady extensional viscosities with delayed and reduced strain-hardening, unlike sub-*cac* solutions, particularly at the highest SDS concentrations. Fig. 8.7 shows strain-hardening and viscosity to be reduced around the *cac*, as is expected as polymers go from coils to globules in the presence of SDS and polymer stretching becomes suppressed (Fig. 8.5). Fig. 8.7 also shows that at higher SDS concentrations strain-hardening is delayed and viscosity increases, which is believe to be due to like-charged mixed micelles causing polymer chains to be expanded into large rod-like conformations, even in the absence of flow (Fig. 8.5); the delay of strain-hardening is also expected to occur at HPMC concentrations above c^* due to intermolecular interactions between polymers causing them to partially expand. Furthermore, it is known that polymer-surfactant networking through hydrophobic associations promoted by SDS can constantly break down and reform in very short times [150] (in the order of milliseconds, which is of the same order of time or lower than the break-up of the long-live filaments seen here), creating self-healing networks made up of reversible cross-linkages. This might allow for the polymer-surfactant complex networking that occurs at high SDS concentrations to steadily break and reform, as opposed to the finite stretching that occurs in elongational flows when only polymer molecules are present, which leads to strain-hardening. This may manifest as elevated viscosities and less aggressive stress build up at earlier strains (when compared to SDS-free formulas), as was demonstrated by the non-dilute solutions with the highest SDS concentration (Figs. 8.7b, 8.7c, and 8.7d).

The Weissenberg number $\mathrm{Wi} = \dot{\varepsilon}\lambda_\mathrm{e}$ represents the contribution of elastic *versus* viscous effects and is used here to further analyse the behaviour of the filaments during their final break-up, Fig. 8.9. We can see that most data initially begin to rise, indicating Newtonian like behaviour. Most data then reach a maximum and begin to decrease, meaning filaments become more elastic at this point — except for the highest HPMC concentration with low or no SDS, which immediately decrease to signal increasing elastic behaviour. However, some data flattens or continuously increases in Wi, which indicates that these samples are elastically weak. This behaviour occurs in some samples with SDS content at or above the *cac*. Once again, this is believed to be due to the coil-to-globule conformation of polymers around the *cac*, and the expansion of polymers into long rod-like molecules when mixed micelles form at high SDS concentrations, making these solutions less like typical polymer solutions and more like suspensions of globules and rods, respectively.

8.4 Conclusion

The extensional properties of polymer (HPMC) solutions with surfactant (SDS) additive were analysed using the acoustically driven microfluidic extensional rheometer, which allowed access to the challenging low-viscosity fluids featured in this study. Despite the extensive study of molecular interactions between polymers and surfactants by others, and

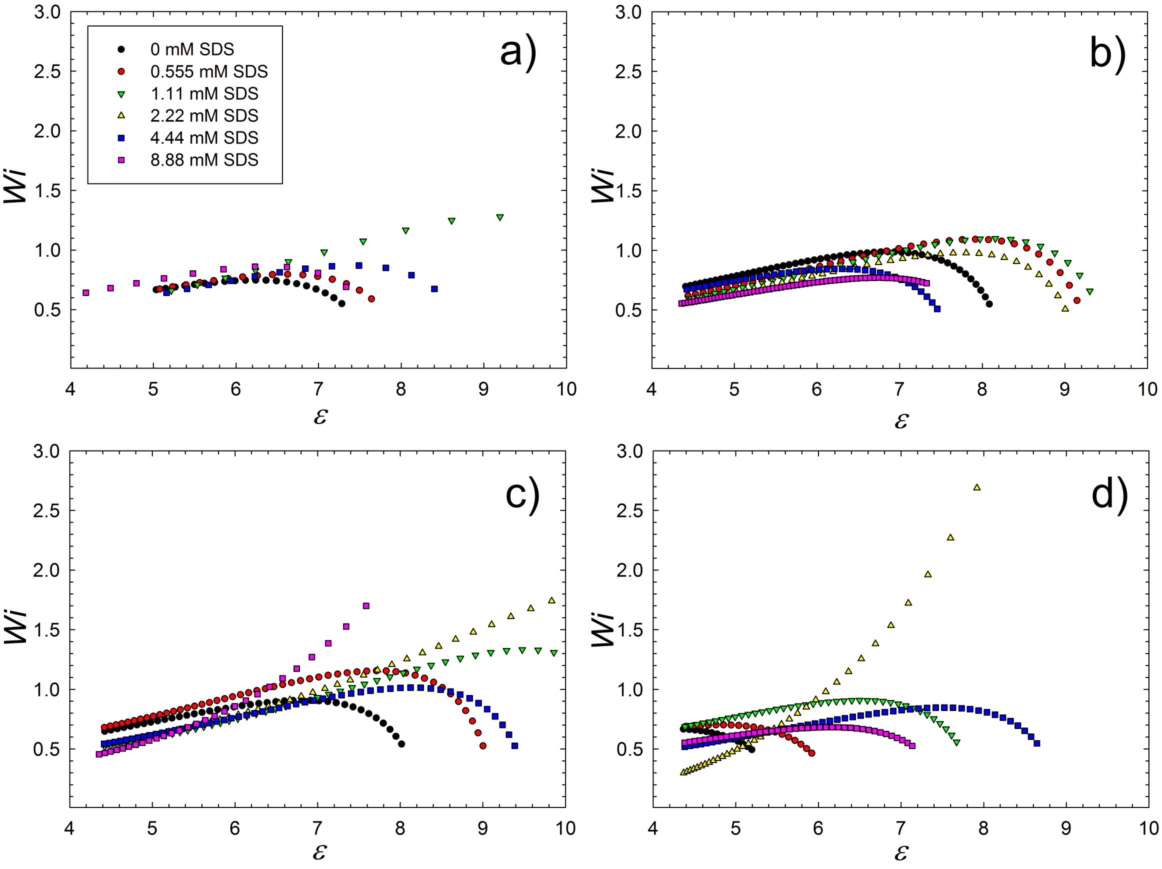

Fig. 8.9 Weissenberg number against strain for: (a) 0.065 % (w/v) HPMC; (b) 0.26 % (w/v) HPMC; (c) 0.52 % (w/v) HPMC; and (d) 1 % (w/v) HPMC. Note: these results were taken towards the end of break-up when filaments were near-cylindrical.

their importance to many industrial processes and applications, there are few studies pertaining to their bulk properties under extensional flow. Furthermore, to our knowledge, there are no studies that have utilised the unique attributes of capillary break-up rheometry in studying these systems.

According to the theory and studies of others [40, 41, 174, 175], the addition of SDS to HPMC in water is expected to cause significant conformation changes to the polymer and also promote networking between hydrophobic sites, and in turn to considerably affect bulk viscosity. We observed order of magnitude changes in extensional properties at early and late stages of filament break that were dependent on the concentration of SDS. These changes were qualitatively reflected in the results acquired through shear rheometry at steady shear rates — the available shear techniques were not able to resolve measurements taken in oscillatory shear experiments for these low-viscosity fluids.

These results are preliminary and require more research, particularly in the form of oscillatory shear experiments and modelling (as has been done for HEUR solutions [156]), in order to predict and fully understand the effects of concentration, flow, and molecular structure — this is beyond the scope of this study. Nevertheless, this investigation demonstrates that the acoustically driven microfluidic extensional rheometer can make quantitative measurements of these systems in extensional flow and demonstrated that these these biocompatible and widely used solutions have interesting behaviours in extensional flow that require further investigation.

Chapter 9

Conclusions

This final chapter summarises the contributions this thesis has made to rheology and the understanding of novel complex fluids. Finally, it concludes with the questions raised by this thesis and provides recommendations on possible future work.

9.1 Contributions

In this study, a new rheometric device has been developed for analysing the extensional properties of challenging but important low-viscosity liquids. The experimental results have been compared with results from established techniques and analysed using standard rheological methods, as well as being modelled, and show good agreement with expectations. The abilities and advantages of this system hinge on the unique capabilities that SAWs possess, which can dramatically and harmlessly manipulate sophisticated low-viscosity fluids at small scales. The principal contributions of this thesis are summarised in the following paragraphs.

Chapter 2 explores the development of the system and how it overcomes the problems faced by conventional methods, and emphasises its advantages.

Chapter 3 defines the conditions under which SAWs can be used to generate fluid filaments for the uses of filament break-up rheometry. Additionally, it validates several results from acoustically-driven microfluidic extensional rheometry against data from an established technique using conventional analysis methods, and demonstrates the potential of the technique to assess the extensional properties of challenging dilute polymer solutions. Finally, the potential for extensional flow analysis to be used in the study of complicated biological material is demonstrated in the unusual break-up profile of a low-viscosity dilute multimeric protein solution.

Chapter 4 highlights the problems of two-dimensional stress-balance analysis when analysing the filament break-up of low-viscosity fluids that are sensitive to both inertial and viscous contributions. Importantly, it defines a method for normalising experimental data to enable the extraction of the extensional viscosities of unknown low-viscosity fluids.

Chapter 5 validates predictions on the effect that swimming microbes have on extensional viscosity for the first time. The variety of delicate microbes tested here are prohibitively difficult to produce in large amounts and do not remain motile for long periods of time, which made the acoustically-driven system's ability to quickly test tiny volumes without causing damage to delicate particles critical. The results here were modelled, leading to the conclusion that key particle parameters that are challenging to define can greatly influence bulk fluid properties.

Chapter 6 presents the extensional data of a variety of suspensions contain containing micro and nano particles of different morphologies. Empirical modelling showed extensional viscosity to have a strong dependency on particle size for cuboidal particles. More advanced modelling of particles with appreciable aspect ratios showed good agreement with large particles, but poor agreement with nano particles. The reasons for the above observations were believed to be due to particle clustering caused by DLCA, which was visually confirmed for some particles. Thus, the results here demonstrated that purely accounting for hydrodynamic stresses does not predict experimental viscosities well for suspensions of small particles. The results presented here are also anticipated to be useful for the development and application of several of the particles in inks and coatings.

Chapter 7 documents the utility of the new system in analysing the extensional properties of copper nanowires, which have a promising future in the advancement of electronics, where their likely industrial application through inkjetting and sprays requires knowledge of their extensional properties. The analysis, made possible using our system, showed an extremely high viscosity sensitivity to volume fraction, important for extensional application processes that operate with narrow viscosity ranges. It was also found that the necessary polymer additive that maintained particle suspension could greatly affect filament break-up, but also that it was dependent on the ratio between particle and polymer content, which can be manipulated to optimise solution formulation.

Chapter 8 focuses on the analysis of dilute and concentrated polymer-surfactant solutions, which have wide-ranging industrial applications, using our capillary break-up experiments. The high sensitivity of extensional viscosity to surfactant concentration of these solutions was illustrated. Furthermore, these experiments showed that material properties were also dependent on the evolution of filament break-up, where it is believed that capillary thinning flow can significantly affect rheological behaviour, particularly for dilute suspensions. It was found that filament evolution profiles near final break-up were affected by surfactant concentrations, which is believed to be due to the rapid and reversible cross-linking induced by surfactant hydrophobic associations at higher concentrations.

Techniques that allow us to understand the properties of fluids are indispensable as we seek to better understand the complex fluids around us, and constantly develop more fluids to be used in an ever increasing number of applications. Extensional flows constitute a fundamental branch in the study of fluid properties, and low-viscosity fluids represent an incredibly wide range of diverse fluids that are of industrial, biological, and academic interest. Therefore, the ability to analyse low-viscosity fluids using the unique capabilities of this acoustically-driven technique has led to the answering and raising of questions that are important to the advancement of our understanding of material properties and can be of utility in future studies of thin complex fluids.

9.2 Continuing and future work

The studies conducted in this thesis highlight opportunities for further research into important questions.

Chapter 3 also raises the possibility of using extensional flow to analyse complicated protein molecules. Such a study would require standard but complicated analysis techniques to contrast with extensional measurements, but may pave the way for simple extensional measurements to be used to conduct quick assays of protein molecules.

Chapter 4 explored the difficulties associated with a two dimensional analytical approach to extracting the extensional viscosity of low-viscosity fluids due to the competing influences of interia, viscosity, and dynamic filament curvature. There is perhaps scope to further develop this analytical approach, which focuses on the mid-filament of a thinning liquid bridge, since it would maintain the practicality of taking simple filament radius measurements. However, it would also be possible to investigate a full filament approach to analysing experimental data, which would require more advanced image analysis and the employment of a more sophisticated stress-balance expression [5] that takes into account more detail, such as axial curvature. There are also many improvements that could be made to the operation of the experimental technique that would make it even quicker and simpler to use. It could also benefit from more advanced features, such as temperature control, and the measurement of tensile force, for example. However, such improvements were not necessary for the work presented in this thesis.

The complexities of the microbe particles in Chapter 5 led to several open questions regarding particle properties and how they affect bulk fluid properties. Two important unknowns were the effect of extensional flow on particle swimming speed, and the effect on changes in their swimming direction; it is known that shear gradients affect the swimming of algal microbes [179], for example.

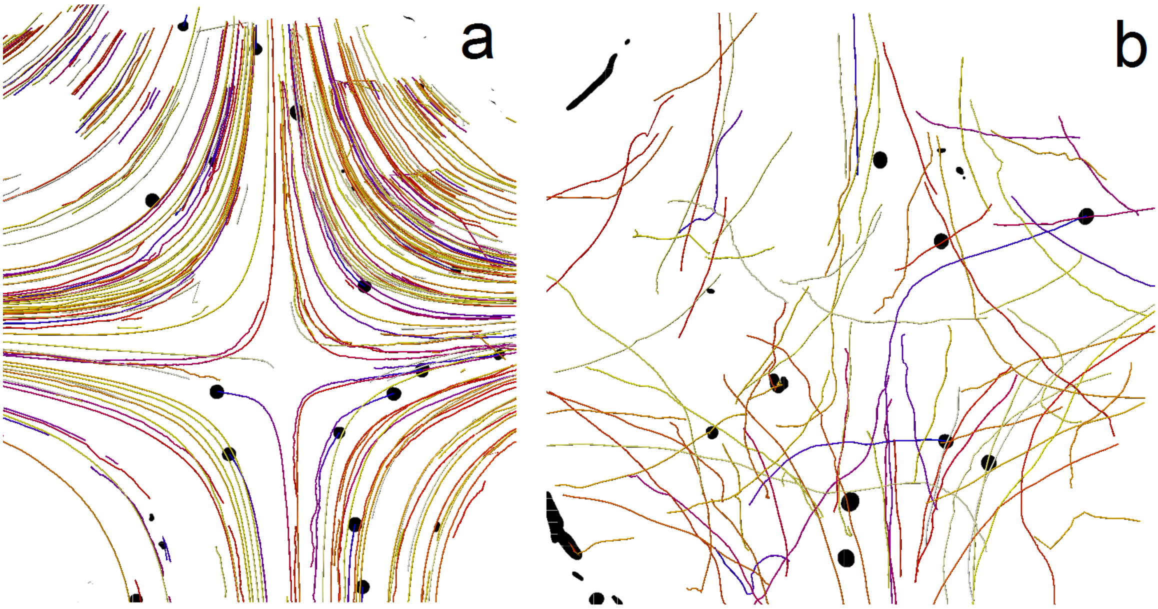

Fig. 9.1 Particle trajectories in cross-slot extensional flow of passive algal swimmers (left) and active algal swimmers (right). Both images are taken at a strain rate of 1 s^{-1} using *Dunaliella tertiolecta*.

Preliminary investigations using a microfluidic cross-slot extensional flow device, like the type discussed in by Perkins (1997) [180], were conducted and showed that live algal microbes did not allow themselves to be simply carried by flow, but swam across and against extensional flow streamlines, see Figs. 9.1. The data from these observations was quantified using mean squared displacement analysis, like that seen in Chapter 5, and revealed a distinct difference between live and dead algal particles, perhaps hinting at their resistance to flow.

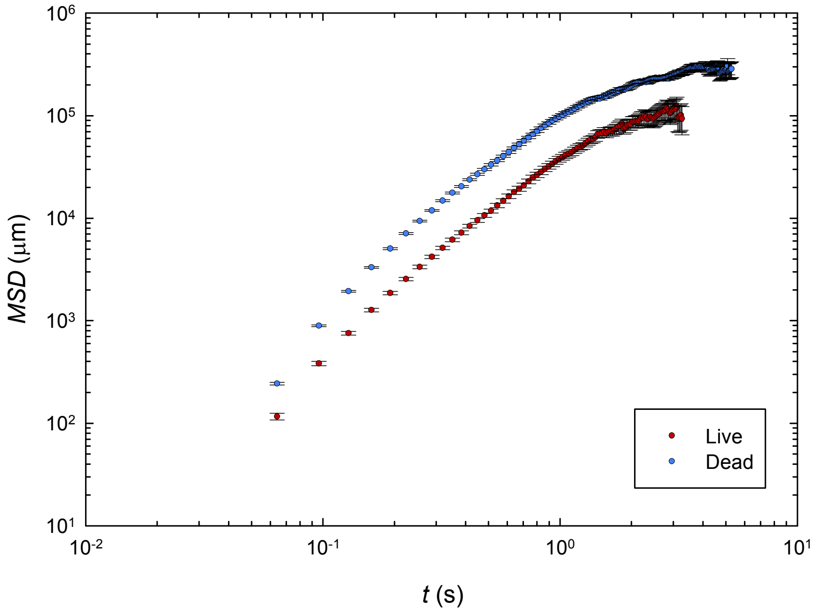

Fig. 9.2 Mean square displacement against time for the experiments seen in Figs. 9.1

Further quantification could be made by comparing the trajectories of swimming particles to the streamlines predicted for cross-slot extensional flow. Such an investigation would also benefit from quantifying particle orientation. Obviously an investigation like this would require substantial sophistication. Regardless, there appears to be definite differences between live and dead algal microbes in extensional flow. Another approach may be to use artificial motile particles, such as Janus particles [181], to eliminate some of these uncertainties and further hone the predictive models of active matter effects on bulk viscosities.

Limitations in Chapter 6 leave scope for further exploration into the role of particle clustering in viscosity changes. First, visualisation of clustering in suspensions under flow would be valuable in confirming suspicions regarding their role in viscosity changes. Second, it would also be interesting to further prove predictions *via* the direct control of particle aggregation, potentially through fields, modifiers of particle charge, or dispersants. Finally, there is a place here for more advanced modelling.

Chapter 8 showed that bulk properties of polymer-surfactant aqueous mixtures are very sensitive to both polymer and surfactant concentration, and probably flow too. Thorough modelling of these systems, like that done by [156], would no doubt provide deeper insights and understanding into these systems, which may prove useful to the many industrial users of such solutions.

References

[1] A. Bazilevsky, V. Entov, and A. Rozhkov, “Liquid filament microrheometer and some of its applications,” in *Third European Rheology Conference and Golden Jubilee Meeting of the British Society of Rheology*, pp. 41–43, Springer, 1990.

[2] G. H. McKinley and T. Sridhar, “Filament-stretching rheometry of complex fluids,” *Annu. Rev. Fluid Mech.*, vol. 34, no. 1, pp. 375–415, 2002.

[3] P. Dontula, C. W. Macosko, and L. Scriven, “Origins of concentric cylinders viscometry,” *J. Rheol. (1978-present)*, vol. 49, no. 4, pp. 807–818, 2005.

[4] V. Tirtaatmadja and T. Sridhar, “A filament stretching device for measurement of extensional viscosity,” *J. Rheol. (1978-present)*, vol. 37, no. 6, pp. 1081–1102, 1993.

[5] P. Szabo, “Transient filament stretching rheometer,” *Rheologica Acta*, vol. 36, no. 3, pp. 277–284, 1997.

[6] G. H. McKinley and A. Tripathi, “How to extract the Newtonian viscosity from capillary breakup measurements in a filament rheometer,” *J. Rheol.*, vol. 44, no. 3, pp. 653–670, 2000.

[7] L. E. Rodd, T. P. Scott, J. J. Cooper-White, and G. H. McKinley, “Capillary break-up rheometry of low-viscosity elastic fluids,” 2004.

[8] Y. W. Ooi and T. Sridhar, “Resistance to uniaxial extensional flow of fibre suspensions,” *Rheologica acta*, vol. 43, no. 3, pp. 223–231, 2004.

[9] D. Vadillo, T. Tuladhar, A. Mulji, S. Jung, S. Hoath, and M. Mackley, “Evaluation of the inkjet fluid’s performance using the "cambridge trimaster" filament stretch and break-up device,” *J. Rheol. (1978-present)*, vol. 54, no. 2, pp. 261–282, 2010.

[10] D. C. Vadillo, W. Mathues, and C. Clasen, “Microsecond relaxation processes in shear and extensional flows of weakly elastic polymer solutions,” *Rheol. Acta*, vol. 51, no. 8, pp. 755–769, 2012.

[11] L. Campo-Deano and C. Clasen, “The slow retraction method (srm) for the determination of ultra-short relaxation times in capillary breakup extensional rheometry experiments,” *J. Non-Newtonian Fluid Mech.*, vol. 165, no. 23, pp. 1688–1699, 2010.

[12] W. C. Nelson, H. P. Kavehpour, and C.-J. C. J. Kim, “A miniature capillary breakup extensional rheometer by electrostatically assisted generation of liquid filaments.,” *Lab Chip*, vol. 11, pp. 2424–31, Jul 2011.

[13] B. Keshavarz, V. Sharma, E. C. Houze, M. R. Koerner, J. R. Moore, P. M. Cotts, P. Threlfall-Holmes, and G. H. McKinley, “Studying the effects of elongational properties on atomization of weakly viscoelastic solutions using rayleigh ohnesorge jetting extensional rheometry (rojer),” *Journal of Non-Newtonian Fluid Mechanics*, vol. 222, pp. 171–189, August 2015.

[14] P. E. Arratia, J. P. Gollub, and D. J. Durian, “Polymeric filament thinning and breakup in microchannels,” *Phys. Rev. E: Stat., Nonlinear, Soft Matter Phys.*, vol. 77, no. 3, p. 036309, 2008.

[15] P. Bhattacharjee, A. M^{c}Donnell, R. Prabhakar, L. Yeo, and J. Friend, “Extensional flow of low-viscosity fluids in capillary bridges formed by pulsed surface acoustic wave jetting,” *New J. Phys.*, vol. 13, no. 2, p. 023005, 2011.

[16] A. G. McDonnell, T. C. Gopesh, J. Lo, M. O’Bryan, L. Y. Yeo, J. R. Friend, and R. Prabhakar, “Motility induced changes in viscosity of suspensions of swimming microbes in extensional flows,” *Soft matter*, vol. 11, pp. 4658–4668, 2015.

[17] Y. Hatwalne, S. Ramaswamy, M. Rao, and R. A. Simha, “Rheology of active-particle suspensions,” *Physical review letters*, vol. 92, no. 11, p. 118101, 2004.

[18] S. Ramaswamy, “The mechanics and statistics of active matter,” *The Mechanics and Statistics of Active Matter*, vol. 1, pp. 323–345, 2010.

[19] M. Marchetti, J. Joanny, S. Ramaswamy, T. Liverpool, J. Prost, M. Rao, and R. A. Simha, “Hydrodynamics of soft active matter,” *Reviews of Modern Physics*, vol. 85, no. 3, p. 1143, 2013.

[20] K. Drescher, J. Dunkel, L. H. Cisneros, S. Ganguly, and R. E. Goldstein, “Fluid dynamics and noise in bacterial cell–cell and cell–surface scattering,” *Proceedings of the National Academy of Sciences*, vol. 108, no. 27, pp. 10940–10945, 2011.

[21] A. Sokolov and I. S. Aranson, “Reduction of viscosity in suspension of swimming bacteria,” *Physical Review Letters*, vol. 103, no. 14, p. 148101, 2009.

[22] J. Gachelin, G. Miño, H. Berthet, A. Lindner, A. Rousselet, and É. Clément, “Non-Newtonian viscosity of escherichia coli suspensions,” *Physical review letters*, vol. 110, no. 26, p. 268103, 2013.

[23] R. Karmakar, R. Gulvady, M. S. Tirumkudulu, and K. Venkatesh, “Motor characteristics determine the rheological behavior of a suspension of microswimmers,” *Physics of Fluids (1994-present)*, vol. 26, no. 7, p. 071905, 2014.

[24] S. Rafaï, L. Jibuti, and P. Peyla, “Effective viscosity of microswimmer suspensions,” *Physical Review Letters*, vol. 104, no. 9, p. 098102, 2010.

[25] E.-o.-l. Ettefaghi, H. Ahmadi, A. Rashidi, S. Mohtasebi, and M. Alaei, “Experimental evaluation of engine oil properties containing copper oxide nanoparticles as a nanoadditive,” *Int. J. Ind. Chem.*, vol. 4, no. 1, pp. 1–6, 2013.

[26] W. Shen, X. Zhang, Q. Huang, Q. Xu, and W. Song, “Preparation of solid silver nanoparticles for inkjet printed flexible electronics with high conductivity.,” *Nanoscale*, vol. 6, no. 3, pp. 1622–8, 2014.

[27] S. Xie, Z. Ouyang, B. Jia, and M. Gu, “Large-size, high-uniformity, random silver nanowire networks as transparent electrodes for crystalline silicon wafer solar cells,” *Opt. Express*, vol. 21, no. 103, pp. A355–A362, 2013.

[28] S. E. Habas, H. A. Platt, M. F. van Hest, and D. S. Ginley, “Low-cost inorganic solar cells: from ink to printed device,” *Chem. Rev.*, vol. 110, no. 11, pp. 6571–6594, 2010.

[29] H. Guo, N. Lin, Y. Chen, Z. Wang, Q. Xie, T. Zheng, N. Gao, S. Li, J. Kang, D. Cai, and D.-L. Peng, “Copper nanowires as fully transparent conductive electrodes.,” *Sci. Rep.*, vol. 3, p. 2323, 2013.

[30] A. C. Myers, H. Huang, and Y. Zhu, “Wearable silver nanowire dry electrodes for electrophysiological sensing,” *RSC Adv.*, vol. 5, no. 15, pp. 11627–11632, 2015.

[31] S. Gong, W. Schwalb, Y. Wang, Y. Chen, Y. Tang, J. Si, B. Shirinzadeh, and W. Cheng, “A wearable and highly sensitive pressure sensor with ultrathin gold nanowires,” *Nat. Commun.*, vol. 5, 2014.

[32] S. Yao and Y. Zhu, “Wearable multifunctional sensors using printed stretchable conductors made of silver nanowires.,” *Nanoscale*, vol. 6, pp. 2345–52, Feb 2014.

[33] A. G. McDonnell, N. N. Jason, L. Y. Yeo, J. R. Friend, W. Cheng, and R. Prabhakar, "Extensional viscosity of copper nanowire suspensions in an aqueous polymer solution," *Soft matter*, 2015.

[34] S. Bhanushali, P. Ghosh, A. Ganesh, and W. Cheng, "1d copper nanostructures: Progress, challenges and opportunities," *Small*, vol. 11, pp. 1232–1252, 2015.

[35] J. Wu, J. Zang, A. R. Rathmell, X. Zhao, and B. J. Wiley, "Reversible sliding in networks of nanowires," *Nano Lett.*, vol. 13, no. 6, pp. 2381–2386, 2013.

[36] I. E. Stewart, A. R. Rathmell, L. Yan, S. Ye, P. F. Flowers, W. You, and B. J. Wiley, "Solution-processed copper–nickel nanowire anodes for organic solar cells," *Nanoscale*, vol. 6, no. 11, pp. 5980–5988, 2014.

[37] Y. Tang, S. Gong, Y. Chen, L. W. Yap, and W. Cheng, "Manufacturable conducting rubber ambers and stretchable conductors from copper nanowire aerogel monoliths," *ACS Nano*, vol. 8, no. 6, pp. 5707–5714, 2014.

[38] S. Han, S. Hong, J. Ham, J. Yeo, J. Lee, B. Kang, P. Lee, J. Kwon, S. S. Lee, M.-Y. Yang, *et al.*, "Fast plasmonic laser nanowelding for a cu-nanowire percolation network for flexible transparent conductors and stretchable electronics," *Adv. Mater.*, vol. 26, no. 33, pp. 5808–5814, 2014.

[39] Y. Tang, K. L. Yeo, Y. Chen, L. W. Yap, W. Xiong, and W. Cheng, "Ultralow-density copper nanowire aerogel monoliths with tunable mechanical and electrical properties," *J. Mater. Chem. A*, vol. 1, no. 23, pp. 6723–6726, 2013.

[40] V. J. Sovilj and L. B. Petrović, "Influence of hydroxypropylmethyl cellulose–sodium dodecylsulfate interaction on the solution conductivity and viscosity and emulsion stability," *Carbohydrate polymers*, vol. 64, no. 1, pp. 41–49, 2006.

[41] S. M. Silva, F. E. Antunes, J. J. Sousa, A. J. Valente, and A. A. Pais, "New insights on the interaction between hydroxypropylmethyl cellulose and sodium dodecyl sulfate," *Carbohydrate Polymers*, vol. 86, no. 1, pp. 35–44, 2011.

[42] L. E. Rodd, T. P. Scott, J. J. Cooper-White, and G. H. McKinley, "Capillary break-up rheometry of low-viscosity elastic fluids," *Applied Rheology*, vol. 15, no. 1, pp. 12–27, 2005.

[43] L. Y. Yeo and J. R. Friend, "Ultrafast microfluidics using surface acoustic waves," *Biomicrofluidics*, vol. 3, no. 1, p. 012002, 2009.

[44] M. K. Tan, J. R. Friend, and L. Y. Yeo, "Interfacial jetting phenomena induced by focused surface vibrations," *Physical Review Letters*, vol. 103, no. 2, p. 024501, 2009.

[45] A. Alexandrou, A. Bazilevskii, V. Entov, A. Rozhkov, and A. Sharaf, "Breakup of a capillary bridge of suspensions," *Fluid Dyn.*, vol. 45, no. 6, pp. 952–964, 2010.

[46] V. T. O'Brien and M. E. Mackay, "Shear and elongation flow properties of kaolin suspensions," *J. Rheol. (1978-present)*, vol. 46, no. 3, pp. 557–572, 2002.

[47] B. B. Mandelbrot, *The fractal geometry of nature*, vol. 173. Macmillan, 1983.

[48] B. B. Mandelbrot, "How long is the coast of Britain," *Science*, vol. 156, no. 3775, pp. 636–638, 1967.

[49] C. Keary, "Characterization of methocel cellulose ethers by aqueous sec with multiple detectors," *Carbohydrate polymers*, vol. 45, no. 3, pp. 293–303, 2001.

[50] C. Dushkin and T. H. Iliev, "Dynamic surface tension of micellar solutions studied by the maximum bubble pressure method," *Colloid and Polymer Science*, vol. 272, no. 9, pp. 1157–1165, 1994.

[51] R. B. Bird, R. Armstrong, and O. Hassager, "Dynamics of polymeric liquids. vol. 1: Fluid mechanics," 1987.

[52] S. Magdassi, *The chemistry of inkjet inks.* World scientific Singapore, 2010.

[53] A. A. Tracton, *Coatings technology handbook.* CRC Press, 2005.

[54] R. Fernando, L.-L. Xing, and J. Glass, "Rheology parameters controlling spray atomization and roll misting behavior of waterborne coatings," *Prog. Org. Coat.*, vol. 40, no. 1, pp. 35–38, 2000.

[55] V. Bergeron, D. Bonn, J. Y. Martin, and L. Vovelle, "Controlling droplet deposition with polymer additives," *Nature*, vol. 405, no. 6788, pp. 772–775, 2000.

[56] G. G. Fuller, C. A. Cathey, B. Hubbard, and B. E. Zebrowski, "Extensional viscosity measurements for low-viscosity fluids," *Journal of Rheology (1978-present)*, vol. 31, no. 3, pp. 235–249, 1987.

[57] American Institute of Physics, Monterey, 2008.

[58] V. V. Varadan, V. K. Varadan, X. Bao, S. Ramanathan, and D. Piscotty, "Wireless passive idt strain microsensor," *Smart Materials and Structures*, vol. 6, no. 6, p. 745, 1997.

[59] H. Meier, T. Baier, and G. Riha, "Miniaturization and advanced functionalities of saw devices," *Microwave Theory and Techniques, IEEE Transactions on*, vol. 49, no. 4, pp. 743–748, 2001.

[60] C. Campbell, *Surface acoustic wave devices and their signal processing applications.* Elsevier, 2012.

[61] G. McHale, M. Newton, M. Banerjee, and J. Cowen, "Acoustic wave–liquid interactions," *Materials Science and Engineering: C*, vol. 12, no. 1, pp. 17–22, 2000.

[62] J. Friend and L. Y. Yeo, "Microscale acoustofluidics: Microfluidics driven via acoustics and ultrasonics," *Reviews of Modern Physics*, vol. 83, no. 2, p. 647, 2011.

[63] D. Royer and E. Dieulesaint, "Elastic waves in solids i: Free and guided propagation, translated by dp morgan," *Springer-Verlag, New York*, 2000.

[64] M. K. Tan, J. R. Friend, and L. Y. Yeo, "Microparticle collection and concentration via a miniature surface acoustic wave device," *Lab on a Chip*, vol. 7, no. 5, pp. 618–625, 2007.

[65] R. Cox and H. Brenner, "The lateral migration of solid particles in poiseuille flow—i theory," *Chemical Engineering Science*, vol. 23, no. 2, pp. 147–173, 1968.

[66] P. Vasseur and R. Cox, "The lateral migration of a spherical particle in two-dimensional shear flows," *Journal of Fluid Mechanics*, vol. 78, no. 02, pp. 385–413, 1976.

[67] D. Leighton and A. Acrivos, "The shear-induced migration of particles in concentrated suspensions," *Journal of Fluid Mechanics*, vol. 181, pp. 415–439, 1987.

[68] M. B. Dentry, L. Y. Yeo, and J. R. Friend, "Frequency effects on the scale and behavior of acoustic streaming," *Physical Review E*, vol. 89, no. 1, p. 013203, 2014.

[69] P. Brunet, M. Baudoin, O. B. Matar, and F. Zoueshtiagh, "Droplet displacements and oscillations induced by ultrasonic surface acoustic waves: a quantitative study," *Physical Review E*, vol. 81, no. 3, p. 036315, 2010.

[70] Z. Guttenberg, H. Müller, H. Habermüller, A. Geisbauer, J. Pipper, J. Felbel, M. Kielpinski, J. Scriba, and A. Wixforth, "Planar chip device for pcr and hybridization with surface acoustic wave pump," *Lab on a Chip*, vol. 5, no. 3, pp. 308–317, 2005.

[71] A. Wixforth, C. Strobl, C. Gauer, A. Toegl, J. Scriba, and Z. v. Guttenberg, "Acoustic manipulation of small droplets," *Analytical and bioanalytical chemistry*, vol. 379, no. 7-8, pp. 982–991, 2004.

[72] A. E. Rajapaksa, J. J. Ho, A. Qi, R. Bischof, T.-H. Nguyen, M. Tate, D. Piedrafita, M. P. McIntosh, L. Y. Yeo, E. Meeusen, R. L. Coppel, and J. R. Friend, "Effective pulmonary delivery of an aerosolized plasmid DNA vaccine via surface acoustic wave nebulization.," *Respir. Res.*, vol. 15, p. 60, 2014.

[73] M. Alvarez, J. Friend, and L. Y. Yeo, "Rapid generation of protein aerosols and nanoparticles via surface acoustic wave atomization," *Nanotechnology*, vol. 19, no. 45, p. 455103, 2008.

[74] A. Qi, J. R. Friend, L. Y. Yeo, D. A. Morton, M. P. McIntosh, and L. Spiccia, "Miniature inhalation therapy platform using surface acoustic wave microfluidic atomization," *Lab on a Chip*, vol. 9, no. 15, pp. 2184–2193, 2009.

[75] A. S. Dukhin and P. J. Goetz, "Bulk viscosity and compressibility measurement using acoustic spectroscopy," *The Journal of chemical physics*, vol. 130, no. 12, p. 124519, 2009.

[76] J. David and N. Cheeke, "Fundamentals and applications of ultrasonic waves," *Physics Department Concordia University Montreal, Quebec, Canada*, 2002.

[77] S. Shiokawa, Y. Matsui, and T. Ueda, "Liquid streaming and droplet formation caused by leaky rayleigh waves," in *Ultrasonics Symposium, 1989. Proceedings., IEEE 1989*, pp. 643–646, IEEE, 1989.

[78] K. Dransfeld and E. Salzmann, "Excitation, detection, and attenuation of high-frequency elastic surface waves," *Physical acoustics*, vol. 7, pp. 219–272, 2012.

[79] J. Lighthill, "Acoustic streaming," *Journal of sound and vibration*, vol. 61, no. 3, pp. 391–418, 1978.

[80] M. K. Tan, J. R. Friend, O. K. Matar, and L. Y. Yeo, "Capillary wave motion excited by high frequency surface acoustic waves," *Physics of Fluids (1994-present)*, vol. 22, no. 11, p. 112112, 2010.

[81] O. Manor, M. Dentry, J. R. Friend, and L. Y. Yeo, "Substrate dependent drop deformation and wetting under high frequency vibration," *Soft Matter*, vol. 7, no. 18, pp. 7976–7979, 2011.

[82] H. Gonzalez, F. McCluskey, A. Castellanos, and A. Barrero, "Stabilization of dielectric liquid bridges by electric fields in the absence of gravity," *Journal of Fluid Mechanics*, vol. 206, pp. 545–561, 1989.

[83] B. Derby, "Bioprinting: inkjet printing proteins and hybrid cell-containing materials and structures," *J. Mater. Chem.*, vol. 18, no. 47, pp. 5717–5721, 2008.

[84] G. M. Nishioka, A. A. Markey, and C. K. Holloway, "Protein damage in drop-on-demand printers," *J. Am. Chem. Soc.*, vol. 126, no. 50, pp. 16320–16321, 2004.

[85] C. C. Cook, T. Wang, and B. Derby, "Inkjet delivery of glucose oxidase.," *Chem. Commun. (Cambridge, U. K.)*, vol. 46, pp. 5452–4, Aug 2010.

[86] S. L. Anna and G. H. McKinley, "Elasto-capillary thinning and breakup of model elastic liquids," *Journal of Rheology (1978-present)*, vol. 45, no. 1, pp. 115–138, 2001.

[87] V. Entov and E. Hinch, "Effect of a spectrum of relaxation times on the capillary thinning of a filament of elastic liquid," *J. Non-Newtonian Fluid Mech.*, vol. 72, no. 1, pp. 31–53, 1997.

[88] V. Tirtaatmadja, G. H. McKinley, and J. J. Cooper-White, "Drop formation and breakup of low viscosity elastic fluids: Effects of molecular weight and concentration," *Physics of Fluids (1994-present)*, vol. 18, no. 4, p. 043101, 2006.

[89] G. Tilvawala, *Using inertia-viscous stress-balances to model the mid-filament dynamics of capillary-thinning of Newtonian and non-Newtonian liquid bridges.* PhD thesis, Monash University. Faculty of Engineering. Department of Mechanical and Aerospace Engineering, 2014.

[90] M. I. Kolte and P. Szabo, "Capillary thinning of polymeric filaments," *Journal of Rheology (1978-present)*, vol. 43, no. 3, pp. 609–625, 1999.

[91] A. U. Chen, P. K. Notz, and O. A. Basaran, "Computational and experimental analysis of pinch-off and scaling.," *Phys. Rev. Lett.*, vol. 88, p. 174501, Apr 2002.

[92] M. Renardy, “A numerical study of the asymptotic evolution and breakup of Newtonian and viscoelastic jets,” *Journal of non-Newtonian fluid mechanics*, vol. 59, no. 2, pp. 267–282, 1995.

[93] D. T. Papageorgiou, “On the breakup of viscous liquid threads,” *Physics of Fluids (1994-present)*, vol. 7, no. 7, pp. 1529–1544, 1995.

[94] J. Eggers, “Universal pinching of 3d axisymmetric free-surface flow,” *Physical Review Letters*, vol. 71, no. 21, p. 3458, 1993.

[95] J. Eggers, “Nonlinear dynamics and breakup of free-surface flows,” *Reviews of modern physics*, vol. 69, no. 3, p. 865, 1997.

[96] M. P. Brenner, J. R. Lister, and H. A. Stone, “Pinching threads, singularities and the number 0.0304...,” *Physics of Fluids (1994-present)*, vol. 8, no. 11, pp. 2827–2836, 1996.

[97] W. Press, S. Teukolsky, W. Vetterling, and B. Flannery, “Numerical recipes in fortran 77: The art of scientific computing, 933 pp,” 1992.

[98] M. P. Brenner, X. Shi, and S. R. Nagel, “Iterated instabilities during droplet fission,” *Physical review letters*, vol. 73, no. 25, p. 3391, 1994.

[99] H. M. López, J. Gachelin, C. Douarche, H. Auradou, and E. Clément, “Turning bacteria suspensions into superfluids,” *Physical review letters*, vol. 115, no. 2, p. 028301, 2015.

[100] D. Saintillan, “Extensional rheology of active suspensions,” *Physical Review E*, vol. 81, no. 5, p. 056307, 2010.

[101] S. J. Tan, M. J. Campolongo, D. Luo, and W. Cheng, “Building plasmonic nanostructures with DNA,” *Nat. Nanotechnol.*, vol. 6, no. 5, pp. 268–276, 2011.

[102] B. K. Park, D. Kim, S. Jeong, J. Moon, and J. S. Kim, “Direct writing of copper conductive patterns by ink-jet printing,” *Thin Solid Films*, vol. 515, no. 19, pp. 7706–7711, 2007.

[103] Y. Lee, J.-r. Choi, K. J. Lee, N. E. Stott, and D. Kim, “Large-scale synthesis of copper nanoparticles by chemically controlled reduction for applications of inkjet-printed electronics,” *Nanotechnology*, vol. 19, no. 41, p. 415604, 2008.

[104] K. Lawrie, A. Mills, and D. Hazafy, “Simple inkjet-printed, uv-activated oxygen indicator,” *Sens. Actuators, B*, vol. 176, pp. 1154–1159, 2013.

[105] M. Grouchko, A. Kamyshny, and S. Magdassi, “Formation of air-stable copper–silver core–shell nanoparticles for inkjet printing,” *J. Mater. Chem.*, vol. 19, no. 19, pp. 3057–3062, 2009.

[106] J.-W. Song, J. Kim, Y.-H. Yoon, B.-S. Choi, J.-H. Kim, and C.-S. Han, “Inkjet printing of single-walled carbon nanotubes and electrical characterization of the line pattern,” *Nanotechnology*, vol. 19, no. 9, p. 095702, 2008.

[107] P. Chen, H. Chen, J. Qiu, and C. Zhou, “Inkjet printing of single-walled carbon nanotube/ruo2 nanowire supercapacitors on cloth fabrics and flexible substrates,” *Nano Res.*, vol. 3, no. 8, pp. 594–603, 2010.

[108] A. Russo, B. Y. Ahn, J. J. Adams, E. B. Duoss, J. T. Bernhard, and J. A. Lewis, “Pen-on-paper flexible electronics,” *Adv. Mater.*, vol. 23, no. 30, pp. 3426–3430, 2011.

[109] Y. Tao, Y. Tao, L. Wang, B. Wang, Z. Yang, and Y. Tai, “High-reproducibility, flexible conductive patterns fabricated with silver nanowire by drop or fit-to-flow method.,” *Nanoscale Res. Lett.*, vol. 8, no. 1, p. 147, 2013.

[110] I. N. Kholmanov, S. H. Domingues, H. Chou, X. Wang, C. Tan, J.-Y. Kim, H. Li, R. Piner, A. J. Zarbin, and R. S. Ruoff, “Reduced graphene oxide/copper nanowire hybrid films as high-performance transparent electrodes,” *ACS nano*, vol. 7, no. 2, pp. 1811–1816, 2013.

[111] S. Nam, H. W. Cho, S. Lim, D. Kim, H. Kim, and B. J. Sung, "Enhancement of electrical and thermomechanical properties of silver nanowire composites by the introduction of nonconductive nanoparticles: experiment and simulation," *ACS nano*, vol. 7, no. 1, pp. 851–856, 2012.

[112] C. Subramaniam, T. Yamada, K. Kobashi, A. Sekiguchi, D. N. Futaba, M. Yumura, and K. Hata, "One hundred fold increase in current carrying capacity in a carbon nanotube-copper composite," *Nature communications*, vol. 4, 2013.

[113] M. Amjadi, A. Pichitpajongkit, S. Lee, S. Ryu, and I. Park, "Highly stretchable and sensitive strain sensor based on silver nanowire–elastomer nanocomposite," *ACS nano*, vol. 8, no. 5, pp. 5154–5163, 2014.

[114] Y. Chen, Z. Ouyang, M. Gu, and W. Cheng, "Mechanically strong, optically transparent, giant metal superlattice nanomembranes from ultrathin gold nanowires," *Advanced Materials*, vol. 25, no. 1, pp. 80–85, 2013.

[115] J. H. Lee, P. Lee, D. Lee, S. S. Lee, and S. H. Ko, "Large-scale synthesis and characterization of very long silver nanowires via successive multistep growth," *Cryst. Growth Des.*, vol. 12, no. 11, pp. 5598–5605, 2012.

[116] H. Wu, D. Kong, Z. Ruan, P.-C. Hsu, S. Wang, Z. Yu, T. J. Carney, L. Hu, S. Fan, and Y. Cui, "A transparent electrode based on a metal nanotrough network," *Nat. Nanotechnol.*, vol. 8, no. 6, pp. 421–425, 2013.

[117] C. Mayousse, C. Celle, E. Moreau, J.-F. Mainguet, A. Carella, and J.-P. Simonato, "Improvements in purification of silver nanowires by decantation and fabrication of flexible transparent electrodes. application to capacitive touch sensors," *Nanotechnology*, vol. 24, no. 21, p. 215501, 2013.

[118] J. LaDou, "Printed circuit board industry," *International journal of hygiene and environmental health*, vol. 209, no. 3, pp. 211–219, 2006.

[119] A. R. Rathmell and B. J. Wiley, "The synthesis and coating of long, thin copper nanowires to make flexible, transparent conducting films on plastic substrates," *Adv. Mater.*, vol. 23, no. 41, pp. 4798–4803, 2011.

[120] C.-H. Liu and X. Yu, "Silver nanowire-based transparent, flexible, and conductive thin film," *Nanoscale Res. Lett*, vol. 6, no. 1, p. 75, 2011.

[121] A. R. Rathmell, M. Nguyen, M. Chi, and B. J. Wiley, "Synthesis of oxidation-resistant cupronickel nanowires for transparent conducting nanowire networks," *Nano Lett.*, vol. 12, no. 6, pp. 3193–3199, 2012.

[122] G. Kim, L. Shao, K. Zhang, and K. P. Pipe, "Engineered doping of organic semiconductors for enhanced thermoelectric efficiency," *Nat. Mater.*, vol. 12, no. 8, pp. 719–723, 2013.

[123] J.-W. Lim, D.-Y. Cho, S.-I. Na, H.-K. Kim, *et al.*, "Simple brush-painting of flexible and transparent ag nanowire network electrodes as an alternative ito anode for cost-efficient flexible organic solar cells," *Sol. Energy Mater. Sol. Cells*, vol. 107, pp. 348–354, 2012.

[124] J.-A. Jeong and H.-K. Kim, "Ag nanowire percolating network embedded in indium tin oxide nanoparticles for printable transparent conducting electrodes," *Appl. Phys. Lett.*, vol. 104, no. 7, p. 071906, 2014.

[125] J. Mewis and A. Metzner, "The rheological properties of suspensions of fibres in Newtonian fluids subjected to extensional deformations," *J. Fluid Mech.*, vol. 62, no. 03, pp. 593–600, 1974.

[126] G. Batchelor, "The effect of brownian motion on the bulk stress in a suspension of non-spherical particles," *J. Fluid Mech.*, vol. 83, no. 01, pp. 97–117, 1977.

[127] C. J. Petrie, “The rheology of fibre suspensions,” *J. Non-Newtonian Fluid Mech.*, vol. 87, no. 2, pp. 369–402, 1999.

[128] M. Layani, M. Grouchko, S. Shemesh, and S. Magdassi, “Conductive patterns on plastic substrates by sequential inkjet printing of silver nanoparticles and electrolyte sintering solutions,” *J. Mater. Chem.*, vol. 22, no. 29, pp. 14349–14352, 2012.

[129] A. M. Van den Berg, A. W. de Laat, P. J. Smith, J. Perelaer, and U. S. Schubert, “Geometric control of inkjet printed features using a gelating polymer,” *J. Mater. Chem.*, vol. 17, no. 7, pp. 677–683, 2007.

[130] I. M. Krieger and T. J. Dougherty, “A mechanism for non-Newtonian flow in suspensions of rigid spheres,” *Journal of Rheology*, vol. 3, p. 137, 1959.

[131] R. C. Ball and P. Richmond, “Dynamics of colloidal dispersions,” *Physics and Chemistry of Liquids*, vol. 9, no. 2, pp. 99–116, 1980.

[132] R. G. Larson, *The Structure and Rheology of Complex Fluids*. Oxford University Press: Oxford, 1999.

[133] P. Meakin, “Fractal aggregates,” *Advances in Colloid and Interface science*, vol. 28, pp. 249–331, 1987.

[134] R. Klein and P. Meakin, “Universality in colloid aggregation,” *Nature*, vol. 339, 1989.

[135] A. O. Pinchuk, “Size-dependent hamaker constant for silver nanoparticles,” *The Journal of Physical Chemistry C*, vol. 116, no. 37, pp. 20099–20102, 2012.

[136] F. Duan, D. Kwek, and A. Crivoi, “Viscosity affected by nanoparticle aggregation in al2o3-water nanofluids,” *Nanoscale research letters*, vol. 6, no. 1, pp. 1–5, 2011.

[137] M. Pastoriza-Gallego, C. Casanova, R. Páramo, B. Barbés, J. Legido, and M. Piñeiro, “A study on stability and thermophysical properties (density and viscosity) of al2o3 in water nanofluid,” *Journal of Applied Physics*, vol. 106, no. 6, p. 064301, 2009.

[138] V. Starov, V. Zhdanov, M. Meireles, and C. Molle, “Viscosity of concentrated suspensions: influence of cluster formation.,” *Advances in colloid and interface science*, vol. 96, pp. 279–93, Feb 2002.

[139] P. d’Haene, J. Mewis, and G. Fuller, “Scattering dichroism measurements of flow-induced structure of a shear thickening suspension,” *Journal of colloid and interface science*, vol. 156, no. 2, pp. 350–358, 1993.

[140] J. W. Bender and N. J. Wagner, “Optical measurement of the contributions of colloidal forces to the rheology of concentrated suspensions,” *Journal of colloid and interface science*, vol. 172, no. 1, pp. 171–184, 1995.

[141] V. T. O’Brien and M. E. Mackay, “Stress components and shear thickening of concentrated hard sphere suspensions,” *Langmuir*, vol. 16, no. 21, pp. 7931–7938, 2000.

[142] J. F. Brady and G. Bossis, “The rheology of concentrated suspensions of spheres in simple shear flow by numerical simulation,” *Journal of Fluid Mechanics*, vol. 155, pp. 105–129, 1985.

[143] P. Perepelkin, V. Starov, and A. Filippov, “Permeability of a suspension of porous particles. cellular model,” *Colloid journal of the Russian Academy of Sciences*, vol. 54, no. 2, pp. 257–262, 1992.

[144] H. Brenner and J. Happel, “Low reynolds number hydrodynamics,” 1965.

[145] S.-Q. Zhou, R. Ni, and D. Funfschilling, “Effects of shear rate and temperature on viscosity of alumina polyalphaolefins nanofluids,” *Journal of Applied Physics*, vol. 107, no. 5, p. 054317, 2010.

[146] G. Bossis and J. F. Brady, “The rheology of brownian suspensions,” *The Journal of chemical physics*, vol. 91, no. 3, pp. 1866–1874, 1989.

[147] I. Bashkirtseva, A. Y. Zubarev, L. Y. Iskakova, and L. Ryashko, “On rheophysics of high-concentrated suspensions,” *Colloid J.*, vol. 71, no. 4, pp. 446–454, 2009.

[148] E. D. Goddard, K. P. Ananthapadmanabhan, *et al.*, *Interactions of surfactants with polymers and proteins*. CRC press, 1993.

[149] E. Goddard, “Polymer/surfactant interaction: interfacial aspects,” *Journal of Colloid and Interface Science*, vol. 256, no. 1, pp. 228–235, 2002.

[150] G. Akay, A. Hassan-Raeisi, D. C. Tuncaboylu, N. Orakdogen, S. Abdurrahmanoglu, W. Oppermann, and O. Okay, “Self-healing hydrogels formed in catanionic surfactant solutions,” *Soft Matter*, vol. 9, no. 7, pp. 2254–2261, 2013.

[151] J. F. Kennedy, G. O. Phillips, P. A. Williams, and J. Piculell, *Cellulose and cellulose derivatives: Cellucon’93 proceedings: Physico-chemical aspects and industrial applications*. Elsevier, 1995.

[152] B. Lindman and K. Thalberg, *Polymer-surfactant interactions-recent developments*. CRC Press: Boca Raton, FL, 1993.

[153] F. M. Winnik and S. T. Regismond, “Fluorescence methods in the study of the interactions of surfactants with polymers,” *Colloids and Surfaces A: Physicochemical and Engineering Aspects*, vol. 118, no. 1, pp. 1–39, 1996.

[154] C. A. Herb, R. K. Prud’homme, *et al.*, *Structure and flow in surfactant solutions*. American Chemical Society Washington, DC, 1994.

[155] H. Tan, K. Tam, V. Tirtaatmadja, R. Jenkins, and D. Bassett, “Extensional properties of model hydrophobically modified alkali-soluble associative (hase) polymer solutions,” *Journal of non-Newtonian fluid mechanics*, vol. 92, no. 2, pp. 167–185, 2000.

[156] A. Tripathi, K. C. Tam, and G. H. McKinley, “Rheology and dynamics of associative polymers in shear and extension: theory and experiments,” *Macromolecules*, vol. 39, no. 5, pp. 1981–1999, 2006.

[157] C. Rosell, J. Rojas, and C. B. De Barber, “Influence of hydrocolloids on dough rheology and bread quality,” *Food hydrocolloids*, vol. 15, no. 1, pp. 75–81, 2001.

[158] T. Sanz, A. Salvador, and S. Fiszman, “Innovative method for preparing a frozen, battered food without a prefrying step,” *Food Hydrocolloids*, vol. 18, no. 2, pp. 227–231, 2004.

[159] L.-M. Zhang, “Cellulosic associative thickeners,” *Carbohydrate Polymers*, vol. 45, no. 1, pp. 1–10, 2001.

[160] J. Siepmann and N. Peppas, “Modeling of drug release from delivery systems based on hydroxypropyl methylcellulose (hpmc),” *Advanced drug delivery reviews*, vol. 64, pp. 163–174, 2012.

[161] C.-C. Wang, M. R. Tejwani, W. J. Roach, J. L. Kay, J. Yoo, H. L. Surprenant, D. C. Monkhouse, and T. J. Pryor, “Development of near zero-order release dosage forms using three-dimensional printing (3-dp™) technology,” *Drug development and industrial pharmacy*, vol. 32, no. 3, pp. 367–376, 2006.

[162] O. E. Pérez, C. C. Sánchez, A. M. Pilosof, and J. M. R. Patino, “Kinetics of adsorption of whey proteins and hydroxypropyl-methyl-cellulose mixtures at the air–water interface,” *Journal of colloid and interface science*, vol. 336, no. 2, pp. 485–496, 2009.

[163] E. Kientz and Y. Holl, “Interactions in solution between a hydrophobic polymer and various kinds of surfactants,” *Colloid and Polymer Science*, vol. 272, no. 2, pp. 141–150, 1994.

[164] C. Clasen and W.-M. Kulicke, “Determination of viscoelastic and rheo-optical material functions of water-soluble cellulose derivatives,” *Progress in polymer science*, vol. 26, no. 9, pp. 1839–1919, 2001.

[165] F. E. Antunes, L. Gentile, L. Tavano, and C. O. Rossi, “Rheological characterization of the thermal gelation of poly (n-isopropyl-acrylamide) and poly (n-isopropylacrylamide) co-acrylic acid gum hydrogels,” *Applied Rheology*, vol. 19, no. 4, p. 42064, 2009.

[166] R. Barreiro-Iglesias, C. Alvarez-Lorenzo, and A. Concheiro, “Poly (acrylic acid) microgels (carbopol® 934)/surfactant interactions in aqueous media: Part ii: ionic surfactants,” *International journal of pharmaceutics*, vol. 258, no. 1, pp. 179–191, 2003.

[167] B. Cabane and R. Duplessix, “Organization of surfactant micelles adsorbed on a polymer molecule in water: a neutron scattering study,” *Journal de Physique*, vol. 43, no. 10, pp. 1529–1542, 1982.

[168] J. Francois, J. Dayantis, and J. Sabbadin, “Hydrodynamical behaviour of the poly (ethylene oxide)-sodium dodecylsulphate complex,” *European polymer journal*, vol. 21, no. 2, pp. 165–174, 1985.

[169] K. Holmberg, B. Jönsson, B. Kronberg, and B. Lindman, *Surfactants and polymers in aqueous solution*. Wiley, 2003.

[170] H. Lange, “Interaction between sodium alkylsulfates and polyvinylpyrrolidone in aqueous solutions,” *Kolloid-Zeitschrift and Zeitschrift fur Polymere*, vol. 243, no. 2, p. 101, 1971.

[171] L.-T. Lee, “Polymer–surfactant interactions: neutron scattering and reflectivity,” *Current opinion in colloid & interface science*, vol. 4, no. 3, pp. 205–213, 1999.

[172] R. S. Dias, A. A. Pais, M. G. Miguel, and B. Lindman, “DNA and surfactants in bulk and at interfaces,” *Colloids and Surfaces A: Physicochemical and Engineering Aspects*, vol. 250, no. 1, pp. 115–131, 2004.

[173] A. Hammarström and L.-O. Sundelöf, “Nmr study of polymer surfactant interaction in the system hpmc/sds/water,” *Colloid and Polymer Science*, vol. 271, no. 12, pp. 1129–1133, 1993.

[174] L. Patruyo, A. Müller, and A. Sáez, “Shear and extensional rheology of solutions of modified hydroxyethyl celluloses and sodium dodecyl sulfate,” *Polymer*, vol. 43, no. 24, pp. 6481–6493, 2002.

[175] M. F. Torres, A. J. Müller, M. A. Szidarovszky, and A. E. Sáez, “Shear and extensional rheology of solutions of mixtures of poly (ethylene oxide) and anionic surfactants in ionic environments,” *Journal of colloid and interface science*, vol. 326, no. 1, pp. 254–260, 2008.

[176] L. M. Landoll, “Hydrophobically modified polymers,” July 16 1985. US Patent 4,529,523.

[177] M. Bercea, C. Ioan, S. Ioan, B. Simionescu, and C. Simionescu, “Ultrahigh molecular weight polymers in dilute solutions,” *Progress in polymer science*, vol. 24, no. 3, pp. 379–424, 1999.

[178] P. P. Bhat, S. Appathurai, M. T. Harris, M. Pasquali, G. H. McKinley, and O. A. Basaran, “Formation of beads-on-a-string structures during break-up of viscoelastic filaments,” *Nature Physics*, vol. 6, no. 8, pp. 625–631, 2010.

[179] M. A. Bees and O. A. Croze, “Dispersion of biased swimming micro-organisms in a fluid flowing through a tube,” in *Proceedings of the Royal Society of London A: Mathematical, Physical and Engineering Sciences*, vol. 466, pp. 2057–2077, The Royal Society, 2010.

[180] T. T. Perkins, D. E. Smith, and S. Chu, “Single polymer dynamics in an elongational flow,” *Science*, vol. 276, no. 5321, pp. 2016–2021, 1997.

[181] A. Walther and A. H. Müller, “Janus particles,” *Soft Matter*, vol. 4, no. 4, pp. 663–668, 2008.